MEDNARODNA PODIPLOMSKA ŠOLA JOŽEFA STEFANA

JOŽEF STEFAN INTERNATIONAL POSTGRADUATE SCHOOL

JAKOB KÖNIG

$Na_{0.5}Bi_{0.5}TiO_3$-BASED MATERIALS WITH MECHANICAL-STRESS-DEPENDENT DIELECTRIC PROPERTIES

DOCTORAL DISSERTATION

LJUBLJANA, JULY 2009

$Na_{0.5}Bi_{0.5}TiO_3$-BASED MATERIALS WITH MECHANICAL-STRESS-DEPENDENT DIELECTRIC PROPERTIES

Doctoral Dissertation
Jožef Stefan International Postgraduate School
Ljubljana, Slovenia, July 2009

Supervisor: *Prof. Dr. Danilo Suvorov*

Co-supervisor: *Assist. Prof. Dr. Boštjan Jančar*

Evaluation Board:

Prof. Dr. Boštjan Zalar, "Jožef Stefan" Institute, Ljubljana, Slovenia
Prof. Dr. Zdravko Kutnjak, "Jožef Stefan" Institute, Ljubljana, Slovenia
Prof. Dr Klaus Reichmann, Technical University, Graz, Austria

Jakob König

$Na_{0.5}Bi_{0.5}TiO_3$-based materials with mechanical-stress-dependent dielectric properties

Doctoral Dissertation

Materiali s tlačno odvisnimi dielektričnimi lastnostmi na osnovi $Na_{0,5}Bi_{0,5}TiO_3$

Doktorska disertacija

Supervisor: Prof. Dr. Danilo Suvorov

Co-Supervisor: Assist. Prof. Dr. Boštjan Jančar

July 2009

MEDNARODNA PODIPLOMSKA ŠOLA JOŽEFA STEFANA
JOŽEF STEFAN INTERNATIONAL POSTGRADUATE SCHOOL
Ljubljana, Slovenia

Index

Abstract

The stress dependence of the electrical permittivity offers a convenient way of measuring pressure. This effect is suitable for static and quasi-static stress applications, where the conventional method based on the piezoelectric effect becomes inadequate. Although the principle of applying this effect for pressure sensing has been known for almost thirty years, the literature reports on the stress dependence of the permittivity are scarce. The change of the permittivity under an applied pressure is connected with the converse electrostrictive effect. This, in principle, linear effect, is of practical use in materials with a high permittivity and the associated pressure dependence. Therefore, it is of interest to study the stress dependence of high-permittivity materials like ferroelectrics and relaxor ferroelectrics.

This dissertation presents a systematic study of the characteristic features of the uniaxial stress dependence of the permittivity in lead-free $Na_{0.5}Bi_{0.5}TiO_3$-based materials that influence the applicability of the materials for pressure sensing. In the study, the properties of the relaxor ferroelectric $Na_{0.5}Bi_{0.5}TiO_3$ were modified by tailoring the samples' composition using the incipient ferroelectrics $NaTaO_3$ and $KTaO_3$, and a ferroelectric, $K_{0.5}Bi_{0.5}TiO_3$.

In the first part of the work, the mechanisms of the solid-state reaction synthesis of the materials from the $Na_{0.5}Bi_{0.5}TiO_3$–$NaTaO_3$, $Na_{0.5}Bi_{0.5}TiO_3$–$KTaO_3$ and $Na_{0.5}Bi_{0.5}TiO_3$–$K_{0.5}Bi_{0.5}TiO_3$ systems were investigated. It was found that in all three systems solid solutions were formed across the whole concentration range. However, in systems that contain potassium oxide, volatilization was observed and small quantities of potassium poly-titanate secondary phases were formed. The electrical properties of the prepared samples were measured and related to their structural characteristics. With the addition of $NaTaO_3$ and $KTaO_3$, shifting of the $Na_{0.5}Bi_{0.5}TiO_3$ phase transitions toward lower temperatures and broadening of the dielectric maximum were observed. These systems are characterized by a strong dielectric dispersion, indicating relaxor properties. Materials from the $Na_{0.5}Bi_{0.5}TiO_3$–$NaTaO_3$ system were found to be ferroelastic as well, while the materials from the $Na_{0.5}Bi_{0.5}TiO_3$–$K_{0.5}Bi_{0.5}TiO_3$ system showed ferroelectric properties at room temperature.

The uniaxial stress dependence of the permittivity was measured in materials with different polar and elastic order. The highest influence of the stress was observed in samples with a morphotropic phase composition and samples with relaxor properties. These compounds also showed the highest values of the permittivity. Materials in the ferroelectric and/or ferroelastic phase showed strong dynamic and irreversible changes of the permittivity on the application of stress and release. Such behaviour was connected with the extrinsic contributions of the macroscopic domain structure existing in these materials. The reversibility of the permittivity under cycling the uniaxial pressure was observed in the relaxor compositions of the $Na_{0.5}Bi_{0.5}TiO_3$–$KTaO_3$ system. The reversibility was related to the relaxor structure of the material, in which the polar nanoregions are dispersed in the cubic matrix and can re-orient back into the equilibrium position after the removal of the stress. Among the investigated systems, the most applicable properties were found for the compositions with the addition of 10 to 30 mol% of $KTaO_3$.

A comprehensive examination of the behaviour of the permittivity in $Na_{0.5}Bi_{0.5}TiO_3$-based materials under an applied uniaxial pressure has been carried out. It was found that materials with a macroscopic domain structure are less appropriate for pressure-sensing applications, and relaxors are preferred in order to use the converse electrostrictive effect for pressure sensing.

Povzetek

Odvisnost dielektrične konstante od zunanje (tlačne) obremenitve nudi možnost merjenja tlaka. Ta pojav je primeren predvsem za statične in kvazistatične aplikacije, kjer je običajna metoda, ki temelji na izrabi piezoelektričnega pojava, nezadostna. Čeprav je princip uporabe tega pojava za detekcijo tlaka poznan že skoraj trideset let, so literaturi podatki o tlačni odvisnosti dielektrične konstante zelo redki. Sprememba dielektričnosti v odvisnosti od zunanjega tlaka je povezana s pojavom nasprotne elektrostrikcije. Ta pojav, ki je v osnovi linearen, ima uporabno vrednost v materialih z visoko dielektričnostjo in njeno tlačno odvisnostjo. Zato je tlačno odvisnost dielektričnosti zanimivo raziskovati v materialih z visoko dielektrično konstanto, kot so feroelektriki in relaksorski feroelektriki.

V tej disertaciji je predstavljena sistematična študija karakteristik enoosne tlačne odvisnosti dielektričnosti, ki vplivajo na potencialno uporabnost materialov pri uporabi za detekcijo tlaka. V delu sem se omejil na materiale na osnovi $Na_{0,5}Bi_{0,5}TiO_3$, ki ne vsebujejo svinca. Lastnosti relaksorskega feroelektrika $Na_{0,5}Bi_{0,5}TiO_3$ sem spreminjal z modifikacijo sestave vzorcev z dodatkom $NaTaO_3$ in $KTaO_3$, ki izkazujeta lastnosti feroelektrikov v zametku, ter feroelektrika $K_{0,5}Bi_{0,5}TiO_3$.

V prvem delu študije sem raziskal sintezne mehanizme reakcije v trdnem za materiale iz sistemov $Na_{0,5}Bi_{0,5}TiO_3$–$NaTaO_3$, $Na_{0,5}Bi_{0,5}TiO_3$–$KTaO_3$ in $Na_{0,5}Bi_{0,5}TiO_3$–$K_{0,5}Bi_{0,5}TiO_3$. Ugotovil sem, da se v vseh treh sistemih trdna raztopina tvori v celotnem področju sestav. V sistemih, ki vsebujeta kalijev oksid, pa je prisotno izhlapevanje in formacija manjše količine sekundarnih faz – kalijevih polititanatov. Izmeril sem električne lastnosti sintetiziranih materialov in jih povezal z njihovimi strukturnimi lastnostmi. Z dodatkom $NaTaO_3$ in $KTaO_3$ se fazne transformacije $Na_{0,5}Bi_{0,5}TiO_3$ pomaknejo k nižjim temperaturam, dielektrični maksimum pa se razširi preko širšega temperaturnega območja. Ta dva sistema zaznamuje frekvenčna disperzija dielektričnih lastnosti, kar kaže na relaksorske lastnosti materialov iz teh sistemov. Materiali iz sistema $Na_{0,5}Bi_{0,5}TiO_3$–$NaTaO_3$ izkazujejo tudi feroelastične lastnosti, medtem ko so materiali iz sistema $Na_{0,5}Bi_{0,5}TiO_3$–$K_{0,5}Bi_{0,5}TiO_3$ pri sobni temperaturi feroelektrični.

Enoosno tlačno odvisnost dielektričnosti sem izmeril za materiale z različnim polarnim in elastičnim redom. Vpliv tlaka je bil največji v vzorcih z morfotropno fazno sestavo in v vzorcih z relaksorskimi lastnostmi. Ti vzorci so izkazovali tudi največjo vrednost dielektrične konstante. Materiali v feroelektrični in/ali feroelastični fazi so kazali izrazite dinamične in ireverzibilne spremembe dielektričnosti ob obremenitvi in po razbremenitvi. Tako obnašanje je povezano z ekstrinzičnimi prispevki makroskopske domenske strukture, ki je prisotna v teh materialih. Vzorci iz sistema $Na_{0,5}Bi_{0,5}TiO_3$–$KTaO_3$ z relaksorsko strukturo pa izkazujejo reverzibilno dielektričnost ob spreminjanju tlaka in razbremenitvi. Reverzibilnost v teh vzorcih je povezana z relaksorsko strukturo materialov, v kateri so polarni nanoskupki razpršeni po nepolarni kubični matrici in se lahko orientirajo nazaj v začetno pozicijo po prenehanju tlačne obremenitve. Med vsemi raziskanimi materiali imajo najbolj uporabne lastnosti materiali z 10 do 30 mol% $KTaO_3$.

V tej študiji sem opravil obsežno raziskavo vpliva enoosne tlačne obremenitve na dielektrične lastnosti materialov na osnovi $Na_{0,5}Bi_{0,5}TiO_3$. Ugotovil sem, da so materiali z makroskopsko domensko strukturo manj primerni za detekcijo tlaka, medtem ko so materiali z relaksorsko strukturo potencialno uporabni za merjenje tlaka na osnovi nasprotnega elektrostrikcijskega pojava.

Symbols and abbreviations

C	=	Curie-Weiss constant [/]
d	=	piezoelectric coefficient [/]
d_{50}	=	median particle size [m]
D	=	dielectric displacement [C/m^2]
e	=	strain, deformation of the sample [/]
e_s	=	spontaneous deformation [/]
E	=	electric field [V/m]
E_c	=	coercive field [V/m^2]
E_{eff}	=	effective electric field [V/m^2]
f	=	frequency [Hz]
F_e	=	electrical energy [J]
F_m	=	mechanical energy [J]
G	=	Gibbs free energy [J]
$I^+_{i,j}$	=	*j*-th ion abundance of a neutral precursor *i* [counts/s]
k	=	instrumental sensitivity constant [PaK/Hz]
K_{diss}	=	dissociation constant [/]
l	=	length [m]
M	=	voltage electrostrictive coefficient [m^2/V^2]
p	=	pressure [Pa]
p_a	=	axial pressure [Pa]
p_i	=	partial pressure [Pa]
P	=	polarization [C/m^2]
P_r	=	remanent polarization [C/m^2]
P_s	=	spontaneous polarization [C/m^2]
P_{sat}	=	saturation polarization [C/m^2]
Q	=	polarization electrostrictive coefficient [m^4/C^2]
$\tan\delta$	=	dielectric loss tangent [/]
t	=	time [s]
T_0	=	Curie-Weiss temperature [K]
T_B	=	Burns temperature [K]
T_C	=	Curie temperature [K]
T_f	=	freezing temperature [K]
T_m	=	temperature of the dielectric maximum [K]
T_t	=	ordering temperature [K]
χ	=	dielectric susceptibility [F/m]
δ	=	diffusivity of the permittivity peak [/]
ε	=	permittivity [F/m]
ε_0	=	permittivity of vacuum [8.854×10^{-12} F/m]
ε_{max}	=	permittivity of the dielectric maximum [F/m]
ε_r	=	relative permittivity [/]
σ	=	stress [N/m^2]
σ_C	=	coercive stress [N/m^2]

BM = ball milling
BSE = backscattered electrons
BT = $BaTiO_3$
CIP = cold isostatic pressing
DTA = differential thermal analysis
EDS = energy-dispersive X-ray spectroscopy
KBT = $K_{0.5}Bi_{0.5}TiO_3$
KEMS = Knudsen effusion mass spectroscopy
KTa = $KTaO_3$
MPB = morphotropic phase boundary
NBT = $Na_{0.5}Bi_{0.5}TiO_3$
NTa = $NaTaO_3$
PLZT = $Pb_{1-x}La_x(Zr_{1-y}Ti_y)_{1-x/4}O_3$
PMN = $Pb(Mg_{1/3}Nb_{2/3})O_3$
PZT = $Pb(Zr_{1-x}Ti_x)O_3$
SEI = secondary electron imaging
SEM = scanning electron microscopy
TGA = thermo-gravimetric analysis
WDS = wavelength-dispersive X-ray spectroscopy
XAFS = X-ray absorption fine structure
XRD = X-ray diffraction

1 Introduction

Nowadays, so-called “smart” materials [1] are being implemented in almost every system to control or adapt its operation. In the field of pressure sensing several methods are used, depending on the frequency of the measured signal. The methods are based on various physical phenomena, such as piezoelectricity, piezoresistivity, capacitance, etc. For high-frequency applications the piezoelectric effect is exploited. Piezoelectric materials are usually in the form of a polycrystalline ceramic material and have to be poled to show an applicable macroscopic effect. The drawbacks of the piezoelectric effect are the depolarization at high temperatures (above, or even below, the temperature of the phase transition) or under high stress conditions, and its limited capability to be used for static applications. Additionally, in piezoelectric materials (in general they are polycrystalline ferroelectric materials) multiple electromechanical coupling phenomena coexist, i.e., ferroelectricity, ferroelasticity, piezoelectricity, electrostriction, etc. Thus, a variety of linear and nonlinear coupling and hysteresis phenomena can be observed in these materials [2].

A classic solution for static and quasi-static applications is the use of capacitive sensors [3], based on the change of the dimensions and, therefore, the capacitance of a cavity under pressure. The converse electrostrictive effect, i.e., the stress dependence of the permittivity, offers another possible method for measuring the stress or pressure, known for almost thirty years [4]. This, in principle, linear effect, has potential applicability for pressure-sensor applications. The practical use of the converse electrostrictive effect requires materials with a high permittivity and the associated pressure dependence, a permittivity stable with time and a low temperature coefficient of the permittivity [4]. Relaxor ferroelectrics, with their diffuse phase transition, possessing a high permittivity and a small temperature dependence of the permittivity are good candidates for this type of sensors.

The stress dependence of the permittivity is based on the electrostrictive effect, which is the basic nonlinear electromechanical coupling phenomenon present in all materials, regardless of their symmetry group. It is proportional to the square of the permittivity and it is therefore of interest to study the stress sensitivity of high-permittivity materials like ferroelectrics and relaxor ferroelectrics.

The purpose of this chapter is to provide a general overview of the present knowledge in the field of ferroelectric and relaxor materials. The electromechanical phenomena inherent to these materials are introduced. In addition, the existing literature on the stress dependence of the permittivity and $Na_{0.5}Bi_{0.5}TiO_3$ is presented.

1.1 Dielectrics and ferroelectrics

1.1.1 Dielectric response

A dielectric is a material that becomes polarized in an electric field, and thus exhibits a bulk dipole moment. The dipole moment results from the reversible displacements of the centres of positive and negative charges from their equilibrium positions (Figure 1).

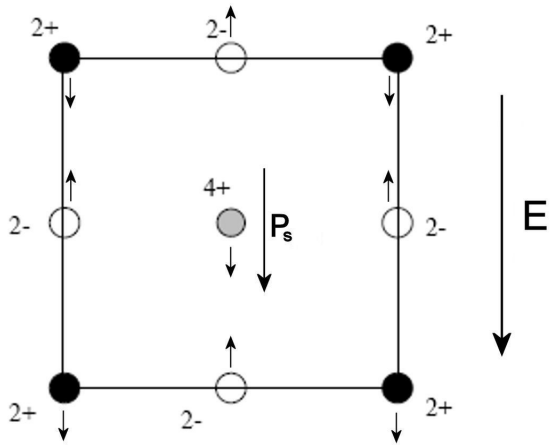

Figure 1: Plane view of a unit cell possessing a centre of symmetry. In the unloaded state, the centres of positive and negative charges are located in the same position in the centre of the unit cell. Under the action of an electric field (E), the centres of the positive and negative charges will be shifted in opposite directions (indicated by the small arrows) and, thus, a dipole moment will be induced (P_s).

For a linear dielectric response [5], observed in paraelectric materials, the dipole moment per unit volume, i.e., the electric polarization P, is related to the applied field E as:

$$P = \chi E \tag{1}$$

where χ is the electric susceptibility. The physical quantity corresponding to the stored electric charge per unit area is called the electric displacement D, and is defined as follows:

$$D = \varepsilon_0 E + P \tag{2}$$

where ε_0 is the permittivity of vacuum (8.854×10^{-12} F/m). Combining Equations 1 and 2:

$$D = \varepsilon_0 E + \chi E = (\varepsilon_0 + \chi)E = \varepsilon E = \varepsilon_0 \varepsilon_r E \tag{3}$$

where ε is the dielectric permittivity and ε_r is the relative dielectric permittivity (or usually the dielectric constant or permittivity). For materials with large ε we have $D \approx P$, since $\chi \approx \varepsilon$.

A high polarizability is observed in paraelectric materials near the phase transition to the ferroelectric phase. Since the permittivity is proportional to the polarizability, these materials show a high value of the permittivity. The origin of the high permittivity in the paraelectric phase is the compensation for various kinds of microscopic forces that preserves the material in a non-polar state [5]. Because of this compensation, the force opposing the poling action of the applied electric field is relatively weak, which results in a high permittivity. The polarization in the paraelectric phase is induced only by the applied field as the centres of the positive and negative charges in these materials coincide (Figure 1).

1.1.2 Ferroelectrics

1.1.2.1 Thermodynamical description

The thermodynamic description [6] of the behaviour of a ferroelectric crystal can be obtained by considering the form of the expansion of the free energy as a function of the polarization. The free energy G, at zero stress, given by the Landau theory [5] is represented as:

$$G = G_0 + \frac{1}{2}\alpha P^2 + \frac{1}{4}\beta P^4 + \frac{1}{6}\gamma P^6 \ldots \tag{4}$$

where the coefficients α, β, γ depend on the temperature. For general considerations the first two terms of this expansion are sufficient. The equilibrium polarization in an electric field, at constant temperature, satisfies the condition:

$$\left(\frac{\partial G}{\partial P}\right) = E = \alpha P + \beta P^3 \qquad (5)$$

For stabilization of the polarized state (ferroelectric state) the coefficient α must be negative, while in the paraelectric state it must be positive. It is assumed to be a linear function of the temperature passing through zero at the Curie-Weiss temperature (T_0):

$$\alpha = \frac{(T - T_0)}{C} \qquad (6)$$

where C is the Curie-Weiss constant and T_0 is equal to, or lower than, the actual transition temperature T_C (Curie temperature). The term β determines the type of the phase transition. It is positive for a first-order phase transition and negative for a second-order phase transition.

1.1.2.2 Ferroelectric materials

The non-centrosymmetric structure of a material is a pre-requisite condition for the occurrence of the polarization. From the 32 crystal classes or point groups [7], 21 are non-centrosymmetric. In 20 of these classes one or more polar directions exist that cannot be reversed by an operation of symmetry. Materials from these classes exhibit the piezoelectric effect. In ten of this classes, called pyroelectric, polarization appears spontaneously, even in the absence of an electric field. Ferroelectrics are a subgroup of these materials, in which the spontaneous polarization vector may be switched between the equilibrium orientations by an electric field.

On the basis of crystal symmetry alone it is possible to determine which materials are piezoelectric and/or pyroelectric. In contrast, it is not possible to determine which material is ferroelectric only on the basis of crystal symmetry. Rather, ferroelectricity is an empirical distinction between one type of a pyroelectric crystal and another on the basis of an experimental observation [8]. In ferroelectrics the field required for the reorientation of the polarization is smaller than the breakdown field of the material.

When a ferroelectric crystal is cooled through the Curie temperature, a spontaneous polarization develops as the shifts of the ions decrease the symmetry of the crystal. Thus, the ferroelectric phase transition is a structural phase transition from a high-temperature non-ferroelectric (paraelectric) phase to a low-temperature ferroelectric phase. The spontaneous polarization in a ferroelectric material is defined as the difference in the dipole moment density between the paraelectric and the ferroelectric phases. Within a ferroelectric crystal, not all the unit cells have an equal direction of the spontaneous polarization. Rather, it is divided into domains. These domains are regions with unit cells of equal orientation of the polarization to maintain the electrostatic energy of the crystal at a minimum. Therefore, a cooling process through the Curie temperature does not lead to a unique orientation of the spontaneous polarization throughout a grain. If we observe a material from the macroscopic level, ceramics consist of randomly oriented grains that are further divided into domains with different orientations of the spontaneous polarizations. Thereafter, the contributions of randomly oriented domains cancel each other out and there is no net macroscopic polarization. The typical domain size in ferroelectric materials is of the order of μm [5].

The existence of multiple possible dipole orientations within the unit cell and the domain structure in ferroelectrics gives rise to a distinctive feature of the polarization hysteresis [2]. Such a hysteresis loop is shown schematically in Figure 2a. In the initial state (1) the domains are randomly oriented within the material, as indicated in the corresponding

schematic domain structure. There is no macroscopic polarization present in this state. For small electric fields, the domain structure is unchanged and the ions are only slightly shifted within their equilibrium positions. The slope of the curve is approximately linear and corresponds to the permittivity of the material measured in a weak field ($D = \varepsilon E$).

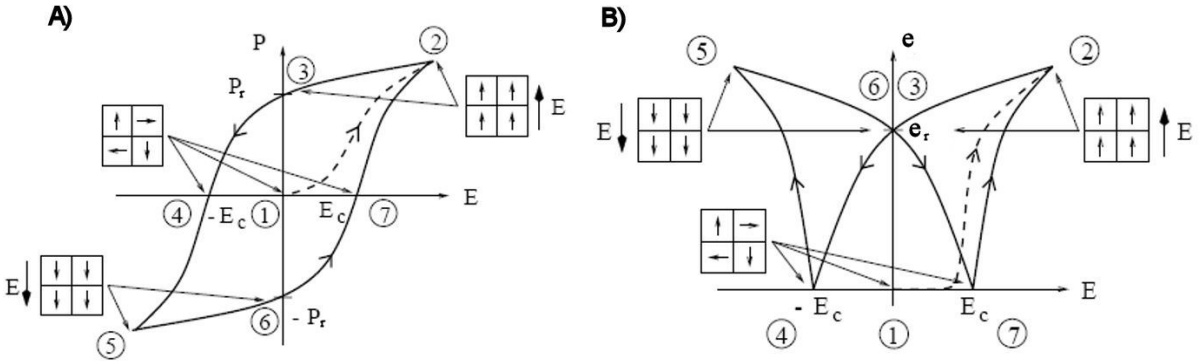

Figure 2: Schematic of A) the polarization hysteresis and B) the corresponding strain (butterfly) hysteresis, showing simplified domain-state symbols in the boxes assigned to the selected states marked by numbers. The dashed line corresponds to the first polarization process of the initially unpoled material (virgin sample). E_c, P_r and P_{sat} are the coercive field, the remanent polarization and the saturation polarization, respectively.

With an increasing electric field the slope steepens as the irreversible switching processes are initiated. This process starts at a characteristic field strength called the coercive field (E_c). As all the domains align in the direction of the electric field (2), the polarization of the material saturates, giving the maximum polarization, i.e., the saturation polarization (P_{sat}). This new equilibrium domain state is stable; therefore, when reducing the electric field to zero the polarization is preserved (3). This residual macroscopic polarization is called the remanent polarization (P_r) and is equal to, or smaller than, the saturation polarization. If the electric field is applied in the opposite direction, the material first becomes depolarized when reaching the negative value of the coercive field (4) and then saturates in (5) when all the domains are aligned in the opposite direction. Upon reversing the electric field again, the material retains the negative remanent polarization in (6) and depoles when the coercive field is reached (7).

The switching processes caused by the cycling electric field also affect the deformation state of the material. The corresponding strain hysteresis is shown in Figure 2b. Due to its distinctive shape the deformation loop is called the butterfly hysteresis. According to the domain structure, the highest elongation of the sample is achieved when all the domains are aligned in the same direction, (2) and (5). On the other hand, the macroscopically isotropic states (4), (1) and (7) exhibit no macroscopic strain. In the transverse direction the strains have opposite signs, leading to the volume-preserving changes during the switching processes [9]. The symmetry of the butterfly loop with respect to the strain axis results from the fact that only the degree of alignment of the polarization axis counts for the strain, and not the orientation of the spontaneous polarization, which can differ by 180°.

The domain-switching processes are the result of domain-wall motion. Transmission electron microscopy has shown that domain walls are usually of the order of 1–10 nm [5]. The walls separating the domains are divided into two groups: 180° domain walls, separating domains with antiparallel polarization orientation; and non-180° domain walls, separating other domains. Domain-wall motion under an applied electric field contributes to the polarization (dielectric) and deformation state of the material, thus coupling the electromechanical properties of the material. Both 180° and non-180° domain-wall motions contribute to the polarization. In contrast, only non-180° contributes to the strain (Figure 3). The switching of the polarization is assumed to be a long-distance motion of the domain walls. Short-distance motion occurs under weak (sub-switching) fields, either by vibration

and bending around an equilibrium position, or by small jumps into a new equilibrium state [10].

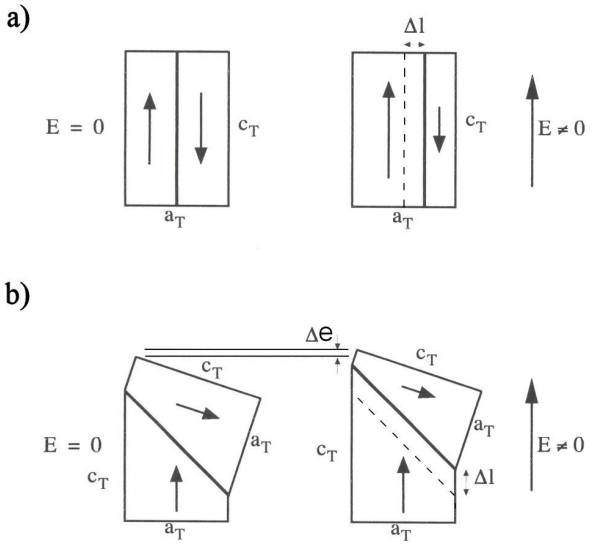

Figure 3: Domain-wall contribution to the electromechanical properties of the material (for tetragonal lattice): a) 180° domain-wall motion contributes to the polarization (Δl), and b) non-180° domain-wall motion contributes to the polarization (Δl) and strain (Δe). The arrows represent the polarization and the electric field orientation, and the broken lines denote the original positions of the domain walls.

Real ferroelectrics nearly always contain electric and elastic defects and imperfections that can interfere with the domain walls and the polarization, thus modifying the materials' properties. These extrinsic contributions may be comparable to the intrinsic contribution [11]. The role of different types of defects is emphasized by the "soft" and "hard" doping of the $Pb(Zr_{1-x}Ti_x)O_3$ (PZT) material [8], and the internal stresses decisively affect the properties of thin films [12].

A very important group of ferroelectric materials possesses the oxide perovskite structure [13] with a general formula ABX_3, where oxygen ions occupy the X-site of the structure. The ideal cubic unit cell of this relatively simple structure is shown in Figure 4. The cations on the A-site of the structure are surrounded by twelve anions in a cubo-octahedral configuration and the B-site cations are surrounded by six anions in an octahedral coordination. The A-site cations are typically larger than the B-site cations. In most cases, the structure is distorted from the ideal cubic structure with the $Pm\bar{3}m$ symmetry. This distortion of the structure arises from the distortion of the oxygen octahedra network due to the different sizes of the involved cations and their chemical nature (the mixing of molecular orbitals and/or lone-pair effects) [13].

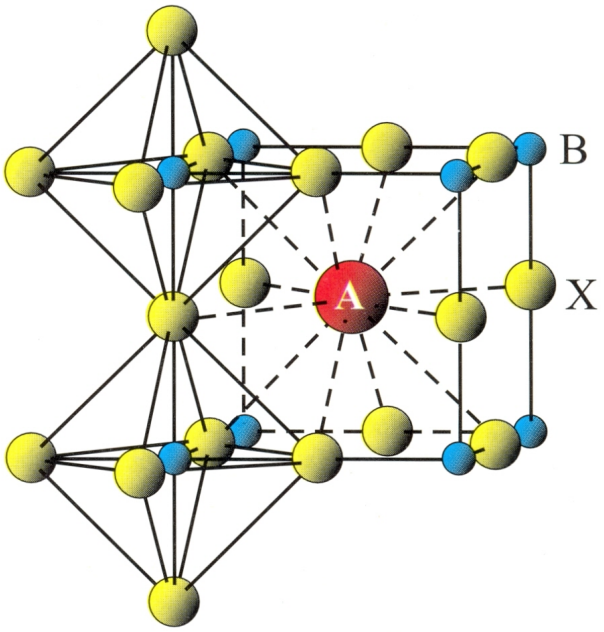

Figure 4: The ideal ABX_3 perovskite structure. The dashed and full lines designate the coordination of the A- and B-site cations, respectively.

1.2 Ferroelastics

The term ferroelasticity was introduced by Aizu [14] for crystals where the strain-stress behaviour exhibits a hysteresis (Figure 5) that is characterized by a spontaneous strain e_s, and coercive stress σ_c [15], while so-called paraelastic crystals exhibit a linear strain-stress behaviour with no hysteresis loop. There are two ingredients that make a crystal ferroelastic: (i) a phase transition between the paraelastic high-temperature, high-symmetry phase and the ferroelastic low-temperature, low-symmetry phase (this ferroelastic phase transition creates a lattice distortion); and (ii) this lattice distortion can be reoriented by an external mechanical stress.

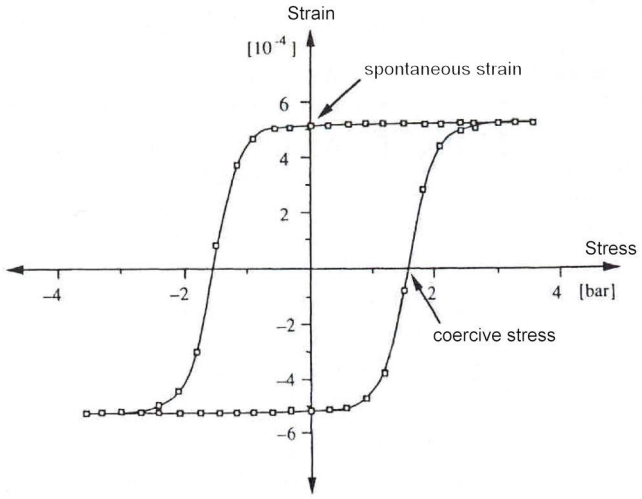

Figure 5: Strain–stress hysteresis of $Pb_3(P_{0.8}V_{0.2}O_4)_2$ showing the characteristic macroscopic spontaneous distortion and the coercive stress of the crystal.

The type of phase transition that is accompanied by a change of the point-group symmetry is called a ferroic phase transition. Ferroelectric and ferromagnetic materials are typical examples of ferroics, and ferroelastic materials are simply the mechanical analogues.

In a ferroelastic phase transition, the decrease of the symmetry is accompanied by the onset of a spontaneous strain. Thus, ferroelasticity is associated with the occurrence of spontaneous strain; spontaneous because it has a nonzero magnitude, even when no external force is applied to the crystal. The spontaneous strain is strongly influenced by the domain structure of the crystal. This domain structure is a consequence of a transformation from the paraelastic phase to the ferroelastic phase. Domains can coexist in a ferroic crystal because they are energetically equivalent, and because the crystal can minimize its free energy by splitting into an optimum number of domains. When stress is applied to a ferroelastic crystal, one direction of the domains remains stable and displays classic elastic behaviour, whereas the second direction of the domains is unstable and changes through the switching processes into the first one when the coercive stress is surpassed.

Materials exist that are simultaneously ferroelectric and ferroelastic, as do materials that are only ferroelectric or only ferroelastic. In some materials both transitions occur at the same temperature, while in others the ferroelectric and ferroelastic transitions occur at different temperatures. A great majority of the ferroelectric materials also exhibit ferroelasticity. In these materials the ferroelectric and ferroelastic domain structures coexist and are interconnected; thus, modifying one induces changes to the other (Figure 6). The ferroelastic domain structure is somewhat different to the ferroelectric one. For the mechanical stresses, the domains with the polarization switched by 180° have the same potential. Therefore, the mechanical stress will induce non-180° polarization switching only [16].

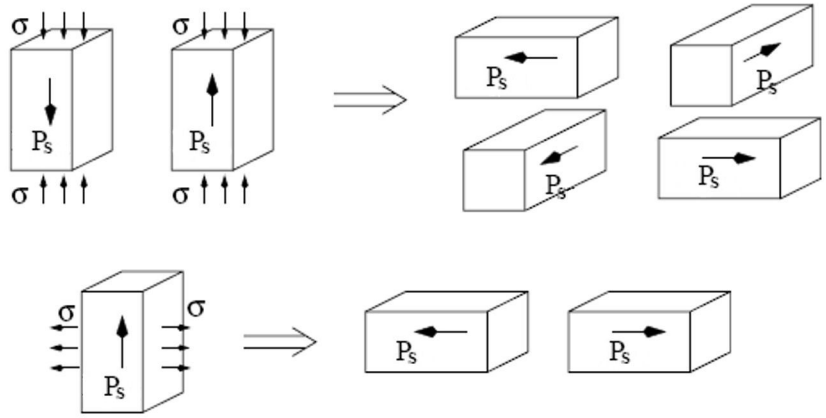

Figure 6: A mechanical stress of sufficient magnitude can switch a unit cell by 90° to the energetically more favourable position. In this way no specific orientation of the spontaneous polarization (P_s) is preferred, also when the initial polarization differs for 180°. Instead, all of the choices on the right-hand side are possible.

If a compressive stress is applied to an initially isotropic ferroelectric (and ferroelastic) material, it will deform as shown in Figure 7. For small loadings around (1), the ions will be displaced only slightly from their equilibrium positions and the material shows a linear elastic response. With a further increase in the load, switching processes start to occur at the coercive stress and a fully switched domain structure is achieved in (2). After unloading, the domain structure is basically preserved (3) and the macroscopic remanent strain induced during the compression is observed. However, the domain structure in (3) shows that the material is transversely isotropic and possess no macroscopic polarization.

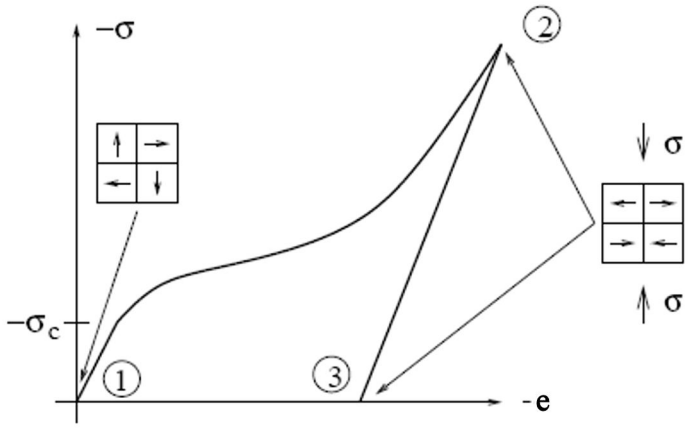

Figure 7: Schematic of the ferroelastic behaviour for the compression loading of initially unpoled material. The simplified domain state symbols in the boxes are assigned to selected states, marked by numbers.

In general, ferroelasticity is not considered as an electromechanical coupling phenomenon. However, in a simultaneously ferroelectric and ferroelastic material, in which the domain structures are interconnected, a mechanical stress that induces ferroelastic switching will change the electrical properties of the material, e.g., the dielectric and piezoelectric properties. Also, in a centrosymmetric non-ferroelectric material that possesses ferroelastic domains, the ferroelastic domain switching will modify the dielectric properties, if the permittivity of the material is non-isotropic [17].

1.3 Relaxors

Relaxors or relaxor ferroelectrics are a vast group of compounds with diffuse phase transitions. Some authors differentiate between the two terms, and define relaxor ferroelectrics as a solid-solution between a relaxor and a ferroelectric material [18]. The oxide perovskite solid solutions and complex oxide perovskites are the most investigated relaxor materials, and these are of great technological importance. Although they have been known for more than 50 years the background for the diffusion character of these materials is still not completely understood [19]. Nevertheless, according to the experimental and theoretical data in the literature, compositional disorder and the related polar nanoregions, formed at lower temperatures, are the required conditions, giving rise to unique physical properties.

In contrast to normal ferroelectrics some of the typical properties of relaxors are:

- a strong frequency dispersion of the dielectric properties and the temperature of the permittivity maximum (T_m),
- broad permittivity maxima,
- no structural phase transition across T_m,
- nano-sized polar domains that persist well above T_m,
- slim ferroelectric hysteresis loops with a small remanent polarization and a high saturation polarization,
- a field-induced transition to the ferroelectric state.

$Pb(Mg_{1/3}Nb_{2/3})O_3$ (PMN) [20] is a prototypic representative of the relaxors. It has the stoichiometric complex perovskite structure in which Mg and Nb ions fill the B-sites of the ABO_3 perovskite structure in the ratio 1:2. Other examples of relaxors are the complex perovskites ($Pb(Sc_{1/2}Nb_{1/2})O_3$, $Pb(In_{1/2}Nb_{1/2})O_3$) [21, 22], non-stoichiometric solid-solutions

($Pb_{1-x}La_x(Zr_{1-y}Ti_y)_{1-x/4}O_3$ – PLZT) [23], and homovalent solid-solutions ($Ba(Ti_{1-x}Zr_x)O_3$) [24] as well as tungsten-bronze structure oxides ($Pb_xBa_{1-x}Nb_2O_6$) [25].

Compositional disorder, i.e., the disordered distribution of different ions on the crystallographically equivalent lattice sites, is the fundamental structural characteristic of relaxor materials. The disorder that is believed to be responsible for the relaxational properties is brought about by the differences in the valence, ionic radii and electronegativities between ions on the same crystallographic positions [19]. Because of these differences, the electrostatic and elastic energies of the complex perovskite structure are minimized in the ordered state that should be the ground state of a relaxor. The ordered state can be established by site exchange via diffusion. However, due to the relaxational nature of the diffusion a nearly infinite time would be necessary to achieve order at low temperatures. Ordering is accelerated at higher temperatures, but this should not exceed the ordering temperature (T_t), at which the order can be destroyed by thermal motion [19]. In complex perovskites (e.g., $Pb(Sc_{1/2}Nb_{1/2})O_3$) T_t was experimentally determined to be around 1230°C. Metastable states with different ordering rates were obtained by annealing at temperatures around T_t and subsequent quenching. In contrast, in some other materials (e.g., PMN) the compositional order cannot be improved because the relaxation time is too long.

In real complex perovskite ceramics the quenched disorder is compositionally inhomogeneous and small ordered regions are embedded in a disordered matrix. High-resolution transmission electron microscopy on PMN revealed nano-size (2-5 nm) ordered regions [26]. The ordering of these chemical nanoregions in $Pb(B^{2+}_{1/3}B^{5+}_{2/3})O_3$ perovskites is represented in Figure 8. Such ordering [22] preserves the local stoichiometry and the B^{2+}/B^{5+} ratio is the same in the nano-regions as in the disordered regions of the material, as experimentally detected in PMN [27]. The degree of compositional disorder greatly influences the ferroelectric properties. It was shown that ordered crystals of $Pb(In_{1/2}Nb_{1/2})O_3$ [28] exhibit antiferroelectric behaviour with sharp phase transition, while in the disordered state they are relaxors. This confirms the general rule that relaxor behaviour can only be observed in compositionally disordered crystals.

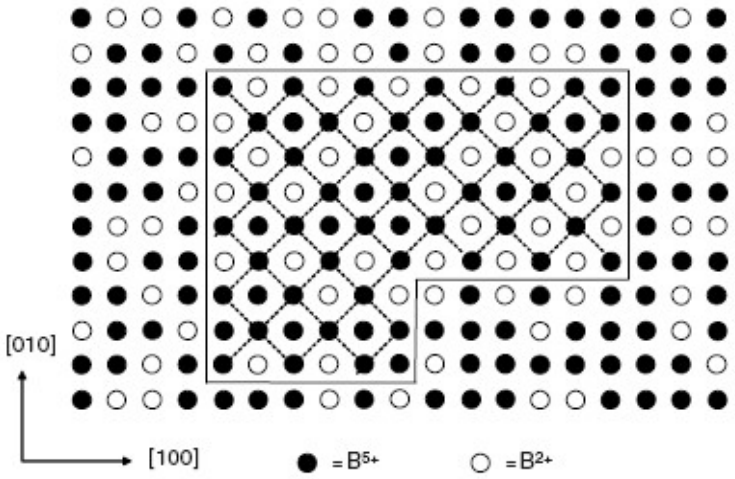

Figure 8: Schematic of the ordered chemical nanoregion (the area within the solid line) within the disordered matrix in $Pb(B^{2+}_{1/3}B^{5+}_{2/3})O_3$ perovskites according to the random-site model showing the existing B-sites. One of the two sublattices inside the ordered nanoregion (connected by dashed lines) is formed by B^{5+} ions only, while the second sublattice contains a random distribution of the B^{2+} and B^{5+} ions in the 2:1 ratio.

The average symmetry of the high-temperature paraelectric phase of all the perovskite ferroelectrics is cubic. Despite this, the local ion configuration can be distorted since the bonding between the cations and oxygen is not wholly ionic. Therefore, random displacements of the cations that are connected with ferroelectric instability [29] are present in

ferroelectrics and are also expected to occur in perovskite relaxors. Due to the different sizes and the different charges of the cations on the same lattice positions in relaxors, all ions are expected to be displaced from the special sites of the ideal perovskite structure. These permanent uncorrelated shifts of ions from the high-symmetry positions should exist in the paraelectric phase as well as at lower temperatures and were indeed detected by X-ray and neutron diffraction in PMN [30-32] and other lead-containing relaxors. They are shown schematically in Figure 9. According to the proposed spherical layer model [32], the distribution of the shifts of the Pb ion is isotropic within the spherical layer centred on the ideal Pb site with a typical radius of about 0.3 Å. The shifts of the oxygen ions form two rings parallel to the face of the cube (about 0.2 Å parallel and 0.06 Å perpendicular to the face of the cube in PMN). The displacements of the B-site ions are smaller and oriented in the direction close to [001] [33].

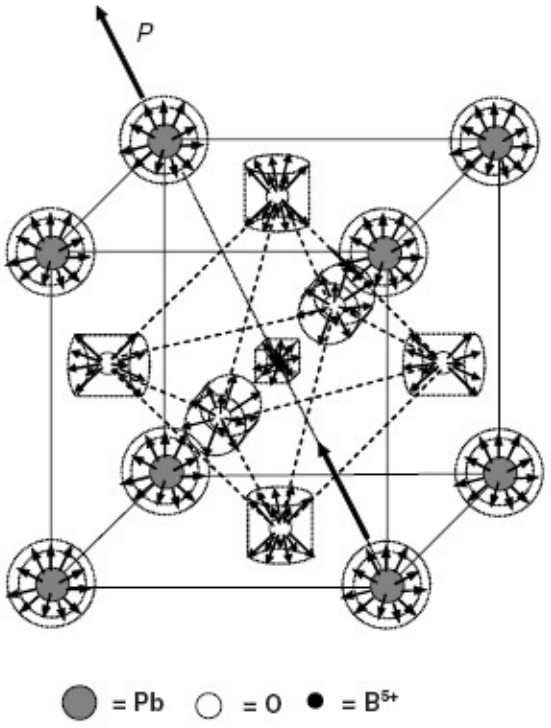

Figure 9: Characteristic uncorrelated ion displacements (shown by the small arrows) in the unit cell of the lead-containing perovskite relaxor. Below a certain temperature the displacements become correlated and thick arrows show the direction of the local spontaneous polarization caused by the correlated displacements of ions inside the polar nanoregions.

Upon cooling below a certain temperature, the displacements of some neighbouring ions become correlated and fluctuating polar nanoregions with randomly distributed directions of the dipole moments appear. This is the so-called Burns temperature T_B [34], which may occur hundreds of degrees higher than T_m and at the same time much lower than T_t [19]. The latter fact condradicts earlier suggestions that the appearance of the polar nanoregions is connected with ordering of ions on the B-site of the lattice since the compositional disorder is already frozen at that temperature. The transition at T_B can also not be considered a structural phase transition since it is not accompanied by any change of the crystal structure on the macroscopic scale. Below T_B the symmetry remains cubic; however, in some diffraction experiments weak superlattice reflections were observed, which are connected with the existence of polar nanoregions [35].

With a further decrease in the temperature the correlation and the volume fraction of the polar nanoregions increase. Moreover, their dynamics slow down enormously and, finally, two possibilities arise. If the regions become large enough (macrodomains) so as to percolate the whole sample, then the sample will be transformed to a ferroelectric phase at T_C. On the

other hand, if the nanoregions grow with decreasing temperature but do not become large enough or percolate the sample, then they will exhibit a dynamic slowing down of their fluctuations and ultimately freeze at T_f, leading to an isotropic relaxor state with a random orientation of the polar domains. The latter is typical for so-called canonical relaxors, e.g., PMN and PLZT. Different possibilities for the temperature evolution of the dielectric properties and associated different types of relaxors [19] are shown in Figure 10.

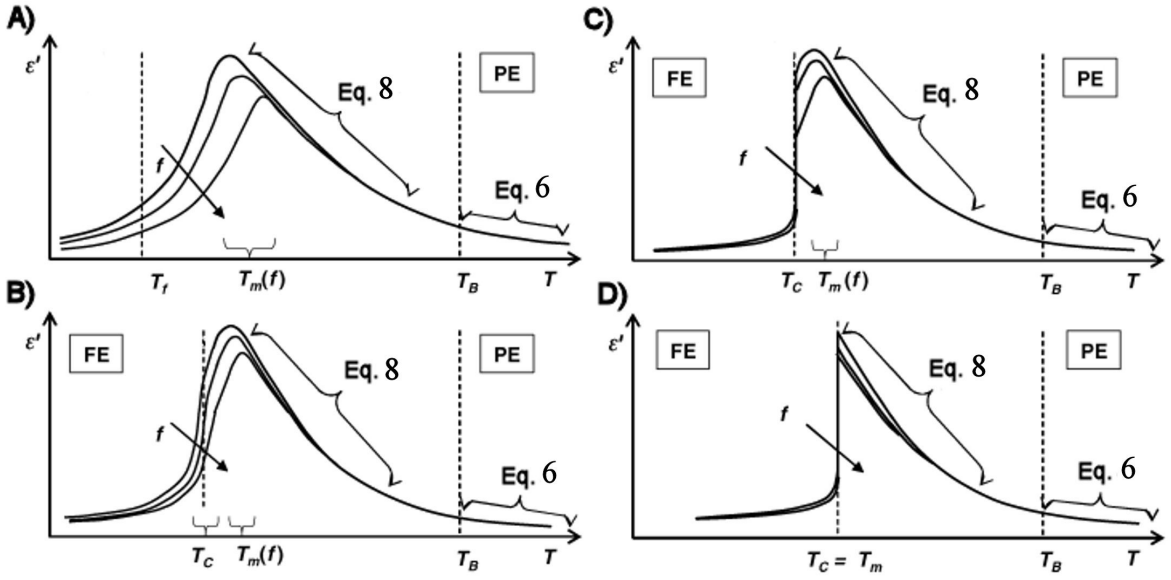

Figure 10: Different possibilities for the temperature evolution of dielectric properties in compositionally disordered perovskites: A) canonical relaxor; B) material with a diffuse relaxor-to-ferroelectric phase transition at $T_C < T_m$; C) material with a sharp relaxor-to-ferroelectric phase transition at $T_C < T_m$; D) material with a sharp relaxor-to-ferroelectric phase transition at $T_C = T_m$. The temperature intervals in which the Curie-Weiss law (Equation 6) and the Lorenz-type relation (Equation 8) hold are identified. The temperature dependencies of the dielectric properties at different frequencies, *f*, are schematically shown, with arrows indicating frequency increase.

While the existence of polar nanoregions in relaxors seems to be beyond doubt, the cause and mechanisms of their formation are not completely understood. One of the possible explanations is that the appearance of polar nanoregions is the result of local phase transitions of compositionally disordered regions [36]. Thereafter, the crystal consists of nano-sized polar islands embedded into a non-polar cubic matrix. Since the T_C of polar nanoregions is higher, local ferroelectric phase transitions occur first in those regions, while the other parts of the crystal remain in the paraelectric phase.

The most distinctive feature of a relaxor material is the significant dielectric dispersion of the permittivity maximum. This dispersion exists across the whole spectrum of frequencies, from the frequency of lattice vibrations (10^{15}–10^{17}) down to the lowest measurable frequency (10^{-5}) [19]. Different contributions can be recognized in the field-induced polarization in the temperature range of the permittivity maximum

$$\varepsilon = 1 + \chi_e + \chi_{Ph} + \chi_R + \chi_U + \chi_{LF} \qquad (7)$$

where χ_e, χ_{Ph}, χ_R, χ_U and χ_{LF} are the susceptibilities representing the electronic, phonon, conventional relaxor, universal relaxor, and low-frequency contributions, respectively.

The electronic contribution at lower frequencies is small compared with the other contributions; however, it persist up to the highest frequencies. Also, the phonon polarization is comparatively small, adding up to approximately 1% of the total low-frequency permittivity at T_m. This is in contrast to ordinary ferroelectrics where the phonon contribution totally accounts for the permittivity at the phase transition. The relaxor susceptibilities χ_R and

χ_U are the main contributions connected with peculiar relaxation-type peaks in the temperature dependences of the permittivity. The contribution of the former is constant at low enough frequencies and decreases when the frequency reaches the temperature-dependent characteristic value, while the contribution of the latter continuously decreases in the whole frequency range. These values are extraordinarily large compared to other dielectrics. The contribution of the conventional relaxor is dominant, giving rise to the diffuse peak in the vicinity of T_m. The last term in Equation 7 combines other possible relaxational contributions that are not related to the relaxor ferroelectricity (e.g., the polarization of the hopping charge carriers) and become significant at comparatively low/high frequencies.

The dielectric response of a relaxor material can be divided into several parts and described by several equations. In the paraelectric phase above T_B the dielectric constant obeys the conventional Curie-Weiss law (Equation 6), where the Curie-Weiss constant has the same order of magnitude as in ordinary ferroelectrics (~10^5 K) and T_0 is higher than T_m (except at high frequencies, where it can be smaller) [19].

$$\varepsilon = \frac{C}{(T - T_0)} \tag{6}$$

The major part of the high-temperature slope of the diffuse peak can be represented by the empirical Lorenz-type relation [37],

$$\frac{\varepsilon_A}{\varepsilon - 1} = \frac{(T - T_A)^2}{2\delta^2} \tag{8}$$

where ε_A and T_A are the fitting parameters and δ is a measure of the degree of the diffusivity of the peak. This equation is valid from a temperature that is typically several degrees higher than T_m, to a temperature which is a few dozens of degrees lower than T_B.

The third equation, the Vogel-Fulcher law, relates the temperature and the frequency of the permittivity peak [38], which is a distinctive feature of relaxors:

$$f = (2\pi\tau_0)^{-1} \exp\left[\frac{-E_a}{(T_m - T_{VF})}\right] \tag{9}$$

where f is the measurement frequency, and τ_0, E_a and T_{VF} are the fitting parameters.

The polarization mechanisms responsible for the large and diffuse permittivity peak have not been conclusively identified due to incomplete knowledge of the cause and mechanisms of the polar nanoregion's formation. Several explanations that relate the dielectric relaxation in relaxors to the polar nanoregions exist. Many authors [20, 39, 40] proceed upon the assumption that polar nanoregions can be considered as individual thermally activated dipoles giving rise to the orientation polarization. Thus, the main contribution may be attributed to the thermally activated reorientation of the dipole moments of polar nanoregions. The reorientations may be affected by the random anisotropy and by an environment of random electric and elastic fields. Another possible mechanism was developed by Glazounov and Tangantsev [41]. It predicts the side-way motion of polar nanoregion boundaries without any change of the orientation. According to this motion, the volume of the polar region changes, which gives rise to the distinctive polarization response.

According to the findings described above, the dielectric response of the relaxors arises from the existence and dynamics of the polar nanoregions. Polar nanoregions appear below the Burns temperature, T_B, and grow in number and volume upon further cooling, giving rise to the magnitude of the polarization. As the regions appear at different temperatures they differ in size and characteristic relaxation frequency, thus, their dynamics depend on frequency: the higher the frequency, the lower the number of polar nanoregions

cooperating and the lower the response of the particular nanoregion. Below a certain temperature, T_m, the dynamics of the polar nanoregions starts to slow down and the characteristic frequency-dependent permittivity maximum appears. Finally, the polar nanoregions become frozen at T_f or undergo a spontaneous phase transition into a ferroelectric phase at T_C.

1.4 Electromechanical coupling phenomena

1.4.1 Ferroelectricity and ferroelasticity

Ferroelectricity and ferroelasticity are, as was described in §1.1 and §1.2, two non-linear hysteretic phenomena that contribute to the electromechanical properties of a ceramic material. Ferroelectric domain-wall motion, under an applied electric field, contributes to the polarization and deformation state of the material, by changing the dielectric and piezoelectric properties as well as the strain of the material. In simultaneously ferroelectric and ferroelastic materials, in which the domain structures are interconnected, a mechanical stress that induces ferroelastic switching will change the electrical properties of the materials. Also, in centrosymmetric ferroelastic materials, the ferroelastic domain switching can modify dielectric properties if the permittivity of the materials is non-isotropic.

1.4.2 Piezoelectricity

Piezoelectricity [8] is a linear electromechanical coupling phenomenon observed in all non-centrosymmetric groups, except the group 432 (due to the combination of other symmetry elements). The direct piezoelectric effect is defined as a change in the polarization by an applied mechanical load, i.e., the generation of a charge between crystal surfaces on compression (Equation 10a). The converse piezoelectric effect is a linear strain ($e=\Delta l/l$) response of a material to an applied electric field (Equation 10b).

$$D = dX \tag{10a}$$

$$e = dE \tag{10b}$$

The proportional constant d that relates the electrical and mechanical quantities in these materials is called the piezoelectric constant.

The concept of piezoelectricity will be presented on the basis of the converse piezoelectric effect, described by Equation 13b. According to this relation, the electrically induced strain may be an elongation or a shortening, depending on the direction of the applied electric field. Such behaviour is observed in a unit cell that possesses a polar direction, in which the centres of the positive and negative charges are separated (Figure 11). If this unit cell is exposed to a bias DC-voltage, the positive and negative ions will be shifted with respect to each other. If the applied field has the same direction as the spontaneous polarization, the unit cell will elongate, while in the opposite case the unit cell will shorten. If the polarization vector is initially oriented in the opposite direction, the constant d has the same value but a different sign. Therefore, the property of piezoelectricity is related to the polarity of the unit cell of a material.

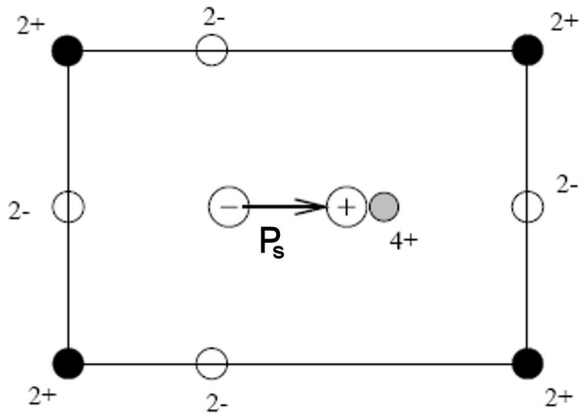

Figure 11: Plan view of a unit cell with different locations of the centres of the positive and negative charges. The arrow indicates the corresponding polarization direction existing in the unit cell.

One the most important groups of piezoelectric ceramic materials comes from the sub-group of ferroelectric materials. The existence of the spontaneous polarization in ferroelectric materials is the basis for the piezoelectric effect that is generally exploited in ferroelectric ceramics [1, 8]. As described above, a ferroelectric ceramic material cooled from a high-temperature phase exhibits a random orientation of unit cells in adjacent domains as well as a random orientation of grains. Thus, no resultant macroscopic piezoelectricity can be observed in the isotropic state of the polycrystalline material. This virgin state of the material observed after cooling from a high temperature is also called the thermally depoled state. To make the ceramics piezo-active, the domains must be aligned in the same direction by poling in an electric field. An electric field with a magnitude higher than the coercive field of the material will align the spontaneous polarization of the domains with the applied electric field. After unloading the domains will basically retain the orientation and the sample will show a macroscopic polarization, i.e., the remanent polarization. This state of a material is called the poled state, and the material now exhibits macroscopic piezoelectricity, which is exploited in technical applications. The as-prepared material exhibits a linear piezoelectricity as long as the electric field or the mechanical pressure is well below that needed to switch the polar axis. Therefore, the piezoelectric effect is applicable for loadings not exceeding certain limits, i.e., a small signal range.

Due to the ceramic nature of the sample, the line-up of domains cannot be perfect as in the single-crystal form of the material. Thus, the ideal value of remanent polarization in ceramics is smaller than that obtained for a single crystal [42]. A better alignment is observed in materials with a larger number of possible polar directions. For example, the number of possible directions of polarization is larger in morphotropic phase boundary compositions where multiple phases coexist. Therefore, the peak piezoelectric coefficients are, in general, found in morphotropic samples [8]. There are additional reasons why the practical dipole orientation in ceramics does not reach the fully oriented value. Intergranual stresses, that tend to keep the polarity of the domains in their initial orientations, and imperfections, that cause strains within the grains, also prevent switching to the most favourable direction.

Switching of the spontaneous polarization during poling is accompanied by a residual deformation of the polycrystalline material. The observed remanent strain is a macroscopic average of the spontaneous strains of the unit cells. The macroscopic strain caused by electrically induced switching contributes an additional nonlinear electromechanical coupling; however, it is usually avoided in technical applications due to fatigue problems [43]. Besides electric fields, mechanical stresses may also give rise to the switching processes since, in general, ferroelectrics are ferroelastic as well. The ferroelastic behaviour induces the non-180° switching of domains under an applied stress, which induces mechanical depolarization of a poled sample and, therefore, is undesired in piezoelectric applications.

The macroscopic piezoelectric effect of a poled ceramic compact can be ruined by the thermal, electrical or mechanical forces. If the material is heated to temperatures higher than, or just near, the Curie temperature, thermal depolarization occurs, destroying the macroscopic piezoelectricity. An electric field exceeding the coercive field of the material induces switching of the ferroelectric domains, and a high enough stress triggers the ferroelastic domain switching. All three scenarios result in a randomly oriented domain structure of the material, and therefore are to be avoided in piezoelectric applications. Nevertheless, it should be noted that the thermally depoled state is different from the electrically or mechanically depoled one.

1.4.3 Electrostriction

Electrostriction is the basic nonlinear electromechanical coupling phenomenon present in all materials, regardless of their symmetry group [44]. Even in totally isotropic materials an electric field induces strains; however, in most non-polar materials, the electrostrictive coupling is too weak to be used for technical implementations.

If an electric field is applied to a centrosymmetric material, the centres of the positive and negative charges will be separated (Figure 1). This leads to the occurrence of polarization in the direction of the electric field. If the electric field is applied in the opposite direction the positive and negative charges will be shifted in the other direction as well. However, in both situations, the centres of the charges will be separated by the same distance, leading to an elongation of the unit cell by an equal amount. Thus, the electrostrictive strain is independent of the sign of the electric field or of the sign of the polarization and can be expressed as [1, 5]

$$e = ME^2 \tag{11a}$$

$$e = QP^2 \tag{11b}$$

where M and Q are the electrostrictive coefficients in voltage and polarization notation, respectively. Consequently, electrostriction is a higher-order effect and is dominated in piezoelectric materials by the linear inverse piezoelectric effect.

The converse electrostrictive effect is related to the stress dependence of the dielectric constant. The connection between the stress or the pressure and the dielectric constant can be obtained in the following way. From Equation 11b, the electrostriction coefficient for a cubic perovskite-type crystal is defined as

$$Q = \frac{1}{2}\left(\frac{\partial^2 e}{\partial P^2}\right) \tag{12}$$

By using the Maxwell's relations, Equation 12 can be transformed to show the relationship with the permittivity

$$Q = -\frac{1}{2}\left(\frac{\partial(1/\varepsilon)}{\partial \sigma}\right) \tag{13}$$

where σ is stress. The converse electrostrictive effect offers a convenient way of measuring the electrostriction coefficients through the pressure dependence of the permittivity.

A dilemma exists regarding the converse (or inverse) effect of electrostriction: sometimes it is written that the converse electrostrictive effect does not exist [45]. The explanation of this inconsistency is as follows [2]: due to symmetry, a mechanical stress cannot induce polarization and a state with no polarization is preserved under a purely mechanical load. However, when the polarization is induced by a bias electric field, a

superposed mechanical stress will influence this polarization. Thus, there will be a change of the electric state due to mechanical loading.

As observed in most of the experimental systems [44], the $1/\varepsilon$ vs. stress curve is a straight line, since the electrostriction coefficients are approximately constant over the range of temperatures and stresses [46]. However, the experimental curves of the ferroelectrics and relaxors are not straight lines [47]. For ferroelectrics it was found that the slope of the curve can change sign over the phase-transition temperature, which indicates a sign change of the Q coefficient. This is not consistent with the directly measured Q value using Equation 11a; however, it can be explained when other effects are considered [47]. The experimental curves are deformed due to the additional contribution of the coupling between the polarization and the stress, whereas the electrostrictive coefficient has the same value. The coupling becomes important since a large part of the permittivity is from the reorientation of the polar nanoregions. This nanoregions' reorientation will also be stress dependent and may have an extra effect on the curve. Therefore, there is no firm basis for the interpretation of the converse electrostrictive effect to give a reliable electrostrictive coefficient in relaxors [47].

The electromechanical coupling behaviour in relaxors, which may be described as electrostriction, is worth examining. The major advantage of electrostrictive relaxors over ferroelectrics is in the reproducibility under cyclic drive conditions with the same order of maximum strain (Figure 12) [48]. The large electrostrictive strains in relaxors are not caused by unusually large electrostriction coefficients, but rather by unusually large induced polarizations, i.e., large dielectric constants.

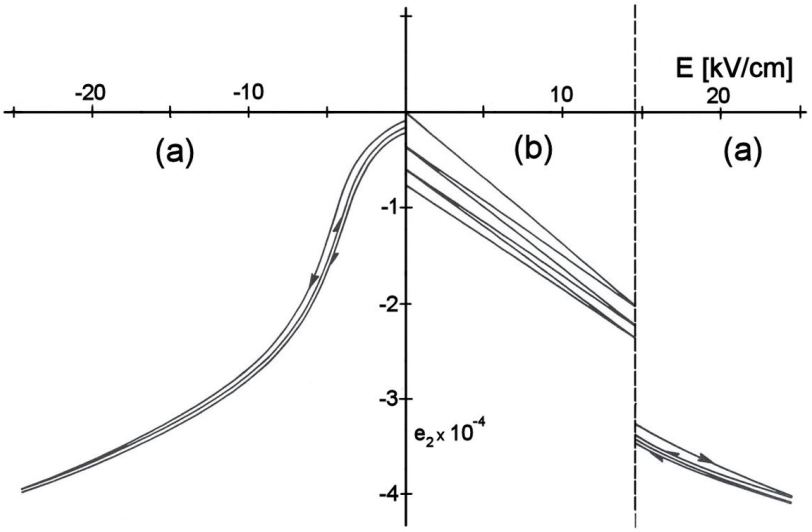

Figure 12: (a) Transverse strain in a ceramic specimen of 0.9PMN–0.1PT and (b) a typical hard PZT8 piezoceramic specimen under slowly varying electric fields. The strains are comparable in the two materials, but are far more reproducible in the electrostrictive relaxor because of the de-aging effects in the piezoelectric PZT.

1.5 Effect of stress on the dielectric permittivity

Earlier studies of the pressure influence, hydrostatic and uniaxial, on the electrical properties of ferroelectric materials were mainly concentrated on thermodynamical considerations of the ferroelectric phase transitions, like the hydrostatic pressure dependence of the Curie temperature of the materials [49]. Some of these studies, performed on the uniaxial stress's (i.e., axial pressure) influence on the properties of ferroelectric single crystals and ceramics, showed a significant influence of the applied stress on the material properties and the diverse relaxation processes [50]. The results were interpreted in terms of a changing

of the domain structure and domain reorientation. However, none of these studies was concentrated on the investigations of the pressure dependence of the permittivity.

Later, extensive measurements of the electrostrictive coefficients were reported [17]. Tests of the direct electrostriction of ferroelectrics and relaxors were employed to obtain the coefficients [51, 52]. However, the direct method was not precise enough for the testing of non-polar materials, like glasses and dielectrics, and the converse electrostrictive effect, i.e., the pressure dependence of permittivity, was used for analyzing these materials [44]. The first author to present the converse electrostrictive effect as a way to sense pressure was Uchino [4], who concentrated on the study of high-permittivity ceramic materials. The results on the converse electrostrictive effect of PMN-based relaxor ferroelectric materials revealed a reversible decrease of the dielectric permittivity when a compressive stress was applied. The observed decrease and reversibility of the permittivity was in accordance with the converse electrostrictive law. However, the apparent temperature dependence of the electrostrictive coefficients was not consistent with the direct measurements of the electrostrictive coefficients. The discrepancy was explained by the relaxor nature of the materials and the local polarization of the material [47].

A stress sensor, based on the converse electrostrictive effect described by Uchino [1], is shown in Figure 13. Its bimorph structure provides superior stress sensitivity and temperature stability. The measuring system subtracts the static capacities of the two dielectric ceramic plates. The capacitance changes of the plates have the opposite sign for uniaxial stress and the same sign for temperature deviation. Higher permittivity and higher stress sensitivity increase the permittivity change, which is detected by the capacitance measuring system, thus increasing the accuracy of the output signal. Electrostrictive sensors are effective in the low-frequency range, i.e., for static and quasi-static applications, where the piezoelectric effect becomes inadequate. Thereafter, a low measuring frequency can be used in non-piezoelectric systems, e.g., 1 kHz or even lower.

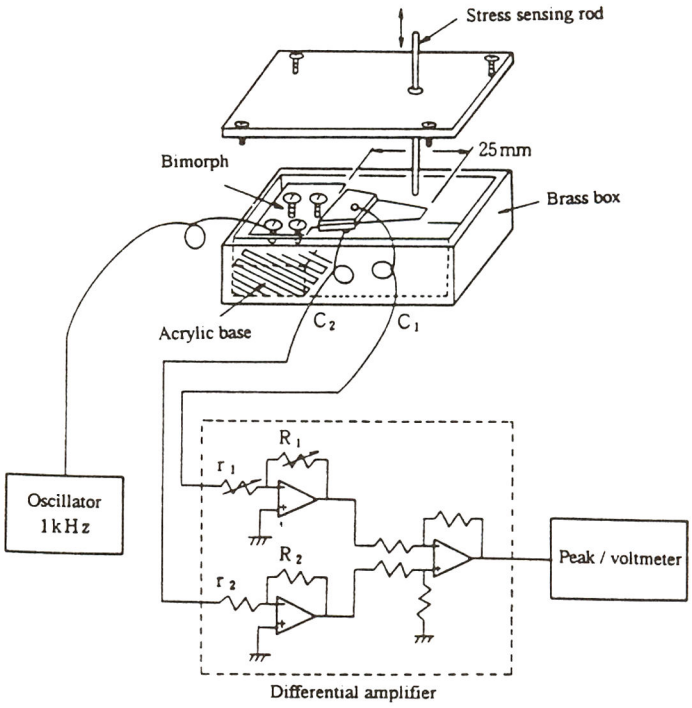

Figure 13: Bimorph type stress sensor based on the electrostrictive properties of the ceramic material.

A few theoretical calculations of the converse electrostrictive effect in the ferroelectric phase were reported by Haun [53], Zhang [47] and Turik [54]. In these investigations not all

the important parameters of a ferroelectric ceramic body were considered. The most detailed and reliable thermodynamical calculations of the stress dependence of the permittivity in ferroelectric ceramics and related high permittivity materials were given by Steiner [55].

The increase in the research activity on the stress dependence of different electrical properties since the late 1990s is connected with the applications of ferroelectric ceramic materials for different actuator, sensor and transducer applications. The ferroelectric materials, shaped into complex geometries, are often used under significant electric and mechanical loads (large signal range) that may give rise to a local stress and/or electric field concentration [56-58]. In such critical regions, the materials may show the full range of ferroelectric and ferroelastic constitutive responses. Therefore, recent experimental [56, 58-61] and modelling [16, 62] efforts have focused on evaluating and understanding the large signal non-linear behaviour of ferroelectric ceramics in the context of domain switching.

The dielectric responses to an applied uniaxial stress for different materials were collected by Steiner *et al*. [63]. The responses of the paraelectric and relaxor materials (at T_m and above) were found to be linear and reversible with cycling stress. Furthermore, no relaxational processes occur after the stress application and release. On the other hand, the behaviour of materials in the ferroelectric phase as well as relaxors well below the T_m was complicated and diverse. It is evident that the extrinsic contributions of the domain structure as well as the internal defect structure essentially influence the dielectric response under applied stress, since it was calculated that the intrinsic effect in all phases results in a decrease of the permittivity under a compressive stress [63].

Some of the distinctive features of the stress dependence of the permittivity observed in ferroelectrics are:

- a decreasing or increasing of the permittivity,
- in some cases the permittivity passes through a maximum on increasing axial pressure,
- a significant instantaneous increase during both stress application and release,
- short-term relaxations,
- long-term logarithmic-like relaxations,
- irreversible changes after the stress cycle,
- difference between the successive stress cycles (history dependence).

The very different responses of the ferroelectric materials were basically divided into two types of behaviour, for which several contributions to the change of the permittivity upon stress application and release were distinguished [63]:

1. the reversible intrinsic converse electrostrictive effect,
2. domain-walls movement and depinning,
3. domain-wall suppression due to stress application,
4. dipole-oriented mechanism (random field defects).

The difference between the two groups of materials showing different behaviours (the prototypic materials of the two groups are soft-doped and hard-doped PZT) is in the presence of random field defects. These random field defects strongly pin the domain walls in hard-doped materials compared to soft-doped materials [64, 65]. The grain size effect on the behaviour of ferroelectrics was also found to be important [66]. The grain size influences the domain structure of the material, and can change the response to the applied stress.

Similarly, the investigations on poled samples of ferroelectric and relaxor compositions showed diverse behaviour [67-70]. The results were explained on the basis of intrinsic and extrinsic contributions, i.e., responses from a single domain and from domain-wall motions, respectively. Under a compressive stress, the domain structure in the material will change to maintain the domain energy at a minimum. During this process some of the domains engulf other domains or change shape irreversibly. Under the applied stress, the domain structure may undergo domain switching through non-180° domain walls, the clamping of domain walls, a stress-induced decrease in the switchable part of spontaneous polarization, de-poling and de-aging. In relaxors, the competing influences of the intrinsic contribution of the non-polar matrix and the extrinsic contribution of the re-polarization and growth of the polar nano-regions dictate the change of the permittivity under the applied stress. With decreasing temperature the polar nano-regions start to prevail, and when the correlation of the polar regions increases, the dielectric response to the applied stress changes away form the original linearity and reversibility.

The temperature dependence of the uniaxial stress effect on the permittivity of NBT [70-73] and related materials [74, 75] was measured by Suchanicz *et al*. The experiments were performed on single crystals and ceramic samples, and showed an increased influence of the axial pressure on the permittivity in the vicinity of the permittivity maximum. More details about these measurements will be described in §1.6.

The major disadvantage of the reported investigations is that the influence of stress on the permittivity was not evaluated as a whole. Typically, the authors concentrated on narrow stress ranges, small applied stresses; they did not performed stress cycling, and repeat the tests on samples that were already stressed. Moreover, most of the tested samples contained lead, which should be avoided in future production and applications, according to the directive of the European commission [76]. Therefore, a lead-free material, NBT, with ferroelectric and relaxor properties, which can be modified by the addition of different materials, was chosen in this work for the study of the effect of uniaxial stress on the dielectric properties.

1.6 Properties of $Na_{0.5}Bi_{0.5}TiO_3$

Sodium bismuth titanate, $Na_{0.5}Bi_{0.5}TiO_3$ (NBT), was first discovered by Smolenskii and Agranovskaya in 1959 [77]. Its complex perovskite structure with two different ions on the A-site of the ABO_3 structure is much less common than the B-site substituted counterpart. It is the most studied material with the A-site substituted structure mainly due to its very different and unique structural and electrical properties. In the past few years, interest has increased because NBT is a lead-free material with a high value of spontaneous polarization.

The currently accepted sequence of the structural phase transition in NBT was determined using neutron diffraction [78]. The investigation showed that with decreasing temperature, the symmetry of NBT changes from prototypic cubic to tetragonal in the temperature range 500–540°C, and then to rhombohedral in the temperature range 255–400°C. The large morphotropic phase boundaries of the rhombohedral–tetragonal and of the tetragonal–cubic phase coexistence are observed in the temperature intervals 255–400°C and 500–540°C, respectively. Both phase transitions were characterized as first-order transitions. The phase coexistence was found by Vakhrusev [79] and was later confirmed and characterized by other authors [80-82]. Just recently, however, a new phase in the phase sequence of NBT was proposed based on a temperature in-situ analysis carried out using transmission electron microscopy [83, 84]. The new orthorhombic phase and the corresponding new model of the phase transitions should explain the not fully understood dielectric peculiarities. The formation of the orthorhombic phase starts slightly above 200°C, with the formation of a modulated phase of newly appearing orthorhombic sheets within the rhombohedral matrix. The intermediate modulated phase exists from 230 to 300°C, and is

then transformed to the pure orthorhombic phase. The phase transition from the orthorhombic phase to the tetragonal one occurs near 320°C. The polar order of the orthorhombic phase is predicted to be antiferroelectric, thus confirming the already disproved existence of the antiferroelectric properties in NBT [79, 81, 85, 86]. Nevertheless, the new investigation emphasizes the complexity of the structure and properties of NBT and the controversy about this material in the literature. In the following text the conventional explanations of the NBT properties will be presented.

The sequence of the phase transitions in NBT is schematically shown in Figure 14, together with the electrical and elastic order of the phases. The low-temperature phases are ferroelastic [79], while their electric order is different. The tetragonal phase exhibits a unique combination of in-phase oxygen octahedra tilts and antiparallel Na/Bi and Ti cation displacements along the polar *c*-axis [78]. This non-centrosymmetric weakly polar nature of the tetragonal phase, confirmed by the observation of a small second-harmonic-generation signal, can be characterized as ferrielectric [78]. The rhombohedral phase is strongly polar and the material exhibits a spontaneous polarization below 200°C. The high-temperature prototypic phase possesses paraelectric and paraelastic properties.

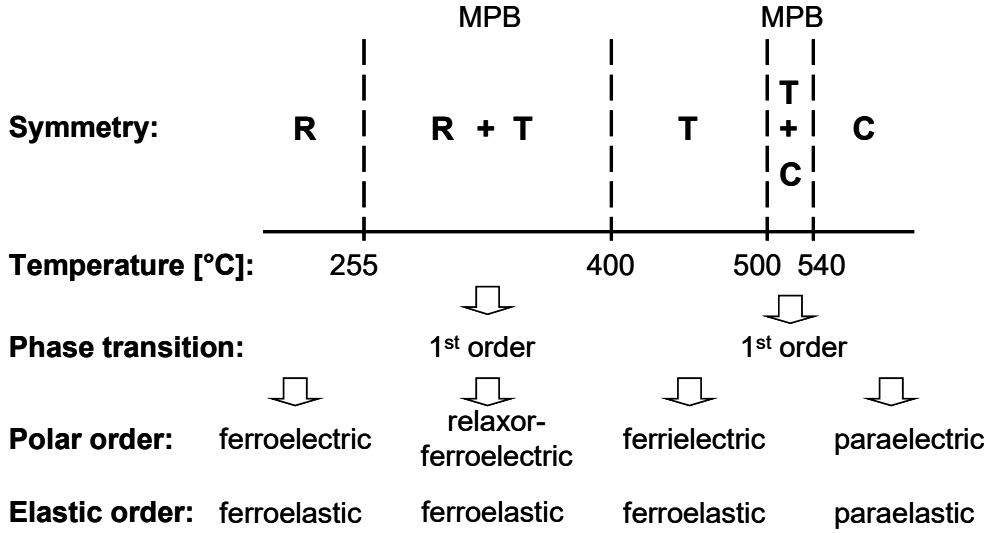

Figure 14: Schematic of the phase-transitions sequence in NBT and the properties of the rhombohedral (R), tetragonal (T) and cubic (C) phases.

The high temperature cubic phase possesses an ideal perovskite structure (space group *Pm*3*m*) with no cation displacements and oxygen octahedra tilts. In the tetragonal phase (*P*4*bm*) in the phase tilt system $a^0a^0c^+$ (in Glazer notation [87]) is combined with the opposite displacements of the A- and B-site ions along the [001] direction [88]. The rhombohedral phase exhibits the $a^-a^-a^-$ tilt system arising from octahedra tilting about their threefold pseudo-cubic axes and parallel cation displacements along $[111]_p$ [78]. Additional displacements of Bi ions along the polar c-axis with respect to Na ions were observed. The valency calculations showed that in the refined structures the ions should be displaced off-centre in order to achieve the ideal valency. The difference between the calculated and the ideal valency is especially big for Bi ions, indicating the shifts of Bi ions in the actual structure.

The local environment of the Bi and Ti atoms has been studied by X-ray absorption fine structure (XAFS) [89]. It was indeed found that the local environment of Bi is much more distorted than that determined from diffraction experiments. The Bi–O distances were found to be shorter than determined from the crystallographic data and a new structural model was proposed (Figure 15), in which the Bi atoms are displaced away from the polar axis in a plane orthogonal to the polar axis. The valency calculations confirmed the improved Bi valency equal to 3.13, which is close to the optimal bonding of the Bi cations, i.e., 3.00.

Despite the off-shifts of the Bi, statistically Bi atoms are positioned in the centre as observed by diffraction measurements. Similar behaviour has been observed for the Pb atom in PMN and PZT [90, 91].

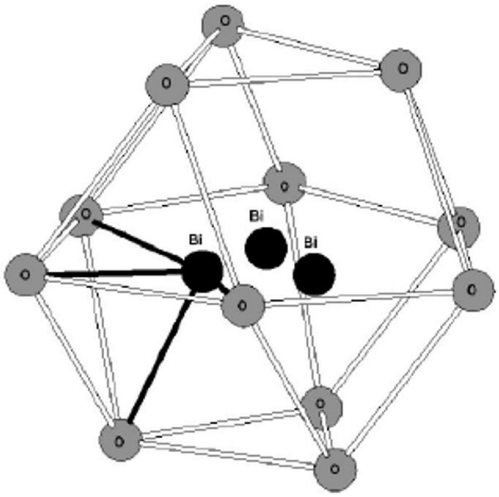

Figure 15: Bi ions statistically disordered around the threefold axis according to the proposed model [89]. The geometry of the Bi–O shortest bonds is shown by the black lines.

The described model was used for the interpretation of the X-ray diffuse scattering studies [92]. Asymmetric peaks and a broad diffuse region of scattering around the origin were observed in these studies. The asymmetric peaks are connected with the correlated <001> displacements of the A-site ions, which can act as templates for the formation of the tetragonal phase. These displacements form a type of planar defects in the structure of NBT. The diffuse scattering around the origin indicates some local short-range ordering of Bi and Na ions. The degree of the short-range ordering is very small but it is significantly different from a purely random distribution. The local ordering was also observed by infrared and Raman spectroscopy [93]. Moreover, the investigation confirmed the formation of polar nanoregions over a wide temperature range. The existence of compositional disorder with local short-range ordering and polar nanoregions over a broad temperature range, the two necessary conditions for a relaxor material [19], indicates the relaxor nature of NBT.

The relaxor behaviour of NBT is observed when measuring the temperature dependence of its dielectric properties (Figure 16) [94]. Two characteristic anomalies can be detected from the dielectric response, the dielectric maximum and the hump. Both anomalies are reflected in the dielectric losses as the local minimum at 320°C and the local maximum at 180°C, respectively. The frequency-dependent hump at around 200°C is connected with the stabilization of the rhombohedral phase. As the temperature decreases the dynamics of the rhombohedral domains decreases and the frequency dependence can be observed at frequencies below 1 MHz. In contrast, the dynamics of the polar nanoregions at temperatures of the permittivity maximum is high and no frequency dependence can be observed. According to the results of the high-frequency dielectric measurements (up to 1.8 GHz) [93], the frequency dispersion occurs only in the GHz frequency region. The exact cause of the formation of the frequency maximum is not known; however, it should be connected with the polar nanoregions [93]. Unlike usual relaxors, where in the range of permittivity maximum the dielectric dispersion has already set in due to the decreasing dynamics of the polar nanoregions, the maximum probably appears as a consequence of a gradual stabilization of the polar clusters into rhombohedral domains. As the clusters are stabilized below the temperature of the permittivity maximum, permittivity decreases due to the decrease in the dynamics of domains in comparison with polar nanoregions [93].

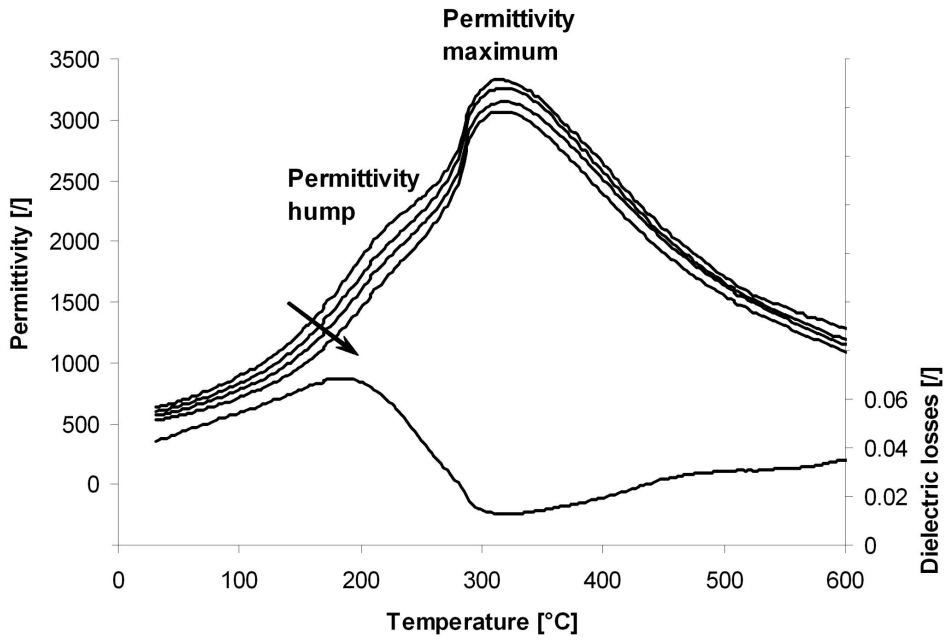

Figure 16: Temperature dependence of the dielectric properties of NBT. Relative permittivity at frequencies 1 kHz, 10 kHz, 100 kHz, 1 MHz and dielectric losses at 1 MHz are shown. The arrow designates the frequency increase.

A study of the synthesis mechanism of NBT showed the existence of a solid-solution region, characterized as $Na_{0.5-x}Bi_{0.5}TiO_{3-x/2}$, where $0 < x < 0.03$ [94]. According to this study, the formation of the stoichiometric NBT starts with the formation of the deficient end-member. It was also shown that the stoichiometry of the final compound greatly influences the properties of the material. For the dielectric properties, the permittivity maximum decreases and shifts towards higher temperatures, while the frequency-dispersive hump becomes more distinctive and is shifted towards lower temperatures.

The effect of axial pressure on the properties of NBT was investigated by Suchanitz [71-73]. These investigations showed that mechanical loading has a significant influence on the dielectric and ferroelectric properties of NBT single crystals and ceramics. The applied pressure reflects in:

- a change of the domain structure,
- a decrease of the permittivity,
- a shift of the anomalies to higher temperatures,
- a reduction of the thermal hysteresis,
- a suppression of the dielectric dispersion,
- a decrease of the ferroelectric hysteresis loop area,
- a decrease of the remanent polarization,
- a stabilization of the ferroelectric phase above 200°C.

The effect of axial pressure on dielectric properties of an NBT single crystal is shown in Figure 17 [71], and identical behaviour was observed for the ceramic material [72]. The influence of the applied pressure is most pronounced at the dielectric maximum and is reduced at room temperature. Similar behaviour was observed for other tested NBT-based materials [74, 75, 95]. The reason for the reduced influence of stress on the permittivity at room temperature was explained in terms of the effective electric field that is equivalent to the

applied stress. It is possible to approximately equalize the mechanical and electrical energy brought to the system [63]:

$$F_m = 2e_S\sigma \tag{14}$$

$$F_e = 2P_S E \tag{15}$$

where σ is the applied mechanical stress, e_S is the spontaneous deformation of the lattice, P_s is the spontaneous polarization, E is the electric field; and calculate the effective electric field:

$$E_{eff} = \frac{\sigma e_S}{P_S} \tag{16}$$

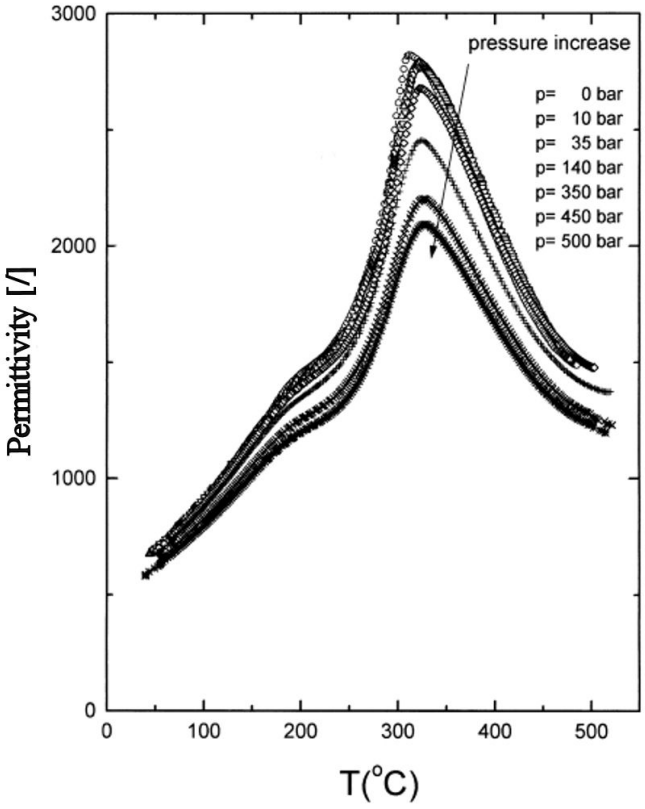

Figure 17: Temperature dependence of the permittivity of an NBT single crystal at various pressures in the [100] direction. The properties were measured during heating at a frequency of 20 kHz.

Calculations showed that at room temperature the effective field equivalent to the applied stress of the order of 100–200 MPa is much lower than the coercive field of NBT [71]. On the other hand, at higher temperatures the effective field becomes comparable to, or higher than, the coercive field. An axial stress that is not comparable to the coercive field at room temperature can move the domain walls, but does not switch the polarizations [63]. However, at higher temperatures, the same axial stress becomes comparable to the coercive field, thus can move and even annihilate the domain walls, which increases its influence on the permittivity. In the first instance the (irreversible) change of the permittivity is smaller than in the second instance.

In the investigations performed by Suchanitz *et al.* [71-75, 95], prior to measurements the samples were heated above the transition temperature to the cubic phase, i.e. to 550–600°C, and annealed for half an hour. Then dielectric properties were recorded under constant pressure during successive heating and cooling cycles. The properties observed were fully reversible by changing the pressure. According to the study of Steiner [63] and to the changes of the domain structure caused by the applied pressure, this full reversibility is not expected.

Instead, the observed reversibility of the properties is caused by the pre-measurement annealing at temperatures where the material is in the cubic phase, thus deleting the pre-history of the material.

The investigation of the room-temperature dependence of the permittivity on the axial pressure in NBT revealed the linear dependence shown in Figure 18 [73]. The authors proposed the possibility of applying these materials as the elements of a nonpiezoelectric sensor of pressure. Again, the results were obtained in the same way as described above and, therefore, no irreversible changes were detected. The reported results [73] presented in Figure 18 show that at 100 MPa (1000 bar) the permittivity of pure NBT decreases from an initial value of approximately 780 to approximately 730 (relative decrease of ~6%). The slope of the axial pressure dependence of the permittivity does not change much with the additions of $BaTiO_3$ (BT).

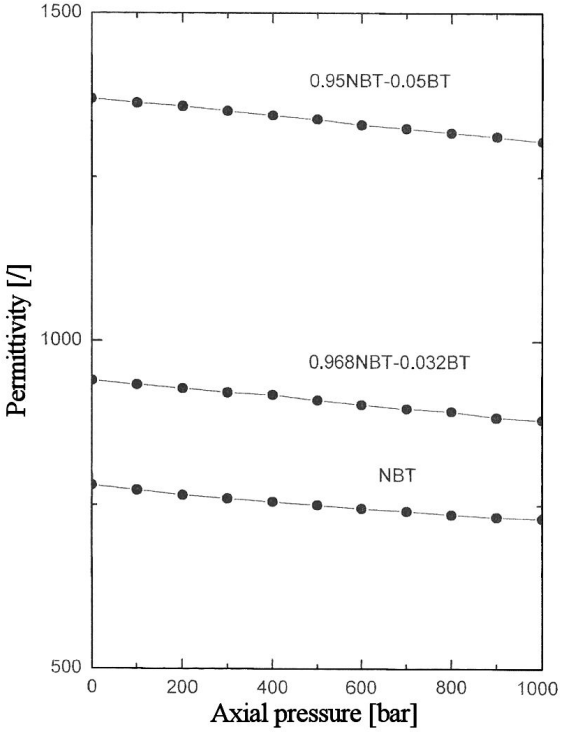

Figure 18: The axial pressure dependence of the permittivity for NBT and NBT–BT single crystals.

In the past decade, several papers on the stress dependence of the permittivity have been published [60, 63, 67-75, 95]. However, just a couple of them [63, 73] investigate the possibility of applying this effect for sensing pressure and searching for materials with suitable properties, although the principle of the application of this effect in well known [4]. The effect of axial pressure on the permittivity in NBT is the highest at the temperature of the permittivity maximum. Therefore, a suitable material has to be added, which would shift the permittivity maximum towards lower temperatures and/or decrease the coercive field.

Incipient ferroelectrics, with a theoretical temperature of the ferroelectric phase transition below 0 K, are known by shifting the dielectric anomalies toward lower temperatures, when forming solid solutions with other materials. $NaTaO_3$ (NTa) [96] and $KTaO_3$ (KTa) [97] are incipient ferroelectrics, and their influence on the properties of NBT has not been investigated yet. $K_{0.5}Bi_{0.5}TiO_3$ (KBT) [98, 99] possesses similar properties to NBT, and exhibits a smaller coercive field at room temperature. The available reports on the synthesis mechanism of KBT are contradictory and incomplete. Therefore, the research work in the present study started with a determination of the synthesis mechanisms and the structural properties of the materials from the NBT–NTa, NBT–KTa and NBT–KBT systems.

These results are important in order to control the synthesis and connect the electrical properties with the structural characteristics of the materials.

2 Aim of the work

In the field of pressure sensing, several methods are used, depending on the frequency of the measured signal. In the case of static and quasi-static stress applications the traditional approach based on the piezoelectric effect becomes inadequate. The stress dependence of the permittivity is another option for measuring stress or pressure, known for almost thirty years. This is, in principle, a linear effect that is promising for static and quasi-static applications. The requirements for such sensors are a high stress sensitivity, a permittivity that is stable over time, and a low temperature coefficient of the permittivity. Relaxor ferroelectrics, with their diffuse phase transition, are good candidates for such sensors.

Most studies reported in the literature on the stress dependence of different properties of the polar electroceramics were performed on poled samples, and aimed to improve the understanding of the piezoelectric properties under large applied signals. Very few studies were focused on the stress dependence of the permittivity and its applicability for pressure sensors. Moreover, a great majority of the investigated materials are lead containing. The purpose of this investigation was to investigate the characteristic parameters of the axial pressure effect on the permittivity in newly appearing lead-free relaxor ferroelectrics.

The shortfall in the existing investigations on the stress dependence of the permittivity is in the incomplete evaluation of such a dependence. Typically, the work was performed at small stresses or in narrow stress ranges, the time and history dependence were not evaluated, and multiple-cycle experiments to monitor the reversibility were not performed. The objective of this work was to experimentally evaluate the characteristic features of the stress dependence of the permittivity that affect the applicability of the materials.

$Na_{0.5}B_{0.5}TiO_3$ exhibits strong ferroelectric properties at room temperature and a dielectric relaxation above ~200°C. It is lead-free, and therefore takes into account health and environmental considerations. The study of the axial pressure's influence on the permittivity at room temperature proposed a linear response for $Na_{0.5}B_{0.5}TiO_3$; however, the dependence is rather weak. The investigation of the temperature dependence of the effect showed that the pressure dependence of the permittivity is emphasized over the temperature of the permittivity maximum, which exists at 320°C. In this temperature range, the coercive field is lowered compared to the room-temperature value. To improve the applicability, the permittivity maximum should be shifted into the room-temperature region. This can be achieved with addition of an appropriate modifying material. In this study $NaTaO_3$ and $KTaO_3$, with incipient ferroelectric properties, and $K_{0.5}B_{0.5}TiO_3$ were used. For incipient ferroelectrics, shifting of the phase transitions toward lower temperatures is well-known, while $K_{0.5}B_{0.5}TiO_3$ decreases the coercive field of $Na_{0.5}B_{0.5}TiO_3$.

The investigation of the stress dependence of the permittivity was performed on polycrystalline materials prepared by the solid-state reaction method. Since there is no available literature data on the synthesis of the $Na_{0.5}B_{0.5}TiO_3$–$NaTaO_3$ and $Na_{0.5}B_{0.5}TiO_3$–$KTaO_3$ systems, this work determines the mechanism of the synthesis, the solid-solution formation and the phase relations in these systems. Similarly, the formation mechanism of $K_{0.5}B_{0.5}TiO_3$ was investigated, since the literature reports are contradictory and inadequate, while the basic properties of the $Na_{0.5}B_{0.5}TiO_3$–$K_{0.5}B_{0.5}TiO_3$ system were given by Žnidaršič *et al.* [100][MŽ]. For the prepared samples, the crystal- and micro-structure properties as well as

the dielectric and ferroelectric properties, and the stress dependence of the permittivity have been determined. The determination of the electrical properties serves as the orientation in improving the stress dependence of the permittivity. Finally, this work attempts to connect the behaviour of the materials under applied stress with the structural and electrical properties, and evaluate the applicability of the investigated materials for pressure-sensor applications.

3 Experimental methods

3.1 Sample preparation

3.1.1 Chemicals used

Na_2CO_3	Alfa Aesar	99.997%
K_2CO_3	Alfa Aesar	99.997%
Bi_2O_3	Alfa Aesar	99.975%
TiO_2 (rutile)	Alfa Aesar	99.8% and 99.99%
Ta_2O_5	Alfa Aesar	99.993%

3.1.2 Synthesis of the ceramic samples

The ceramic samples were prepared by a solid-state reaction method. Prior to weighing, the $NaCO_3$ and KCO_3 powders were dried at 200°C for 2–4 h to remove any water content, and cooled to room temperature in a silica-gel-filled desiccator. Stoichiometric amounts of reagent-grade powders were weighted with 0.1-mg accuracy, using a Mettler H35AR analytical balance, and mixed thoroughly in an agate mortar under ethanol. In the case of the KBT synthesis, reagents were additionally homogenized in a planetary ball mill (Fritsch, Pulversette 5), using 3-mm yttria-stabilized zirconia balls, at 200 rpm for 1 h under ethanol. The homogenized powders were dried, uniaxially pressed into pellets under a pressure of 100 MPa and calcined in air at 750 and 850°C for 10h with intermediate cooling and grinding. The calcined samples were milled in the planetary mill under the same conditions (at 200 rpm for 1 h under ethanol). The size of the particles after the milling was analyzed using a HR 850 Alcatel Cilas laser granulometer, which showed that the median size (d_{50}) was 0.6–0.9 μm. Fine powders, with a median size of particles below 1 μm, required no additional milling. The milled powders were dried, uniaxially pressed into pellets and sintered. In some compositions, additional calcinations and cold isostatic pressings were applied, as stated within the text. The prepared compositions and examples of the marking of the samples are shown in Table 1.

In order to estimate the sintering temperature, the sintering of a compact sample, uniaxially compressed at 100 MPa, was observed by means of a heating microscope (EM201, Hesse Instruments), with a heating rate of 10°C/min. The optimal sintering temperature was then determined according to the development of the microstructure of the samples. The sintering was performed in a tube furnace in an atmosphere of air with heating and cooling rates of 10°C/min. The density of the sintered samples was measured using Archimedes' method.

Table 1: Prepared compositions and marking of the samples.

System and corresponding label	Prepared compositions – mol% of addition to NBT	Example of a sample label
$Na_{0.5}Bi_{0.5}TiO_3$–$NaTaO_3$ NBT–NTa	5, 10, 15, 20, 25, 30, 50, 70, 90, NTa	10 mol% addition = NBT–10NTa
$Na_{0.5}Bi_{0.5}TiO_3$–$K_{0.5}Bi_{0.5}TiO_3$ NBT–KBT	20, 30, 50, KBT	20 mol% addition = NBT–20KBT
$Na_{0.5}Bi_{0.5}TiO_3$–$KTaO_3$ NBT–KTa	5, 10, 20, 30, 50, 70, 90	30 mol% addition = NBT–30KTa

3.2 Characterization of the samples

3.2.1 X-ray powder diffraction

The phase compositions of the samples were analyzed using a D4 Endeavor, Bruker AXS powder diffractometer with Cu*K*α radiation. Room-temperature XRD patterns were recorded in the 2θ range 10°–70° or 20°–80° with a typical step size and counting time of 0.04° and 1 s, respectively. In order to enhance the resolution, selected reflections were scanned with a 0.01° step size and 5-s counting time. Diffraction patterns were also recorded using a powder diffractometer PANalytical X'Pert PRO with Cu*K*α radiation in configuration with Johannson's monochromator to remove the Cu*K*α2 radiation. In this case, the parameters used were a 0.016° step size and a 200 s counting time. Note that the counting times of the two diffractometers are defined in a different way. The Cu*K*α2 radiation is noted, where used, in the text of the figure captions.

3.2.2 Microstructure analyses

Sintered samples were grinded with SiC papers and polished with diamond paste to a roughness of 1/4 μm. Etched samples were obtained by thermal etching in a tube furnace, typically 50°C below the sintering temperature. The exposure time was between 10 and 30 min.

The microstructures of polished, etched and fractured samples after sintering were observed in a scanning electron microscope (SEM: JEOL JXA 840A and JSM 5800). Backscattered electron (BSE) imaging in the compositional contrast mode was applied to expose the presence of secondary phases in the matrix phase. The chemical composition of the samples was determined with electron-probe microanalysis using energy-dispersive (EDS) and wavelength-dispersive (WDS) X-ray spectroscopy. The EDS standardless quantitative analyses were performed at a 20-keV beam energy using a SEMQUANT program with a virtual standards package data library (EDS Oxford Instruments Link ISIS 300) and a ZAF matrix correction.

The accurate elemental composition of the KBT matrix phase was determined with optimized, WDS quantitative microanalysis. The WDS measurements were carried out in a JXA 840A microanalyzer at 14 keV, with a 40-nA beam current and a 40° take-off angle. The intensities of the K-Kα, Bi-Mα and Ti-Kα spectral lines were measured. The standard reference materials were single crystals of $SrTiO_3$ and $KNbO_3$ and a polycrystalline Bi_2O_3 ceramic. The elemental ratios were quantified with conventional ZAF and Φ(ρz)-XPHI [101] matrix corrections. The oxygen content was calculated according to the nominal cation valency. High analytical precision was ensured with counting times set to achieve a counting error of less than 0.4% relative. The detection limits [102], expressed in wt%, were low (0.006 for K, 0.054 for Bi and 0.011 for Ti), which confirmed the high sensitivity attained

with the WDS method and consequently allowed the determination of the elemental composition of the KBT matrix with high accuracy.

3.2.3 Thermal analysis

The mass losses and the melting temperature of the sample were determined with thermogravimetric (TGA) and differential thermal analyses (DTA) using a simultaneous thermal analysis instrument (STA 449 C/6/G Jupiter, Netsch). The experiments were performed in an atmosphere of air using platinum crucibles. The heating rate was 10°C/min.

3.2.4 Knudsen effusion mass spectrometry

During the synthesis of the KBT the volatile species were determined using Knudsen effusion combined with mass spectrometry (KEMS) [103]. The latter is used to identify and measure the vapour pressure of the molecular species that are in equilibrium with the solid sample in the Knudsen cell. This is accomplished by letting the effusing molecules pass the ion source, become ionised, and finally be analyzed according to their masses and abundance.

In a typical experiment a sample (approximately 100 mg) was loaded in a platinum Knudsen cell with an orifice diameter of 0.5 mm, and placed into the evaporator of a Nier-type mass spectrometer. After evacuation to 10^{-6} Pa the sample was first degassed at 120°C. Next, the temperature was stepwise increased (10°C/min heating rate, 5 min dwell time, before collecting data at the measured temperature) and the abundances of all the ion species that appeared in the mass spectrum were recorded. The equilibrium pressures of the neutral precursors were calculated using Equation 17.

$$p_i = k \cdot (\sum_j I^+_{i,j} T) \qquad (17)$$

The symbols represent:

$I^+_{i,j}$ - the j-th ion abundance of a neutral precursor i /counts per second,

p_i - the pressure of the neutral species/precursor i /Pa,

T - the absolute temperature /K,

k - the instrumental sensitivity constant /(Pa $\cdot K^{-1} \cdot Hz^{-1}$).

3.2.5 Dielectric and ferroelectric measurements

Weak-field dielectric properties were measured using a precision LCR meter (HP 4284A, Hewlett–Packard). Measurements were performed at frequencies from 1 kHz to 1 MHz with an applied voltage of 1 V. A Delta Design 9039 chamber and a home-constructed furnace were used to measure the temperature dependence of the permittivity between –170°C and 600°C. All the presented dielectric properties were measured on heating with a heating rate of 2°C/min. Silver paste was fired onto the samples at 550°C for 15 min to serve as the electrode.

Polarization–electric field hystereses were measured at room temperature using a Precision LC 10V Radiant Technology apparatus and a Trek 10-kV voltage amplifier. The measurements were performed at a frequency of 10 Hz. The amplitude of the applied signal was 90–100 kV/cm, depending on the dielectric strength of the samples.

3.2.6 Measurement of the ferroelastic properties

The surfaces of the cylindrical samples (approximately 5 mm in diameter and 7.5 mm in height) to be exposed to compression were polished to obtain smooth parallel surfaces. Compression tests were performed in a Dartec Servohydraoulic Universal Testing machine, with a 20-kN load cell. The dilatation for the calculation of strain was measured by an extensometer of the MTS 634.31F-25 S/N 1144123 type, with a 10-mm gauge length. Measurements were performed at room temperature, with a loading rate of approximately 20 MPa/min.

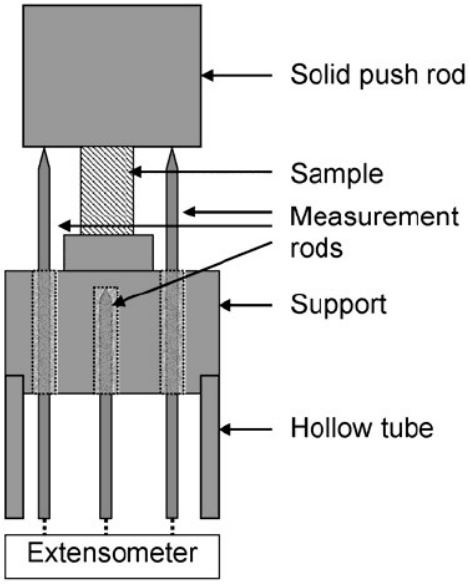

Figure 19: Schematic of the sample testing system. All components shown are fabricated from SiC and are placed in between the upper and lower metal load-cell fixtures.

3.2.7 Measurement of the stress dependence of the permittivity

The axial pressure, i.e., the uniaxial stress, dependence of the permittivity was measured using a mechanical lever press (Figure 20). A high ratio between the fulcrum–weight and the fulcrum–sample distances makes it possible to apply a high axial pressure to the sample. Ten weights, each of a mass of 1 kg, can be hung on the lever arm. Additional weights can be added without the need to unload the already applied ones. The stress applied to the sample by the lever arm alone is termed the pre-stress. The pre-stress is around 8 MPa for a 5-mm sample diameter. The maximal load, created by the 10 kg hanging on the lever arm, creates a pressure of approximately 200 MPa on a sample with a diameter of 5 mm. The accurate pressure, which depends on the sample diameter, is given in the text for each presented measurement. The accuracy of the pressure is ± 1%, estimated from the lever configuration and a measurement of the sample diameter.

The stress is transmitted to the sample through two alumina plates that also isolate the sample from the press. Cupper-foil electrodes, directly connected to the measurement set-up, are placed between the sample and the alumina plates. An additional metallic disc is placed between the upper metallic cylinder and the upper alumina plate. The upper metallic cylinder is shaped into a hemisphere to prevent any misalignment problems. Adjustment to the height of the sample can be made by the lower metallic cylinder with an inner coil. The lever set-up can be placed into the chamber in such way that the lever arm sticks out from the chamber (Delta Design 9039).

Sintered disc shaped ceramic samples with a diameter of ~5 mm and a height of 1.5–2 mm were grinded from both sides to obtain plan-parallel faces. In order to maintain the perfect faces of the sample, gold was sputtered onto the samples to serve as the electrode.

Dielectric measurements were performed at room temperature at frequencies from 1 kHz to 1 MHz with an applied voltage of 1 V, using the HP 4284A LCR meter. Simultaneous measurement at multiple frequencies with a long integration time took approximately 4 seconds to complete. The long integration time was used to obtain a good signal-to-noise ratio. In a typical experiment, a stepwise increase of the pressure in 1 minute intervals was used. The permittivity was measured 1 minute after the increase of the pressure, just before the next increase.

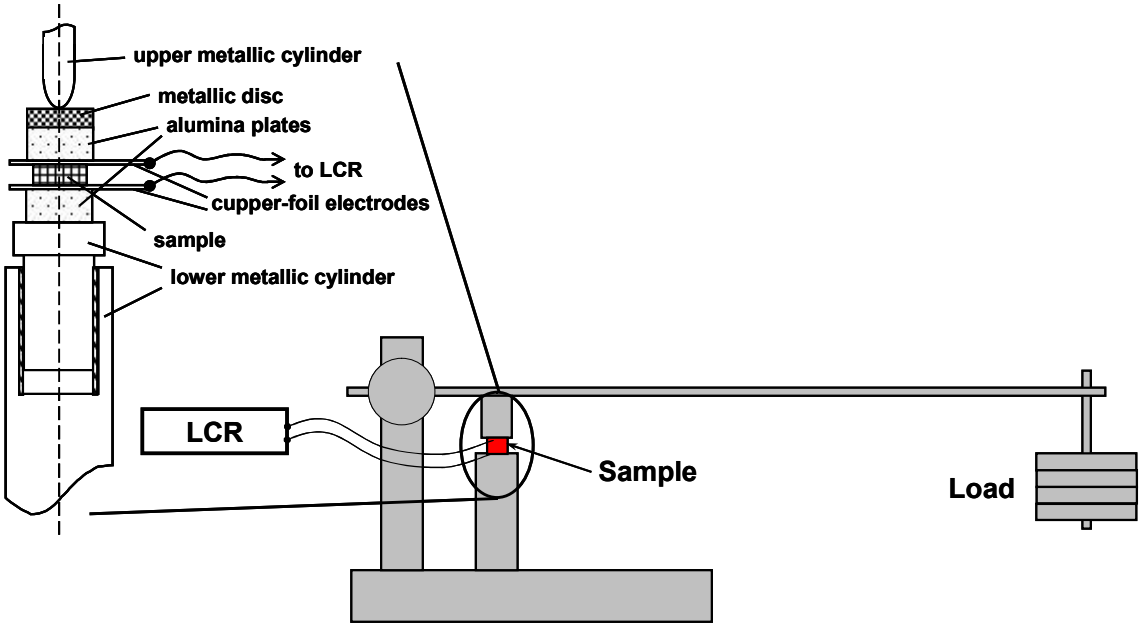

Figure 20: Schematic of the lever press and the fixture of the sample.

4 Results and discussion

4.1 $Na_{0.5}Bi_{0.5}TiO_3$–$NaTaO_3$ system

4.1.1 Synthesis

The orientation for the solid-state synthesis of the ceramics from the $Na_{0.5}Bi_{0.5}TiO_3$–$NaTaO_3$ (NBT–NTa) system was taken from the synthesis of pure NBT [94]. Two calcination steps at 750°C and 850°C were applied. The samples were heat treated at relatively low temperatures due to the low melting temperatures of Bi_2O_3 and Na_2CO_3, i.e., 817°C and 851°C, respectively. The calcination time was set to 10 h to enable the reaction between the four different oxides. The X-ray pattern of the samples after the first calcination showed a perovskite-type solid solution as well as the presence of other crystalline phases. The intensities of the secondary phases were small and, therefore, they were not identified. After a subsequent calcination and after the sintering process the XRD patterns revealed single-phase samples. A typical evolution of the XRD patterns at different stages of the synthesis is shown for the sample NBT–30NTa in Figure 21. With increasing firing temperature, the diffraction peaks become sharper and the intensity of the peaks changed. The intensity of the diffraction peaks of sintered samples continuously changed throughout the solid solution as shown in Figure 22, where selected XRD patterns of the sintered samples from the NBT–NTa series are

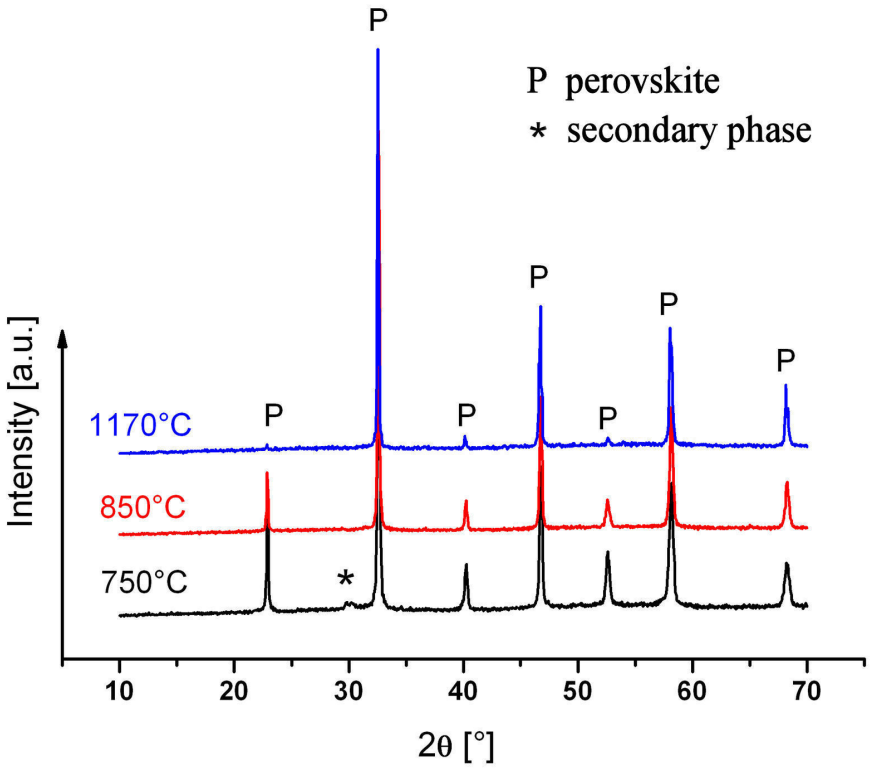

Figure 21: XRD patterns of the NBT–30NTa sample after 10 h calcinations at 750°C and 850°C, and after 5 h of sintering at 1170°C. The diffraction peaks of the perovskite matrix phase and the secondary phase are indicated.

presented. The changing of the intensity of the diffraction peaks is caused by the occupancy of the same lattice sites by different atoms in different proportions.

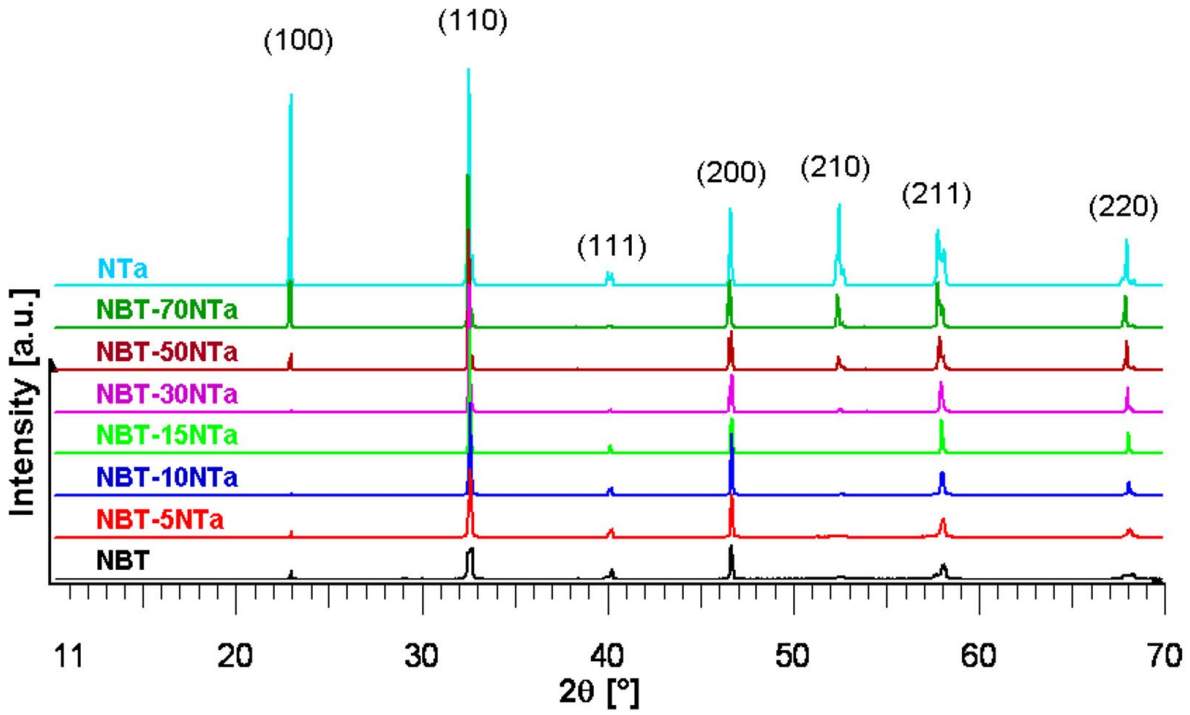

Figure 22: Selected XRD patterns of the samples from the NBT–NTa system after sintering at the corresponding temperatures (Table 2). The diffraction peaks are indexed according to the cubic perovskite structure.

The XRD results indicate the formation of the solid solutions between NBT and NTa across the whole concentration range. This is not surprising since both compounds adopt a fully occupied perovskite structure and the broad solid-solution regions between the perovskites are well known. NBT adopts a $A^{2+}B^{4+}O_3$ perovskite structure [78] with a $(Na,Bi)^{2+}$ pseudo-divalent cation on the A site, whereas NTa adopts an $A^{+}B^{5+}O_3$ perovskite structure [104]. In the most probable mechanism of substitution, the $(Na,Bi)^{2+}$ pseudo-divalent cation on the A site of the perovskite ABO_3 structure of NBT is replaced by a Na^{+} cation, while Ta^{5+} ions substitute for the Ti^{4+} ions on the B site of the perovskite structure. Such a mechanism of substitution does not require ionic or electronic compensation since the charge balance is maintained.

A detailed XRD scan of selected diffraction peaks is shown in Figure 23. A slight shift in the diffraction peaks indicates a small change in the unit-cell parameters. The unit-cell size slightly increases throughout the solid-solution series from NBT to NBT–90NTa; however, the peaks for pure NTa are shifted in the opposite direction. This observation will be discussed later, together with the synthesis characteristics of pure NTa. The small change in the unit-cell size is connected with a small change in the radii of the substituted ions. The differences in the radii of the A- and B-site ions between NBT and NTa are 0.025 Å and 0.035 Å, respectively. The differences were calculated for the coordination numbers according to the ideal ABO_3 cubic perovskite structure, i.e., 12, 6, and 6 for A, B, and O ions, respectively [8]. The individual radii of the ions were taken after Shannon [105] (Na^{+} = 1.18 Å, Ti^{4+} = 0.605 Å, Ta^{5+} = 0.64 Å, O^{2-} = 1.40 Å) and Eitel *et al.* [106] (Bi^{3+} = 1.34 Å). The atomic radius for Bi^{3+} (1.34 Å) [106] was estimated specially for the perovskite structure and the coordination number 12.

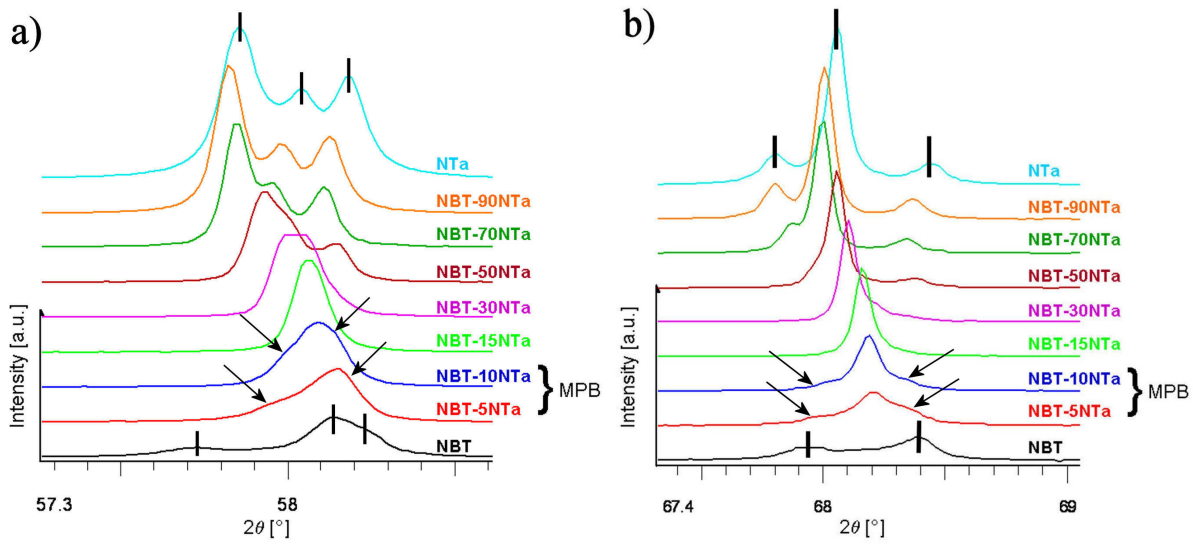

Figure 23: a) (211) and b) (220) reflections (indexed according to cubic symmetry) of the NBT–NTa solid-solution series. The NBT sample was prepared according to Spreitzer *et al.* [94]. The vertical lines represent the diffraction lines of the rhombohedral NBT and orthorhombic NTa phases. The arrows indicate the distortion due to the rhombohedral phase present in the MPB compositions.

At room temperature NBT exhibits rhombohedral symmetry with an *R*3*c* space group [78], whereas NTa has orthorhombic symmetry with a *Pbnm* space group [104]. The transition of the crystal symmetry across the solid solution is diffuse, and it is difficult to determine the boundary composition separating the rhombohedral and orthorhombic phases. The $K\alpha_2$ contribution makes this determination even more difficult. Therefore, a detailed XRD scan using monochromatic $K\alpha_1$ radiation was employed to determine the symmetry of the individual compositions. Figure 23 presents the (211) and (220) perovskite reflections of the NBT–NTa series from such a scan. NBT, prepared according to the procedure described by Spreitzer *et al.* [94], exhibits rhombohedral symmetry, which then changes to 'cubic-like' in the sample NBT–15NTa. However, with respect to all the reflections in the XRD pattern, the symmetry of the NBT–15NTa sample is distorted from cubic and could also be regarded as orthorhombic with a small deviation from cubic. In the samples NBT–5NTa and NBT–10NTa reflections of multiple symmetries were observed, indicating phase coexistence. In these samples the rhombohedral distortion and the content of the rhombohedral phase gradually decrease. With the increase of NTa concentration from 15% to 100% the orthorhombic distortion then gradually increases and the orthorhombic reflections become clearly evident.

However, an alternative explanation for the evolution of the symmetry across the NBT–NTa solid solutions can be proposed. This explanation takes into account the existence of another intermediate phase, since there is a big difference in the shape of the diffraction peaks between the samples with 15 and 50 mol% of NTa (Figure 23). In pure NBT the intermediate tetragonal phase is stable over the morphotropic phase boundary interval (255–400°C) and in the intermediate temperature range (400–500°C). With the addition of NTa, the stabilization of the rhombohedral phase and most probably also the stabilization of the intermediate phase are shifted toward lower temperatures. Thereafter, at some point the intermediate phase should be stable in the room-temperature region. Accordingly, the phase sequence is described as follows: in samples with 5 to 10 mol% of NTa and the sample with 30 mol% of NTa the coexistence of the rhombohedral–intermediate and the intermediate–orthorhombic phases, respectively, is found; samples with 15 to 25 mol% of NTa are of the intermediate symmetry, while samples with 50 mol% or more of NTa exhibit the orthorhombic symmetry. For the exact determination of the symmetry of the samples with the intermediate symmetry a more precise technique should be used, e.g., neutron diffraction [78,

107]. Since the symmetry of the intermediate phase was not determined it will be referred to as the "intermediate" phase.

To determine the optimal sintering temperature of the individual composition, first, the sintering behaviour was observed using a heating microscope. Then, sintering was performed and the samples were examined using an SEM. In the case that the quality of the samples was not sufficient, i.e., low density, the presence of secondary phases, the sintering temperature was appropriately increased or decreased. The optimal sintering temperature determined by the described procedure (Table 2) increased with increasing content of NTa, which was to be expected, since high sintering temperatures are reported for Ta-compounds [108]. Samples sintered at the estimated optimal temperatures contained no, or only traces of, secondary phases (Figure 24a). EDS analyses showed no deviations from the nominal compositions within the experimental error of the method, which confirms the formation of the solid solution, in agreement with XRD analyses. However, sintering at a higher temperature than the optimal sintering temperature resulted in the formation of secondary phases and, moreover, the concentration of the secondary phases increased with increasing sintering temperature, which suggests the thermal decomposition of the samples (Figure 24b). A semi-quantitative EDS analysis showed the presence of only TiO_2-rich secondary phases, which can be explained by the volatilization of Bi and Na oxides from the matrix of solid solutions, when the thermal decomposition appears at high temperatures.

Table 2: Optimal sintering temperature of the samples from the NBT–NTa series for a 5-h sintering time. The NBT sample was prepared according to Spreitzer *et al*. [94] (sintered for 2.5 h).

Sample, mol% NTa	Sintering temperature [°C]
NBT	1100
5–10	1150
15–30	1170
50	1230
70	1250
90	1320
NTa	1600

Due to scarce literature reports on the synthesis and sintering of pure NTa, the formation of NTa ceramics was investigated. Already after the first calcination no secondary-phase diffractions were observed in the XRD pattern of NTa, and after sintering, the orthorhombic symmetry was confirmed from a detailed scan. However, the shift in the XRD peak positions of pure NTa (sintered at 1600°C) toward higher 2θ angles is not consistent

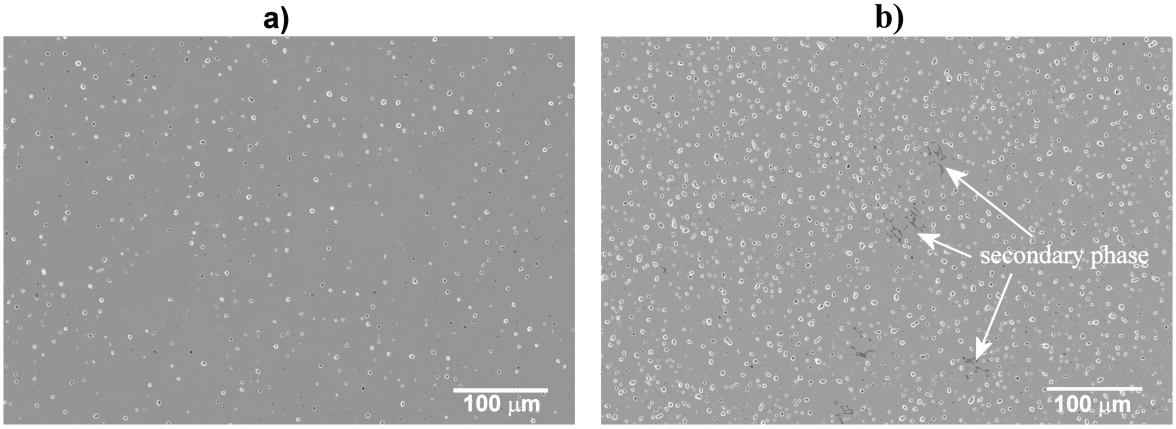

Figure 24: SEM micrographs of samples a) NBT-10NTa; sintered at the optimal sintering temperature (5 h at 1150°C); and b) NBT-30NTa; sintered at 1200°C for 5 h, i.e., higher than the determined optimal sintering temperature at 1170°C. In b) a TiO_2-rich secondary phase is observed.

with the observed trend in the NBT–NTa solid solution (Figure 23). Moreover, a bright secondary phase (indicating the increased content of tantalum oxide compared to the matrix phase) was observed when sintering the samples at temperatures higher than 1550°C. The formation of such a secondary phase was not previously documented; however, the volatilization of sodium oxide at higher temperatures was reported in the literature [109, 110]. Therefore, sodium oxide volatilization was presumed to occur during the sintering of NTa.

A significant influence of the secondary phase on the density of the samples was detected during preliminary sintering experiments. Therefore, a sintering experiment was conducted to investigate the influence of the volatilization on the density of the sintered compacts: one sample was muffled with a powder of the same composition in a closed platinum crucible (in order to reduce the volatilization), and a second sample was sintered unprotected from the surrounding atmosphere. No secondary phase was observed in the muffled sample; however, the ceramic was not fully dense after sintering at temperatures as high as 1640°C (Figure 25a). In contrast, a bright secondary phase was formed in the unprotected sample and a dense ceramic was obtained after sintering at 1600°C for 5 h (Figure 25b). The content of the secondary phase was estimated from SEM images at 1–2 vol%, which is below the detection limit of the XRD analysis, and therefore cannot be observed in the XRD pattern.

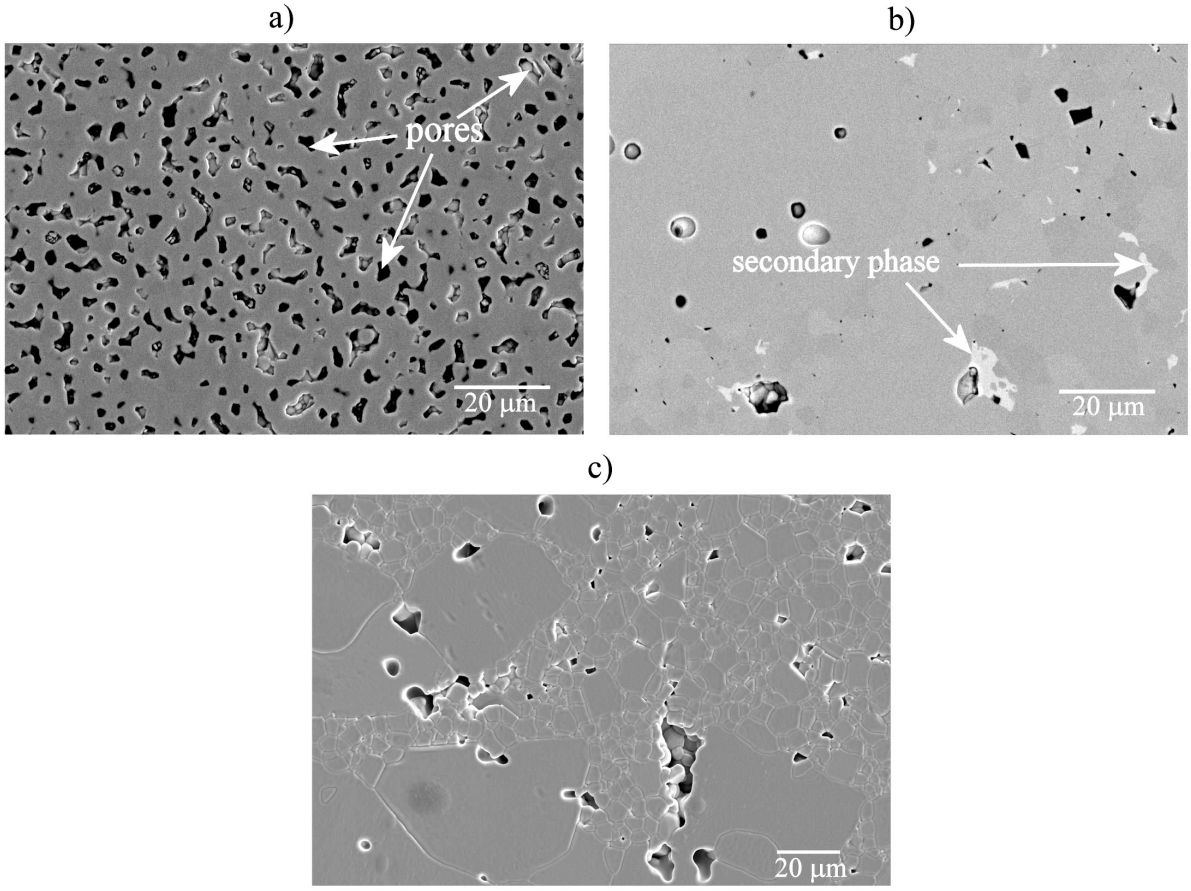

Figure 25: SEM micrographs of the NTa sample sintered in different conditions: a) BSE image of the muffled sample sintered for 5 h at 1640°C; b) BSE image of the sample sintered unprotected in air for 5 h at 1600°C and c) the corresponding SEI image of the etched sample sintered in air for 5 h at 1600°C. In a) no secondary phase is present, while a bright secondary phase is seen in b). In c) a inhomogeneous grain size distribution is observed.

According to the existing phase-equilibra diagram [111] the volatilization of sodium from NTa causes the formation of a $Na_2Ta_4O_{11}$ secondary phase. However, a semi-quantitative EDS analysis of the bright phase showed a higher Ta:Na ratio than that of $Na_2Ta_4O_{11}$. The following experiment was performed in order to identify the secondary phase:

finely ground uncompressed powder of NTa was fired in air, unprotected from the surrounding atmosphere at 1600°C for 10 h and analyzed using XRD. The XRD pattern of the as-prepared sample is shown in Figure 26. The diffraction lines of the secondary phase were consistent with the $Na_2Ta_8O_{21}$ phase. The formation of the $Na_2Ta_8O_{21}$ phase is not consistent with the existing phase-equilibra diagram [111]. The difference is believed to be due to the different experimental conditions and procedures used. Nevertheless, the formation of the secondary phase increases the density of the ceramics (Figure 25b) and causes an inhomogeneous grain size distribution, seen from the thermally etched sample in Figure 25c (the microstructure characteristics will be discussed in the next section). For the dielectric and stress-dependence characterization, a sample sintered at 1600°C in air was used, since the density of the single-phase sample obtained at 1640°C and muffled, was too low.

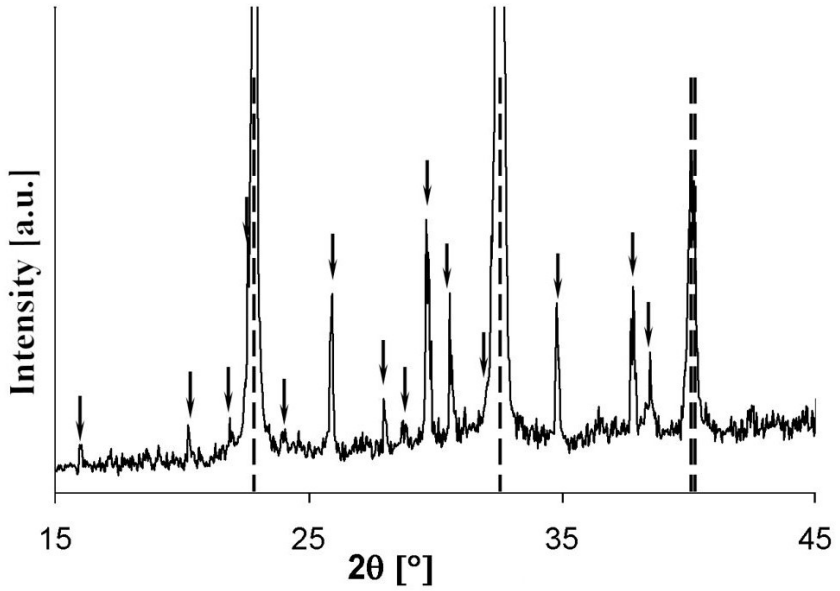

Figure 26: XRD pattern of NTa powder fired at 1600°C for 10 h. Broken lines indicate the diffraction peaks of NTa, and arrows indicate the diffraction peaks of the $Na_2Ta_8O_{21}$ secondary phase, according to the JCPDS card number 28-1137.

The formation of the secondary phase most probably occurs due to the volatilization of sodium oxide from the sample. However, the volatilization of the sodium oxide itself does not explain the shift in the XRD peak positions observed in pure NTa (Figure 23). These could appear if the NTa structure would tolerate the deficiency of sodium on the A site of the perovskite structure. In that case the peak positions would be shifted toward higher 2θ angles, since the cell parameter would decrease. However, no evidence for sodium deficiency was observed by the experiments performed in this study.

4.1.2 Microstructure analysis

The prepared materials, except pure NTa, were classified into three groups according to the microstructure characteristics. Typical micrographs of the samples from the three groups are shown in Figure 27.

Samples NBT–5NTa and NBT–10NTa were classified into the first group (Figure 27a). The density of these samples, measured using Archimedes' method, was around 98% of the theoretical density. Only traces of the secondary phases were observed in these samples. The average grain size was estimated to be 30 to 35 μm. Another feature is the closed porosity observed from the thermally etched samples. Relatively big grains and closed porosity

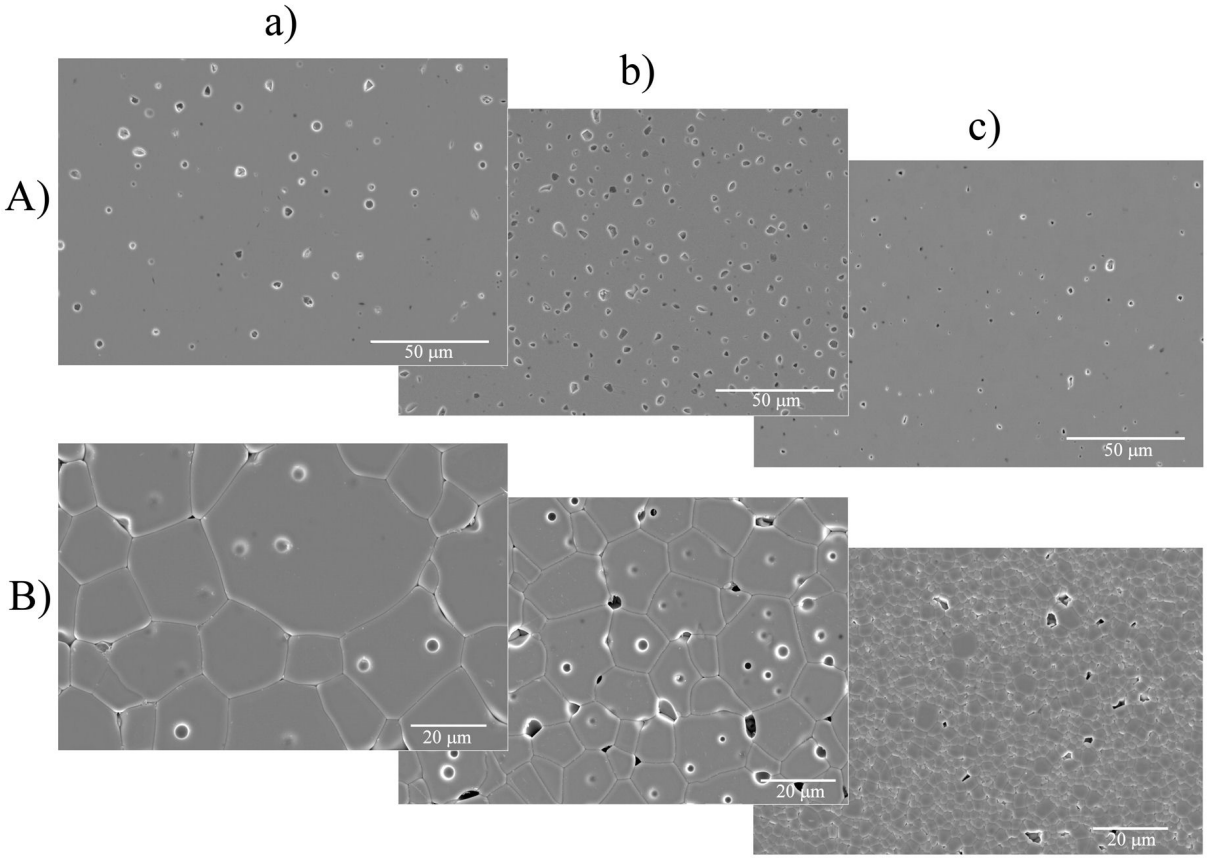

Figure 27: Microstructures of the sintered samples a) NBT–5NTa, b) NBT–30NTa, c) NBT–90NTa, showing SEM images of A) polished and B) etched samples.

indicate a high grain-boundary mobility during the sintering process. The reason for such behaviour is believed to be melt-assisted grain growth. It is known [94] that a small amount of liquid phase is formed during the synthesis of NBT. Thereafter, a similar mechanism is very likely to be present also in the NBT-rich compositions.

Samples with a content of NTa from 15 to 50 mol% were classified into the second group (Figure 27b). The density of these samples was lower, around 94–95% of the theoretical density; this is except for the sample NBT–50NTa, for which it was around 97% of the theoretical density. In order to improve the rather low density of the samples the sintering temperature was increased; however, secondary phases started to form as the thermal decomposition of the samples was strongly increased (Figure 24b). Cold isostatic pressing was used to reduce the residual porosity in the sintered samples; in contrast, a slight increase in the porosity was observed. The concentration of the secondary phases was the highest in samples NBT–30NTa and NBT–50NTa. However, the concentration was still of the order of trace amounts, i.e., below 0.5%. The average grain size further decreased with the increasing content of NTa from 18 µm to 6 µm. The concentration of closed porosity was lower when compared to the materials from the first group.

The samples with the highest concentration of NTa, i.e., NBT–70NTa and NBT–90NTa, were classified into the third group (Figure 27c). The density of these samples is above 98% of the theoretical density. The content of residual porosity is even smaller than the materials from the first group. No secondary phases were observed in these samples, and the average grain size was around 3–4 µm.

The characteristics of pure NTa are somewhat different. The density of the sample sintered in a closed crucible was very low, below 90% of the theoretical density (Figure 25a), and the average grain size was around 5 µm. No secondary phase was observed in this

sample. In contrast, the sample that was sintered unprotected from the surrounding atmosphere contained a secondary phase and its density was much higher, around 97% of the theoretical density (Figure 25b). The grain size distribution in this sample was very inhomogeneous (Figure 25c), containing a smaller number of big grains (up to 100 μm) and a larger number of small grains (smaller than 10 μm). The exaggerated grain growth was ascribed to the presence of a liquid phase formed during the sintering. The liquid phase is believed to be the $Na_2Ta_8O_{21}$ phase that was formed as a consequence of the sodium oxide volatilization and the decomposition of the matrix phase.

The grain size decreases and the sintering temperature (Table 2) increases with increasing content of NTa throughout the solid-solution series. Such behaviour is ascribed to the lower sinterability of the materials due to the increasing content of tantalum oxide [108]. The obtained ceramic compacts were mainly single phase with a high density; thus, they were of sufficient quality for a proper characterization of their electrical properties.

4.1.3 Dielectric properties

The temperature dependence of the dielectric properties of the sintered samples from the NBT–NTa solid solutions is shown in Figure 28. As the concentration of NTa increases, three main changes can be observed:

(i) decreasing and broadening of the permittivity maximum,

(ii) decreasing of the temperatures of the dielectric anomalies (T_m, T_{hump}),

(iii) decreasing of the dielectric losses at room temperature.

The changing of the dielectric properties is gradual and continuous over the whole concentration range. Some of the distinctive features observed are:

- In samples NBT–5NTa and NBT–10NTa the characteristics of the dielectric response are similar to those of pure NBT (Figure U16). Both the frequency-dispersive anomaly and the dielectric maximum are present, and the permittivity of the maximum is higher than the permittivity of the frequency-dispersive anomaly.
- In samples with 15 to 25 mol% of NTa the dielectric maximum strongly decreases and its permittivity is only slightly higher than the permittivity at the frequency-dispersive anomaly.
- The dielectric maximum then disappears for sample NBT–30NTa, for which only the frequency-dispersive anomaly is observed.
- The temperature of the dielectric maximum for sample NBT–10NTa decreases to 270°C, while ε_{max} decreases to 1350 (for comparison: in pure NBT T_m = 320°C and ε_{max} = 3070; see Figure 16). The data correspond to a measuring frequency of 1 MHz.
- In samples with 15 to 25 mol% of NTa, a broad maximum, or more likely a plateau, is observed ranging over 200 to 300°C. The value of the dielectric constant at the dielectric maximum falls below 1000.
- In samples with 5 to 25 mol% of NTa the dielectric maximum is frequency independent in the measured frequency range and is not reflected in an anomaly of the dielectric losses (Figure 28b).
- The frequency-dispersive anomaly shifts toward lower temperatures and broadens over a wider temperature range for the samples NBT–5NTa and NBT–10NTa. It is

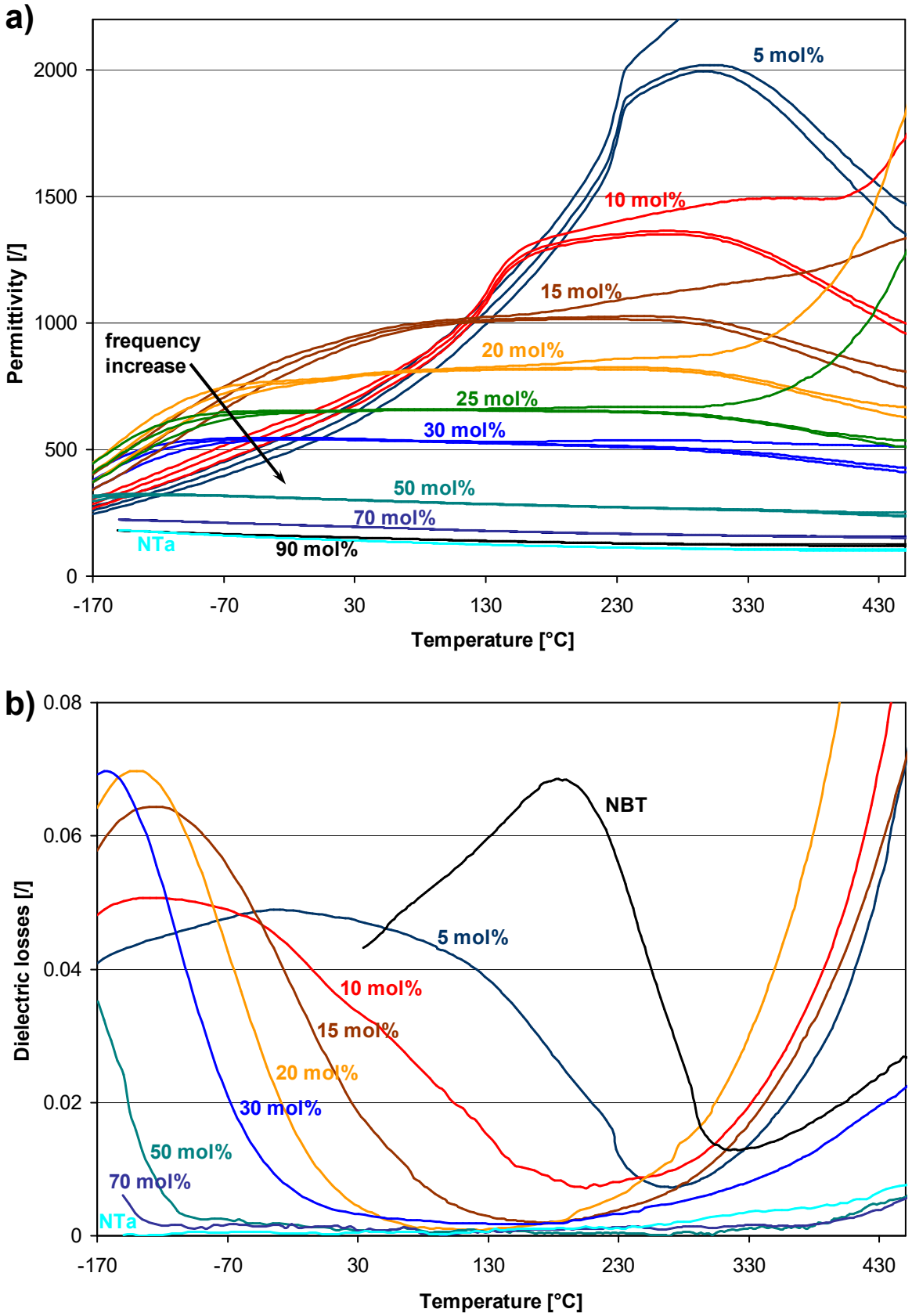

Figure 28: Temperature dependence of a) the relative permittivity and b) the dielectric losses of the samples from the NBT–NTa series. In a), the permittivity data obtained at the frequencies 10 kHz, 100 kHz, and 1 MHz are shown (the data obtained at 1 kHz are excluded for clarity). In b), the dielectric losses at 1 MHz are shown, together with the data for pure NBT.

less distinctive and is better seen from the temperature dependence of the dielectric losses.

- In samples with 15 to 25 mol% of NTa the frequency-dispersive anomaly again becomes more evident and is gradually shifted below room temperature. With a larger addition of NTa further shift to even lower temperatures is observed and the anomaly is clearly evident. The shift is better seen from the temperature dependence of the dielectric losses.
- The maximum of the dielectric losses gradually shifts toward lower temperatures with increasing content of NTa. A noticeable broadening of the loss maximum for samples with 5 and 10 mol% of NTa is observed.
- The minimum of the dielectric losses gradually expands over a broader temperature range with the increasing content of NTa.

According to the widely accepted explanation for the dielectric properties of pure NBT, the frequency-dependent anomaly at around 200°C is a result of the gradual stabilization of the rhombohedral phase into the macroscopic ferroelectric domains, while the dielectric maximum is ascribed to the dynamics of the polar nanoregions, which are formed after the destabilization of the tetragonal phase on cooling. When a small amount of NTa, i.e. 5 to 10 mol%, is added, the temperature interval of the stabilization of the rhombohedral phase is shifted toward lower temperatures and expands over a broader temperature range, as seen from the temperature dependence of the dielectric losses (Figure 28b). This is likely to be connected with the decreasing and broadening of the temperature interval of the stabilization of the rhombohedral phase. Such an explanation is supported by the XRD measurements showing the morphotropic phase composition at room temperature (Figure 23). In sample NBT–5NTa, where the rhombohedral phase still dominates, the frequency dispersion appears mainly above room temperature. With a decrease of the content of the rhombohedral phase in sample NBT–10NTa, the temperature interval of the frequency dispersion shifts into the room-temperature region.

The upper temperature of the dielectric loss maximum (i.e., the temperature at which the losses start to increase on cooling) corresponds to the starting point of the stabilization of the rhombohedral phase. With decreasing temperature, the content of the rhombohedral phase and the correlation between the rhombohedral regions increase, causing a decrease in the dynamics and polarizability of the rhombohedral regions. This results in a decrease of the permittivity. In sample NBT–15NTa, the upper temperature of the dielectric loss maximum is above room temperature (at ~120°C, Figure 28b) and the permittivity at room temperature decreases. Such behaviour indicates that the rhombohedral nanoregions are stable at room temperature and the sample possesses relaxor properties. With higher additions of NTa, the dielectric loss maximum shifts to lower temperatures. In sample NBT–30NTa the rhombohedral nanoregions at room temperature are not stable any more. Together with the decrease in the stability of the rhombohedral nanoregions, the properties of the materials change, and paraelectric behaviour is expected from the samples with 30 and more mol% of NTa at room temperature.

With increasing content of NTa the dielectric maximum strongly decreases. This finding is believed to be a consequence of a smaller concentration, size and/or polarizability of the polar nanoregions when the content of NTa increases. However, the temperature interval of the relaxation of the stabilizing rhombohedral regions remains broad. The appearing permittivity maximum therefore expands over a broad temperature range. As described above, in pure NBT the dielectric maximum is ascribed to the dynamics of the polar rhombohedral nanoregions that are formed after the destabilization of the tetragonal phase on cooling (the nanoregions then become stable 40°C below the dielectric maximum).

Thereafter, the existence of the permittivity maximum in samples with 5 to 25 mol% of NTa indicates the presence of an intermediate phase in the NBT–NTa system. A similar situation is observed in pure NBT, where the tetragonal phase exists in the intermediate temperature range between the rhombohedral and cubic phases. The existence of the intermediate phase is in accordance with the phase-transition sequence proposed according to the XRD results (page 37).

In samples with 20 and 25 mol% of NTa the difference in the value of the permittivity of the frequency-dispersion and the maximum is very small; however, both anomalies are separated, as shown in Figure 29. Such behaviour changes for sample NBT–30NTa where only the frequency-dispersive anomaly is evident. It appears that the temperature of the permittivity maximum decreases faster than the temperature of the frequency-dispersive anomaly, and that the temperature of both anomalies is approximately equal in the sample NBT–30NTa. The approaching of both anomalies indicates that the temperature interval in which the intermediate phase is stable narrows. Such behaviour is supported by the XRD analysis and the dielectric measurement. According to the XRD results, a morphotropic composition of the intermediate and orthorhombic phase was detected in the NBT–30NTa sample at room temperature, while the dielectric measurements showed that the stabilization of the rhombohedral phase begins at around 0°C (i.e., at the temperature where the frequency dispersion appears – Figure 29).

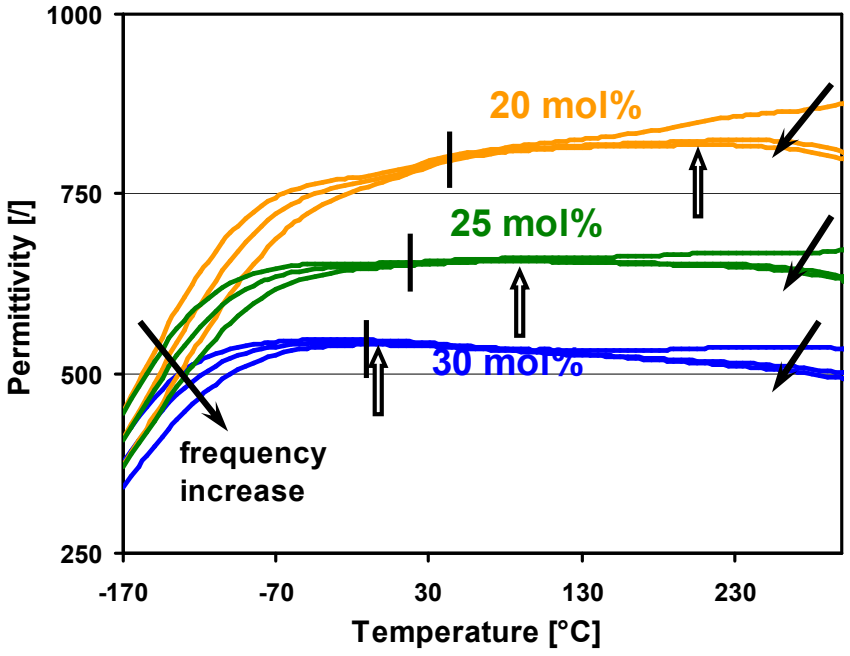

Figure 29: A close-up look at the dielectric properties of samples with 20, 25 and 30 mol% of NTa, at 10 kHz, 100 kHz and 1 MHz (the frequency increase is marked by full arrows). The permittivity maximum at a frequency of 1 MHz (open arrow) and the approximate upper temperature of the dielectric dispersion (black vertical line) are designated.

The value of the permittivity maximum decreased with the increasing content of NTa throughout the solid-solution series; however, an increase in the room-temperature permittivity was observed. The change of the permittivity at 25°C as a function of the composition is shown in Figure 30. The permittivity first increases and reaches the highest value in sample NBT–15NTa, i.e., 908, and then decreases with the further addition of NTa. Such a behaviour of the room-temperature permittivity is a consequence of the shifting of both dielectric anomalies toward lower temperatures. Such an influence is in accordance with the XRD results, which showed the destabilization of the rhombohedral phase with NTa addition, and this is typical for an incipient ferroelectric material [96]. The increasing

permittivity and dielectric losses at higher temperatures (Figure 28), especially at lower frequencies (≤10 kHz), is believed to be connected with the space-charge contributions originating from the high ionic conductivity [112].

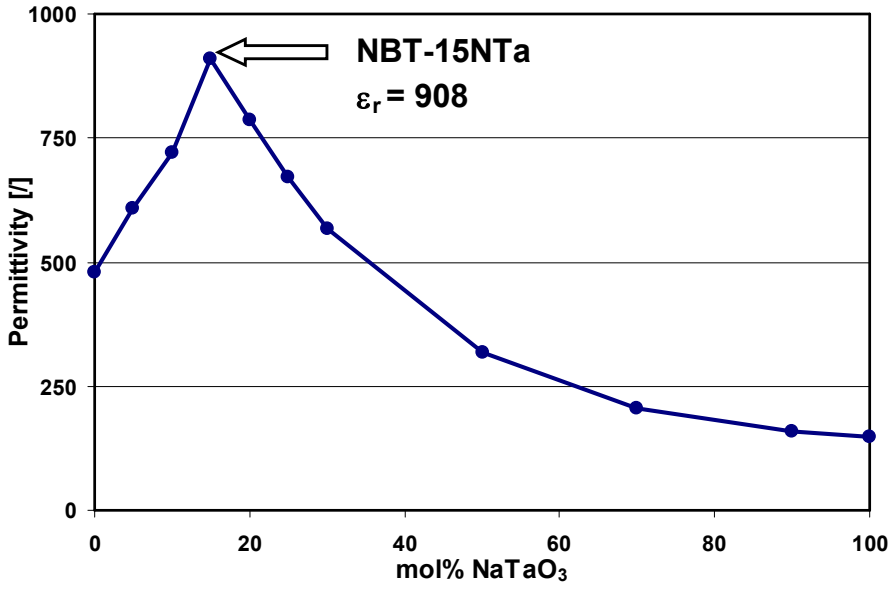

Figure 30: Room-temperature permittivity of materials from the NBT–NTa series.

In compositions with a 5–30 mol% addition of NTa, the room-temperature permittivity increases compared to pure NBT as the phase transitions are shifted into the room-temperature region. According to the theoretical treatment of the pressure dependence of the permittivity (§1.6), an increase in the axial pressure's effect on the permittivity in these samples is expected.

4.1.4 Ferroelectric properties

The results of the ferroelectric hysteresis measurements are presented in Figure 31. The measurements were performed at a frequency of 10 Hz and the highest applied field was 100 kV/cm. For comparison the ferroelectric hysteresis of pure NBT [94] is shown. With small addition of NTa, i.e., 5 mol%, the remanent polarization (P_r) increases. With a larger addition of NTa P_r then quickly decreases. The coercive field (E_c) monotonously decreases with increasing NTa content. The sample NBT–5NTa shows a typical ferroelectric hysteresis loop with P_r=42 μC/m^2 and E_c=53 kV/cm. The NBT–10NTa sample has a slim hysteresis loop with a small P_r (6 μC/m^2) and relatively high saturation polarization (P_{sat}=30 μC/m^2), characteristic for relaxors. Samples with 15 to 30 mol% of NTa show a small hysteresis and somewhat increased saturation polarization, indicating weak relaxor properties, while samples with a larger addition of NTa show linear paraelectric characteristics.

The ferroelectric measurements are consistent with the dielectric and XRD measurements. The rhombohedral phase of NBT is known to be strongly ferroelectric with a high P_r (38 μC/cm^2) and with a rigid domain-wall structure reflected in a high E_c (73 kV/cm) [79, 94]. When NTa is added, the intermediate non-ferroelectric phase (detected by the XRD measurements) appears. Therefore, the content of the rhombohedral phase decreases and, additionally, the rhombohedral distortion decreases. These changes are reflected in the XRD spectra, where phase coexistence and a decrease in the rhombohedral distortion were observed (Figure 23). These changes result in an easier movement of the domain walls and a better orientation of the domains in the direction of the applied field. The former results in a smaller

E_c and the latter in a higher P_r, as observed in the NBT–5NTa sample. Such behaviour is typical for samples from a morphotropic phase boundary region.

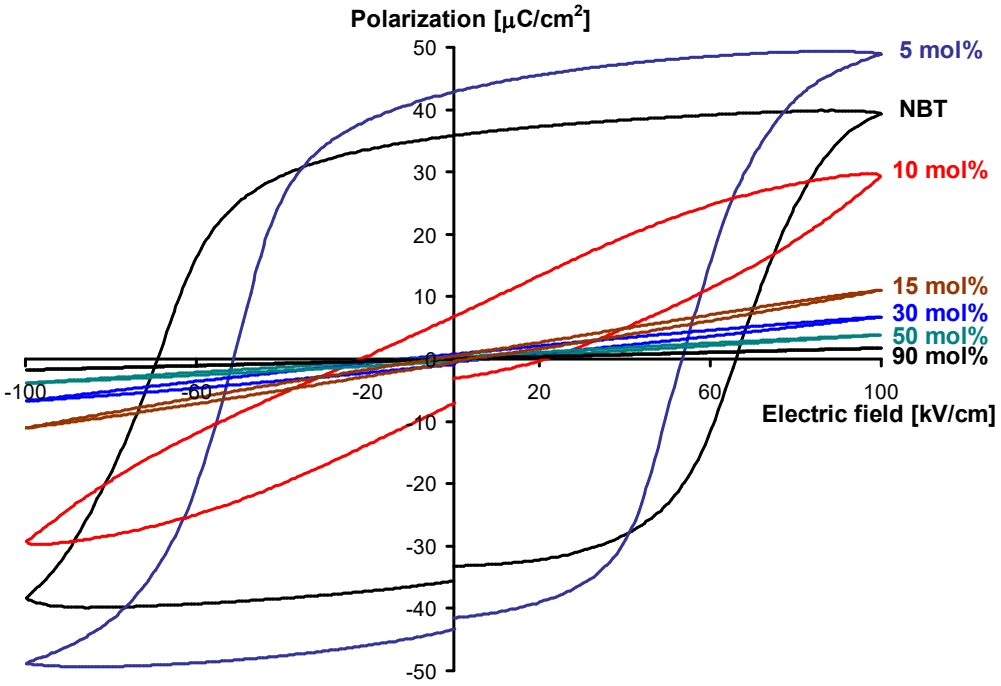

Figure 31: Polarization–electric field hysteresis of samples from the NBT–NTa series. Measurements were performed at a frequency of 10 Hz.

In the NBT–10NTa sample, the portion of the non-ferroelectric phase increases and this reduces the correlation between the rhombohedral regions, resulting in a low value of E_c. Stable rhombohedral regions are dispersed in the non-ferroelectric matrix. This is a phenomenon which is typical of relaxors. Rhombohedral regions are polarized in an applied electric field and their polarization increases in proportion to the applied field. The spontaneous polarization, P_s, of the regions is small, which results in a small value of P_r. The existence of the stable rhombohedral regions is indicated by the XRD analysis (morphotropic phase boundary composition) and the dielectric measurements (frequency dispersion of the dielectric properties).

According to the dielectric measurements, in compositions with 15 to 25 mol% of NTa the stabilization of the rhombohedral phase begins above room temperature. These samples possess relaxor properties; however, due to the small concentration and size of the rhombohedral regions their relaxor properties are less evident in the polarization–electric field measurements. The relaxor properties are indicated by a hysteresis and by an increased saturation polarization. With larger additions of NTa, the properties of the materials changed to paraelectric. The slope of the value of the saturation polarization decreases, according to the decrease of the permittivity, with the increasing concentration of NTa.

According to theory, an applied stress has a bigger influence on the permittivity in a sample with a smaller coercive field (§1.6). Thereafter, an increase in the pressure dependence of the permittivity in samples with NTa additions that possess a reduced value of the coercive field is expected. The results of the ferroelectric measurements showed that particular compositions with 10 to 30 mol% of NTa are interesting due to the change of character from relaxor-like to paraelectric.

4.1.5 Uniaxial stress dependence of the permittivity

4.1.5.1 Experimental setup and measurement method

A mechanical lever press was used that ensure a stable axial stress loading of the sample. The choice of a lever is better than the choice of a hydraulic mechanical testing machine since there is no need to compensate for the possible drifting of the system and sample to maintain a constant stress. The lever system was constructed so as to achieve a high stress loading, i.e., p_a>200 MPa, and multiple measuring points across the measured stress range. To assure consistency at least three samples of each composition were tested. The usual diameter and height of a disc-shaped sample was around 5 mm and 1.5–2 mm, respectively. The height of the sample has to be considered. On one hand, the diameter-to-height ratio for measuring the capacitance should be around 10 [113], while on the other hand, the diameter-to-height ratio in the mechanical testing should be lower than 0.7 to ensure a uniform uniaxial stress and reduce clamping [56, 61]. The high ratio in capacitors is important when measuring low-permittivity materials and is less significant in high permittivity measurements [113], while the low ratio is not suitable from the applications point of view. The diameter-to-height ratio in this study is in between the two mentioned values, i.e., around 2.5–3.3, and is similar as in other investigations performed to study the effect of the pressure on the permittivity. Additionally, a few samples with the ratio around 1 were measured and no significant difference was detected in comparison to samples with a ratio of around 3.

The sequence of the pressure changing used in the present measurements (shown in Figure 32) made it possible to collect data on the stress and time dependence of the permittivity as well as to achieve information on the reversible and irreversible part of the permittivity change. A stepwise increase of the pressure in 1 minute intervals was used in the

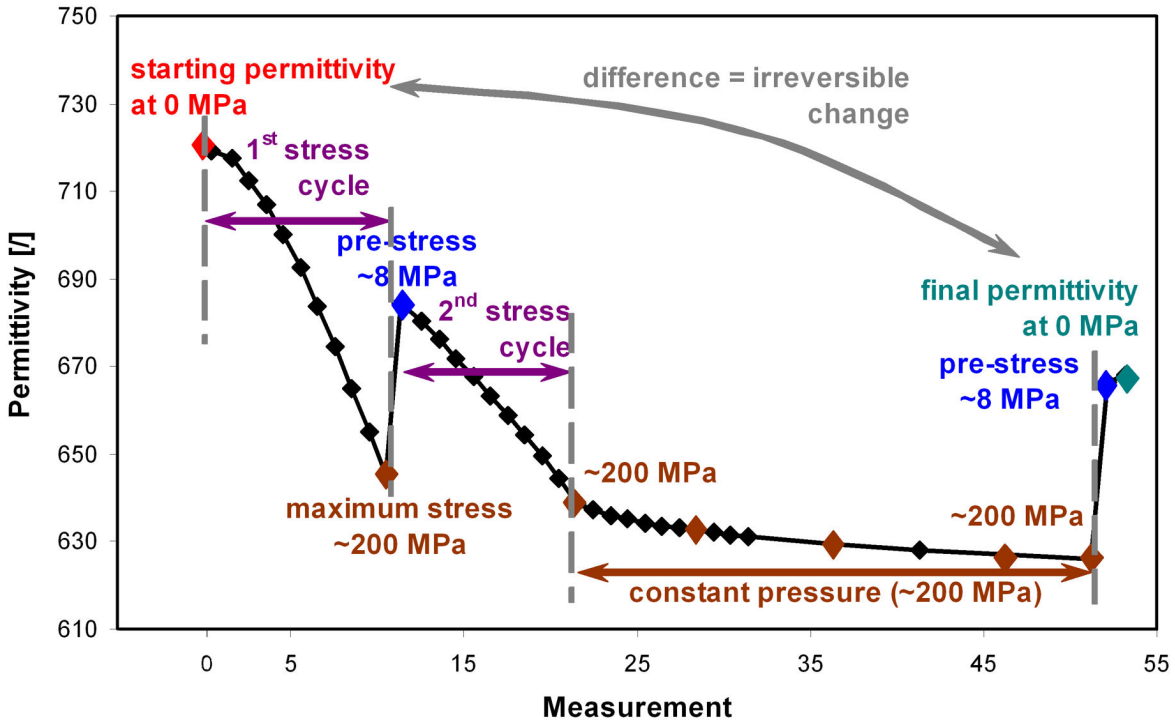

Figure 32: Details of the stress testing sequence and definitions of the expressions used. The colour of the text corresponds to the colour of a distinctive point on the obtained curve marked by diamonds or to a distinctive segment of the measurement marked by arrows. The segments of the compression test are separated with vertical dashed lines, marked on all figures in this study. The measurement number approximately corresponds to the time (in minutes) elapsed from the beginning of the test.

experiments. The permittivity was measured 1 minute after the increase of the pressure, just before the next increase. The compression test, presented in Figure 32, consists of two successive stress cycles and a time interval (usually 10 min) under constant maximum pressure (>200 MPa), followed by a stress release. The two stress cycles and the constant pressure time interval are separated with vertical dashed lines on figures of the results in this study.

Additional dielectric measurements were performed on the tested samples several days after the compression test to monitor changes due to possible relaxational processes. The samples that were tested were thermally depolarized. Then, identical compression tests were performed on thermally depolarized samples to compare the permittivity response to the applied stress with respect to the virgin state. In this way, the effect of microcracking, which can appear during pressure loading and can change the properties of the tested material, can be eliminated [68]; according to the theory, the thermally depolarized state is equivalent to the virgin state of the sample [2].

The measurement setup also enabled simultaneous assembling of the results at multiple measuring frequencies (1, 10 and 100 kHz, and 1 MHz). Under stress-free conditions on the mechanical testing system, the contact between the sample and the Cu-foil electrode was not perfect; therefore, minor deviations at the beginning and the end of the measurements under stress-free conditions were observed. All measurements in this set of experiments were performed at room temperature.

Simultaneously with the measurements of the samples capacity, the data of the dielectric losses were collected. The obtained loss tangent data were less accurate, due to additional contributions from the components of the system (cables, electrodes, contacts, etc.), especially for samples with smaller value of the loss tangent. In the majority of the tests, the loss tangent decreased with increasing axial pressure. From the application point of view, the losses are less decisive [4] (however, a component is more energy-efficient when the losses are small). Accordingly, not much attention was paid to this segment of the dielectric properties and the evolution of the loss tangent during compressive tests is not presented in this study.

4.1.5.2 Pure $Na_{0.5}Bi_{0.5}TiO_3$

The results of the axial pressure's influence on the permittivity of NBT (measurements of three samples) at room temperature for the first stress cycle of virgin samples are shown in Figure 33. The permittivity decreases with increasing axial pressure; however, the dependence is not linear. No saturation can be observed up to the highest applied pressure (>200 MPa). The relative change in the permittivity at 200 MPa is approximately 3%, which is significantly less than reported by Suchanitz *et al.* [72]. This difference is believed to appear due to the different measurement method used, compared to reports in the literature. The measurement method used in the literature is explained in the paragraph below and the reasons for the difference in the sensitivity to the applied stress are explained on pages 57-58.

After the compression test, the starting value of the permittivity was not regained. This finding is not consistent with the literature [71-75, 95], where a full reversibility of the properties with changing pressure was reported. The different behaviour is believed to appear due to a different measurement method used in the literature. There, the samples were heated prior to all the measurements above the transition temperature to the cubic phase, i.e., to 550–600°C, and annealed for 30 min. Such sample preparation causes a deletion of the material's pre-history, as the samples are thermally depolarized at increased temperature. In such an experiment the reversibility of the material's properties can be observed. However, in NBT with a macroscopic domain structure it is far more likely to observe some irreversible

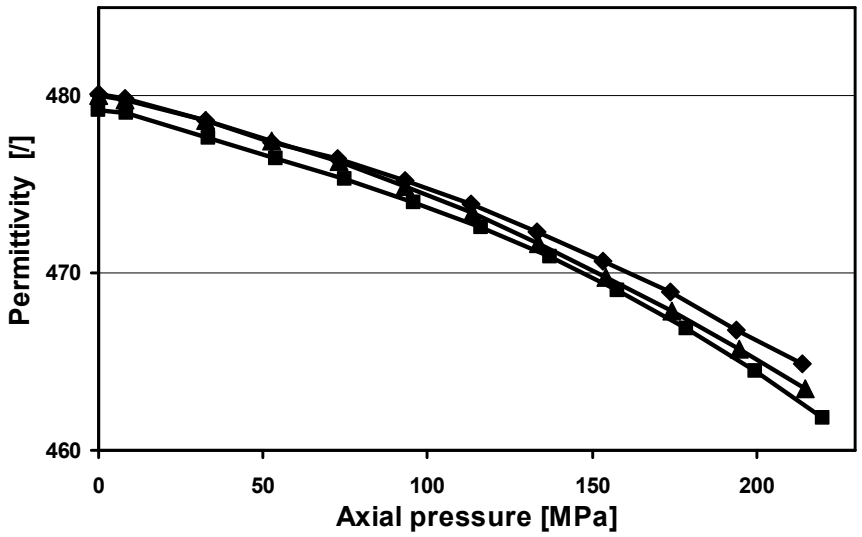

Figure 33: Axial pressure dependence of the permittivity at 1 MHz for three virgin samples of NBT.

variation of the samples properties due to changes of the domain structure caused by the applied pressure. According to domain-switching mechanisms [16], domain-structured material will become mechanically polarized under the applied axial pressure as more domains will align in the plane perpendicular to the applied stress direction, through the non-180° domain-wall switching. Mechanical polarization is responsible for the irreversible change of the dielectric properties observed in NBT samples.

Figure 34 shows the results of the whole stress testing sequence of a NBT sample. Significant differences between the first and the second stress loading/unloading cycle were observed. In the first cycle the permittivity decreases by 3.2% and then increases after stress release to 1.3% below the starting value. In the second stress cycle, the permittivity decreases to –3.8%. After an additional 10 min at the maximum pressure (214 MPa), the permittivity decreases to 4.3% below the original value, and then sets at –2.3% at the end of the test. The difference in the value of the permittivity between the cycles is due to the memory effect of the material, i.e., the mechanical polarization of the material. In the first cycle the domain structure of the sample changes and after stress release a new equilibrium domain structure is established. That is the starting point of the second stress cycle, during which the domain structure is additionally altered. Thereafter, the differences between the starting and final permittivity of the first and second stress cycle arise. This observation indicates that the mechanical polarization of the sample after the first cycle is not completed. The same is valid for the second stress cycle, which was proved by a third pressure cycle that was also found to be different from the second one.

Another difference between the first and the second stress cycle (Figure 34) is in the degree of linearity of the pressure dependence of the permittivity. The second cycle curve is much more linear than the first one. This linearity is related to the contribution of the non-180° domain switching, which is a non-linear process, to the overall change in the permittivity. In the first cycle this contribution is higher since in the virgin sample the domains are randomly oriented. After the first stress cycle the sample is partially polarized and more domains lie in the plane perpendicular to the stress direction. Therefore, fewer domains are switched during the second stress cycle and, thus, the extrinsic contribution, due to the non-180° domain switching, is smaller. Consequently, the stress dependence of the permittivity is more linear. However, the polarization of the sample is not complete, and the third stress cycle is different from the second one.

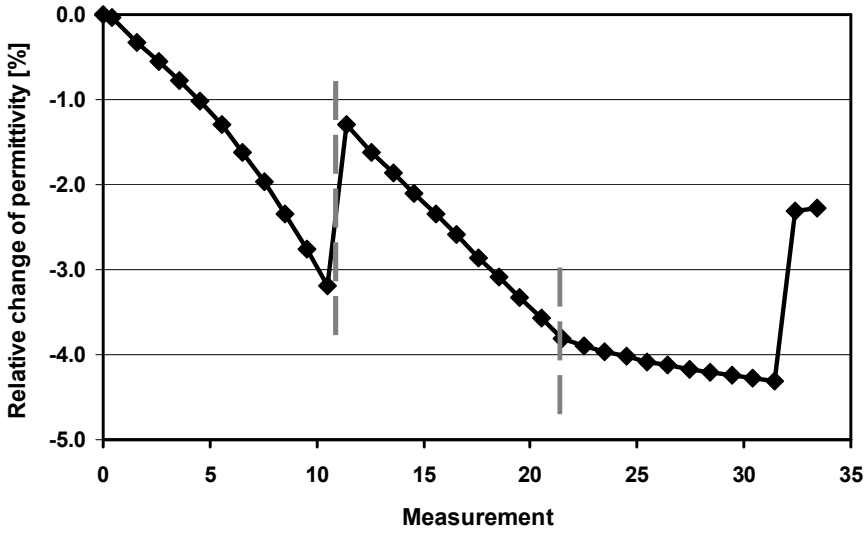

Figure 34: Relative change of the permittivity at 1 MHz during the stress testing of sample NBT. The starting value of the permittivity was 480.1, and the values of the pre-stress and the maximum stress were 8 and 214 MPa, respectively.

An additional feature is seen from the third part of the test (Figure 34), which corresponds to a change of the permittivity with time under the maximum applied stress. In this segment, the permittivity decreases under constant loading by an additional 0.5% in a 10 min period. The change is gradual and the permittivity tends to saturate at a certain value. This long-term relaxation can be explained by the pinning of domain walls with random potential defects [63]. During stress application or release, the domain walls are partially unpinned. A certain time is needed for the restoration of new pinning configurations and for the stabilization of a new domain structure. In the literature [63], this long-term relaxation was found to be significant during both the stress application and the stress release. In this study, the relaxations after the stress application were found to be significant (third part of the test – Figure 34), while only minor relaxations were detected after the stress release. The permittivity of the tested samples that were re-measured a few times after the tests in 24-h intervals was approximately constant.

After the tests an irreversible change of the permittivity was observed and the dielectric properties of the samples were stable and almost unchanged, even after few months. The samples were mechanically polarized and the new domain structure was stable. In theory, a sample should regain the original properties after a thermal depolarization process [2]. To examine the thermal depolarization, samples were annealed for 30 min at 600°C. At this temperature the cubic phase is stable, and when the sample is cooled to room temperature, a new random orientation of the domains is established. The new domain structure is equivalent to the virgin state of the material observed after sintering. Indeed, the virgin properties of the samples were restored after annealing and, moreover, no changes in the samples' response to the applied stress were observed (Figure 35), except for a small difference of 0.2%. Such a finding eliminates the possibility that the changes in the dielectric properties were caused by the formation of microcracks [68].

After the annealing of the NBT samples a significant discrepancy was observed. The value of the permittivity was ~7% higher than the virgin sample, and then slowly decreased to the original value after several days. Such behaviour is believed to be the cause for the minor discrepancy observed in Figure 35. Similar behaviour, although much less pronounced, was detected for virgin samples after sintering. The decreasing of the permittivity after cooling

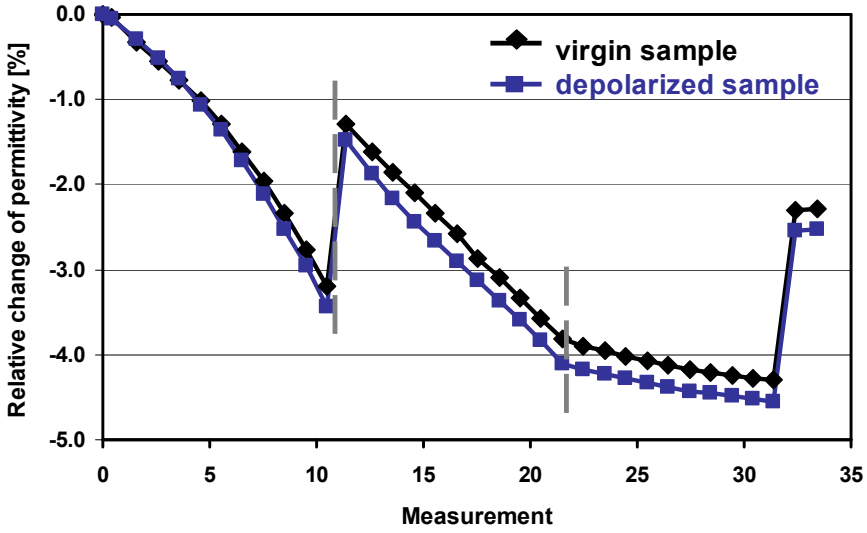

Figure 35: Relative change of the permittivity at 1 MHz during the stress testing of the virgin and thermally depolarized sample of NBT. The starting values of the permittivity were 480.1 and 485.4 for the virgin and thermally depolarized samples, respectively. The values of the pre-stress and the maximum stress were 8 and 214 MPa, respectively.

from high temperature could be explained by the rhombohedral-to-tetragonal phase transition, which appears at rather low temperatures: in the temperature interval between 400 and 255°C. This phase transition is very slow [114]. Traces of the tetragonal phase in rhombohedral NBT were found even at room temperature [92]. To investigate whether the amplification of this behaviour is related to the compression measurements, which were performed on the samples, the following test was performed: two samples were sintered at the same time, one sample was regularly tested for the stress dependence of the permittivity and annealed, while a reference sample went through the same procedure at the same time except for the stress measurements. It was found that after annealing both samples showed identical behaviour. Thus, the observed behaviour is believed to be inherent to the material; however, it is amplified in an annealed sample in comparison to a virgin sample.

The influence of the measuring frequency on the materials´ response to the applied stress was small. The shape of the response remained unchanged at all measured frequencies from 1 kHz to 1 MHz. The sensitivity to the applied stress increased with decreasing frequency and the relative change of the permittivity was approximately 1.5% higher at a frequency of 1 kHz as compared to a frequency of 1 MHz. Such results indicate that domain walls or mechanisms, which contribute to the polarization and the permittivity of the sample at lower frequencies, possess a higher stress dependence. Therefore, the absolute change as well as the relative change of the permittivity is higher at a lower measuring frequency.

4.1.5.3 $Na_{0.5}Bi_{0.5}TiO_3$–$NaTaO_3$ compositions

Similar behaviour as in pure NBT was observed in all the samples from the NBT–NTa solid-solution series, including the NTa sample. The results of the pressure dependence of the permittivity for selected compositions are shown in Figure 36. For all compositions the differences between the first and the second stress cycle, the irreversible change after stress release and the time dependence of the permittivity under constant pressure were found. Again, the curve of the second stress cycle is much more linear than the first one due to a smaller contribution of the non-180° domain switching. The curve of the first stress cycle was slightly more curved in samples with 50 and 70 mol% of NTa; however, the absolute change of the permittivity in these samples is small.

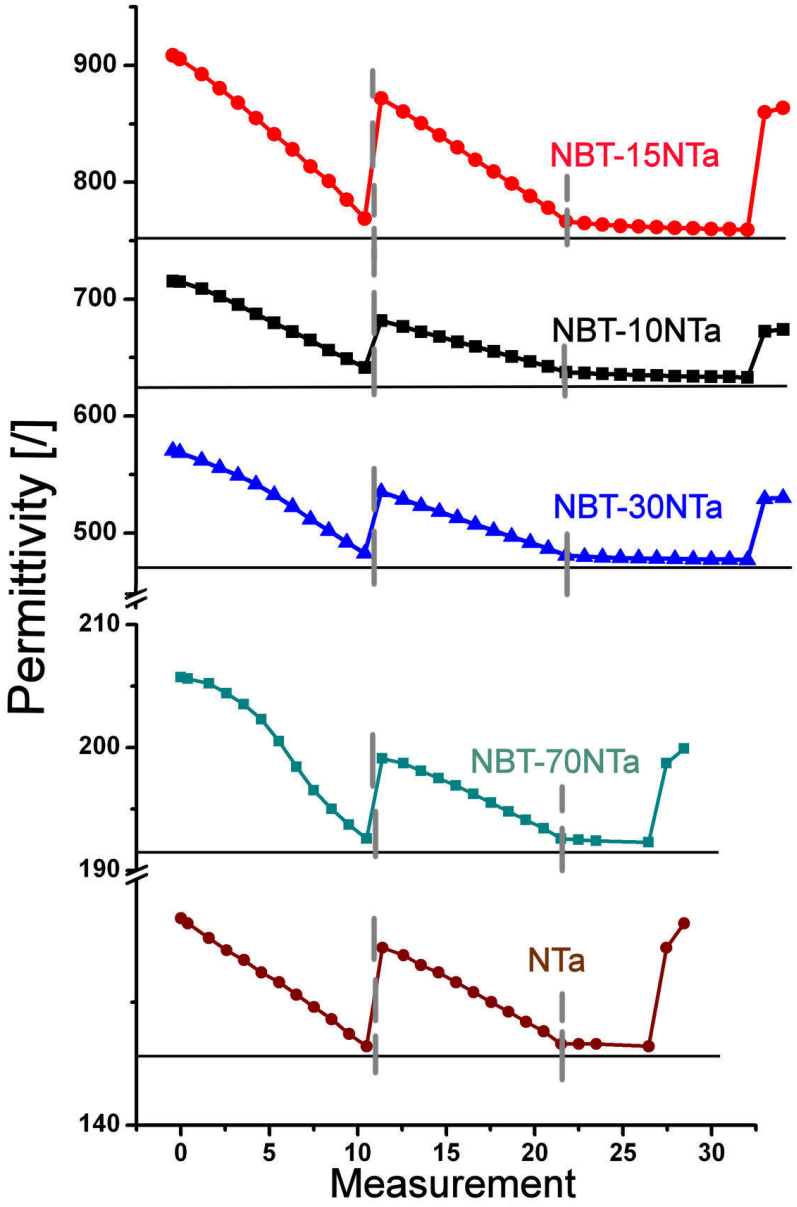

Figure 36: Axial pressure dependence of the permittivity at 1 MHz of selected samples from the NBT–NTa series.

Figure 37a shows the room-temperature permittivity of samples under stress-free conditions and at 200 MPa as a function of the composition. Permittivity values were taken from the first stress cycle of virgin samples at a frequency of 1 MHz. The biggest change in the permittivity was observed in compositions with higher initial value of permittivity, i.e., samples with 5 to 30 mol% of NTa. The change in the permittivity with applied stress then decreases toward the end members of the NBT–NTa solid solution. The absolute and relative difference between the permittivity values under stress-free conditions and at 200 MPa is shown in Figure 37b. The maximum absolute and relative difference was found for sample NBT–15NTa, i.e., 126.7, and 14%, respectively. There is a second peak in the relative change of the permittivity (red curve in Figure 37b) observed in sample NBT–30NTa. The influence of the pressure then decreases toward the NBT and NTa end members. The important parameters of the compressive stress measurements for the NBT–NTa series are collected in Table 3. In general, the parameters are the highest in compositions with 10 to 30 mol% of NTa. Such behaviour was expected since in these samples the phase transitions are in, or near, the room-temperature region and the samples exhibit high values of the permittivity. The

irreversible change was the highest in sample NBT–10NTa, which also showed the highest change under constant stress (at ~200 MPa) in a 10 min period.

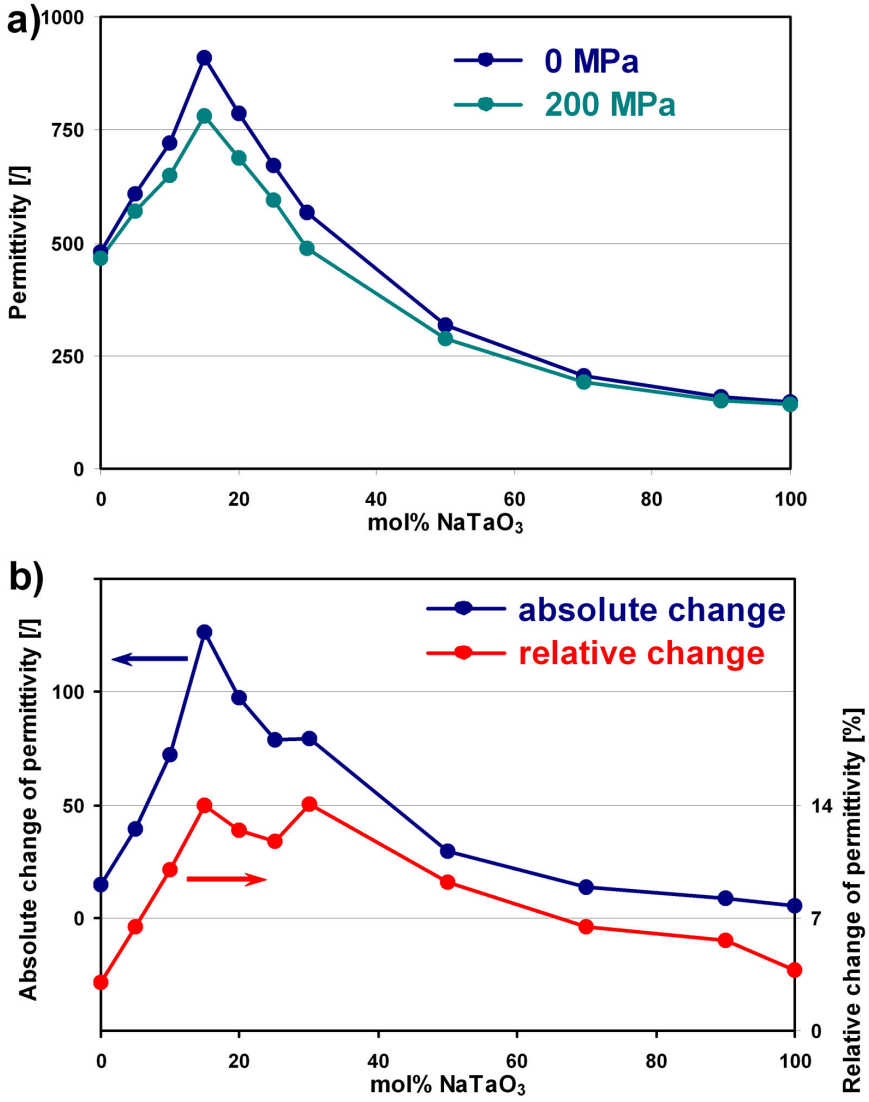

Figure 37: a) Room-temperature permittivity at 1 MHz before stress application and at 200 MPa for samples from the NBT–NTa series. b) Corresponding absolute and relative change of the permittivity. The data were obtained from the first stress cycle of the virgin samples.

The biggest influence of the axial pressure on the permittivity was observed in samples that exhibit a phase transition near room temperature. This was expected since the materials are soft in the vicinity of the phase transitions, thus the permittivity is increased in this temperature region and the influence of the external fields on the properties of the materials is increased. A similar influence is observed for morphotropic phase compositions. This also explains the anomaly observed in the morphotropic NBT–30NTa sample, which shows a local increase of the relative change of the permittivity.

As in pure NBT, also in other samples from the NBT–NTa series no saturation was observed up to the highest applied pressures. In order to investigate if the saturation occurs at a higher pressure a sample with smaller diameter was prepared. Composition NBT–15NTa with the highest permittivity change was tested at elevated pressures. The results of the experiment are shown in Figure 38. With the increase of the maximum applied pressure to approximately 500 MPa the characteristics of the response basically stayed unchanged. The

Table 3: Characteristic parameters of the pressure testing sequence for samples from the NBT–NTa series. The second and third columns corresponds to the first stress cycle. The maximum values of the columns are indicated by a red font colour. Note that the last column relates to a frequency of 1 kHz, while other data correspond to 1 MHz.

Sample, mol% NTa	$\Delta\varepsilon$ [/] 0–200 MPa (1 MHz)	$\Delta\varepsilon/\varepsilon$ [%] 0–200 MPa (1 MHz)	$\Delta\varepsilon/\varepsilon$ [%] irreversible (1 MHz)	$\Delta\varepsilon/\varepsilon$ [%] in 10 min at ~200 MPa (1 MHz)	$\Delta\varepsilon/\varepsilon$ [%] 0–200 MPa (1 kHz)
NBT	14.5	3.0	2.4	0.5	4.2
5	39.3	6.4	2.7	0.5	8.1
10	72.0	10.0	7.1	0.9	10.4
15	126.7	14.0	4.8	0.8	14.8
20	97.4	12.4	3.7	0.5	12.8
25	79.0	11.8	4.3	0.6	12.4
30	79.5	13.9	7	0.7	13.8
50	29.3	9.2	6.0	0.4	9.3
70	13.3	6.5	4.6	0.3	6.8
90	8.9	5.6	3.3	0.3	5.4
NTa	5.6	3.8	0.9	0.3	3.8

slope of the curve of the virgin sample slightly decreased at high pressures; however, no strong saturation was observed. The curve of the second stress cycle showed a more linear dependence for the first cycle. The relative decrease of the permittivity in the first stress cycle was 33% at 512 MPa and the irreversible change at the end of the test was almost 16%. From the third part of the test, a suppression of the relaxation processes can be observed. The permittivity change in this part was 50% smaller than in the tests where the highest pressure was approximately 200 MPa.

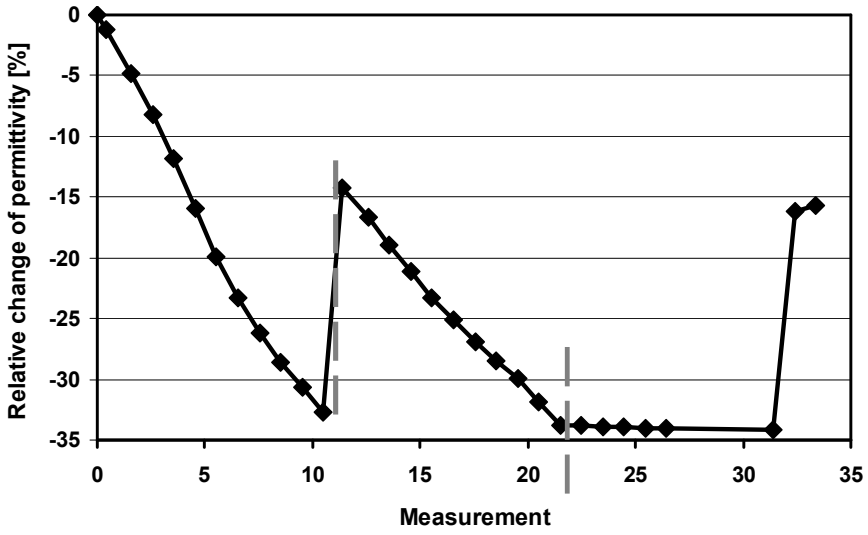

Figure 38: Relative change of the permittivity at 1 MHz during the stress testing of the NBT–15NTa sample. The starting value of the permittivity was 920.7, and the values of the pre-stress and the maximum stress were 19 and 512 MPa, respectively.

No change in the characteristics of the materials' response to the applied stress at different measuring frequencies was observed. An increase in the sensitivity, similar to the pure NBT, was observed in samples with 5 and 10 mol% of NTa, while the difference then decreased, and practically disappeared for samples with 30 or more mol% of NTa. The difference was observed in samples that show a frequency dispersion of the permittivity in the room-temperature region (see the dielectric properties in Figure 28). In these samples, the

mechanisms with different stress sensitivity contribute to the permittivity. The stress sensitivity of the mechanisms increases with a decreasing measuring frequency.

As predicted from the dielectric and ferroelectric measurements, the highest influence of the pressure on the permittivity was observed in samples with 10 to 30 mol% of NTa. These measurements also confirmed that no macroscopic domains with a different electric potential exist in samples with 15 and more mol% of NTa. Thereafter, the irreversible changes were not expected to appear in these compositions. The irreversible changes observed in the stress testing of samples with 15 and more mol% of NTa indicate the existence of a macroscopic domain structure also in the orthorhombic NTa that possesses paraelectric polar order. These domains have the same electrical potential but different mechanical potential and are, therefore, modified only by the external mechanical load [45]. There is only one study on the domain structure in NTa in the literature [115]. According to this study, NTa is a partial ferroelastic in which a single-domain crystal is switched when the stress axis is directed along the [010] of the pseudocubic cell. This direction is actually the direction of the longest edge of the orthorhombic unit cell. Thus, under an applied uniaxial stress domains aligned parallel with the stress switch to the plane perpendicular to the stress. Such switching is called non-180° domain switching, and is characteristic of a ferroelastic material. The tetragonal phase of NBT is also known to exhibit ferroelastic properties [79]. Thereafter, the intermediate phase in samples with 15 to 30 mol% of NTa, presumed to be connected with the tetragonal phase (page 37), is also expected to possess ferroelastic properties. Thus, the irreversible changes observed in the paraelectric samples are believed to occur due to a modification of the ferroelastic domain structure existing in the intermediate and orthorhombic phases.

The mechanical hysteresis of the samples was investigated to confirm the ferroelastic properties in the NBT–NTa solid solutions. Samples with 5, 15 and 50 mol% of NTa were selected, which consist predominantly of rhombohedral, intermediate and orthorhombic phases, respectively. For these measurements samples with a diameter-to-height ratio of 0.7 were prepared. Due to problems with the cracking of the samples, tests with loading only up to 150 MPa were performed. The results of the strain–stress measurements are presented in Figure 39. All the tested samples exhibit a remanent deformation after the stress release, i.e., they are ferroelastic. The ferroelastic properties of the materials explain the irreversible changes also observed in the paraelectric compositions of the solid solution.

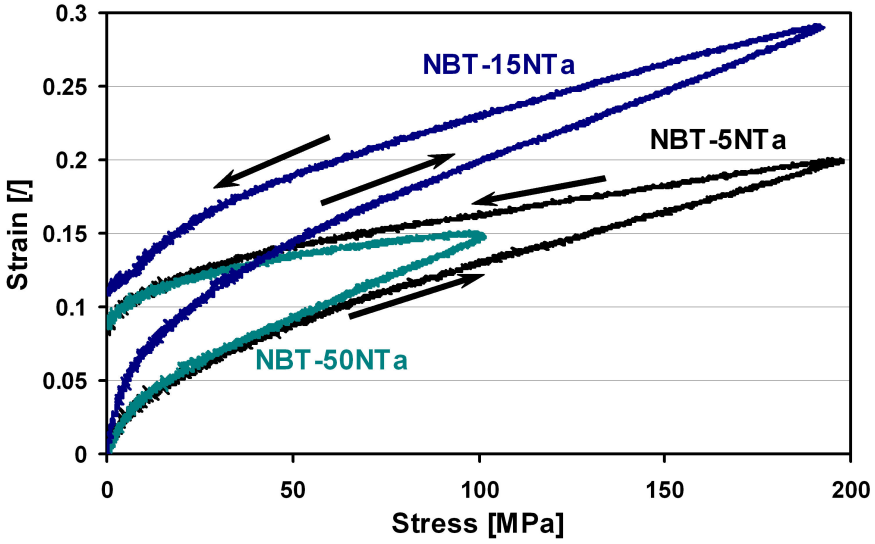

Figure 39: Strain–stress behaviour under stress loading/unloading of samples with 5, 15 and 50 mol% of NTa. Permanent deformation of the samples after the stress release is observed.

The relaxation under constant pressure observed in the third part of the pressure tests was additionally investigated. A pressure equal to 200 MPa was applied to the samples and

the change in the permittivity with time was monitored. A substantial short-term decrease and a much slower long-term negative relaxation of the permittivity (like for sample NBT–15NTa shown in Figure 40) were observed in all the samples. Such behaviour was also reported in the literature [63]. The change of the permittivity during the long-term relaxation was the highest in samples with 5 to 30 mol% of NTa that exhibit a phase transition near room temperature and a higher permittivity. Such behaviour is due to the complex domain and phase structure of these morphotropic and relaxor-like materials.

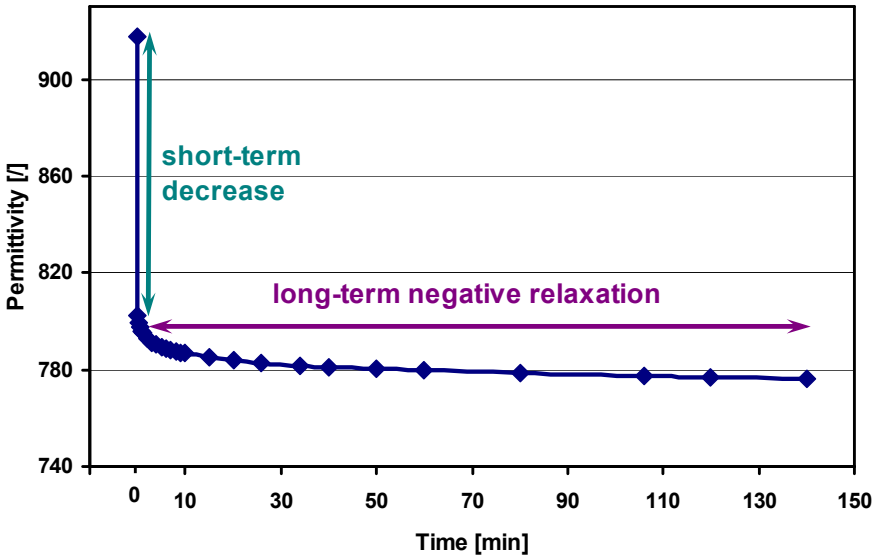

Figure 40: Change of the permittivity at constant pressure (200 MPa) at 1 MHz for a virgin sample NBT–15NTa. The starting and final values of the permittivity were 917.3 and 776.4, respectively.

The temperature dependence of the axial pressure's dependence of the permittivity was studied to detect any hysteresis behaviour and to compare the results with those known from the literature [72]. Sample NBT–50NTa was cooled to –50°C, then a 50 MPa load was applied. The temperature was then held constant for 1 hour to allow stabilization of the permittivity. Thereafter, successive heating and cooling cycles at a rate 2°C/min to 300°C were performed. The results of the test (Figure 41) show a gradual decrease of the permittivity on heating, which is consistent with the temperature dependence of the dielectric properties. During cooling the permittivity does not follow the same curve and the hysteresis is observed. The observed change in the permittivity at –50°C, before and after the test, is rather high (approximately 4%). According to the tests on the samples under constant pressure, only a fraction of this change was probably caused by the relaxational processes. More likely, the change appears due to a bigger influence of the pressure on the domain structure of the material at higher temperatures [71]. More domains reorientate in the direction perpendicular to the applied stress and, thus, the sample is more polarized at 300°C than it was at –50°C. Consequently, when the sample is cooled, the permittivity is lower than it was before the heating. A similar concept is often used in the electrical polarization of ferroelectric ceramics for piezoelectric applications [8]. The material is first heated, then a voltage is applied, which is followed by a field-cooling of the sample. Such a polarization procedure requires a smaller voltage, i.e., smaller than the coercive field at room temperature, which decreases the possibility of an electrical breakdown of the material.

The hysteresis observed in this study is not consistent with the research of Suchanicz *et al.* [71, 72, 74, 75], where no hysteresis on successive heating/cooling cycle under constant pressure was observed. In the reported experiments the sample was annealed at high temperature, followed by successive measurements at constant pressure on heating and

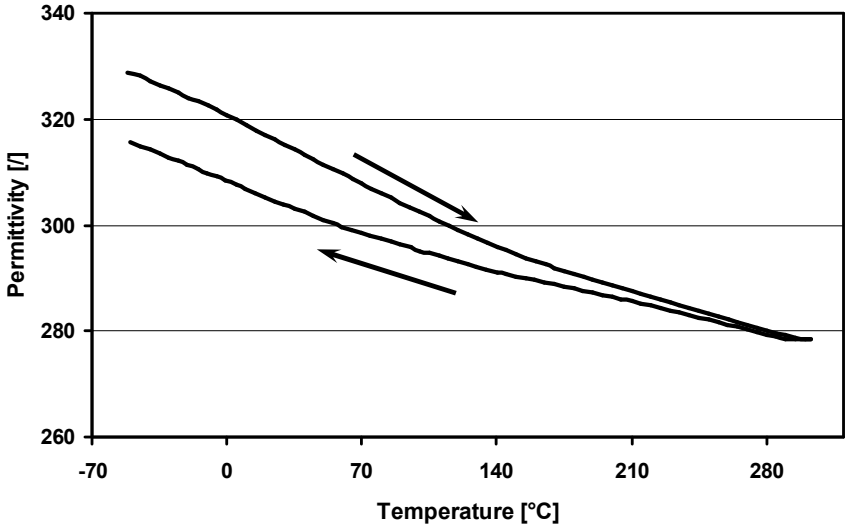

Figure 41: Temperature dependence of the permittivity of a virgin NBT–50NTa sample under a constant pressure (50 MPa) on a subsequent heating/cooling cycle (measured at 1 MHz). The starting and final values of the permittivity at –50°C were 328.7 and 315.7, respectively.

cooling. A possible explanation for the differences is that in the reported experiments the sample, when cooled from the annealing temperature, was already loaded with pressure. In this way, the results can be reversible, as stated in the literature. Moreover, a higher influence of pressure on the permittivity can be observed due to the higher influence of the pressure on the domain structure at higher temperatures.

To improve the reversibility of the pressure dependence of the permittivity, the concept of polarization, similar as in ferroelectric materials for piezoelectric applications, was applied. According to this concept, a NBT–15NTa sample was mechanically polarized at high pressure, i.e., 227 MPa, for a 24 h period. Then, the sample was kept under the pre-stress and, subsequently, the stress dependence of the permittivity was measured in multiple stress cycles. The results are shown in Figure 42. The reversibility of the measurements is very

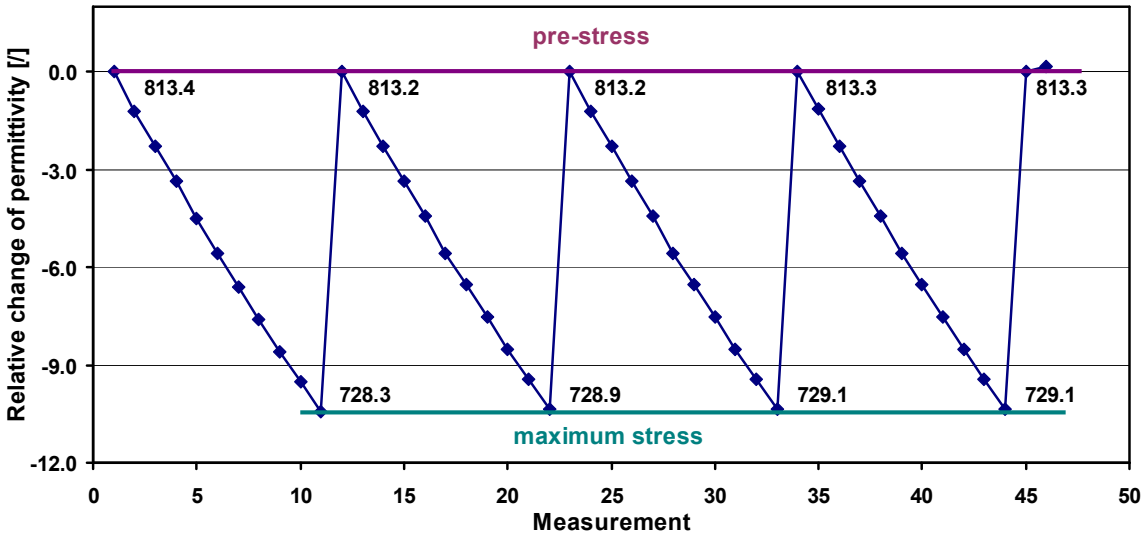

Figure 42: Reversibility test of the permittivity at 1 MHz under cycling axial pressure for the mechanically polarized (24 h at 227 MPa) NBT–15NTa sample, showing the relative change of the permittivity. The values of the permittivity before and after the polarization were 907 and 811.1. The values of the pre-stress and the maximum stress were 8 and 211 MPa, respectively. The numbers correspond to the permittivity at pre-stress and maximum stress for separate stress cycles.

good; however, the response of the poled sample to the applied stress is still time dependent (similar to that shown in Figure 40). Although no relaxations were observed after the tests described above, relaxations were detected after the polarization of the sample, most likely because of the extreme polarizing conditions that were applied. The material was overstressed after the load was removed; therefore, domain back-switching and relaxational processes occurred to compensate for the internal stresses.

The measurements of the pressure dependence of the permittivity showed that potential applicability of the materials from the NBT–NTa system is smaller than expected. It was found that in pure NBT the permittivity is not reversible under cycling pressure as reported in the literature [73]. The addition of NTa increased the stress dependence of permittivity; however, irreversible changes of the permittivity after the pressure tests were observed in samples from the whole concentration range. The reason for such behaviour is ascribed to the ferroelasticity existing in the NBT–NTa materials. Significant relaxations under constant pressure result in a time dependence of the permittivity. Although the reversibility was improved by a pre-use mechanical polarization process, the response of the poled sample to the applied stress is time dependent. The polarizing process is also time consuming and, moreover, polarized materials are prone to depolarization and aging processes. Such processes occur at increased temperature or with an increased number of stress cycles, similar as in piezoelectric materials [18].

4.1.6 Summary

NTa was added to NBT in order to shift the dielectric maximum toward lower temperatures and, thus, to increase the influence of axial pressure on the permittivity at room temperature. XRD and SEM analyses showed that a solid solution between NBT and NTa forms across the whole concentration range. Dense and mainly single-phase ceramic samples were obtained for all the prepared compositions. With an increasing content of NTa, the dielectric maximum shifts toward lower temperatures and decreases, while the permittivity at room temperature first increases and later starts to decrease. The maximum value of the room-temperature permittivity was found for the sample with 15 mol% of NTa, i.e., 908 at 1 MHz. The dielectric losses decrease with increasing content of NTa. The shape of the polarization–electric field hysteresis gradually changes from ferroelectric (5 mol% NTa) through relaxor-like (10 mol% NTa) to paraelectric (15 to 100 mol% NTa). Similar features of the axial pressure effect on the permittivity were observed in all samples: a decrease of the permittivity with increasing pressure, a difference between successive stress cycles, a relaxation under constant pressure and an irreversible change after stress removing. Such behaviour was expected for ferroelectric compositions, while in the paraelectric samples it is a consequence of the inherent ferroelastic properties of the material. For pure NBT the relative change of the permittivity at a pressure of 200 MPa is only 3%, while the highest change in the permittivity was found for sample NBT–15NTa, i.e., a relative change of 14% or 126.7 in absolute value (the data correspond to the first stress cycle at a frequency of 1 MHz). A considerable improvement in the reversibility was attained by a mechanical polarization of the samples before the stress cycling. However, the response of the polarized material to the applied stress is time dependent. Thus, the potential applicability of the materials from the NBT–NTa solid-solution system for pressure sensing is rather small.

4.2 $Na_{0.5}Bi_{0.5}TiO_3$–$K_{0.5}Bi_{0.5}TiO_3$ system

4.2.1 Synthesis

Similar to NBT, sodium bismuth titanate, $K_{0.5}Bi_{0.5}TiO_3$ (KBT), is a complex perovskite. It exhibits tetragonal symmetry (space group *P*4*mm*) at room temperature [107]. It is ferroelectric up to 300°C [116] and shows a broad dielectric maximum at 380°C. The published data [98, 107, 117, 118] on the NBT–KBT solid-solutions are inconsistent regarding the phase boundary between the rhombohedral and tetragonal regions (Figure 43), the position of a morphotropic phase boundary and other properties. According to the literature [119], a KBT addition decreases the coercive field of NBT. Therefore, it is of interest to study the effect of stress on the permittivity of materials from the NBT–KBT system. The basic properties of the $Na_{0.5}B_{0.5}TiO_3$–$K_{0.5}B_{0.5}TiO_3$ system were given by Žnidaršič *et al.* [100].

The published data on the synthesis of pure KBT [119-125], related to the determination and identification of possible secondary phases and volatile components, and the determination of the sintering and melting temperatures, are inconsistent as well. Therefore, first the synthesis of pure KBT was investigated in this study. The knowledge of the features of the KBT synthesis and the characteristics of the KBT ceramics makes it possible to control the synthesis of materials from the NBT–KBT system and to connect the properties of the materials with their structural characteristics.

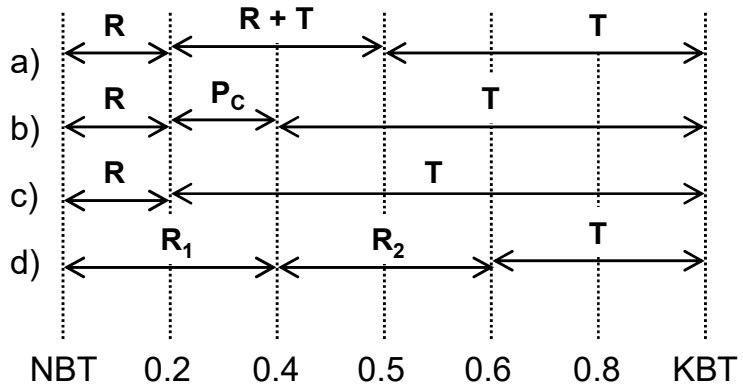

Figure 43: Crystal structures of the NBT–KBT solid solutions (R-rhombohedral, T-tetragonal, P_C-pseudocubic) as reported in the literature; a) Elkechai *et al.* [98], b) Pronin *et al.* [117], c) Yamada *et al.* [118], d) Jones *et al.* [107].

4.2.1.1 Synthesis of $K_{0.5}Bi_{0.5}TiO_3$ ceramics

The solid-state synthesis of KBT started with successive 10 h calcinations at 750°C and 850°C, to pre-react powders below the melting points of Bi_2O_3 and K_2CO_3. In this synthesis, two types of TiO_2 powder were used (i.e., 99.8% and 99.99% pure). Better results were obtained with 99.99% pure TiO_2, and the results presented below were obtained with this powder. The XRD analysis of the sample with the nominal composition KBT is presented in Figure 44. The sample calcined at 750°C for 10 h consists of a KBT perovskite phase as well as some other crystalline phases. Though the reflections of the secondary phases were weak, the majority of the reflections were attributed to a $K_2Ti_4O_9$ phase (Figure 44B). After a subsequent calcination at 850°C for 10 h the XRD pattern showed the same characteristics; however, after a subsequent sintering at 1030°C for 5 h the positions of the weak reflections changed and were attributed to a $K_2Ti_6O_{13}$ secondary phase (Figure 44B). The change in the secondary phase will be discussed later in relation to the stability of potassium titanates.

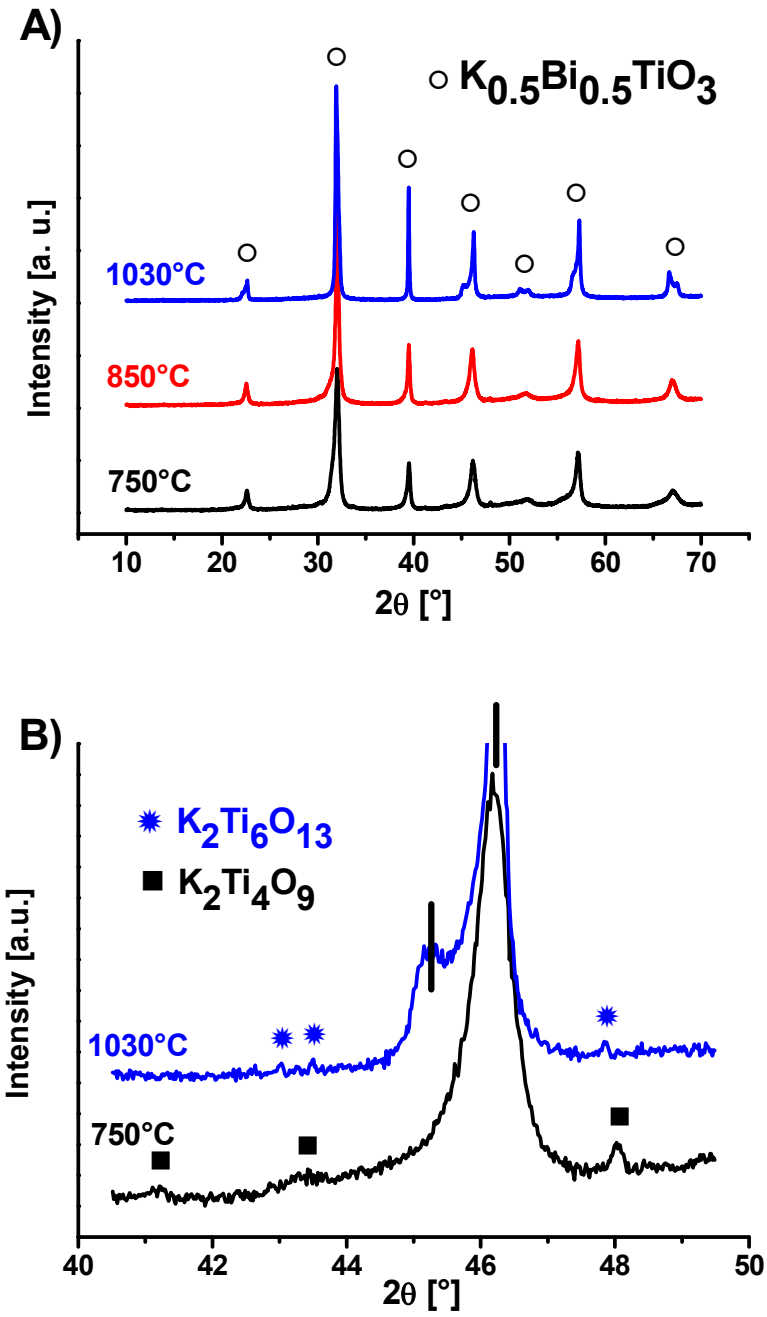

Figure 44: A) XRD patterns of the KBT sample after a 10 h calcination at 750°C, after a subsequent 10 h calcination at 850°C and after a subsequent 5 h sintering at 1030°C. B) A detail of the XRD patterns after the first calcination and after sintering; the weak reflections of the $K_2Ti_4O_9$ and $K_2Ti_6O_{13}$ secondary phases are designated. The vertical lines represent the diffraction lines of the tetragonal KBT matrix.

The SEM-BSE micrographs of the sample sintered at 1030°C clearly revealed the presence of a dark secondary phase in the form of whisker-like grains (Figure 45A). The composition of the dark phase, determined using EDS, corresponds to the $K_2Ti_6O_{13}$ phase, which is in accordance with the weak reflections observed in the XRD pattern (Figure 44B). With a prolonged 80-h sintering the concentration of the dark phase in the interior of the sample slightly increased; however, on the surface of the pellet the dark phase prevailed (Figure 45B). Furthermore, a bright secondary phase in the form of large, elongated grains (>100 μm in length) was formed, predominantly near to the surface of the sample. The semi-quantitative EDS analysis of the bright phase suggested the composition $K_{0.1}Bi_{0.9}Ti_{0.8}O_3$. The

bright phase will be hereafter referred to as the Bi-rich phase, since it contains more bismuth compared to the other phases.

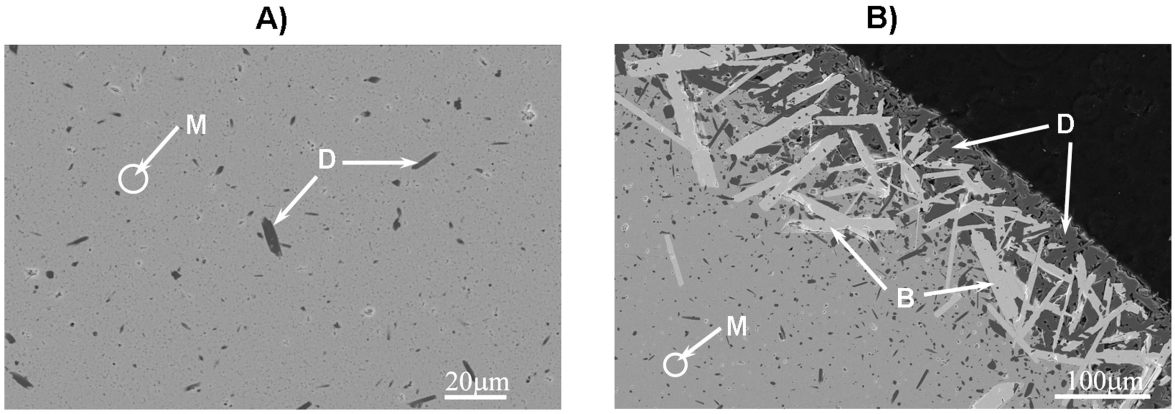

Figure 45: SEM-BSE micrographs of the KBT sample sintered at 1030°C for A) 5 h and B) 80 h; Matrix phase (M), $K_2Ti_6O_{13}$ (D; dark grains) and Bi-rich secondary phase (B; bright grains) are designated.

SEM observations indicate that the formation of the secondary phases is accelerated on the surface of the pellet and is most probably connected with volatilization. An experiment on a finely grinded powder sample that has a greater surface area was performed, which enabled a more accurate identification of the secondary phases that form. The finely grounded, uncompressed, calcined KBT powder was fired in air at 1030°C for 20 h, and analyzed using XRD. Figure 46a shows the pattern of the as-prepared sample. The main reflections belong to the KBT perovskite phase, the second phase identified from the spectra is $K_2Ti_6O_{13}$, while the other reflections could not be identified on the basis of any file from

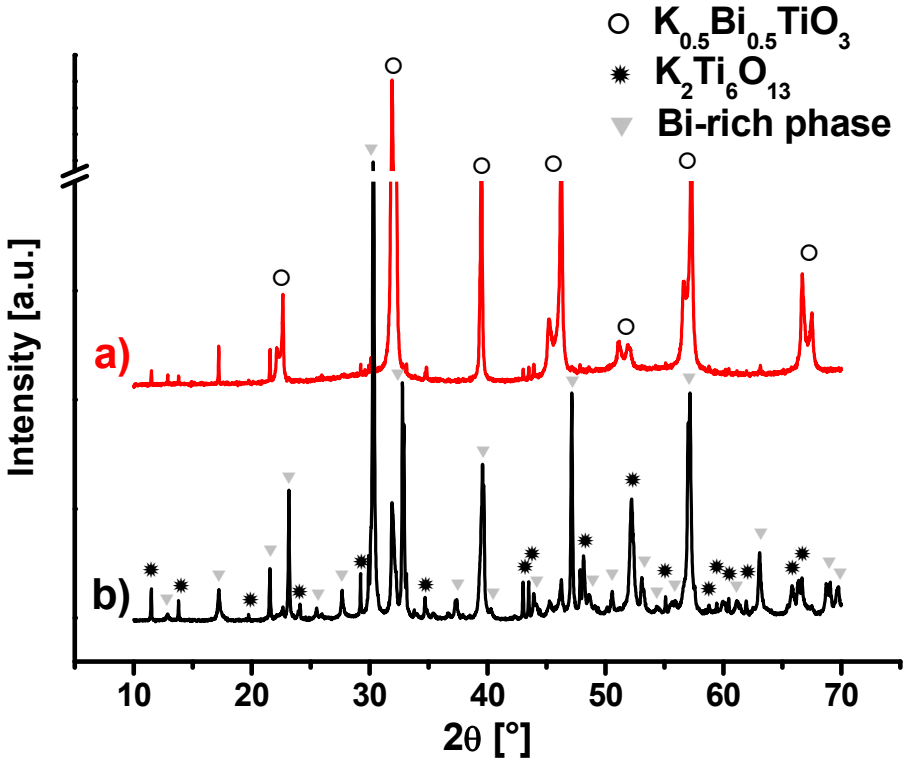

Figure 46: XRD patterns of a) a powdered KBT sample fired at 1030°C for 20 h and b) K sample (with less potassium oxide) sintered at 1030°C for 5 h. The reflections of KBT are marked only on the a) pattern; the reflections of $K_2Ti_6O_{13}$ and Bi-rich phase are marked only on the b) pattern.

the JCPDS database. The unidentified reflections are most probably connected with the Bi-rich phase, observed in the microstructure after the prolonged sintering (Figure 45B). The identification of the Bi-rich phase by XRD is discussed below.

Secondary phases can be formed due to volatilization and/or an unfinished reaction of the reacting powders. To decrease the volatilization and, thus, the formation of the secondary phases, sintering in a closed platinum crucible and spark-plasma sintering were applied. The results are shown in Figure 47. The sample muffled with a powder with the same composition and sintered in a closed crucible shows a similar amount of the dark secondary phase as the sample sintered in air. The spark plasma sintering was performed at a fairly low temperature, i.e., 950°C, however, a very inhomogeneous composition of the sample was observed. A significant amount of a dark phase and small amount of a bright phase were present. The dark and bright grains are believed to be connected with potassium titanate and a Bi-rich phase, respectively. These results indicate that the secondary phases are present in the system even before the sintering process, which is in accordance with the XRD analysis (Figure 44B). In order to reduce the secondary-phase formation during the calcination steps, pre-calcination homogenization using a ball mill was applied to increase the homogeneity and the surface area, and enable a faster and better reaction between the reacting powders. However, the formation of the dark secondary phase was not reduced.

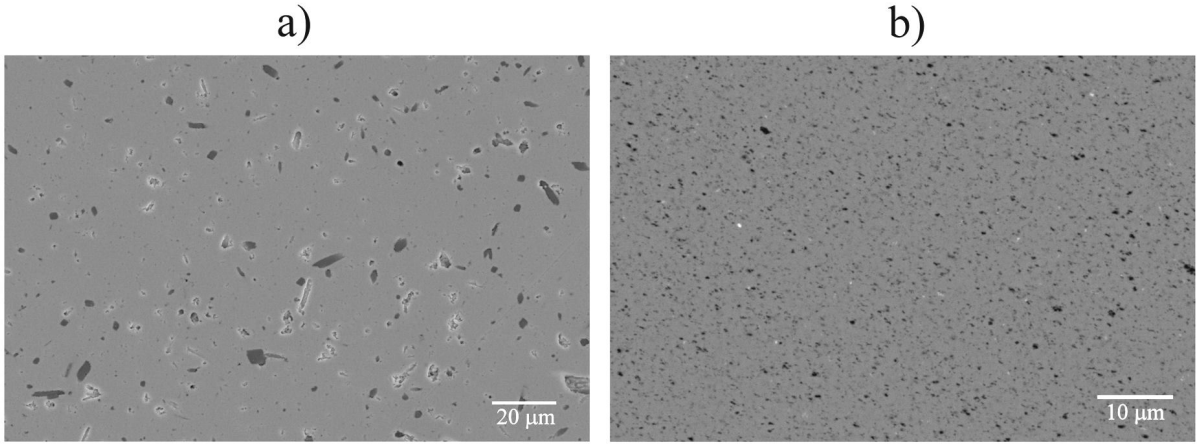

Figure 47: SEM-BSE micrographs of the KBT sample: a) sintered in a closed platinum crucible at 1030°C for 20 h and b) spark-plasma sintered at 950°C for 1 min. The dark and bright grains correspond to the $K_2Ti_6O_{13}$ and Bi-rich phases, respectively.

In order to get a clearer insight into the processes that occur during the synthesis of the KBT ceramics, the phase relations around KBT were investigated. Compositions with less potassium oxide ($K_{0.3}Bi_{0.5}TiO_{2.9}$ – K), less bismuth oxide ($K_{0.5}Bi_{0.2}TiO_{2.55}$ – B) and less titanium oxide ($K_{0.5}Bi_{0.5}Ti_{0.85}O_{2.7}$ – T) relative to KBT were prepared and are shown in the tentative phase diagram (Figure 48). The XRD pattern of sample K (with less potassium) shows weak reflections identified as KBT and $K_2Ti_6O_{13}$ (Figure 46b); however, the main reflections could not be identified using the JCPDS database. These reflections are consistent with the unidentified reflections from the uncompressed KBT powder fired at the sintering temperature (Figure 46a). The unidentified reflections are believed to be connected with the Bi-rich phase. This was confirmed by the EDS analysis, which showed the same composition for the bright Bi-rich phase in sample K as in the KBT pellet, and thus the unidentified peaks in Figure 46 were denoted as the Bi-rich phase. The mismatch between the intensities of the peaks of the Bi-rich phase is most probably due to the different morphology of this phase observed with the SEM (isotropic in sample K and anisotropic in KBT).

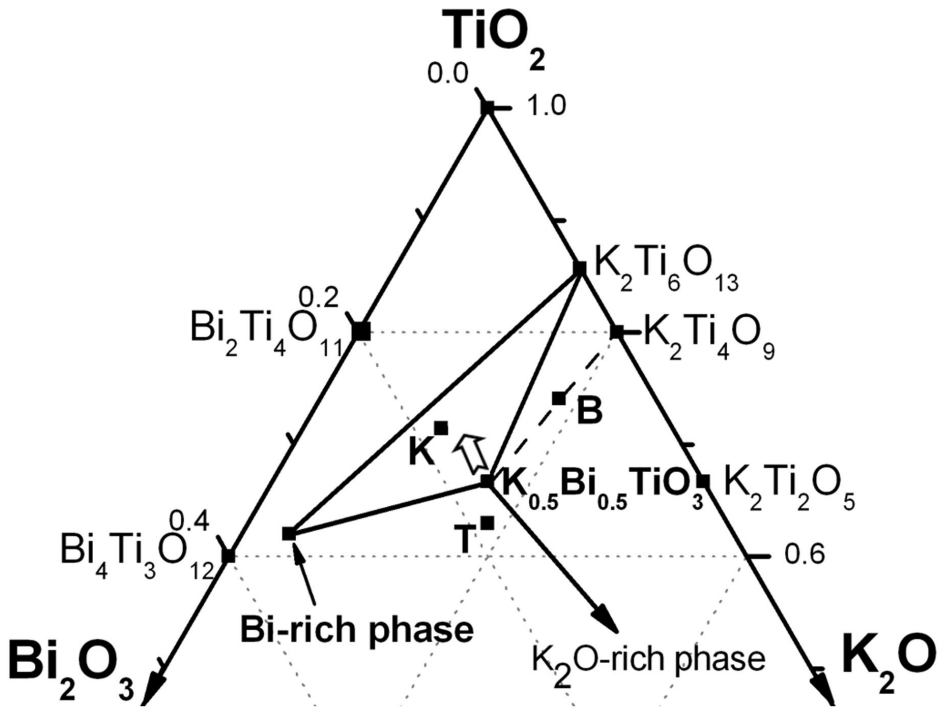

Figure 48: Part of the tentative phase diagram around $K_{0.5}Bi_{0.5}TiO_3$ at 1030°C (solid lines) derived from the described experiments. The dashed line corresponds to 900°C. The position of the Bi-rich phase is as determined by EDS. The open arrow marks the direction of a nominal composition change as a function of the sintering time.

The XRD pattern of sample B (with less bismuth oxide) fired at 900°C for 5 h shows the presence of two phases, identified as KBT and $K_2Ti_4O_9$ (Figure 49a); however, after firing at 1030°C the intensity of the $K_2Ti_4O_9$ reflections decreased and the $K_2Ti_6O_{13}$ reflections appeared in the XRD pattern (Figure 49b), which indicates the decomposition of the $K_2Ti_4O_9$ phase. The instability of $K_2Ti_4O_9$ was observed in a study of the synthesis of potassium titanate whiskers, where the decomposition of $K_2Ti_4O_9$ into $K_2Ti_6O_{13}$ whiskers and a K_2O-rich liquid phase is reported [126]. The authors report that the temperature of the $K_2Ti_4O_9$ decomposition in the TiO_2-K_2O system is around 1120°C. Nevertheless, according to the experiments presented above, the temperature of the $K_2Ti_4O_9$ phase decomposition in the investigated part of the K_2O-Bi_2O_3-TiO_2 system is below 1000°C, while the $K_2Ti_6O_{13}$ phase appears in whisker-like grains, as reported in the literature [126]. The presence of a liquid phase also explains the growth of whisker-like grains of the secondary phases observed by the SEM analysis (Figure 45A). The secondary phase recrystallizes from the liquid phase. The other reflections in the XRD pattern (Figure 49b) that could not be identified using the JCPDS database most probably belong to the K_2O-rich phase that is formed during the decomposition of the $K_2Ti_4O_9$ phase. It should be noted that the $K_2Ti_6O_{13}$ phase has a high thermal stability [127] and is impossible to eliminate with a heat-treatment process [123], i.e., the $K_2Ti_6O_{13}$ phase does not react with other secondary phases toward the composition of the matrix. The XRD pattern of sample T contained the reflections of KBT (Figure 50). The other reflections in the XRD pattern of sample T could not be identified using the JCPDS database, which is believed to be due to unknown phase relations in the K_2O-Bi_2O_3-TiO_2 system.

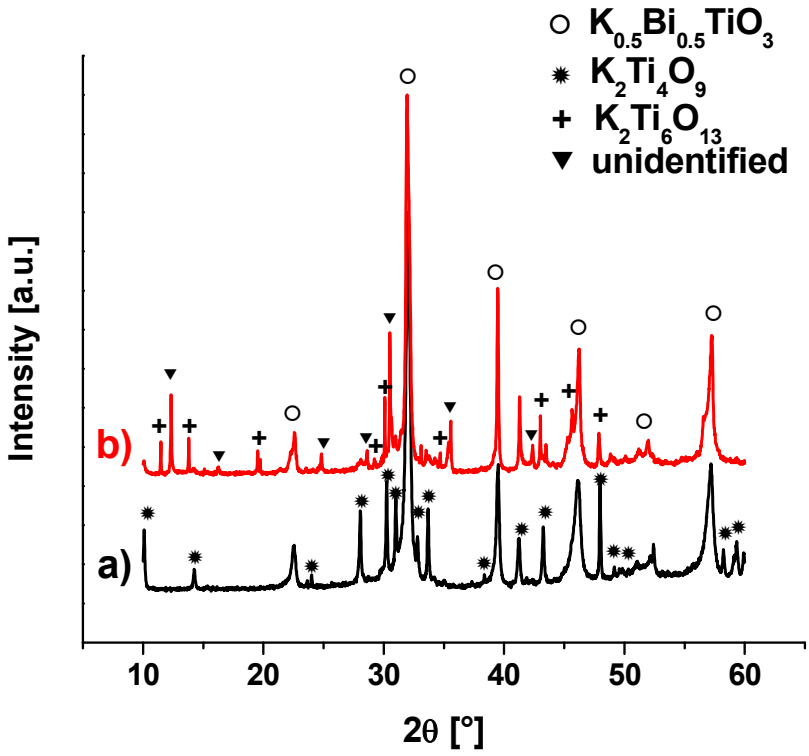

Figure 49: XRD patterns of sample B (with less bismuth oxide) fired for 5 h at a) 900°C and b) 1030°C. The reflections of KBT and $K_2Ti_6O_{13}$ are marked on one pattern only (on b) pattern). The reflections of $K_2Ti_6O_{13}$ and the unidentified phase appear in the b) pattern only.

The XRD and SEM results confirmed that the $K_2Ti_6O_{13}$ secondary phase is present in KBT ceramics. Also, no evidence was found for $K_4Ti_3O_8$, in contrast to some literature reports [119-121, 128]. Furthermore, another ternary phase in KBT ceramics, which has not been previously observed, is the Bi-rich phase that forms after prolonged sintering. On the basis of the described experiments, phase relations around KBT at 1030°C were proposed (Figure 48).

The firing of KBT shifts the nominal composition to the three-phase region (marked by an open arrow in Figure 48), which indicates the loss of potassium and bismuth oxides from the sample. In order to quantify the mass loss, a TGA analysis of the KBT powder was performed. The analysis showed that as much as 6 wt% of the powdered sample volatized over the 20-h period at 1030°C. The volatilization during the sintering of the KBT ceramics has been predicted in the literature; however, it is inconsistent, assuming that only the potassium component [122, 129] or only the bismuth [119, 121, 128] component volatizes from the sample. Furthermore, there is no exact experiment documented that would confirm the predicted volatilization. For this reason the Knudsen effusion mass spectrometry (KEMS) method was used to determine the volatile components at elevated temperatures. This method is a combination of the standard Knudsen effusion method and mass spectrometry [103]. The combined method makes it possible to identify the gaseous species and to determine their vapour pressure, being in thermodynamic equilibrium with the solid sample.

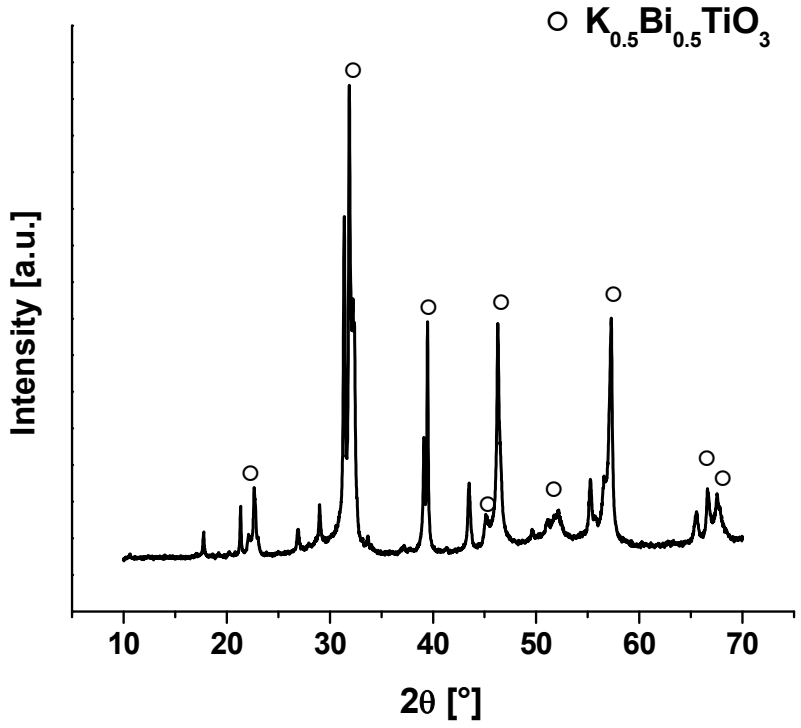

Figure 50: XRD pattern of sample T (with less titanium oxide) fired at 1000°C for 5 h. Diffraction peaks of KBT are marked; other diffractions could not be identified using the JCPDS database.

Two sets of KEMS experiments were performed, one on a previously calcined sample (750 and 850°C for 10 h) and one on a starting carbonate/oxides mixture, Figure 51. In both cases the only metal-containing ionic species found in the mass spectrum were Bi^+, Bi^{++}, K^+ and BiO^+. The additional mass spectrometric measurements of the ionization energies proved that those ions come from gaseous Bi, K and BiO, respectively. The concentration of the latter molecule is extremely low; therefore, it is considered to be of minor importance. For pure metal oxides in general, the formation of bismuth and potassium vapours within the Knudsen cell at the measured temperatures can be represented by the following equilibrium reactions:

$$K_2O(s) \leftrightarrow 2K(g) + 1/2O_2 \quad (18)$$

$$Bi_2O_3(s) \leftrightarrow 2Bi(g) + 3/2\ O_2 \quad (19)$$

The result of the KEMS measurements of the previously calcined sample are shown in Figure 51A. It is clear that the vapour pressure of bismuth is considerably higher than the pressure of potassium, being almost negligible compared to bismuth. Furthermore, the vapour pressure of all the species monotonically increases with temperature when the dependence is plotted on a logarithmic scale, indicating the thermodynamic equilibrium of the system. However, the volatilization of just the bismuth component from the system does not coincide with the observed phase relations presented in Figure 48.

Therefore, a further experiment was performed. According to the phase diagram, the complete loss of bismuth oxide would result in the formation of the pure $K_2Ti_4O_9$ phase. To verify this, the calcined sample was annealed in the Knudsen cell at 940°C until the signal of bismuth disappeared from the mass spectra. The mass loss during annealing was found to be noticeably higher than the content of bismuth oxide and, in addition, the remainder of the sample showed the presence of two potassium titanate phases, $K_2Ti_4O_9$ and $K_2Ti_6O_{13}$ (Figure 52). Thus, the results also indicate a sizable volatilization of the potassium oxide. Since the KEMS showed that the vapour pressure of the potassium is considerably lower than that of the bismuth during the annealing in the Knudsen cell, the majority of the potassium losses

probably occurred during the calcinations performed before putting the sample into the Knudsen cell.

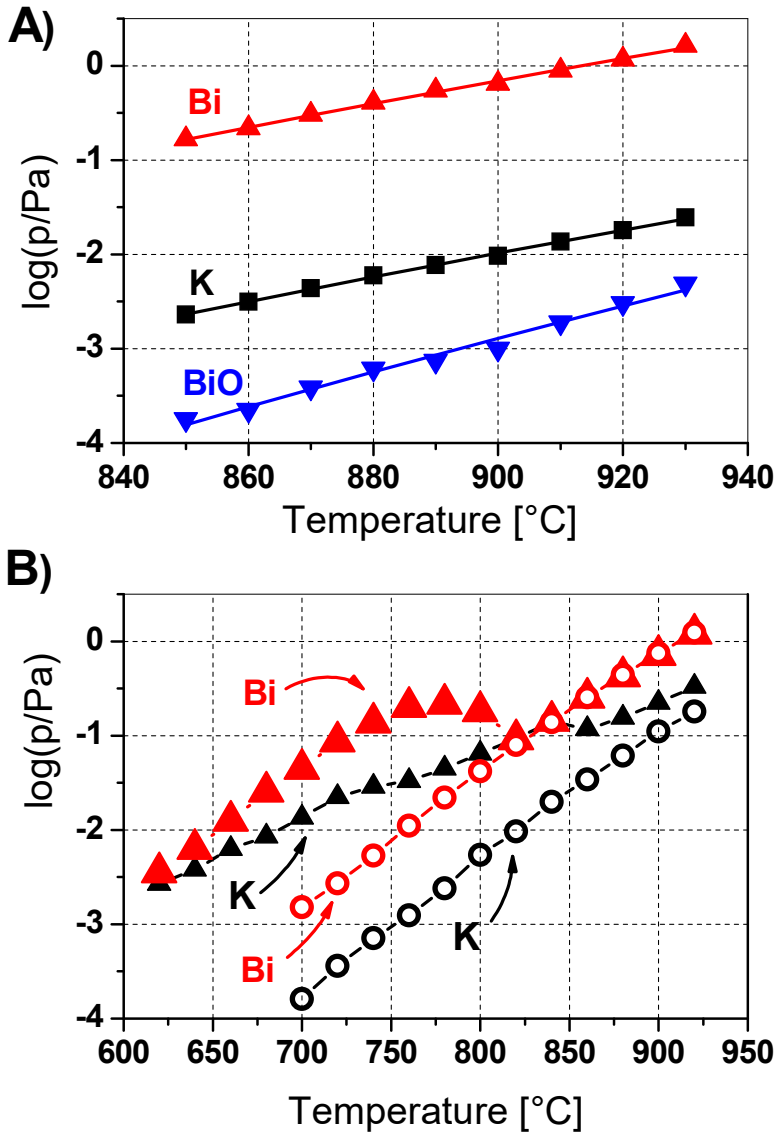

Figure 51: A) The measured vapour pressure of bismuth, potassium and bismuth oxide over calcined KBT. B) The measured vapour pressure of bismuth and potassium over the Bi_2O_3, K_2CO_3, $4TiO_2$ mixture (triangles: first run, open circles: second run).

A second set of KEMS experiments on a carbonate/oxides mixture was performed to investigate the loss of potassium component. The result is shown in Figure 51B, where two successive runs are plotted on the graph. The first run is depicted with triangles. It is evident that at the early stage of the experiment (620°C) the vapour pressures of bismuth and potassium are similar. The increase of the potassium pressure with temperature is somewhat less steep, but it is still comparable to the bismuth, unlike in the case of the calcined sample, where the pressure of bismuth was much higher. At higher temperatures (750–850°C) a distinct drop in the bismuth pressure and a more gradual drop in the potassium pressure are observed, which is believed to be related to the solid-state reaction. Finally, at 900°C the system seems to reach thermodynamic equilibrium, which was checked with a subsequent

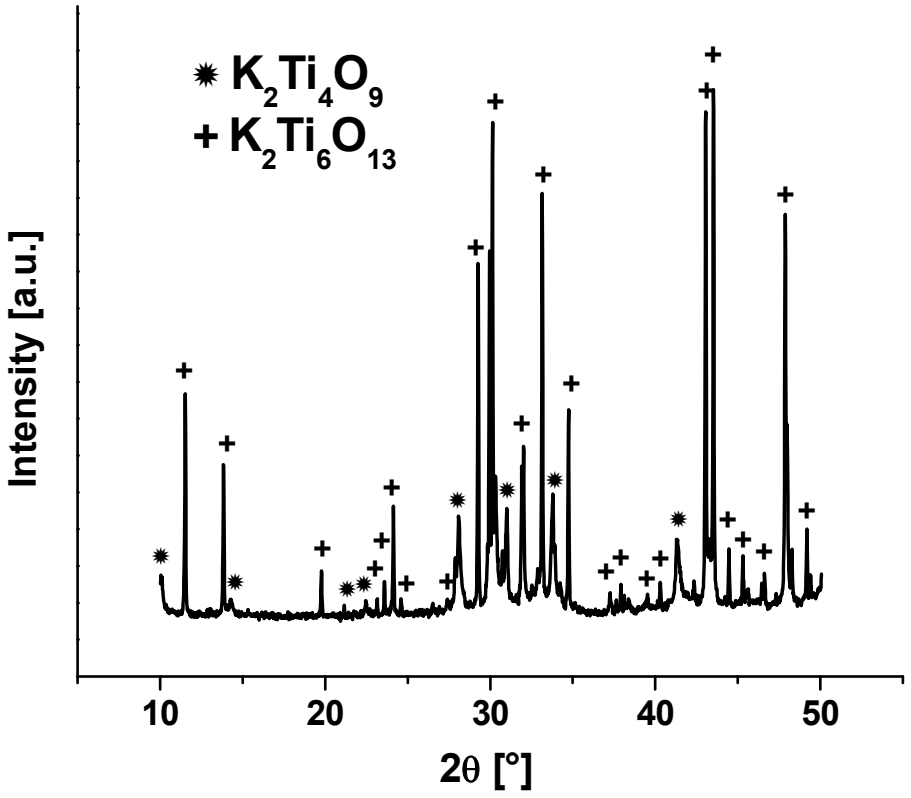

Figure 52: XRD pattern of the previously calcined KBT sample, additionally annealed in the Knudsen cell at 940°C until the bismuth signal disappeared from the spectra. All diffraction peaks were ascribed to $K_2Ti_4O_9$ and $K_2Ti_6O_{13}$.

run, designated by the open circles in Figure 51B. In between the successive runs, the system was cooled to room temperature. In the second run the temperature-pressure dependence is monotonic for potassium and bismuth, which indicates the thermodynamic equilibrium of the system. It appears that the reaction is finished at this stage, and that essentially pure KBT is in equilibrium with the vapours. It should be noted that the loss of components during the first run of this experiment is negligible.

From the comparison of both sets of experiments on a previously calcined sample and on a starting carbonate/oxides mixture the following conclusions can be made. The vapour pressure of the potassium over the carbonate/oxides mixture (second run) is about 6 times higher than over the calcined sample, where being considerably smaller than the pressure of the bismuth, which, in contrast, is almost identical in both cases. The drop in the vapour pressure of potassium during the calcination can be related to the potassium losses detected in the first set of KEMS experiments on a previously calcined sample.

The described KEMS measurements were performed in vacuum. In order to apply the results to atmospheric conditions the influence of oxygen on the reactions described in Equations 18 and 19 have to be considered. For the metal oxide decomposition

$$Me_aO_b(s) \leftrightarrow aMe(g) + {}^{b}\!/_{2}\, O_2\,, \tag{20}$$

the dissociation constant can be calculated according to

$$Kdiss = \left(p_{Me}\right)^a \cdot \left(p_{O2}\right)^{\frac{b}{2}} \tag{21}$$

where *Kdiss* is the dissociation constant of the reaction in Equation 20, and p_{O2} and p_{Me} are the equilibrium vapour pressures over solid Me_aO_b. Equation 21 shows that the oxygen pressure in the surrounding atmosphere significantly influences the decomposition of metal oxides and the volatilization. Taking into consideration the *a* and *b* coefficients from Equation 20 for the potassium and bismuth volatilization described by Equations 18 and 19, the presence of oxygen has a bigger influence on decreasing the volatilization of bismuth in comparison to potassium. Thus, the volatilization of potassium over the calcined sample, which is considerably smaller compared to the volatilization of bismuth in a vacuum, becomes important and even higher than the volatilization of bismuth in an atmosphere of air. However, these are general considerations, for more precise calculations additional measurements should be performed, also on pure oxides. Nevertheless, the KEMS measurements undoubtedly showed the volatilization of both the potassium and bismuth components. It should be mentioned that the vapour pressure of both components increases with temperature; therefore, most of the losses occur during the sintering of the samples, while the losses during calcinations, predominantly potassium, are smaller.

The thermal instability of the KBT matrix causes its slow decomposition and the volatilization of the potassium and bismuth components. A possible reason for the thermal instability is the non-stoichiometry of the matrix phase. Indeed, the EDS analysis of the samples sintered at 1030°C for different times (5, 20 and 80 h) showed that in all the samples the KBT matrix contained less potassium and more bismuth compared to the stoichiometric KBT. Because of the relatively low analytical sensitivity of the EDS method this deviation from the stoichiometric KBT composition was additionally checked and determined with WDS. A quantitative WDS analysis of the KBT matrix phase was performed on a sample sintered at 1030°C for 20 h. The average composition of the matrix was determined from six point-beam analyses performed on randomly selected matrix regions. The composition of the KBT matrix was calculated using the quantitative WDS data obtained from two quantitative matrix-correction methods, XPHI [101] and ZAF, and can be described by $K_{0.478\pm0.002}Bi_{0.508\pm0.002}Ti_{1.000\pm0.002}O_3$ and $K_{0.477\pm0.002}Bi_{0.509\pm0.002}Ti_{0.999\pm0.002}O_3$, respectively. Both formulas are consistent and equivalent within the range of statistical uncertainty. The relative standard deviation of the formula coefficients, calculated from the elemental concentrations, is less than 0.3 % (between the points), which also confirms that the KBT matrix is compositionally homogeneous. The presented results show that the synthesized KBT compound is not stoichiometric KBT; it is potassium-deficient and contains an excess of bismuth.

The non-stoichiometry in KBT has not been reported before; however, A-site deficiency was documented in a related NBT compound, where sodium deficiency was ascribed to the pseudo-cubic symmetry of NBT [94]. The authors found a stable sodium-deficient compound that forms a solid-solution with NBT and the formation of stoichiometric NBT starts with the formation of the sodium-deficient end-member, which then reacts toward the nominal composition when a sufficiently high temperature and/or a long firing time is used. A similar crystal-symmetry variation with the firing temperature was also observed in KBT. The symmetry of the KBT is pseudo-cubic after the calcinations, and this changes to tetragonal during the sintering at higher temperatures (Figure 53). Due to the similarity with NBT, the existence of a solid-solution around KBT was investigated. The symmetry of KBT and the compositions K, B and T, heat treated at different temperatures and for different firing periods, was carefully investigated by XRD. The analysis showed a pseudo-cubic symmetry after the calcinations and a tetragonal symmetry after the sintering for all samples, and furthermore, the positions of the reflections were identical, i.e., no shifting of the reflection positions was observed. Therefore, we concluded that the stoichiometry of the synthesized compound is always the same and there is no evidence of a solid solution existing around that compound.

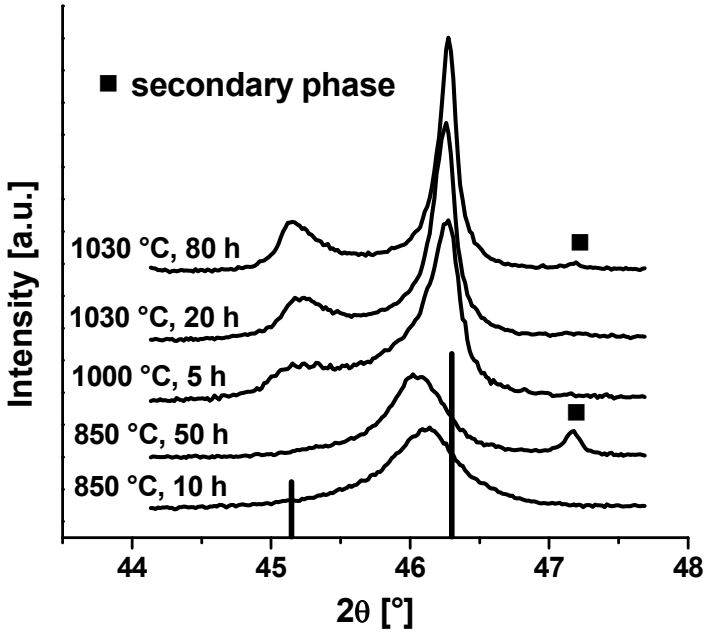

Figure 53: XRD results of KBT samples fired at different temperatures for different times. The vertical lines represent the diffraction lines of KBT according to PDF card number 36-0339.

The results of the WDS and the XRD analyses showed that an off-stoichiometric matrix phase, compared to KBT, forms in the system and that there is no solid solution around it. Rather, it appears that only a discrete composition forms in the system, which has a stoichiometry slightly shifted from the ideal one, i.e., from KBT. Thus, during the sintering the matrix phase slowly decomposes and forms the $K_2Ti_6O_{13}$ and Bi-rich secondary phases (as observed by XRD and SEM analyses), as well as Bi and K vapours above the solid sample (as determined by TGA and KEMS).

According to a report [99] the melting temperature of KBT is around 1070°C. However, the preliminary test in this study showed melting already at 1050°C and, additionally, a reaction with the alumina crucible was detected. Therefore, the sintering behaviour was carefully investigated and all heat treatments of samples containing KBT were performed on a platinum foil. The melting temperature of the KBT powders and the sintering behaviour of the KBT compact were investigated by means of DTA and a heating microscope. The DTA curve (Figure 54A) shows that the endothermic signal, ascribed to the

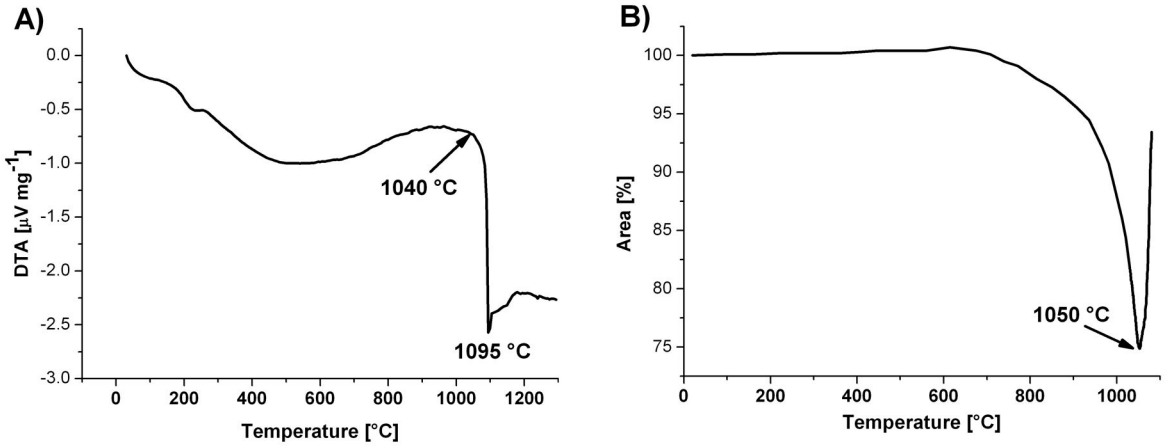

Figure 54: The results of A) the DTA and B) the heating-microscope analysis. In both experiments the heating rate was 10°C/min.

melting of the sample, starts at 1040°C and peaks at 1095°C. The heating-microscope analysis (Figure 54B) shows the maximum shrinkage of the compact at 1050°C, while at higher temperatures the sample starts to melt and it completely deforms at 1070°C (hemisphere point). In both experiments the heating rate was 10°C/min. The results of the DTA and the heating-microscope analysis are in good agreement and show that the sintering-temperature range is narrow, limited by the melting of the sample above 1040°C and the low density of the ceramics below 1030°C. On the basis of these results, the sintering temperature in was determined to be 1030°C. At this temperature, the optimal ratio between the density of the ceramic compact and the secondary-phase concentration was observed.

4.2.1.2 Synthesis of $Na_{0.5}Bi_{0.5}TiO_3$–$K_{0.5}Bi_{0.5}TiO_3$ ceramics

Samples with 20, 30 and 50 mol% of KBT from the NBT–KBT solid-solution were prepared according to the report of Žnidaršič *et al*. [100]. The stoichiometric mixture of the powders was calcined for 10 h at 750°C and 850°C with intermediate cooling and grinding. After the second calcination the XRD analysis showed single-phase samples. Afterwards the samples were milled and sintered at 1090–1120°C. The XRD results of the sintered samples are shown in Figure 55a. The diffraction peaks correspond to single-phase samples with a perovskite structure. The peaks are shifted to smaller 2θ values with an increasing KBT concentration (close-up look in Figure 55b), indicating an increase in the volume of the pseudo-cubic unit cell, in agreement with the reported values (V_{pc}(NBT)=58.72 Å^3 [78]; V_{pc}(KBT)=61.457 Å^3 [107]). The symmetry changed from rhombohedral on the NBT side to tetragonal on the KBT side. In the sample with 20 mol% of KBT a rhombohedral–tetragonal phase coexistence was observed.

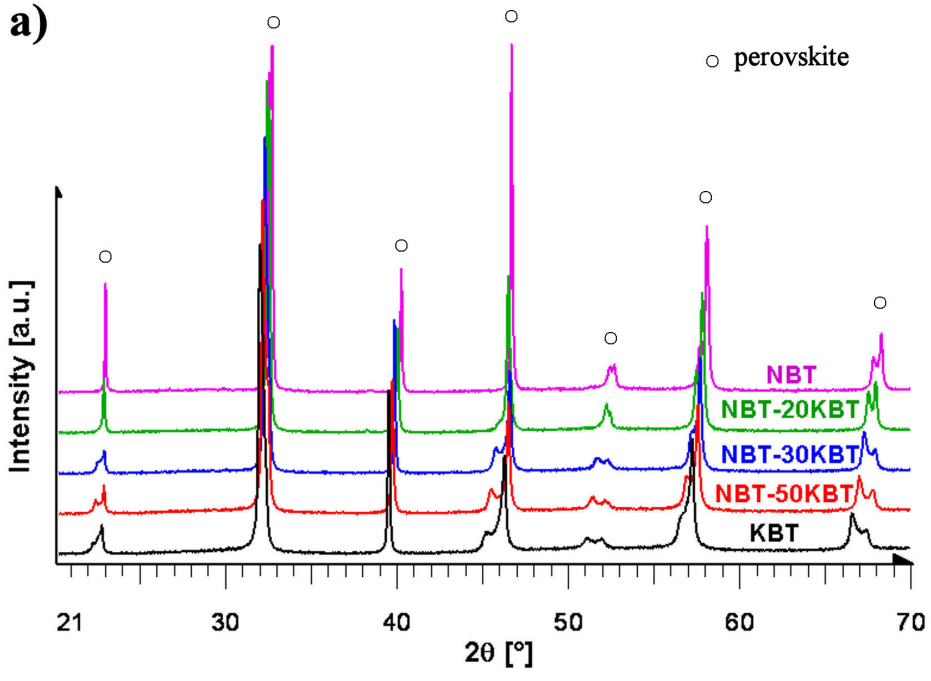

Continued →

→ Continued

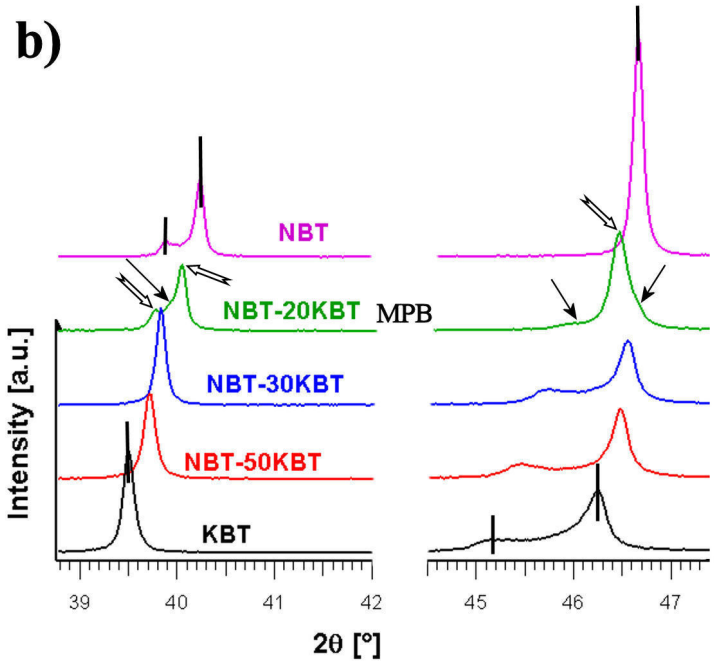

Figure 55: a) XRD patterns of samples from the NBT–KBT solid-solution. In b), close-up look of the diffraction peaks (111) and (200) is shown; the vertical lines represent the diffraction lines of the rhombohedral NBT and tetragonal KBT phases; the open and full arrows indicate the distortion due to the rhombohedral and tetragonal phases, respectively, existing in the MPB composition.

The SEM analysis revealed the presence of a dark secondary phase, which was identified by the use of EDS as $K_2Ti_6O_{13}$ (Figure 56), similar to the case of pure KBT. Also, the whisker-shape of the secondary phase is as observed in KBT. The content of the secondary phase slightly increases with the increasing content of KBT. The reason for the secondary-phase formation is most probably the same as explained in the synthesis of pure KBT, i.e., the instability of the matrix phase.

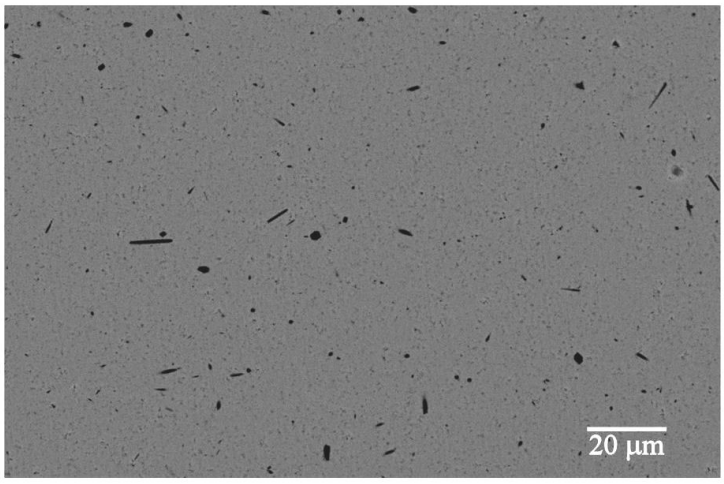

Figure 56: SEM-BSE micrograph of the NBT–20KBT sample sintered at 1120°C for 5 h. Dark grains of the $K_2Ti_6O_{13}$ secondary phase in the whisker-shape are observed.

4.2.2 Microstructure analysis

As described above, the sintering range of the KBT ceramics was very narrow. The density of the KBT samples was improved by the cold isostatic pressing at 750 MPa before

the sintering process. The densities of the cold isostatically pressed samples sintered at 1030°C for 5 and 20 h were 92 and 96%, respectively, of the theoretical density of KBT. The microstructure of the sample sintered for 20 h is shown in Figure 57a. The content of the secondary phase was estimated at 1–2 vol%. The as-prepared KBT ceramics sintered for 20 h were of sufficient quality for electrical and stress-dependence characterization. The average grain size was below 0.5 μm, and remained small, i.e., around 1 μm, even after 80 h of sintering at 1030°C (Figure 57b). Besides the pores larger than 1 μm, a number of small, sub-micron pores were present in the ceramic samples.

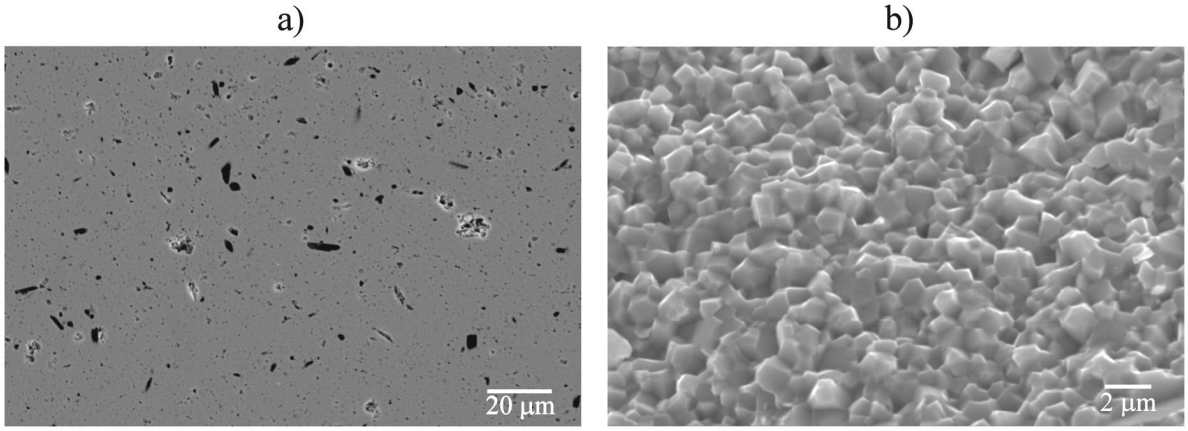

Figure 57: SEM micrographs of sample KBT sintered at 1030°C for a) 20 h – polished surface, and b) 80 h – fracture surface. In a) dark grains of $K_2Ti_6O_{13}$ secondary phase in the matrix phase are observed.

After the prolonged 80-h sintering two secondary phases were present in the samples, i.e., $K_2Ti_6O_{13}$ and Bi-rich phase (Figure 45b). The concentration of the secondary phases was high, especially near the surface of the pellet and the surface was covered with needles and rods of various sizes. Such a behaviour indicates the rapid thermal decomposition of the matrix phase on the surface of the pellet where the volatilization is increased. The formed secondary phases recrystallize into long, highly anisotropic grains [130]. At the same time the grains of the matrix phase remained isotropic and small. Such behaviour is believed to be due to a continuous thermal decomposition of the matrix phase. The purity of the TiO_2 powder showed a great influence on the decomposition of the matrix phase and on the formation of the secondary phases. When a powder with a purity of 99.8%, instead of a powder with a purity of 99.99%, was used, the sample sintered for 20 h looked like the sample sintered for 80 h shown in Figure 45b.

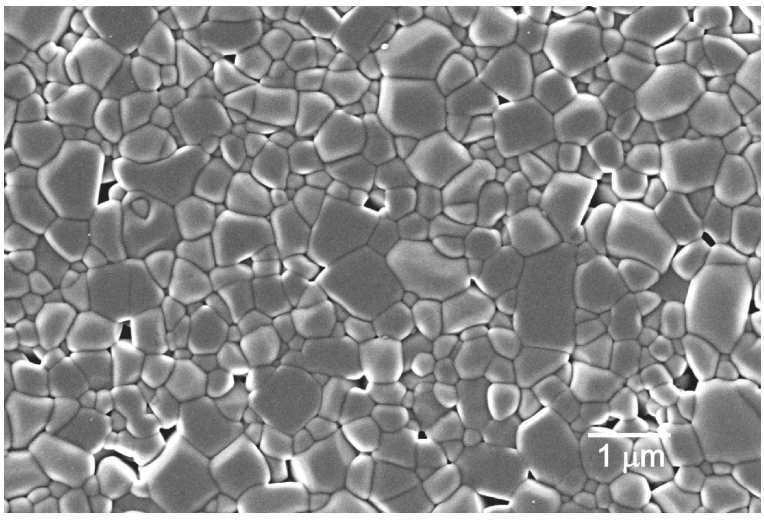

Figure 58: SEM micrograph of the thermally etched NBT–20KBT sample sintered at 1120°C for 5 h.

The microstructure analysis of the NBT–KBT samples revealed similar features as observed in pure KBT. Typical micrographs of a polished and thermally etched sample from the NBT–KBT series are shown in Figure 56 and Figure 58, respectively. The average grain size was very small, i.e., below 0.5 μm. The major part of the pores was sub-micron sized. The obtained samples were of high density, above 98% of the theoretical density. The content of the secondary phase was smaller than in pure KBT and decreased with decreasing content of KBT.

4.2.3 Dielectric properties

The temperature dependence of the dielectric properties of samples from the NBT–KBT solid-solution series is shown in Figure 59. The following characteristics can be observed:

- With the addition of 20 mol% of KBT the permittivity maximum increases to 6500 and shifts to lower temperature, i.e., 270°C. The maximum then slowly decreases and shifts toward higher temperatures with the further addition of KBT. The data correspond to a measuring frequency of 1MHz.
- The value of the permittivity maximum increases with decreasing frequency; however, its temperature is frequency independent in the measuring range from 1 kHz to 1 MHz.
- The frequency-dispersive anomaly becomes less distinctive with increasing content of KBT.
- A distinct maximum-minimum sequence in the dielectric losses is observed in sample NBT–20KBT, similar to pure NBT. It is then lost for samples with larger additions of KBT.
- The temperature of the minimum in the losses first decreases to 270°C for sample NBT–20KBT and then increases with the further addition of KBT.
- The room-temperature permittivity increases to 1150 at 1 MHz for sample NBT–20KBT and then gradually decreases with a larger addition of KBT.
- The frequency dispersion of the permittivity is observed across the whole temperature range for all prepared samples.

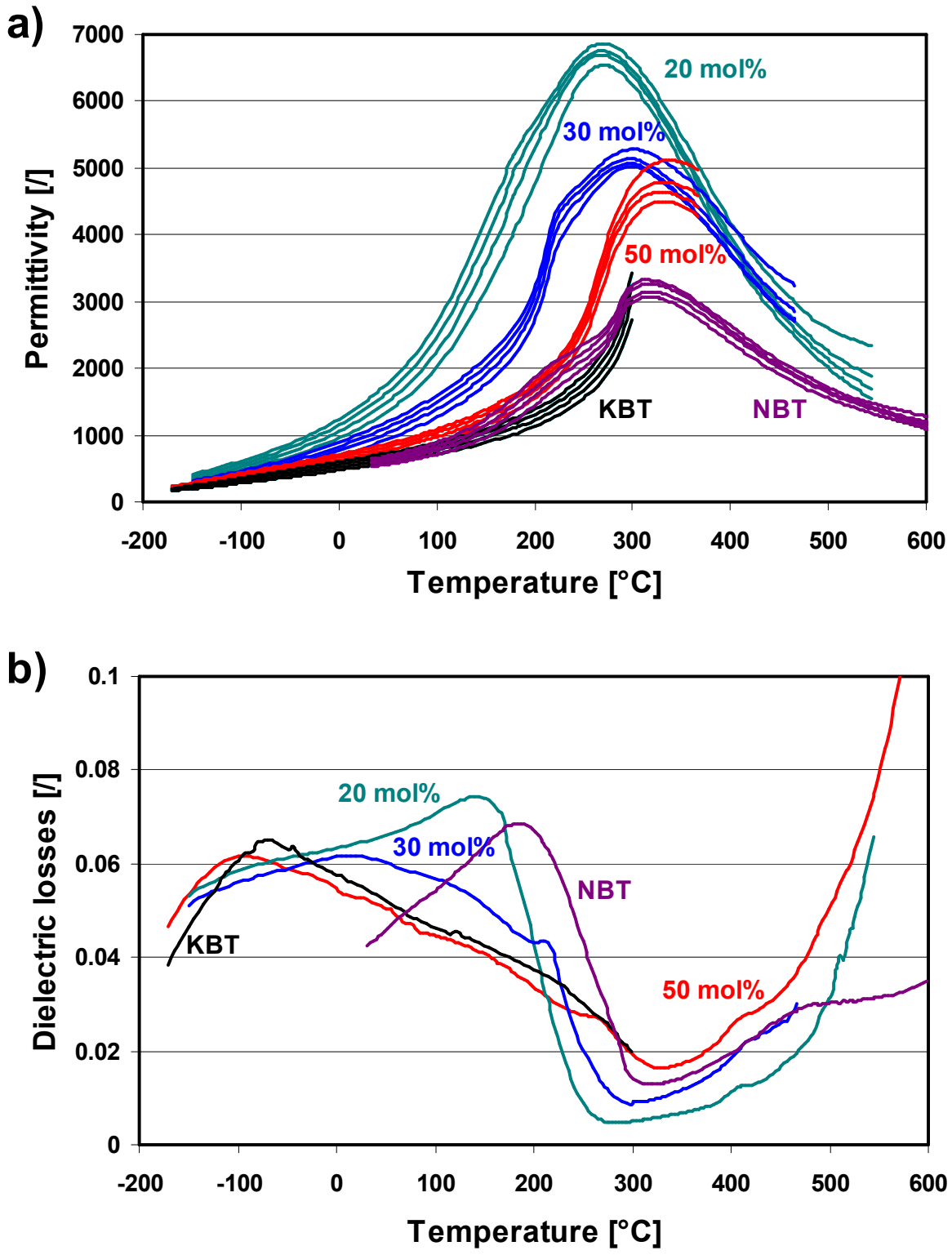

Figure 59: Temperature dependence of a) relative permittivity and b) dielectric losses of the samples from the NBT–KBT series. In a), the permittivity data obtained at frequencies 1, 10, 100 kHz, and 1 MHz are shown; in b), the dielectric losses at 1 MHz are shown.

The addition of KBT with tetragonal symmetry destabilizes the rhombohedral phase of NBT. With the addition of 20 mol% of KBT, the maximum-minimum sequence in the dielectric losses, ascribed to the stabilization of the rhombohedral phase, is still present and is slightly shifted toward lower temperatures. Although it is located above the room temperature, the XRD analysis showed a morphotropic composition of the sample. This indicates that the rhombohedral phase is stable but does not expand over the whole volume of

the sample. With larger additions of KBT, the maximum in the dielectric losses shifts below room temperature and becomes broader and less distinct, as the rhombohedral phase is further destabilized. Additionally, on a closer look a small bump just before the minimum (on increasing temperature) in the dielectric losses can be observed in the samples NBT–30KBT and NBT–50KBT. The bump is ascribed to the stabilization of the spontaneous polarization of the tetragonal phase, since the phase transformation from cubic to tetragonal in KBT exhibits similar features as the transformation from tetragonal to rhombohedral in NBT; the dielectric maximum is observed at 380°C, while the spontaneous polarization appears at around 300°C [116, 131]. Thus, in samples with tetragonal symmetry the permittivity maximum is most probably related to the relaxor-like phase transition from the cubic to tetragonal phase, similar as observed in pure KBT [98].

According to the theory, the increase of the room-temperature permittivity is expected to have a positive effect on the pressure dependence of the permittivity. An additional increase in the pressure dependence of the permittivity is expected to occur in the morphotropic phase composition, i.e., the sample with 20 mol% of KBT.

4.2.4 Ferroelectric properties

The measurements of the ferroelectric hysteresis loops are shown in Figure 60. All prepared materials show typical ferroelectric behaviour, except the KBT sample for which a rather unsaturated polarization–electric field loop is observed. With increasing content of KBT the squareness of the hysteresis loops decreases. In comparison to pure NBT, the P_r at first increases for the sample with 20 mol% of KBT and then decreases with further additions of KBT. The E_c decreases by approximately 50%, to values between 42–35 kV/cm.

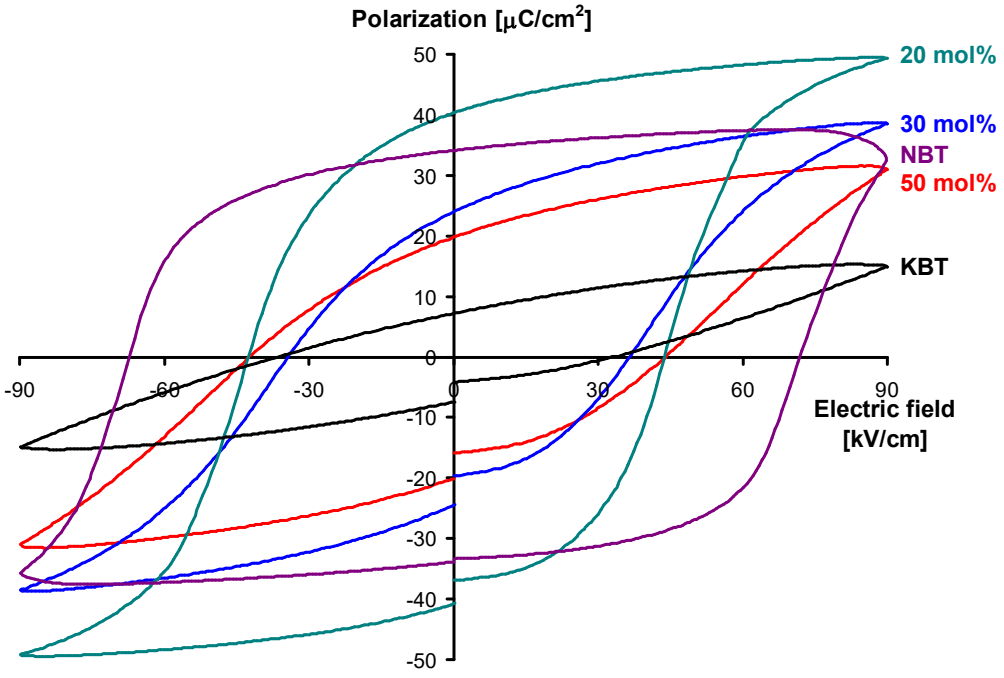

Figure 60: Polarization–electric field hysteresis of samples from the NBT–KBT system. Measurements were performed at a frequency of 10 Hz.

With a 20 mol% addition of KBT the material exhibited improved ferroelectric properties with higher P_r and lower E_c, similar to that observed for a small 5 mol% addition of NTa. This result is compatible with the XRD observation of a morphotropic composition of this sample. The coexistence of the rhombohedral and tetragonal phase enables better alignment of the spontaneous polarization with the field direction, which results in a higher

P_r, and the additional energy minima enable easier switching of the polarization, which results in a smaller E_c. Such behaviour is typical for materials with a morphotropic phase boundary.

With larger additions of KBT, the typical shape of the ferroelectric hysteresis started to diminish and was completely lost for pure KBT. The hysteresis loop of KBT was rounded and unsaturated. However, similar hysteresis was reported in the literature [119, 120, 122]. In the report of Himura *et al*. [99] more conventional, i.e., square, ferroelectric hysteresis was obtained for hot-pressed samples at higher temperatures (1060–1080°C) that were additionally annealed for a longer period of time at 1040°C. In this way, the average grain size was increased, and the polarization–electric field measurements showed an increase in P_r with increasing grain size. The reported measurements were performed at a highest field of 150 kV/cm. Thus, the reason for the untypical ferroelectric hysteresis found in this study is believed to be due to the small grain size (below 0.5 μm) and the small electric field used (90 kV/cm). At higher fields the samples were damaged.

According to the decreased value of the coercive field in samples with KBT additions, an increase in the influence of the axial pressure on the permittivity in these materials compared to pure NBT is expected. However, due to the ferroelectric character of the NBT–KBT materials, irreversible changes of the permittivity are expected to occur after compression tests.

4.2.5 Uniaxial stress dependence of the permittivity

The uniaxial stress dependence of the permittivity for the NBT–20KBT sample is shown in Figure 61. In general, the response to the applied stress has the same characteristics as observed in the NBT–NTa samples: decreasing of the permittivity with increasing stress, irreversible change after removing the stress, differences between the first and the second stress cycles and time dependence under constant pressure are observed. The irreversible change and the time dependence are more emphasized compared to the samples from the NBT–NTa system. Moreover, the curve of the first stress cycle is much more nonlinear, while the second stress cycle is approximately linear. With decreasing measuring frequency, the

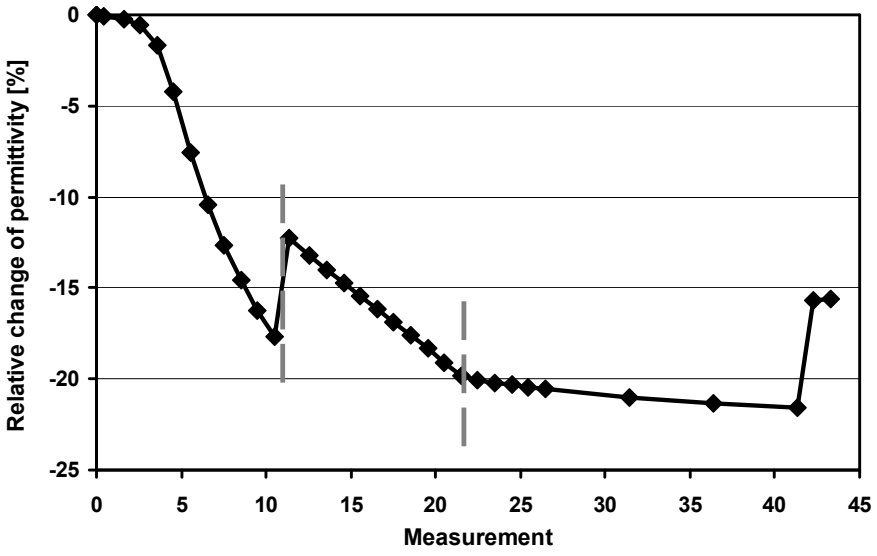

Figure 61: Relative change of the permittivity at 1 MHz during the stress testing of the sample NBT–20KBT. The starting value of the permittivity was 1028.2, and the values of the pre-stress and the maximum stress were 8 and 212 MPa, respectively.

sensitivity increased (Table 4). Such behaviour is ascribed to the frequency dispersion of the permittivity at room temperature, as observed in low NTa-content compositions. The increase in the sensitivity with decreasing frequency is more emphasized than in pure NBT (Table 4), since the dispersion of the permittivity in the NBT–20KBT sample is stronger than in pure NBT.

Table 4: Comparison of the stress sensitivity at 1 kHz and 1 MHz for virgin NBT and NBT–20KBT samples.

Sample	Starting permittivity [/]		$\Delta\varepsilon/\varepsilon$ [%] at maximum stress (213 MPa)	
frequency	1 kHz	1 MHZ	1 kHz	1 MHZ
NBT	590.7	480.1	4.5	3.2
NBT–20KBT	1301.8	1028.2	23.6	17.7

In Figure 62, the first stress cycle for three samples of the NBT–20KBT composition is shown. The stress dependence is very small and approximately linear up to the stress value around 50 MPa. At higher stresses, the decrease of the permittivity is much faster until at high stresses the slope of the curve decreases. However, no strong saturation was observed at pressures up to 220 MPa. Such behaviour is connected with the domain structure of the material and is very similar to the virgin ferroelectric hysteresis curve of a ferroelectric material. At small fields, mechanical or electric field, the domain structure does not change. The change in the permittivity is small, ascribed to the intrinsic response of the unit cells, and is approximately linear. When a critical, i.e., coercive, field is reached, domain switching with an additional contribution occurs and the slope of the curve increases. When at high fields the reservoir of the switchable domains is exhausted the slope of the curve decreases.

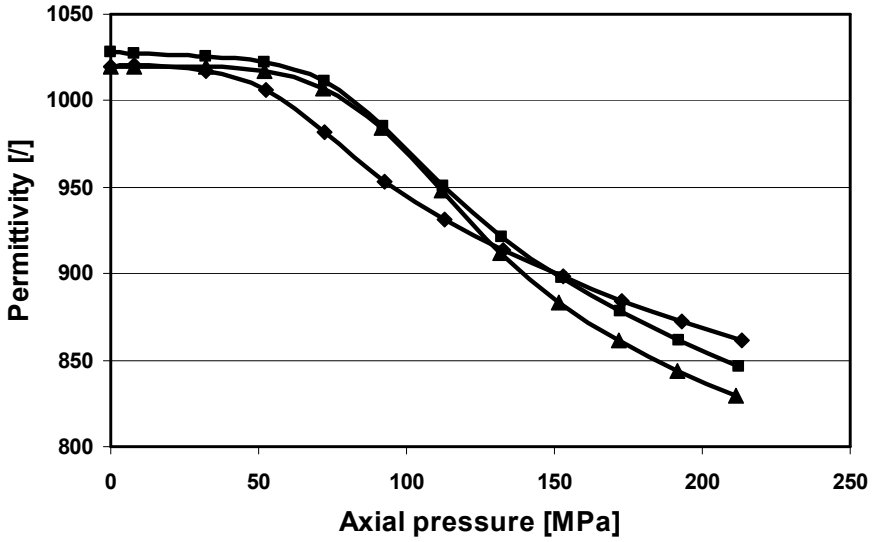

Figure 62: Axial pressure dependence of the permittivity at 1 MHz for three virgin specimens of the NBT–20KBT composition.

As mentioned above, the curve of the first stress cycle in sample NBT–20KBT is much more nonlinear compared to those from the NBT–NTa samples (Figure 36). A comparison of two samples from the different systems that possess very similar properties is shown in Figure 63. Samples NBT–5NTa and NBT–20KBT are both of a morphotropic composition and exhibit typical ferroelectric hysteresis with a comparable remanent polarization and coercive field (Figure 31 and Figure 60). The room-temperature permittivity of the latter is approximately 2/3 higher than that of the former. The stress dependences of the permittivity for the two materials are very different. In addition to the difference in the linearity, a big difference in the amount of the irreversible change is observed.

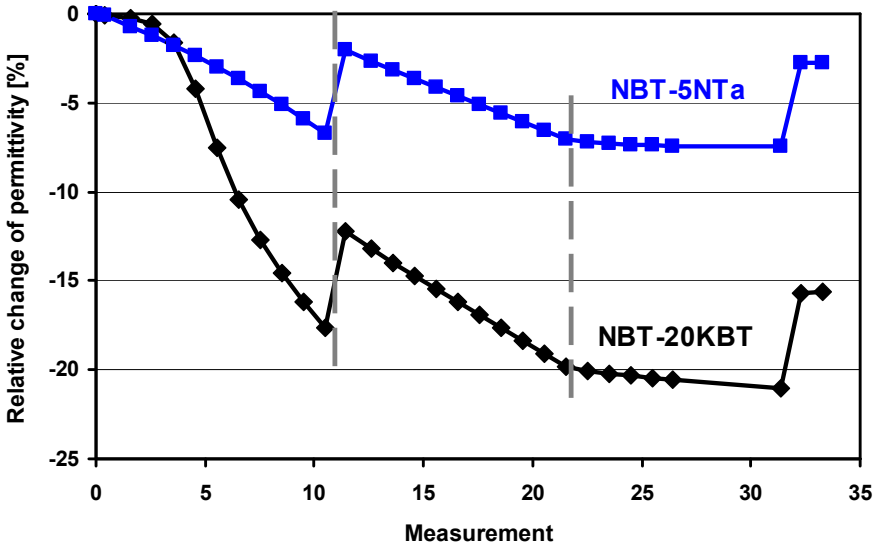

Figure 63: Comparison of the results of the stress dependence of the permittivity for samples NBT–5NTa and NBT–20KBT, with starting values of the permittivity 608.2 and 1028.2, respectively. The values of the pre-stress and the maximum stress were the same for both samples: 8 and 212 MPa, respectively.

The differences between the two samples can be explained if a structural peculiarity is considered to exist in the NBT–20KBT sample, like the defect dipoles in doped materials [61, 63-65]. For example, the "soft" and "hard" behaviour of the PZT ceramics is triggered by the introduction of defects due to donor and acceptor doping, respectively [8]. Hard PZT compositions are obtained by acceptor doping, by replacing the A- or B-site cation with lower-valent ions [8]. Example of M_2O_3 (M stands for metal) doping of PZT in Kröger-Vink notation, where M^{+3} occupies the B-site of the perovskite structure, is represented in the following way. Oxygen vacancy, $V_O^{\bullet\bullet}$, is formed when two B-site ions are replaced by M^{+3} ions, M_{Ti}^{-1}, resulting in the formation of the $2M_{Ti}^{-1} - V_O^{\bullet\bullet}$ defect dipole. Such defect dipoles, also called random field defects, tend to align in the direction of the polarization vector within a domain and are mobile, especially at increased temperatures. Donor doping, i.e., replacing the A- or B-site cation with a higher-valent ions, is compensated for either by electrons or doubly negatively charged lead vacancies, $V_{Pb}^{//}$. These defects, also called random potential defects, form dipoles with the dopants and their mobility is low [61]. The defects significantly influence the degree of the stabilization of the domain structure and, consequently, the properties of the material.

It is believed that in the sample NBT–20KBT defect dipoles are present, which stabilize the domain structure. The stabilization of the domain structure is reflected in only a small change of the permittivity at small applied stresses. However, when enough energy is put into the system by the external pressure, the domains can overcome the defects and/or the defects can find a new energetically more favourable orientation or position. Thereafter, domain switching processes occur at higher pressure and the permittivity decreases. Due to a morphotropic composition of the NBT–20KBT sample, the stabilization of the domain structure by the defect dipoles is rather small. The morphotropic composition, with rhombohedral and tetragonal ferroelectric structures, enables faster switching processes due to larger number of possible orientations of the spontaneous polarization. The change in the domain structure results in a strong permittivity decrease and a big irreversible change of the permittivity. In sample NBT–5NTa, the change of the domain structure, and thus the change of the permittivity, is more proportional to the applied pressure. In this sample, no defect dipoles are expected to exist and the intermediate phase, coexisting with the rhombohedral, is non-ferroelectric. Such properties result in a more proportional change of the permittivity to

the applied stress and a smaller irreversible change, in comparison to the sample NBT–20KBT.

The axial pressure effect on the permittivity then changes considerably for sample NBT–30KBT (Figure 64). Permittivity increases with increasing stress, goes through a maximum and then starts to decrease, thus creating a distinct maximum. Upon stress release, a positive irreversible change in the permittivity is observed. In the second loading cycle the permittivity decreases with increasing stress; however, the dependence is less linear than in the sample NBT–20KBT. Under the constant pressure a small additional decrease of the permittivity is observed.

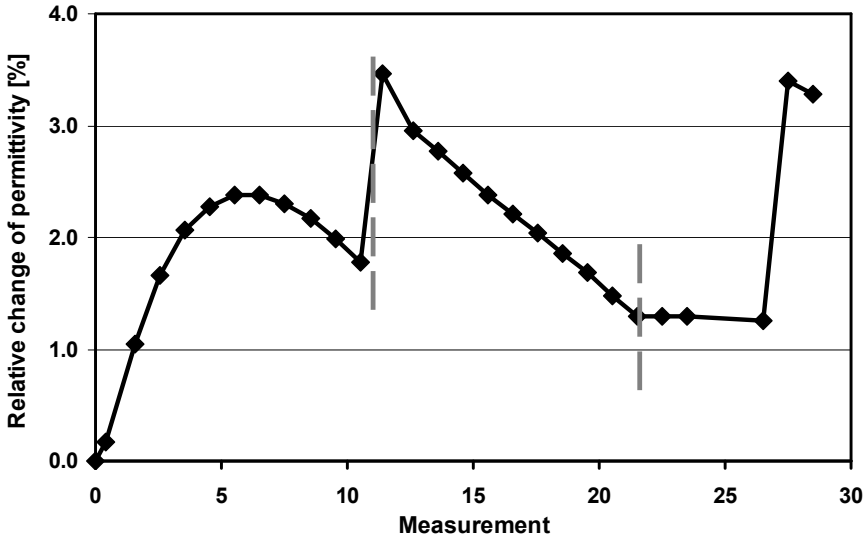

Figure 64: Relative change of the permittivity at 1 MHz during the stress testing of the sample NBT–30KBT. The starting value of the permittivity was 855.7, and the values of the pre-stress and the maximum stress were 8 and 213 MPa, respectively.

The increase of the permittivity with pressure was reported for hard doped PZT materials [63]. However, only individual measurements at relatively small stresses (10 and 20 MPa) were performed. No such maximum like that observed in this study was found, most probably due to the measurements being performed at rather low stresses. A similar maximum in the permittivity–stress dependence was observed in polarized samples [61, 68] but the principle in polarized samples is different. There, the increase in the permittivity is caused by the mechanical depolarization process that induces non-180° domain switching. Such domain switching increases domain wall density, which increases the permittivity. At higher stresses the permittivity starts to decrease as the material becomes polarized in the plane perpendicular to the stress direction.

The proposed mechanism that explains the increase of the permittivity with pressure in non-polarized ferroelectric materials is connected with the before-mentioned defect dipoles [63, 64]. In hard doped materials the defect dipoles are oriented along the internal field of the domains in the grains. In the equilibrium state, the defect dipoles are oriented in different directions on each side of the domain wall, thus stabilizing the domain walls (Figure 65). Under the applied stress, the energetically favourable domains will expand at the expense of other domains and the domain walls will move slightly from their initial position. In this new position the domain wall is more free to move under the small electric signal, as the defect dipoles around it are all oriented in the same direction. Such behaviour results in an increased value of the permittivity. The time needed for a defect dipole to reorient in the direction of the polarization is presumed to take a long time at room temperature. Upon stress release, the domain wall returns to its initial position and becomes pinned again by the different defect orientations around it and, therefore, the permittivity decreases in this ideal model. It should

be mentioned that the changes of materials' properties under different load conditions are understood for a single-domain, single-crystal ferroelectric material (intrinsic contributions) [5]. However, for most of the ferroelectric ceramic materials, it was found that the extrinsic contributions from the domain-boundary motions play a very important, and quite often, a major role in determining the properties of the material [132-134]. Thus, the properties of the material are determined by the domain structure, which can be additionally altered by the defect structure. The information on the extrinsic contributions can be obtained only by carefully measuring of the materials' response to the external conditions [5].

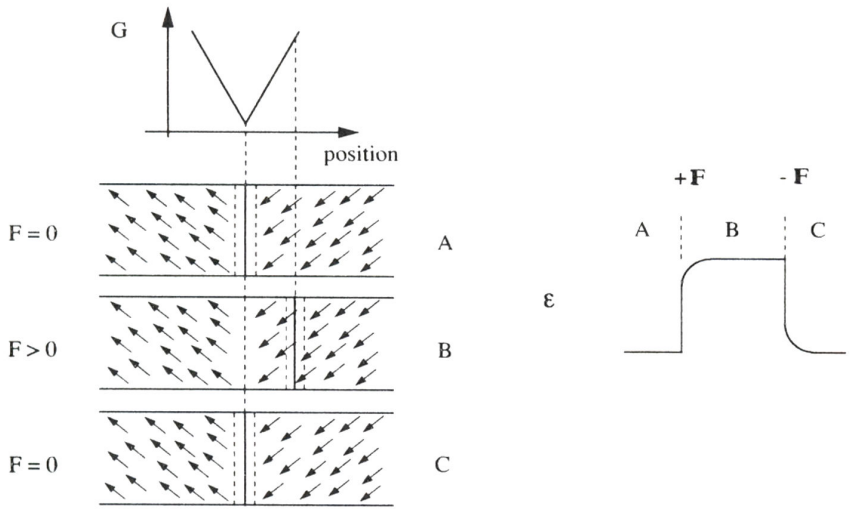

Figure 65: Schematic of the extrinsic contribution to the permittivity from the pinning of domain walls by oriented defect dipoles proposed for hard doped PZT. For oriented defect dipoles, the energy (*G*) of a domain wall is expressed as a potential discontinuity instead of a classic parabolic function. *F* corresponds to the external applied force.

The increase of the permittivity upon stress application in the NBT–30KBT sample is believed to be connected with the existence of the random field defects in the structure of the material. In the sample NBT–30KBT the domain walls are more strongly pinned by the defect dipoles than in the NBT–20KBT sample, as seen from the increase of the permittivity at small stresses. However, when a critical stress (approximately 150 MPa) is reached the permittivity starts to decrease. It appears that at high pressure the existing domain structure as well as its relation to the defect structure irreversibly changes. These changes induce a more conventional response to the applied stress in the second cycle, i.e., a permittivity decrease with increasing stress. Such behaviour indicates a completely different relationship between the domain walls and the dipole defects in the second stress cycle. A major part of the domain walls is not pinned by the defect dipoles, since the dynamics of the defects at room temperature is slow and they cannot find an equilibrium position in a short period of time. Due to a change in the domain-wall mobility, the response to the applied stress is more conventional.

If the presumption of the existence of the critical stress at which the relation between the domain and the defect structures collapses holds, the response at smaller stresses below the critical value should be, at least qualitatively, reproducible. Thereafter, an increase of the permittivity with increasing stress should be observed in the second cycle as well. This was experimentally examined and the results are shown in Figure 66. In the first cycle the maximum load was approximately 90 MPa and an increase of the permittivity was observed. Then, the load was removed, resulting in a decrease of the permittivity, followed by an additional relaxation towards the starting value. Then the second stress cycle was applied up to the maximum load of approximately 210 MPa. During the second stress cycle, the permittivity first increased and then decreased, passing through a maximum at 150 MPa.

Upon stress removing, the permittivity jumped to a higher value and then, in the third stress cycle, decreased with increasing pressure. The experiment confirmed that a critical stress value exists, at which the relation between the domain and defect structures irreversibly changes.

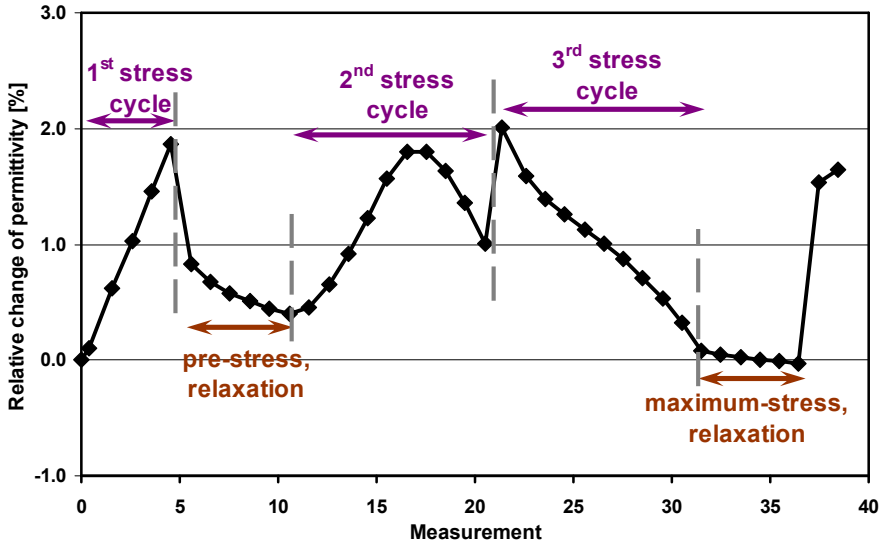

Figure 66: Relative change of the permittivity at 1 MHz during the stress testing of sample NBT–30KBT. The starting value of the permittivity was 866.8, and the values of the pre-stress and the maximum stress were 8 and 213 MPa, respectively. In the first stress cycle the stress was increased up to 90 MPa, while in the second and third stress cycles the stress was increased up to the maximum value (213 MPa).

The dielectric properties of the sample NBT–30KBT show a perceivable frequency dispersion in the room-temperature region. Thus, like with the NBT–20NBT sample, an influence of the measuring frequency on the stress sensitivity was expected. Figure 67 shows the influence of the pressure on the permittivity at different measuring frequencies from 1 kHz to 1 MHz for the NBT–30KBT sample. For a better comparison, the permittivity change with respect to the starting permittivity at each frequency was calculated. With increasing measuring frequency the critical stress increases from ~60 MPa at 1 kHz to ~130 MPa at 1 MHz. Such behaviour is believed to be connected with the domain and defect structures existing in the material. It is presumed that there is a difference in the strength of the pinning of the domain walls: some domain walls are more strongly pinned than the others. When the stress is applied, the strongly pinned domain walls move just slightly away from the original pinning centres and their contribution increases the permittivity. When the stress is removed they return to the original pinned position and the permittivity decreases again, as proposed by the mechanism described above. On the other hand, the loosely pinned domain walls are more mobile and switch under the same applied stress. The switching of domains results in a decrease of the permittivity. The sum of both contributions, at a specific stress value, determines the permittivity change. Higher permittivity and higher stress sensitivity at a lower frequency result in a lower critical stress value at a lower measuring frequency, while the opposite is valid for a higher frequency. Thus, the frequency dependence of the critical stress value is caused by the different strength of the domain-wall pinning and the different stress sensitivity of the mechanisms that contribute to the permittivity at various frequencies.

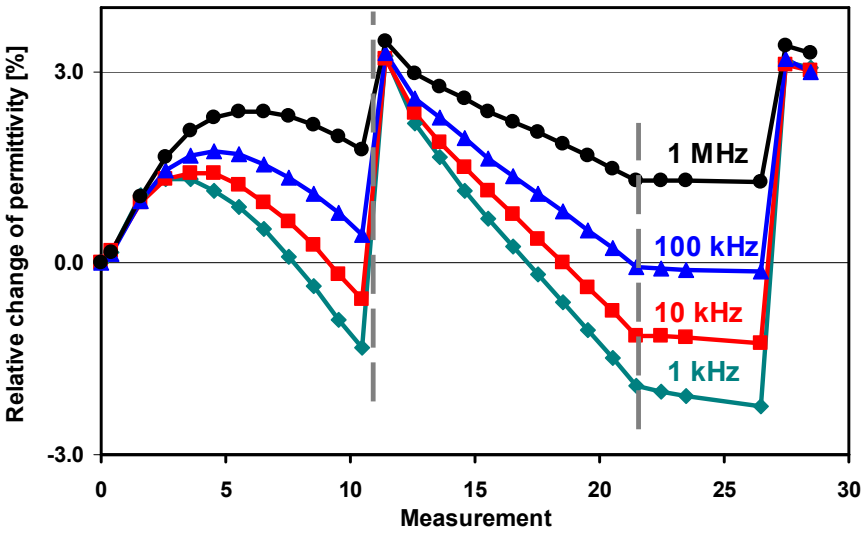

Figure 67: Frequency dependence of the relative change of the permittivity during the stress testing of sample NBT–30KBT. The starting value of the permittivity was 843.5, and the values of the pre-stress and the maximum stress were 8 and 213 MPa, respectively.

In samples with higher contents of KBT, i.e., samples NBT–50KBT and pure KBT, additional changes to the stress dependence of the permittivity were observed. Both samples showed the same behaviour as that shown for sample NBT–50KBT at a frequency of 1 MHz in Figure 68. With increasing stress the permittivity increases and when the load is removed a positive irreversible change in the permittivity is observed. At first, the permittivity–stress dependence of the first cycle is approximately linear and then it starts to saturate at the highest stresses. Also in the second stress cycle the permittivity increases and then remains almost constant under constant pressure.

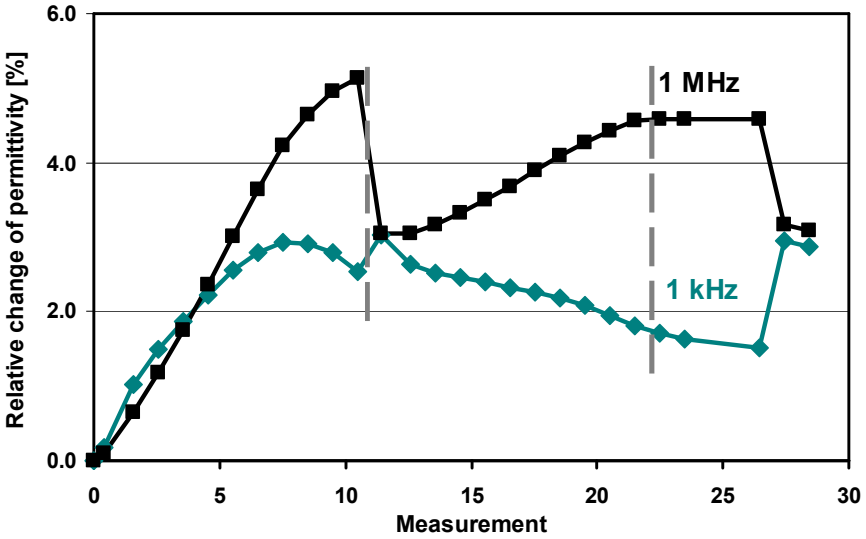

Figure 68: Relative change of the permittivity at 1 MHz and 1 kHz during the stress testing of the NBT–50KBT sample. The starting values of the permittivity were 680.5 and 843.0 at 1 MHz and 1 kHz, respectively, and the values of the pre-stress and the maximum stress were 8 and 212 MPa, respectively.

The behaviour of the NBT–50KBT and KBT samples is different from the behaviour of the NBT–30KBT sample; however, it can be explained on the basis of the same mechanism. In both cases the permittivity increases with increasing stress, thus in both cases an internal defect structure probably exists that triggers such behaviour, as described above. The difference between the compositions is in the value of the critical stress, which is higher

in the samples NBT–50KBT and KBT. Since this value is higher than the maximum applied stress, a turn around in the permittivity trend does not appear. The beginning of the saturation was observed in the sample NBT–50KBT at 1 MHz (Figure 68), at the very end of the first stress cycle. Thus, if a higher stress would be applied to the sample a maximum would be observed. Thereafter, the virgin domain/defect structure in the NBT–50KBT and KBT samples is more stable than in the sample NBT–30KBT.

Like that observed in sample NBT–30KBT, the critical stress decreases with decreasing frequency also in the samples NBT–50KBT and KBT. For sample NBT–50KBT at a frequency of 1 kHz (Figure 68), the permittivity went through a maximum in the first stress cycle and then monotonously decreased in the second stress cycle (Figure 68). At other frequencies, the applied stress was very close to the critical value, i.e., the first stress cycle ended at the turn-around point on the maximum. In this situation, the sum of all the contributions to the permittivity is approximately zero, thus in the second stress cycle the permittivity hardly changed up to the maximum load (Figure 69).

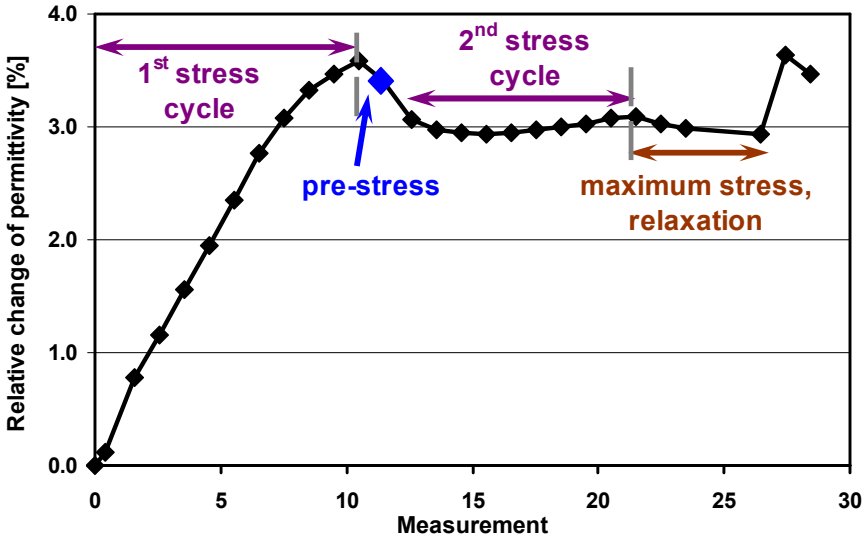

Figure 69: Relative change of the permittivity at 1 kHz during the stress testing of sample KBT. The starting value of the permittivity was 559.6, and the values of the pre-stress and the maximum stress were 8 and 219 MPa, respectively.

The increasing content of KBT induces behaviour similar to that observed in a hard doped PZT in the study of Steiner *et al*. [63]. Such behaviour was not expected according to the ferroelectric hysteresis measurements, since the remanent coercive field decreases with additions of KBT, and the squareness of the loop decreases. Decreasing of the coercive field indicates a decreasing of the "hardness" of the materials. A very different behaviour for materials with similar electrical properties, also reported in the literature [60, 61, 63, 67-70], manifests the complexity of the ferroelectric materials and their behaviour under compressive stress.

For KBT, the WDS analysis showed a non-stoichiometric structure, thus defects are likely to be present within the structure of the material. The observed behaviour under the applied axial pressure shows that the defect structure in KBT triggers a similar response as observed in hard-doped PZT. Therefore, the structure of the defects in KBT is believed to be similar to the random field defects found in hard doped PZT. The results showed that such defects exist across the whole tetragonal region of the NBT–KBT solid solution.

The addition of KBT increased the effect of the axial pressure on the permittivity compared to pure NBT; however, the response to the applied stress is complex. Such a response is caused by the macroscopic domain structure and the defect structure inherent to

materials from the NBT–KBT system. Due to the complex response to the applied stress, the potential applicability of the materials from the NBT–KBT system for pressure sensing is small.

4.2.6 Summary

KBT was added to NBT in order to reduce the high coercive field and, thus, increase the influence of the axial pressure on the permittivity. XRD and SEM analyses showed that the solid solution forms between NBT and KBT across the whole concentration range. However, potassium poly-titanates were formed during the synthesis already at low temperatures and it was not possible to remove them by a heat-treatment process. A detailed investigation of the synthesis of KBT ceramics revealed that the matrix phase formed is non-stoichiometric; it is potassium deficient and contains an excess of bismuth. The matrix phase slowly decomposes during the sintering process and forms $K_2Ti_6O_{13}$ and Bi-rich secondary phases, as well as potassium and bismuth vapours above the solid sample. The obtained ceramic samples were dense but contained a small content of secondary phases (1–2 vol%). The dielectric maxima of the samples from the NBT–KBT system are located well above room temperature (above 270°C), while the room-temperature permittivity is the highest for the NBT–20KBT sample with a morphotropic composition (1150 at a frequency of 1 MHz). In all samples ferroelectric properties were observed and the coercive field decreased with the addition of KBT. Sample NBT–20KBT showed similar features of the axial pressure effect on the permittivity as observed in materials from the NBT–NTa system, consistent with its ferroelectric properties. The response of the compositions with a higher KBT content (30 and more mol%) to the applied stress was considerably different, showing an increase of the permittivity with increasing axial pressure at lower values. Such behaviour then changed to more conventional, i.e., a decrease of the permittivity with increasing pressure, when a specific critical stress value was exceeded. The value of the critical stress increased with the increasing content of KBT and the increasing measuring frequency. Such behaviour can be explained by the existence of an internal defect structure that pins the domain structure of the material. The defects considerably change the materials' response to the applied stress. Though the KBT addition increased the influence of axial pressure on the permittivity, the applicability of these materials is small due to their complex response to the applied stress.

4.3 $Na_{0.5}Bi_{0.5}TiO_3$–$KTaO_3$ system

4.3.1 Synthesis

4.3.1.1 Preliminary synthesis

No reports on the synthesis of the $Na_{0.5}Bi_{0.5}TiO_3$–$KTaO_3$ (NBT–KTa) system were found in the literature. Therefore, a preliminary synthesis of samples with 5, 10 and 20 mol% of KTa was performed, according to the synthesis of materials from the NBT–NTa system. The samples were calcined at 750 and 850°C for 10 h and sintered at 1100°C for 5 h. The XRD analysis of the phase composition during the synthesis of the sample NBT–20KTa is shown in Figure 70. After the first calcination all the samples contained a perovskite matrix phase as well as a small amount of a secondary phase identified as $Bi_4Ti_3O_{12}$. After subsequent calcination and sintering steps, XRD analysis revealed single-phase samples. A section of the XRD patterns of the sintered samples is shown in Figure 71. With the increasing concentration of KTa, the positions of the diffraction peaks shift towards lower 2θ values, in accordance with the larger unit cell of KTa (V_{PC} = 63.48 Å^3 [135]). Shifting of the

perovskite peak positions indicates the existence of solid solutions between NBT and KTa in the investigated concentration range.

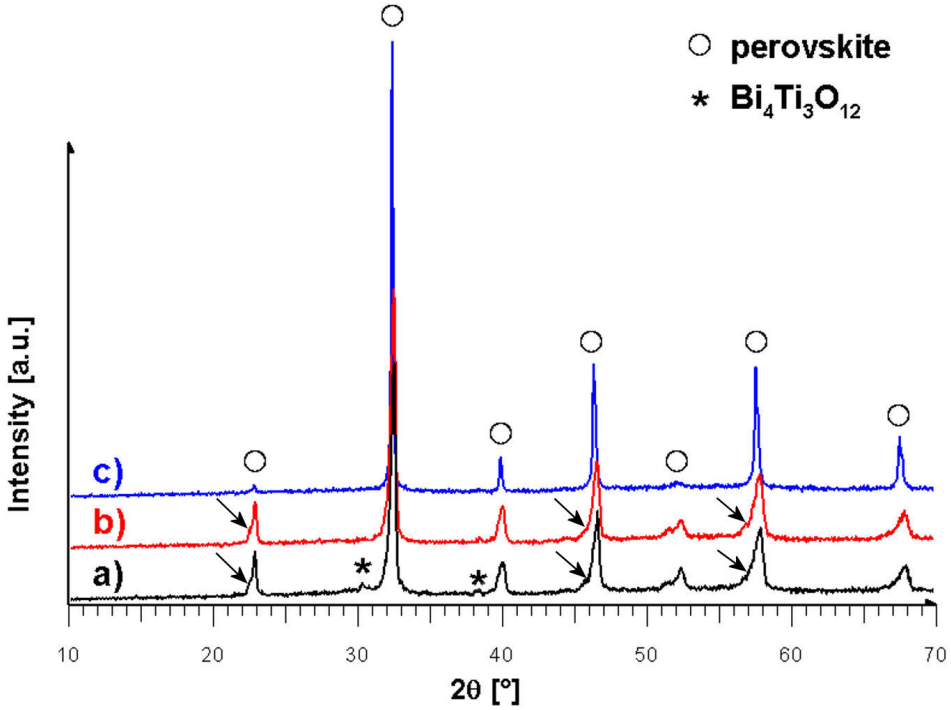

Figure 70: XRD patterns of sample NBT–20KTa after successive firings at a) 750°C, b) 850°C and 1100°C. The arrows indicate the deformation (the tail) of the peaks. Patterns measured using Cu$K\alpha_1$ and Cu$K\alpha_2$ radiation.

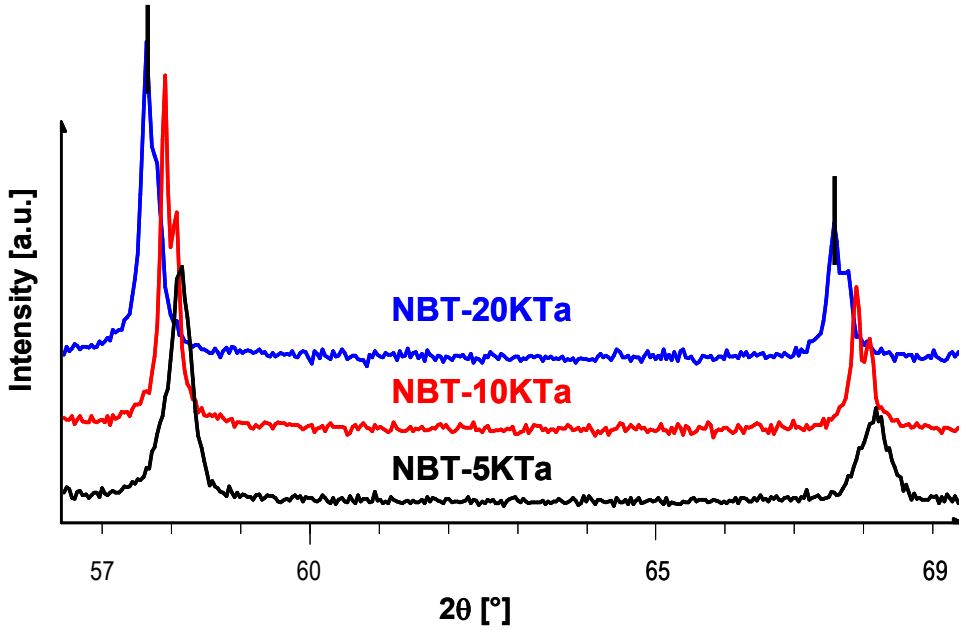

Figure 71: A section of the XRD patterns of the sintered samples from the NBT–KTa series prepared by the preliminary synthesis. The vertical lines represent the diffraction lines of the cubic NBT–20KTa phase. Patterns measured using Cu$K\alpha_1$ and Cu$K\alpha_2$ radiation.

The diffraction peaks that were very broad become more pronounced after the firing at 1100°C; however, the shape of the diffraction peaks was still not well defined (Figure 71). From a detailed examination of the diffraction peaks it was found that they exhibit a deformation (a tail) on the side of the lower 2θ values, indicating the existence of grains with

higher contents of KTa in the material. The deformation of the peaks was clearly evident, especially after low-temperature firings, i.e., 750 and 850°C (Figure 70). Thereafter, the samples were inhomogeneous before the last heat treatment at 1100°C and, according to the not-well-defined shape of the diffraction peaks after the sintering (Figure 71), were not completely homogeneous even after the sintering.

The microstructures of the sintered samples are shown in Figure 72. Small isotropic grains of a dark secondary phase were present in all samples and, additionally, some bigger grains were found in the sample with 20 mol% of KTa. The secondary phase was identified as $K_2Ti_6O_{13}$ using EDS. However, in some of the secondary-phase grains a part of potassium was replaced by sodium. The EDS analysis also revealed that the composition of the matrix phase coincides well with the changing of the nominal composition with increasing content of KTa. Such behaviour confirms the existence of the solid solutions between the end members in this concentration range (5 to 20 mol% of KTa). Nevertheless, the obtained EDS data indicated that the matrix phase is not completely homogeneous and, in particular, the potassium content was slightly smaller than the nominal composition (the detected difference was bigger than the analytical sensitivity of the method). The formation of the $K_2Ti_6O_{13}$ secondary phase and the deficiency of potassium in the matrix phase indicate similar processes as observed during the KBT synthesis.

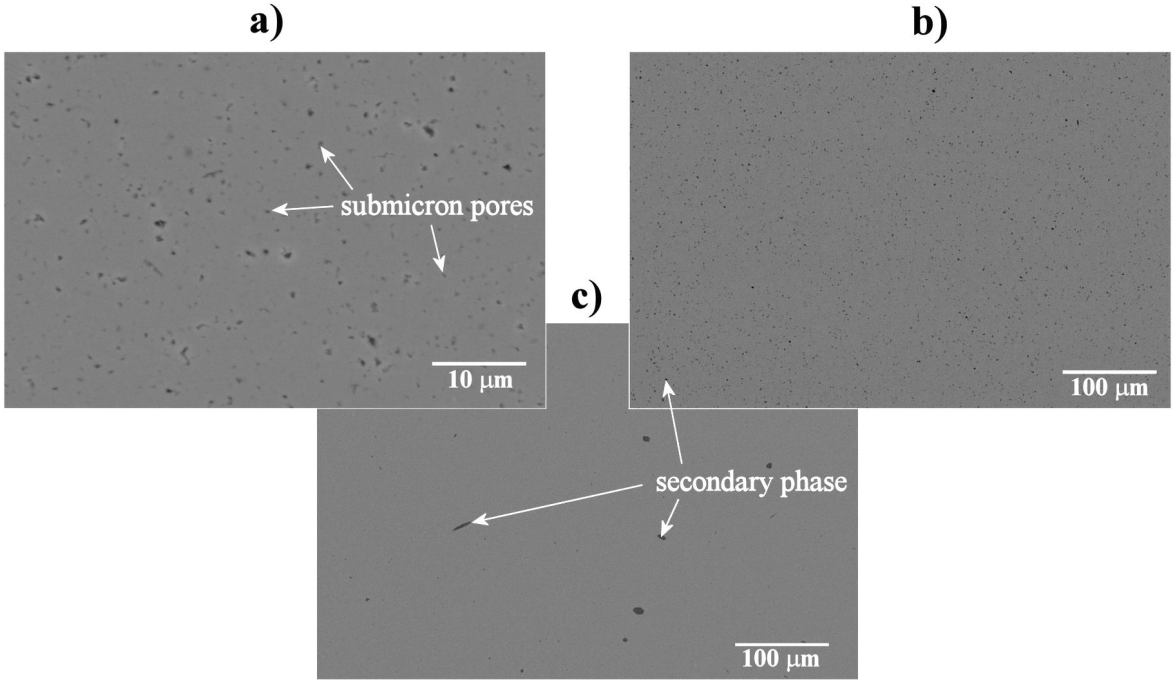

Figure 72: BSE-SEM micrographs of samples a) NBT–5KTa, b) NBT–10KTa and c) NBT–20KTa prepared by the preliminary synthesis. Submicron porosity and the dark secondary phase are indicated.

4.3.1.2 Synthesis with high-temperature annealing

To eliminate the secondary phase and improve the homogeneity of the matrix phase a different synthesis procedure with high-temperature annealing was applied. The samples from the whole concentration range were prepared according to the procedure shown schematically in Figure 73. First, the samples were calcined for 10 h at 750°C and 850°C followed by ball milling, as in the preliminary synthesis. Then, additional firings were performed. After the calcination at 950°C, the characteristics of the XRD spectra were unchanged as compared to 850°C. Obviously, this temperature is not high enough to actuate the homogenization of the matrix phase. Since the symmetry of the materials in the preliminary study changed at 1100°C, this temperature was selected for additional firings. Two 10 h firings were performed

at 1100°C with intermediate cooling and milling, followed by a 5-h sintering stage at 1150°C for samples with up to 70 mol% of KTa and at 1230–1300°C for sample NBT–90KTa.

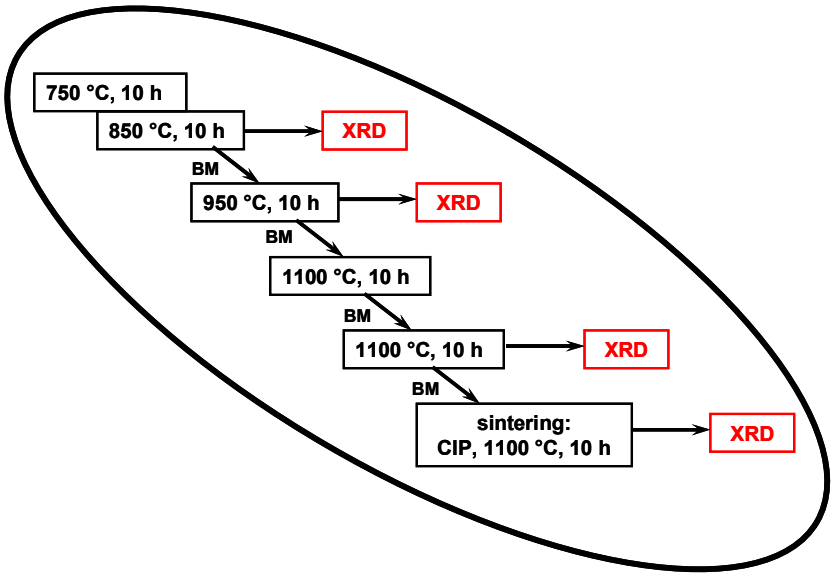

Figure 73: Schematic of the preparation of samples from the NBT–KTa series, according to the synthesis with high-temperature annealing (CIP–cold isostatic pressing, BM–ball milling).

The XRD patterns of the sample NBT–20KTa prepared by the high-temperature annealing route are shown in Figure 74. For comparison, a pattern of the sample prepared by the preliminary synthesis (sintered at 1100°C) is added. No big difference between the successive calcinations at 850 and 950°C was observed; however, significant changes were evident after the high-temperature firings. The intensities of the diffraction peaks at 2θ ~ 23° and 52° decrease with increasing sintering temperature, while the other peaks become sharper and their symmetry characteristics more evident. The very sharp peaks, compared to the preliminary prepared sample, indicate a more homogeneous composition of the matrix phase.

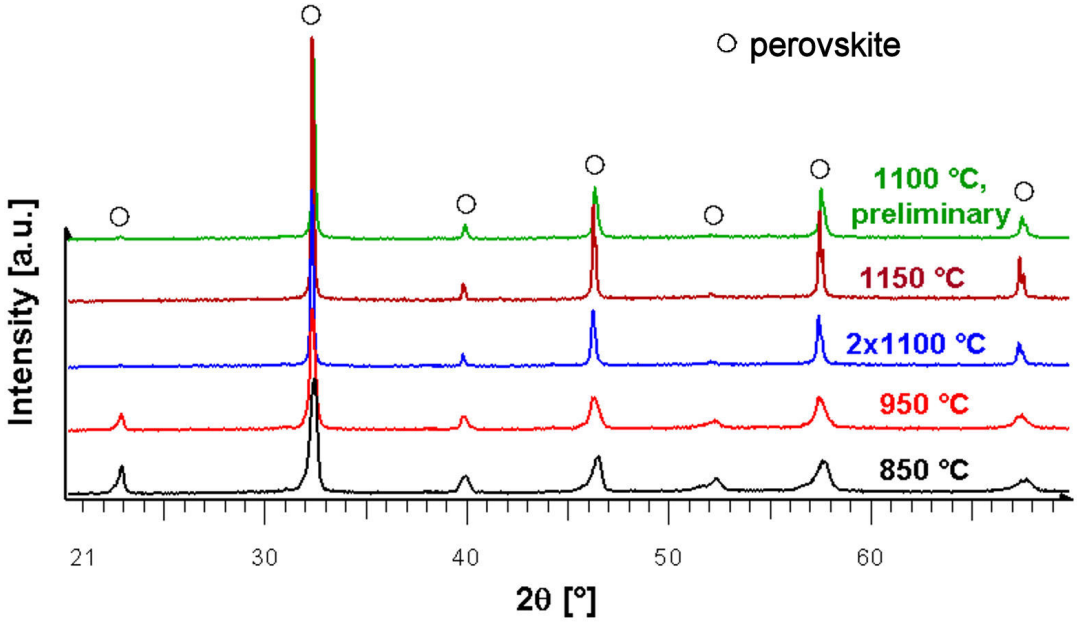

Figure 74: XRD patterns of the NBT–20KTa sample according to the synthesis with high-temperature annealing. For comparison, the XRD pattern of the preliminary prepared sample is added. Patterns were measured using Cu$K\alpha_1$ and Cu$K\alpha_2$ radiation.

The XRD patterns of the sintered samples from the whole NBT–KTa series are shown in Figure 75a. The diffraction peaks are very sharp for all the prepared materials, indicating good homogeneity of the matrix phases. With increasing content of KTa, the peaks are shifted towards lower 2θ values, in accordance with the larger volume of the KTa perovskite cell. The symmetry can be determined from the close-up look of the peak at 2θ ~ 57° in Figure 75b. The symmetry of all the samples except the sample NBT–5KTa is cubic. The composition of the NBT–5KTa sample is morphotropic between the rhombohedral of NBT and the cubic of KTa. No secondary-phase reflections were detected.

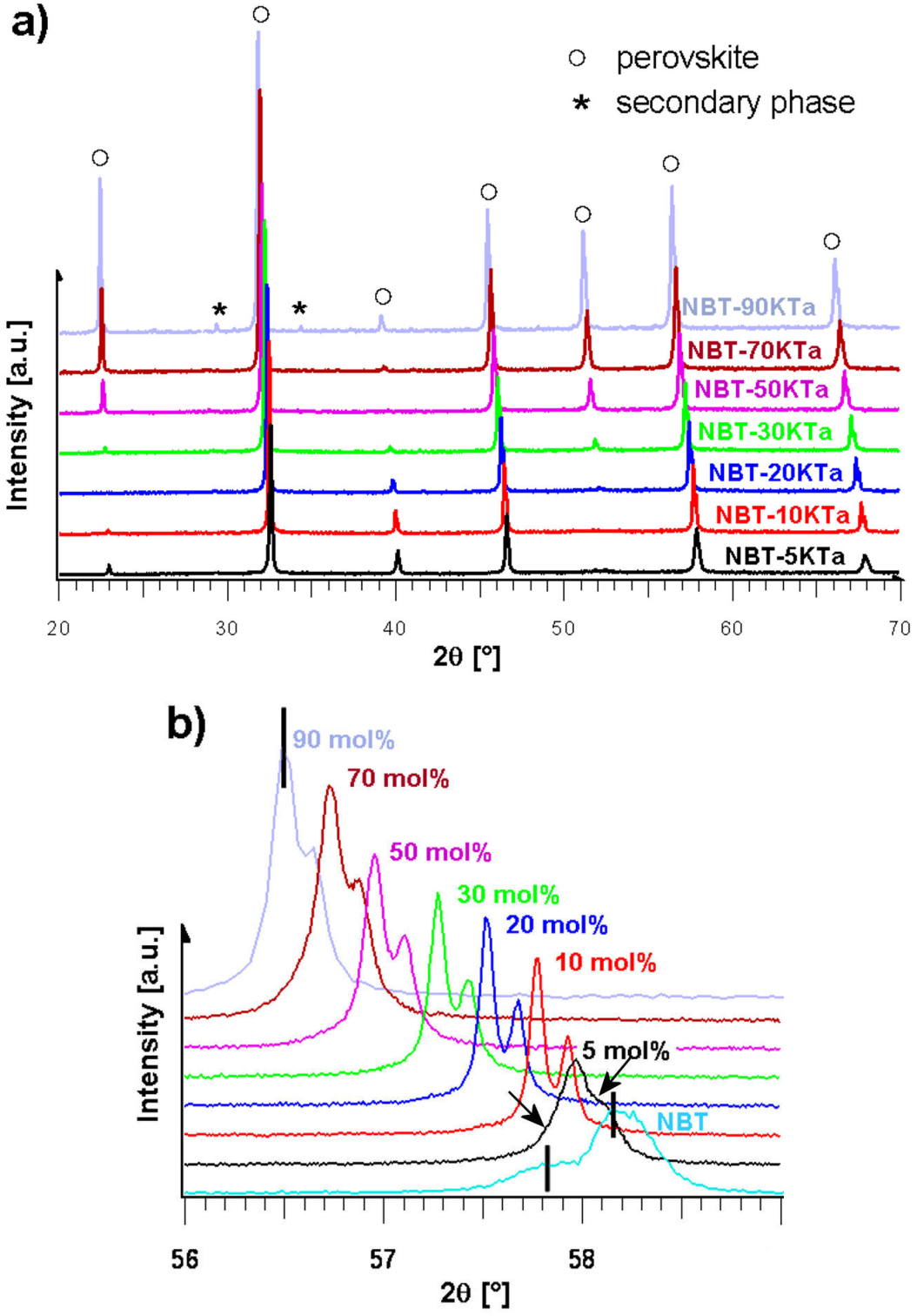

Figure 75: XRD patterns of the sintered samples from the NBT–KTa system prepared according to the synthesis with high-temperature annealing showing a) the whole patterns and b) a detail of the

patterns. In b) the vertical lines represent the diffraction lines of the rhombohedral and cubic phases. The arrows indicate the distortion due to the rhombohedral phase present in the MPB composition. Patterns were measured using Cu$K\alpha_1$ and Cu$K\alpha_2$ radiation.

Unlike the XRD analysis, the SEM analysis revealed the presence of secondary phases (Figure 76). In all samples, except in the NBT–90KTa sample, a dark secondary phase was present. In NBT–5KTa sample, predominantly small grains of the dark phase were present. The number of big grains, some of them with an anisotropic whisker-like shape, increased with increasing KTa content up to 50 mol%; however, in the NBT–70KTa sample again only small grains of a dark phase were present. In the NBT–30KTa and NBT–50KTa samples the concentration of the dark phase was higher near to the surface of the pellet. In samples with 70 and 90 mol% of KTa, a bright secondary phase was formed. In the NBT–70KTa sample only few big rectangular grains (10–50 μm) of the bright phase were found. The NBT–90KTa sample showed very poor sinterability and was sintered as high as 1300°C; however, the porosity was still high. Moreover, the concentration of the bright secondary phase strongly

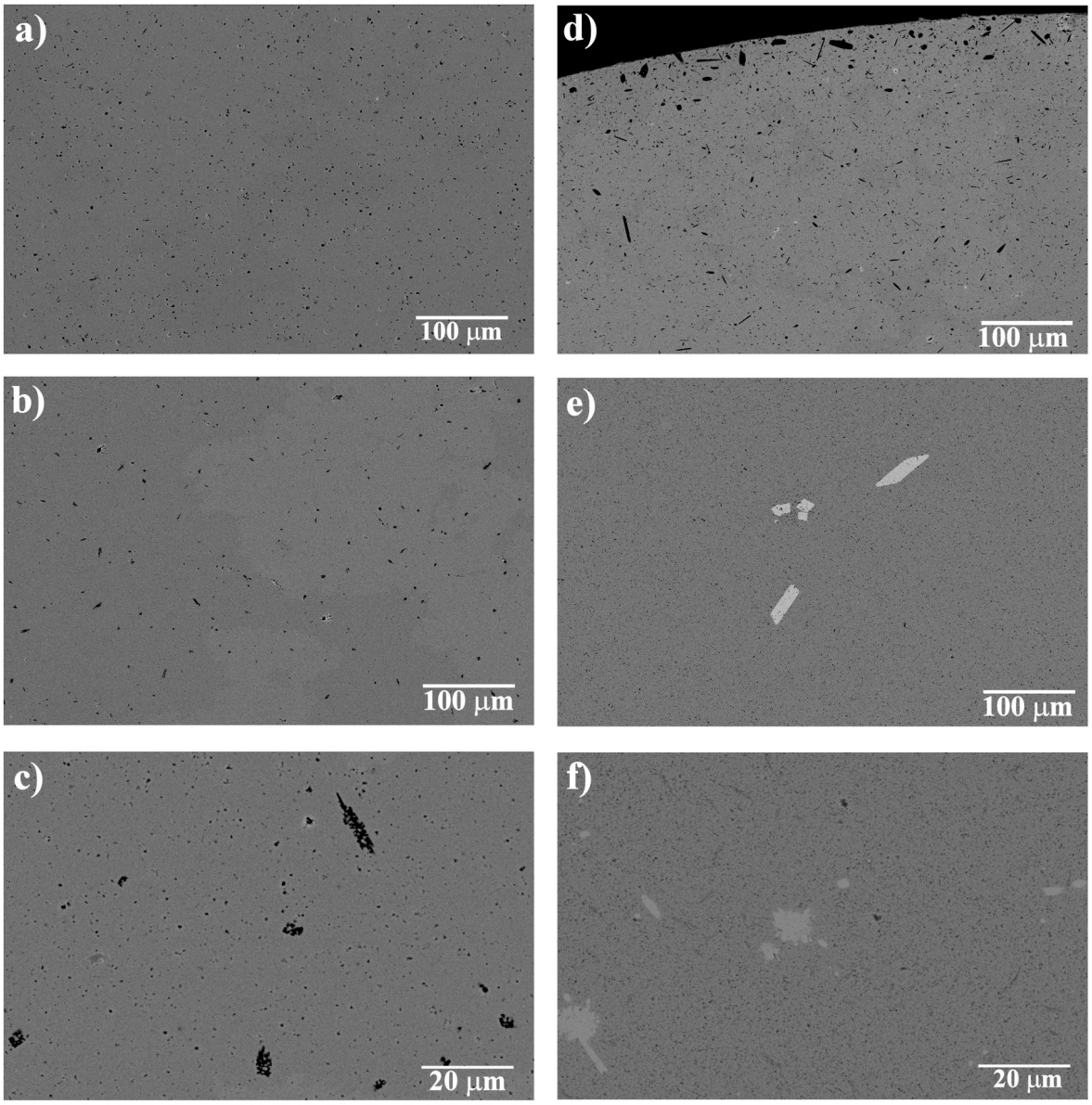

Figure 76: Selected SEM-BSE micrographs of the sintered samples from the NBT–KTa system prepared by the synthesis with high-temperature annealing: a) NBT–5KTa, b) and c) NBT–20KTa, d) NBT–30KTa, e) NBT–70KTa (all sintered at 1150°C), f) NBT–90KTa (sintered at 1230°C). Dark and bright secondary phases were present.

increased with increasing sintering temperature, indicating a rapid decomposition of the matrix phase. The secondary phases formed in the NBT–KTa series were examined using EDS. The dark phase corresponded to the $K_2Ti_6O_{13}$ phase, with a part of the potassium replaced by sodium, and the bright phase was found to be rich in tantalum (K:Ta ratio ~1:2). The EDS analysis of the matrix phase also revealed that the composition of the matrix phase coincides well with the nominal composition, thus confirming the existence of the solid solutions between the NBT and KTa end members in the whole concentration range.

According to the results of the XRD and SEM analyses the synthesis route with high-temperature annealing improved the homogeneity of the matrix phase but did not decrease the content of the secondary phases. On the contrary, the comparison of the samples prepared by different procedures (e.g., sample NBT–20KTa in Figure 72c and Figure 76c) revealed that the content of the dark phase increased after multiple firings at high temperatures. A different approach was investigated to reduce the content of the secondary phases, i.e., the synthesis from the end members; however, with no success, since the formation of a new compound starts only after the decomposition of the reacting perovskites. The performed experiments indicate that potassium and titanium oxides react very quickly to form a potassium poly-titanate phase. This phase is very stable and cannot be removed by a heat-treatment process. At higher temperatures, the volatilization of the potassium and bismuth components is increased and this results in a higher content of secondary phases. According to the EDS analysis and the shifting of the diffraction lines to lower 2θ values, the solid solutions between NBT and KTa exist across the whole concentration range; however, single-phase ceramics could not be obtained. The secondary phase formation is believed to be triggered by the thermal instability of the matrix phase, similar to that observed during the synthesis of KBT (§4.2.1.1).

4.3.2 Microstructure analysis

Selected SEM micrographs of the polished samples prepared by the high-temperature annealing route are shown in Figure 76 (above) and the micrographs of corresponding thermally etched samples in Figure 77 (below). With the exception of the NBT–90KTa sample, the density of the ceramic compacts sintered at 1150°C for 5 h was above 98% of the theoretical value. The fraction of the porosity is low and the size of the pores is mostly below 1 μm. The content of the secondary phases in samples with 5 to 70 mol% of KTa slightly increases with increasing KTa content; however, it stays below 2 vol%. In the sample NBT–90KTa sintered at 1230°C for 5 h (Figure 76f) the content of the bright secondary phase is around 2 vol% and the density around 92% of the theoretical density. The average grain size decreases with increasing KTa content and falls below 1 μm in the sample NBT–20KTa.

Samples with 5 to 70 mol% of KTa sintered at 1150°C were used for the electrical characterization. These samples show high density and low concentration of the secondary phases, thus the characteristics of the samples should predominantly depend on the properties of the matrix phase. Sample NBT–90KTa was excluded from further characterization due to its low density and the high content of the secondary phase.

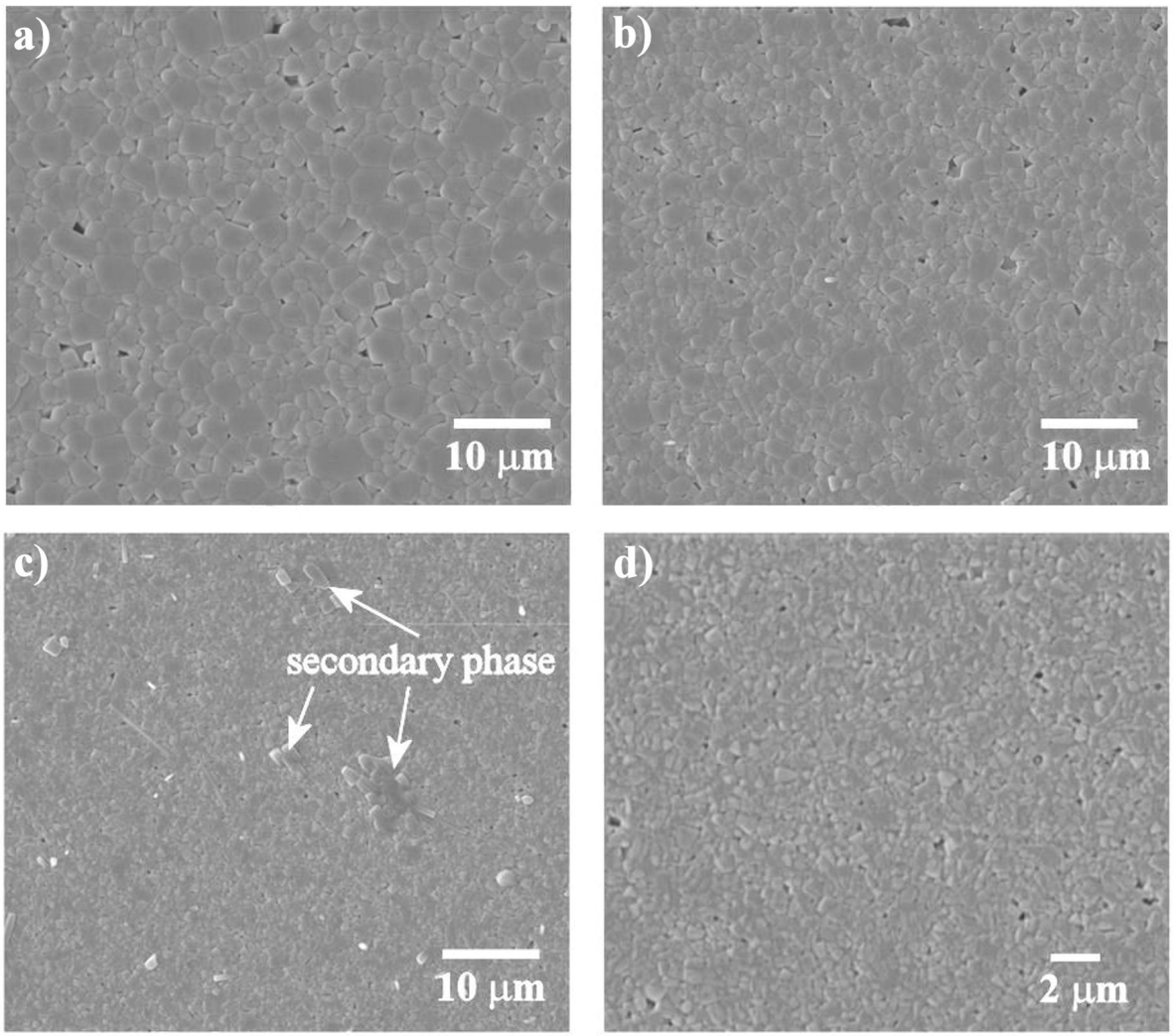

Figure 77: SEM micrographs of the etched samples from the NBT–KTa series prepared by the synthesis with high-temperature annealing: a) NBT–5KTa, b) NBT–20KTa, c) NBT–30KTa, d) NBT–50KTa.

4.3.3 Dielectric properties

The dielectric properties of the samples prepared by the synthesis with high-temperature annealing as well as the samples prepared by the preliminary synthesis were measured. The dielectric properties of the samples with 5 to 20 mol% of KTa, measured at room temperature and a frequency of 1 MHz, are shown in Table 5. The results show that samples prepared by the longer route have much higher dielectric constants and also higher dielectric losses (especially the samples with 10 and 20 mol% of KTa). The higher values of the permittivity indicate the higher polarizability of the polar nanoregions in samples prepared by the high-temperature annealing route compared to the preliminary prepared samples. The difference in the losses of the samples prepared by different routes could be ascribed to the lossy secondary phase [136], since the concentration of the secondary phase is higher in samples prepared by the high-temperature route. However, in the NBT–5KTa sample the difference in losses is minimal, despite the increase in the secondary-phase concentration. The increase of the loss tangent in samples with 10 and 20 mol% of KTa after high-temperature annealing could also be due to better homogenization of the matrix phase. The origin of the dielectric losses can be determined from the temperature dependence of the dielectric properties, and will be discussed below (page 94).

Table 5: Dielectric properties of samples from the NBT–KTa system; preliminarily prepared and prepared by the synthesis with high-temperature annealing.

Sample	Preliminary synthesis		Synthesis with high-temperature annealing	
	ε [/]	$tan\delta$ [/]	ε [/]	$tan\delta$ [/]
NBT–5KTa	456	0.055	878	0.056
NBT–10KTa	780	0.079	1288	0.092
NBT–20KTa	1156	0.096	1337	0.123

The temperature dependence of the dielectric properties of the preliminarily prepared samples is presented in Figure 78. For comparison the dielectric properties of pure NBT are added. With the addition of KTa the permittivity maximum decreases and the hump becomes less evident. The permittivity maximum is shifted toward lower temperatures as the KTa content increases, as expected for an incipient ferroelectric. However, the decreasing of the maximum is not continuous, since the maximum increases for the sample NBT–20KTa compared to the sample NBT–10KTa. Moreover, the maximum noticeably broadens with increasing KTa content. Within the measured frequency range the dielectric properties show a strong frequency dispersion of the permittivity, practically over the whole temperature range, indicating the relaxor nature of the materials. However, the frequency dispersion of the T_m is less evident than observed in a typical relaxor. A broad permittivity maximum and a rather undefined frequency dispersion of T_m indicate a non-homogeneous composition of the matrix phase, detected also by the XRD analysis. The existing polar nano-regions possess different T_m due to a different composition of the grains. Such a difference results in a broader dielectric maximum and an undefined frequency dispersion of T_m.

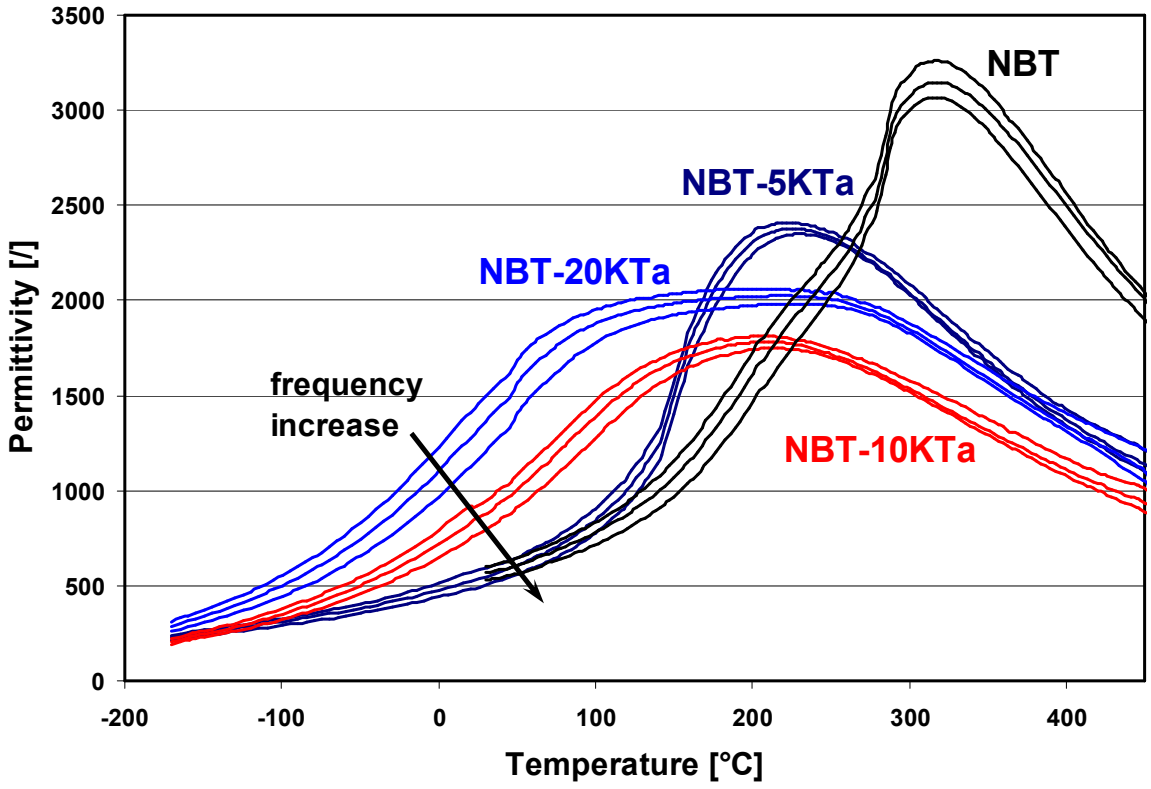

Figure 78: Temperature dependence of the relative permittivity of the preliminary prepared samples from the NBT–KTa series. The data were obtained at frequencies 10, 100 kHz, and 1 MHz.

The dielectric properties of the samples prepared by the high-temperature annealing route are shown in Figure 79. Some distinctive characteristics of the NBT–KTa system are:

- The dielectric maximum is reduced and shifted toward lower temperatures with increasing content of KTa.
- In the NBT–5KTa sample, a dielectric maximum and the frequency-dispersive anomaly are present. Their values of the permittivity are similar, resulting in a broad permittivity maximum.
- In samples with 10 and more mol% of KTa, only the frequency-dispersive anomaly is present.
- With increasing content of KTa, the room-temperature permittivity first increases and then starts to decrease. The highest value of the room-temperature permittivity is observed in sample NBT–20KTa.
- In sample NBT–30KTa the frequency-dispersed maximum is shifted into the room-temperature region.
- The dielectric maximum shows a strong frequency dispersion, which results in an anomaly in the dielectric losses.
- With increasing content of KTa, the maximum in the dielectric losses gradually decreases toward lower temperatures.
- In sample NBT–5KTa the dielectric loss maximum expands over a broad temperature range.

A comparison of the dielectric properties of materials prepared by different routes (Figure 78 and Figure 79) shows big differences. The relaxor characteristics of the materials are much more emphasized in the samples prepared by the high-temperature annealing route. The frequency dispersion of the dielectric maximum is distinct and the dispersion of the permittivity to the right of the maximum is minimized. Such behaviour is typical of a relaxor material. Moreover, the permittivity maximum continuously decreases with the increasing content of KTa and is shifted toward lower temperatures. The samples with 5 and 10 mol% of KTa have noticeably higher values of the permittivity maximum, compared to the preliminarily prepared samples. The observed changes in the dielectric properties indicate that the composition of the matrix phase is much more homogeneous after the high-temperature firings. This is in accordance with the XRD analysis that showed that the diffraction peaks were sharper after the multiple firings at high temperatures. In the samples prepared by the longer route, the local variations of the elements are more pronounced, leading to a distinct frequency dispersive permittivity maximum and a higher value of the permittivity compared to the preliminary prepared samples.

The dielectric losses of the samples from the NBT–KTa series prepared by the high-temperature annealing route are shown in Figure 79b. For all samples a strong temperature and frequency dependence (shown for sample NBT–20KTa) of the dielectric losses was observed. The temperature interval of the loss tangent maximum coincides with the temperature interval of the maximum frequency dispersion of the dielectric properties. The temperature and the value of the dielectric loss maximum increase as the measurement frequency increases, which are characteristics of relaxor materials. Thus, the results of the temperature dependence of the dielectric losses showed that a predominant part of the dielectric losses is attributed to the relaxational processes of the matrix phase. In the temperature range where no frequency dispersion is observed, the dielectric losses are small, below 0.01. Thereafter, the contribution of the $K_2Ti_6O_{13}$ secondary phase to the loss tangent is small.

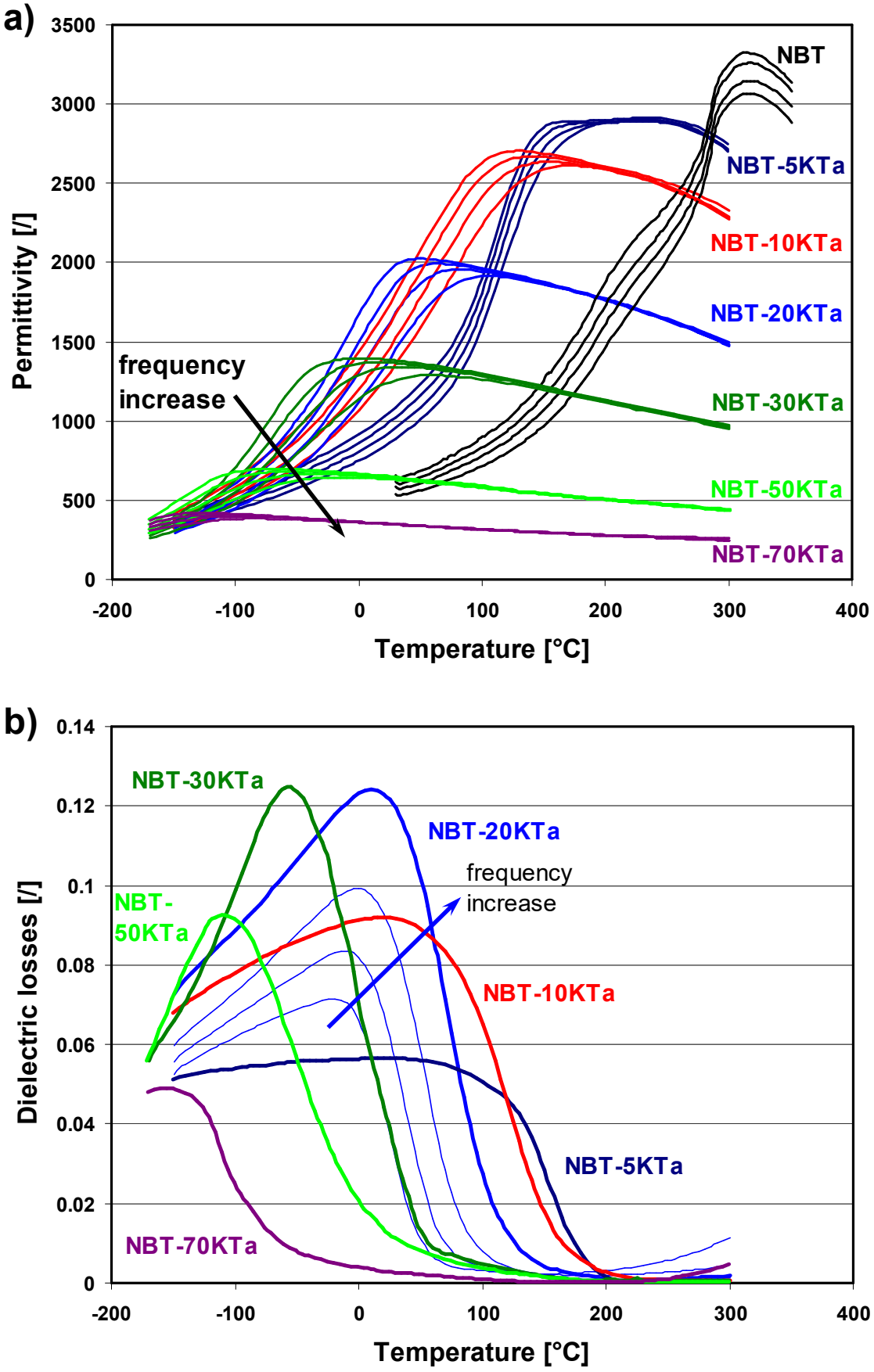

Figure 79: Temperature dependence of a) the relative permittivity and b) the dielectric losses of the samples from the NBT–KTa series. In a), the permittivity data obtained at frequencies 1, 10, 100 kHz, and 1 MHz are shown. In b), the dielectric losses at 1 MHz and, additionally, for sample NBT–20KTa at 1, 10 and 100 kHz are shown.

The temperature of the dielectric maximum (as observed in pure NBT at 320 °C) decreases faster than the temperature of the frequency-dispersive anomaly (at ~200°C in pure NBT). In the NBT–5KTa sample, both anomalies are present, forming a broad dielectric maximum at 220°C. On decreasing the temperature, the dielectric losses start to increase at 190°C and the loss maximum broadens over a wide temperature range. The broad loss maximum, ascribed to the stabilization of the rhombohedral phase, indicates gradual stabilization of the rhombohedral phase, which is not completed at room temperature. This is in accordance with the XRD results that showed symmetry in between the rhombohedral and cubic.

In sample NBT–10KTa only one anomaly is present. The permittivity maximum shifts closer to room temperature and the maximum of the dielectric losses is found in the room-temperature region. In a relaxor phase transition, the correlation and volume fraction of the polar nano-regions increase below the permittivity maximum. The position of the anomaly in the NBT–10KTa sample indicates that the rhombohedral regions are stable in the room-temperature region. However, the cubic matrix phase prevails, as seen from the XRD results that showed the cubic symmetry of the sample (Figure 75). In samples with 20 and 30 mol% of KTa the correlation between the rhombohedral regions as well as their size decreases, and the frequency-dispersive maximum is shifted into the room-temperature region. With larger additions of KTa, the dielectric maximum is shifted below room temperature. In these samples the size and the correlation of the rhombohedral regions strongly decrease.

The dielectric behaviour of the materials from the NBT–KTa system is typical for relaxor phase transitions. The transition from cubic phase to rhombohedral phase is shifted to lower temperatures with the addition of KTa as the stabilization of the rhombohedral phase is suppressed and extended to lower temperatures. The concentration, size and/or polarizability of the polar nanoregions existing in different compositions decrease, resulting in a decreasing value of the permittivity maximum.

The KTa additions to NBT increased the room-temperature permittivity and changed the properties of the materials to relaxor-like. Thereafter, an increase in the axial pressure effect on the permittivity at room temperature is expected. In particular, compositions with 10 to 30 mol% of KTa are interesting due to their high permittivity and the vicinity of the dielectric maximum.

4.3.4 Ferroelectric properties

The results of the ferroelectric measurements for samples from the NBT–KTa series are presented in Figure 80. A decreasing of P_r and E_c with the increasing content of KTa was observed. The shape of the hysteresis loops gradually changed from ferroelectric (5 mol% KTa) through relaxor (10 to 30 mol% KTa) to paraelectric (50 and more mol% of KTa).

With an increasing concentration of KTa, the content of the rhombohedral ferroelectric phase decreases, while the content of the cubic paraelectric phase increases. The temperature of the stabilization of the ferroelectric phase decreases and the polar order changes. In the sample with 5 mol% of KTa, the correlation of the rhombohedral domains remains high as the content of the cubic phase is small, thus a typical ferroelectric hysteresis is obtained. Such behaviour is in accordance with the dielectric and the XRD results of the NBT–5KTa sample. The permittivity maximum is located well above room temperature and the diffraction peaks are distorted from the cubic symmetry.

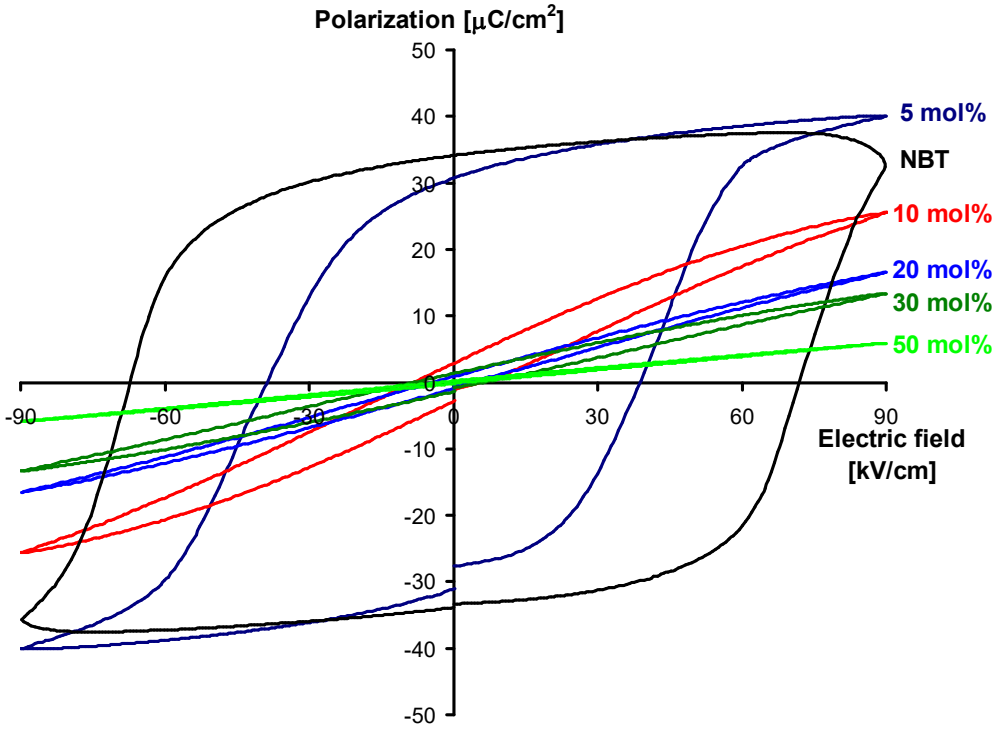

Figure 80: Polarization–electric field hystereses of samples from the NBT–KTa series. Measurements were performed at a frequency of 10 Hz.

In sample with the 10 mol% addition of KTa, slim ferroelectric hysteresis with small P_r and relatively high P_{sat}, characteristic of relaxors, is observed. The small value of the spontaneous polarization is ascribed to the small content of the rhombohedral regions, which are not correlated. Although the cubic symmetry of the sample was observed by XRD analysis, the dielectric properties indicated the existence of stable rhombohedral regions. Due to the presence of the rhombohedral regions, P_{sat} is relatively high as the polarization of the regions increases in proportion to the applied electric field.

In samples with 20 and 30 mol% of KTa, the content and size of the rhombohedral regions decreases, which results in a smaller value of P_{sat}. The shape of the hysteresis retains the relaxor properties. Relaxor properties are supported by the dielectric measurements, as the permittivity maximum is located in the room-temperature region. The rhombohedral regions are small and their content is low, therefore, the XRD analysis showed cubic symmetry of the samples. In samples with 50 and 70 mol% of KTa, the size and volume fraction of the rhombohedral regions further decreases. Thereafter, the contribution of the rhombohedral regions to the polarization at room temperature is small, and a typical linear paraelectric hysteresis is observed. Such behaviour is in accordance with the dielectric measurements, where a shift of the permittivity maximum below room temperature in samples with 50 and 70 mol% of KTa was observed.

Additions of KTa decrease the coercive field and induce relaxor behaviour in the materials. According to the theory, an increase in the axial pressure effect on the permittivity in materials with KTa additions is expected. In particular, samples with 10 to 30 mol% of KTa are interesting for the investigation of the stress dependence of the permittivity.

4.3.5 Uniaxial stress dependence of the permittivity

The influence of the uniaxial stress on the permittivity was tested on samples prepared by a synthesis with high-temperature annealing. The stress dependence of the permittivity for the NBT–5KTa sample is shown in Figure 81. The response to the applied stress is similar to

that observed in the NBT–NTa samples. Decreasing of the permittivity with increasing stress, irreversible change, a difference between the first and the second loading/unloading cycle and time dependence under constant pressure were observed. These features indicate the existence of a domain structure within the material, which is in accordance with the XRD, dielectric and ferroelectric measurements. The average symmetry of the sample is distorted from cubic, the frequency dependent maximum is well above room temperature and the hysteresis measurements showed the ferroelectric nature of the sample. Therefore, the change in the domain structure after the stress release is mainly preserved and the irreversible change is observed.

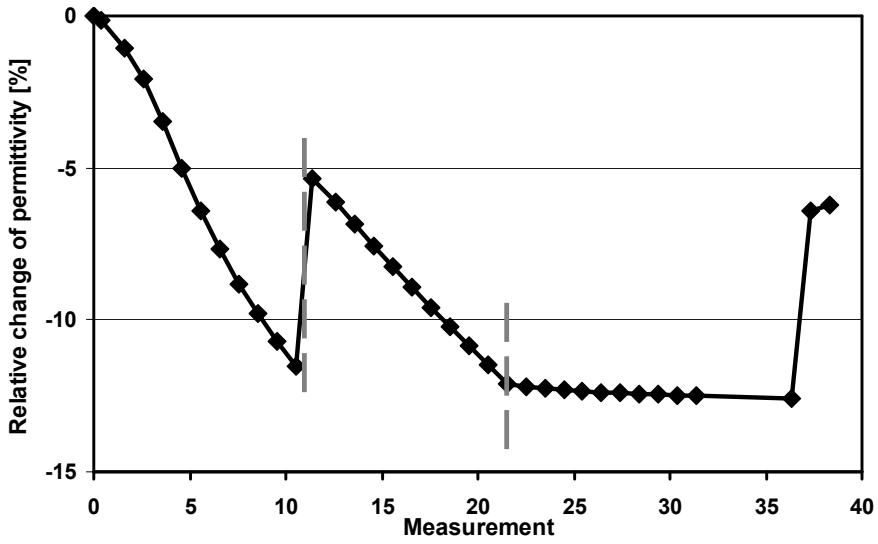

Figure 81: Relative change of the permittivity at 1 MHz during the stress testing of the NBT–5KTa sample. The starting value of the permittivity was 854.3, and the values of the pre-stress and the maximum stress were 8 and 212 MPa, respectively.

With increasing content of KTa, the dielectric maximum shifts toward lower temperatures, therefore, a change in the character of the dielectric response to the applied stress from ferroelectric-like (irreversible) to paraelectric-like (reversible) was expected. The results of the pressure dependence of the permittivity for the NBT–10KTa sample are shown in Figure 82. Important differences compared to the sample NBT–5KTa are:

- the permittivity–stress dependence in the first cycle is almost linear,
- the irreversible change is very small,
- the relaxations under constant pressure are reduced.

Similar behaviour was observed in the samples with larger contents of KTa. The results for the samples from the NBT–KTa series for the first and second stress cycle are collected in Figure 83 (difference between the values of the permittivity at a pressure of 8 and 214 MPa). The change in the permittivity of the samples with 5 to 30 mol% of KTa was 80–104 at a measuring frequency of 1 MHz; however, almost a half of the change in the sample NBT–5KTa was irreversible. The relative change in the samples with 10 to 30 mol% of KTa was around 7% and only a fraction of this change was irreversible, when the sample was held under the pre-stress of ~8 MPa. However, when the pre-stress was removed, a further back relaxation (designated in Figure 82) equal to the irreversible change was observed. Thus, the virgin properties of the samples were fully restored. A small, irreversible change observed in samples with 10 to 30 mol% of KTa ascribed to the dynamics of the rhombohedral nanoregions since the dielectric maximum is located at or above room-temperature region. In

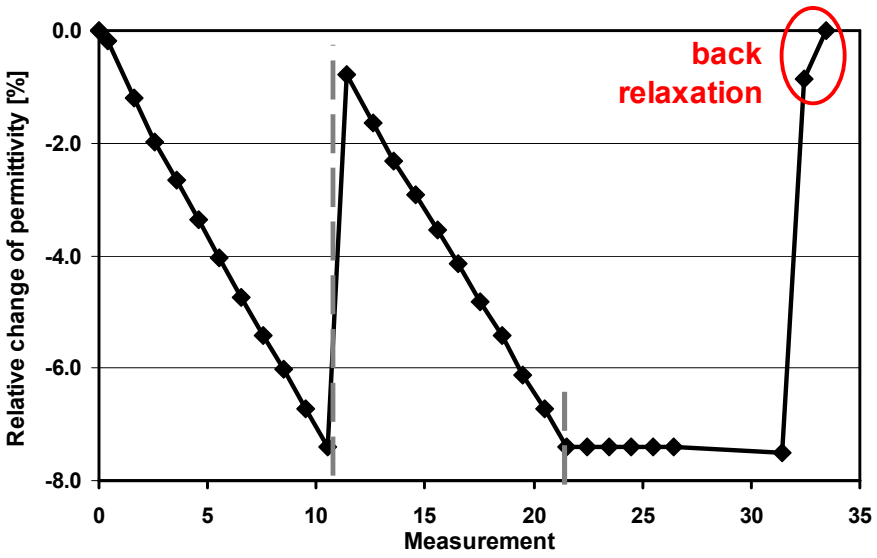

Figure 82: Relative change of the permittivity at 1 MHz during the stress testing of the NBT–10KTa sample. The starting value of the permittivity was 1218.5, and the values of the pre-stress and the maximum stress were 8 and 212 MPa, respectively.

the region slightly below the permittivity maximum, relaxors show a stress response similar to paraelectrics, i.e., an instantaneous and reversible response to the stress; however, minor relaxations can be observed [63]. Samples with 50 and 70 mol% of KTa showed the complete reversibility of the dielectric properties, as expected for paraelectric materials.

The improvement of the reversibility can be explained by the observed relaxor properties of materials with 10 to 30 mol% of KTa. With increasing content of KTa, the concentration and size of the rhombohedral regions as well as their correlation decrease. Thus, the polar nanoregions can reorientate back into the equilibrium, i.e., initial, position after the stress removal. The reorientation results in the reversibility of the dielectric properties. In contrast, in a ferroelectric material the domains switch into a new equilibrium position under the applied stress. The new orientation is then preserved when the stress is removed. Thereafter, the domain structure is modified, resulting in an irreversible change of the dielectric properties.

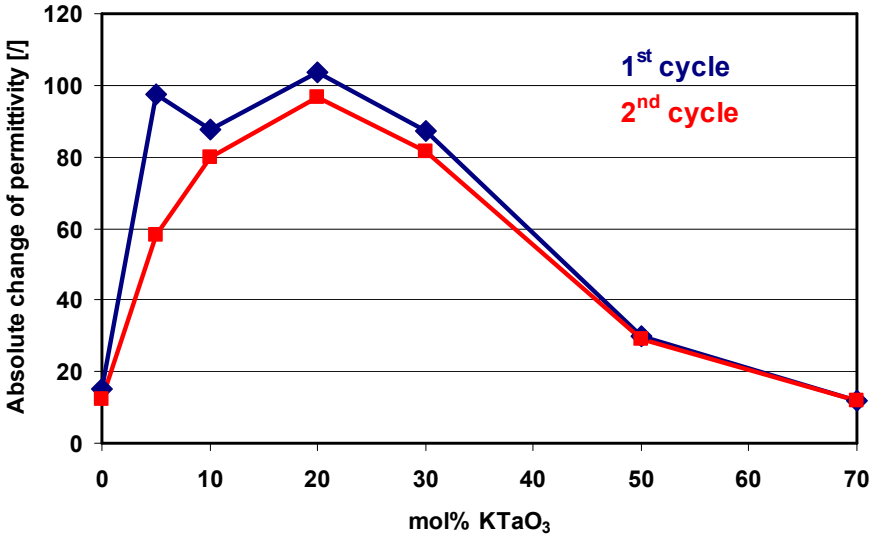

Figure 83: Absolute change of the permittivity with an increase of pressure from 8 to 214 MPa in the first and second stress cycles for samples from the NBT–KTa series; measuring frequency – 1MHz.

The sample NBT–20KTa showed the highest value of the permittivity change, accompanied by a remarkable reversibility. Therefore, a multiple-stress-cycle experiment was performed on this sample. The results are shown in Figure 84. A small difference between the first and the second cycle was observed. From the second stress cycle onward the difference between the cycles is extremely small and this subsequently decreases with every additional cycle. The deviation from the reversibility at the beginning and the end of the experiment is ascribed to a minor relaxation of the material that appears when the pre-stress is removed, as discussed above. If the material is kept under a small pre-stress (~8 MPa in this study), the relaxations are hindered and the reversibility is attained.

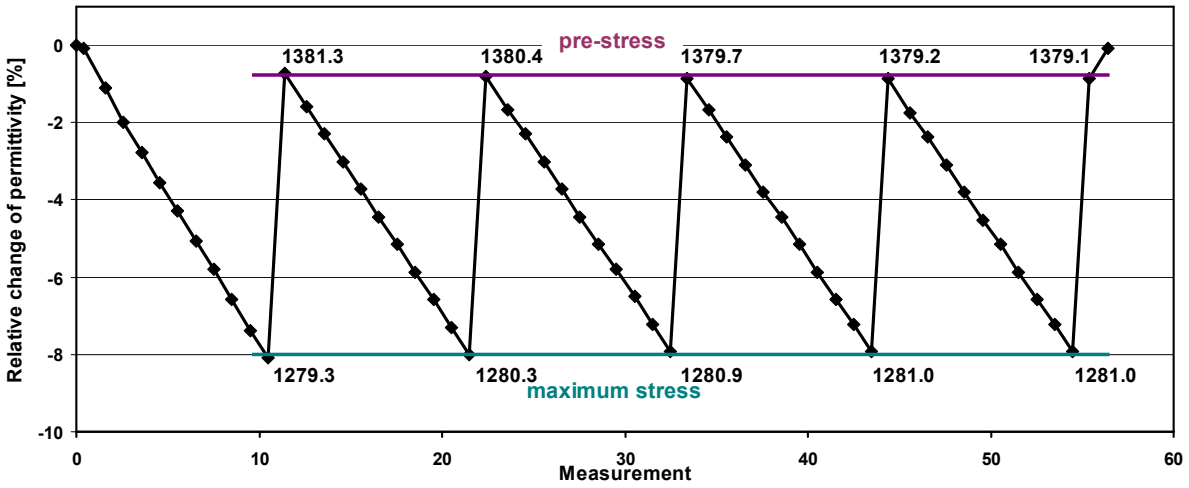

Figure 84: Reversibility test of the permittivity at 1 MHz under cycling axial pressure for sample NBT–20KTa, showing the relative change of the permittivity. The starting and final values of the permittivity were 1391.8 and 1386.2, respectively. The values of the pre-stress and the maximum stress were 8 and 219 MPa, respectively. The numbers correspond to the permittivity at pre-stress and maximum stress for separate stress cycle.

One important issue of the multiple stress cycle test presented in Figure 84 is that in the first two cycles the load was increased in a 1-minute interval and in the next three cycles in a ½-minute interval. Such behaviour shows that the relaxational processes are reduced and indicates an instantaneous response to the applied stress, which was not seen for the ferroelectric/ferroelastic materials.

In samples with a frequency dispersion of the dielectric constant near room temperature, i.e., samples with 10 to 30 mol% of KTa, a strong influence of the measuring frequency on the pressure dependence of the permittivity was observed. The absolute and the relative change of the permittivity at 200 MPa for these samples are shown in Table 6, for measuring frequencies of 1 kHz and 1 MHz. The relative change of the permittivity increased as the measuring frequency decreased. The absolute change of the permittivity at lower frequencies is additionally increased due to a higher dielectric constant at lower frequencies (see the dielectric properties in Figure 79a). The biggest absolute change in the permittivity at a pressure of 200 MPa was found for the NBT–20KTa sample at a frequency of 1 kHz, i.e. 221.5. The results of the stress dependence of the permittivity for the NBT–20KTa sample at 1 kHz and 1 MHz are shown in Figure 85. No changes to the characteristics of the response to the applied stress were observed, except the higher sensitivity at lower measuring frequency.

Materials from the NBT–KTa system exhibit dielectric properties typical of relaxors. Also, their behaviour under the applied stress is characteristic of relaxors. According to the report of Steiner *et al*. [63], the response of relaxor materials to the stress can be classified into three zones, depending on the position of the permittivity maximum. Well below the

Table 6: Absolute and relative change of the permittivity at 200 MPa for virgin samples from the NBT–KTa series at 1 kHz and 1 MHz.

Sample, mol% NTa	Absolute change $\Delta\varepsilon$ [/] 0–200 MPa		Relative change $\Delta\varepsilon/\varepsilon$ [%] 0–200 MPa	
	1 kHz	1MHz	1 kHz	1MHz
NBT	25.2	14.5	4.2	3.0
5	137.7	124.3	14.0	11.0
10	158.4	85.5	9.8	7.0
20	221.5	96.5	11.2	7.2
30	110.0	82.5	8.2	6.8
50	31.2	29.4	5.0	4.8
70	13.1	13.2	6.4	6.4

permittivity maximum (low-temperature zone), the materials exhibit similar behaviour as observed in ferroelectric materials. Such behaviour is also observed in canonical relaxors (e.g., PMN), which show no spontaneous phase transition even at temperatures well below the permittivity maximum [63][6]. In canonical relaxors, the ferroelectric behaviour is induced by an applied stress, similar to that observed in an electric field [137]. In the intermediate zone that includes the temperature region of the frequency dispersion and ends around the temperature of the permittivity maximum, minor relaxations are observed after the stress application or release. Above the temperature of the permittivity maximum (high-temperature zone) the material exhibits linear and reversible behaviour, similar to materials in the paraelectric phase. With the increasing content of KTa, the properties of the materials change from paraelectric through relaxor-like to paraelectric. Thereafter, different compositions can be classified into different zones, according to the permittivity response to the applied stress. Sample NBT–5KTa is classified into the low-temperature zone, samples with 10 to 30 mol% of KTa into the intermediate-temperature zone, and samples with higher content of KTa into the high-temperature zone.

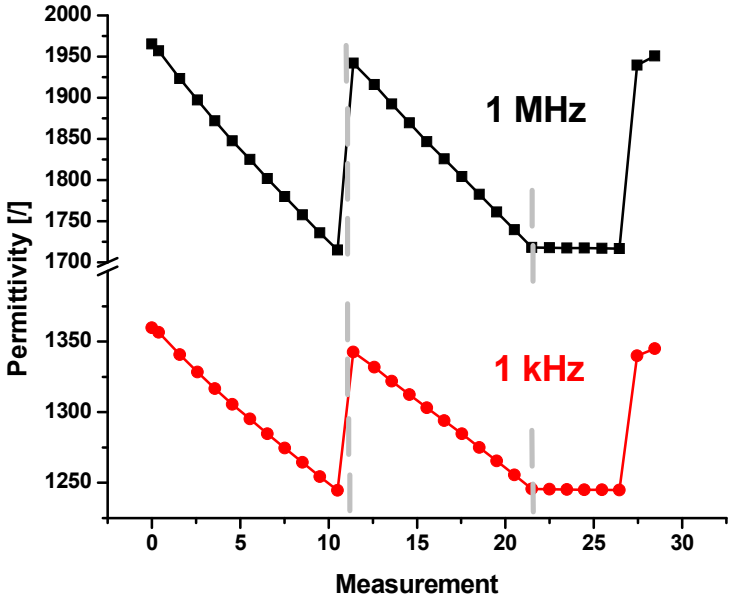

Figure 85: Axial pressure dependence of the permittivity for sample NBT–20KTa at 1 kHz and 1 MHz. The starting values of the permittivity were 1965.4 and 1359.7, respectively, and the values of the pre-stress and the maximum stress were 8 and 219 MPa, respectively.

Compared to the NBT–NTa system, materials from the NBT–KTa system exhibit better properties with regard to their applicability for pressure sensors. The properties of the

compositions with the highest sensitivity from both systems, i.e., NBT–15NTa and NBT–20KTa, are compared in Table 7. The NBT–20KTa sample shows a higher permittivity and absolute change in the permittivity at a frequency of 1 kHz. Its relaxor character results in a remarkable reversibility under cycling pressure. The absence of a macroscopic domain structure eliminates the poling procedure required for the activation of the material as well as the possible depolarization and ageing problems, as known from the piezoelectric applications [18].

Table 7: Comparison of the properties of samples NBT–15NTa and NBT–20KTa, at a frequency of 1 kHz.

Sample	ε [/] at 1 kHz	$\Delta\varepsilon$ [/] 0–200 MPa at 1 kHz	$\Delta\varepsilon/\varepsilon$ [%] 0–200 MPa at 1 kHz	Poling	Reversibility
NBT–15NTa	970	143.7	14.8	227 MPa, 24 h	good but time dependent
NBT–20KTa	1948.1	221.5	11.4	/	good

According to the results of the axial pressure effect on the permittivity at room temperature, materials with 10 to 30 mol% of KTa have potential applicability in pressure-sensor technology. In these materials the highest stress dependence of the permittivity was observed among the materials tested in this study. The relaxor structure of the materials from the NBT–KTa system results in an instantaneous response to the applied stress and the improved reversibility of the permittivity under cycling pressure.

4.3.6 Summary

KTa was added to NBT in order to shift the dielectric maximum toward lower temperatures and, thus, increase the influence of the axial pressure on the permittivity. The XRD and SEM analyses showed the formation of a solid solution across the whole concentration range. However, potassium poly-titanate secondary phases were formed during the synthesis. Additionally, the matrix phase was not homogeneous even after the sintering stage. To improve the homogeneity of the matrix phase multiple firings at high temperature were applied. With increasing content of KTa, the dielectric maximum shifted toward lower temperatures and decreased, while the room-temperature permittivity first increased and then started to decrease, with a maximum value in the sample NBT–20KTa (1340). The polarization–electric field hystereses gradually changed from ferroelectric (5 mol% KTa) through relaxor (10 to 30 mol% KTa) to paraelectric (50 to 70 mol% KTa). In the sample NBT–5KTa similar features of the permittivity response to the applied axial pressure as in the NBT–NTa materials were observed, consistent with its ferroelectric character. In samples with a larger addition of KTa, the response changed: a linear decrease of the permittivity with increasing stress was observed and the irreversible change was reduced. The permittivity response to the stress was instantaneous and reversible. In samples with 10 to 30 mol% of KTa, only minor relaxations were observed, which were suppressed under a small pre-stress. Such behaviour is in accordance with the changing of the character of the materials to relaxor-like and then, at an even higher KTa content, to paraelectric. The highest change of the permittivity at 200 MPa was observed in the sample NBT–20KTa, equal to 11.4% relative or 221.5 in absolute value at a measuring frequency of 1 kHz. The sample also showed a remarkable reversibility when it was held under a small pre-stress. According to the high value of the permittivity, the associated pressure dependence and the reversibility under cycling pressure, samples with 10 to 30 mol% of KTa possess the highest applicability for pressure sensing among all the tested compositions in this investigation.

5 Conclusions

5.1 $Na_{0.5}Bi_{0.5}TiO_3$–$NaTaO_3$

In the $Na_{0.5}Bi_{0.5}TiO_3$–$NaTaO_3$ system, a solid solution forms between $Na_{0.5}Bi_{0.5}TiO_3$ and $NaTaO_3$ across the whole concentration range. Mainly single-phase ceramic samples were prepared by the solid-state reaction method. The addition of $NaTaO_3$ destabilizes the rhombohedral phase and shifts the phase transitions toward lower temperatures. Such an influence is ascribed to the incipient ferroelectric properties of $NaTaO_3$. The destabilization of the rhombohedral phase results in a decreasing of the temperature of the morphotropic phase boundary and the concentration and/or polarizability of the polar nanoregions. Such behaviour influences the properties of the frequency-dispersive anomaly and the dielectric maximum as well as the polar order of the material at room temperature.

5.2 $Na_{0.5}Bi_{0.5}TiO_3$–$K_{0.5}Bi_{0.5}TiO_3$

Like in the $Na_{0.5}Bi_{0.5}TiO_3$–$NaTaO_3$ system, a solid solution forms between $Na_{0.5}Bi_{0.5}TiO_3$ and $K_{0.5}Bi_{0.5}TiO_3$ across the whole concentration range. However, a small amount of a potassium poly-titanate secondary phase is formed during the synthesis. In pure $K_{0.5}Bi_{0.5}TiO_3$ the volatilization of potassium and bismuth oxides appears already during the calcination stage. During the sintering stage, thermal decomposition of the matrix phase is accelerated and the volatilization is further increased, which influences the microstructural properties and sintering behaviour of $K_{0.5}Bi_{0.5}TiO_3$. The volatilization induces a shift of the nominal composition to a composition within the corresponding three-phase region and, consequently, secondary phases are formed: $K_2Ti_6O_{13}$ and a Bi-rich ternary phase. The formed matrix phase is non-stoichiometric compared to the nominal $K_{0.5}Bi_{0.5}TiO_3$, with a deficit of potassium and an excess of bismuth.

The reason for the potassium poly-titanate phase formation in the $Na_{0.5}Bi_{0.5}TiO_3$–$K_{0.5}Bi_{0.5}TiO_3$ compositions is believed to be the same as observed in pure $K_{0.5}Bi_{0.5}TiO_3$. With decreasing content of $K_{0.5}Bi_{0.5}TiO_3$ the concentration of the secondary phase slowly decreases. The morphotropic phase boundary in $Na_{0.5}Bi_{0.5}TiO_3$–$K_{0.5}Bi_{0.5}TiO_3$ system is located around the composition with 20 mol% of $K_{0.5}Bi_{0.5}TiO_3$. The dielectric anomaly connected with the phase transition to the ferroelectric phase stays well above the room temperature, thus all the compositions exhibit ferroelectric properties at room temperature. The addition of $K_{0.5}Bi_{0.5}TiO_3$ decreases the coercive field by approximately 50%.

5.3 $Na_{0.5}Bi_{0.5}TiO_3$–$KTaO_3$

A solid solution forms across the whole concentration range also in the $Na_{0.5}Bi_{0.5}TiO_3$–$KTaO_3$ system. Like in the $Na_{0.5}Bi_{0.5}TiO_3$–$K_{0.5}Bi_{0.5}TiO_3$ system, a potassium poly-titanate secondary phase is formed during the synthesis. A homogeneous composition of the matrix phase is only observed after multiple high-temperature annealing steps. The homogeneity of the matrix phase strongly influences the dielectric properties. On the other hand, annealing at high temperature increases the volatilization, resulting in a higher content

of the secondary phase. However, the influence of the secondary phase on the dielectric properties seems to be small. The addition of $KTaO_3$ destabilizes the rhombohedral phase and shifts the dielectric anomalies toward lower temperatures, as expected for an incipient ferroelectric. It induces typical relaxor behaviour of the material, which is reflected in the dielectric and ferroelectric properties.

5.4 Uniaxial stress dependence of the permittivity

In contrast to the reports found in the literature, a complex response to the applied stress was observed in $Na_{0.5}Bi_{0.5}TiO_3$, which includes decreasing of the permittivity with increasing stress, a difference between successive stress cycles, relaxation under constant pressure and an irreversible change of the permittivity after stress removal. Such behaviour is believed to be connected with the ferroelectric domain structure of the material. Under the applied stress, non-180° domain switching appears, which irreversibly changes the domain structure of the materials. When the stress is removed, the material remains in a mechanically polarized state, showing a smaller value of the permittivity than in the virgin state. Due to the rigidness of the ferroelectric domain structure the switching processes are relaxational in nature, which can be seen from the slow stabilization of the permittivity under constant pressure.

Identical behaviour was found for samples from the whole range of the solid solution between $Na_{0.5}Bi_{0.5}TiO_3$ and $NaTaO_3$. The relative change of the permittivity, at an axial pressure of 200 MPa and a frequency of 1 MHz, increased from 3% in pure $Na_{0.5}Bi_{0.5}TiO_3$ to a maximum of 14% in the sample with 15 mol% of $NaTaO_3$. The untypical behaviour of the paraelectric compositions from the $Na_{0.5}Bi_{0.5}TiO_3$–$NaTaO_3$ system is due to the ferroelastic properties of the materials. A considerable improvement in the reversibility was attained by a mechanical polarization of the samples before the stress testing. However, the response of the polarized material to the applied stress is time dependent and, thus, the potential applicability of materials from the $Na_{0.5}Bi_{0.5}TiO_3$–$NaTaO_3$ solid-solution system in pressure sensing is rather small.

A similar response to the applied stress as in the $Na_{0.5}Bi_{0.5}TiO_3$–$NaTaO_3$ system was observed for a sample with a small addition, i.e., 20 mol%, of $K_{0.5}Bi_{0.5}TiO_3$. With higher additions of $K_{0.5}Bi_{0.5}TiO_3$ the response to the axial pressure changed: the permittivity increased under a small applied pressure. Such behaviour is believed to be connected with an internal defect structure that pins the domain structure of the material and, thus, changes the material's response to the applied stress. When a specific critical stress value is exceeded, the relation between the domain and defect structures irreversibly changes. This results in a more conventional decrease of the permittivity with increasing stress. The frequency dependence of the permittivity also results in the frequency dependence of the permittivity under the applied stress. The stress sensitivity is higher at a lower measuring frequency, resulting in a lower critical stress value observed at a lower measuring frequency. Due to the complex response to the applied stress the applicability of these materials for pressure sensing is small.

In the sample with 5 mol% of $KTaO_3$, similar behaviour as in the $Na_{0.5}Bi_{0.5}TiO_3$–$NaTaO_3$ system was observed, consistent with its ferroelectric character. With larger additions of $KTaO_3$, the irreversible change of the permittivity after the stress cycle strongly decreases. These samples exhibit typical relaxor properties, indicating a relaxor structure with stable rhombohedral nanoregions dispersed over the volume of a cubic non-polar matrix. Since the correlation of the polar nanoregions is small they are more free to move and can reorient back into the equilibrium position when the stress is removed. With increasing the content of $KTaO_3$ the stabilization of the rhombohedral regions shifts toward lower temperatures, and the number, size and correlation of the nanoregions at room temperature decrease. Thereafter, the irreversible change decreases and finally disappears when the dielectric maximum is

shifted below room temperature. The dynamics of the polar nanoregions are strongly frequency dependent, and therefore a strong influence of the measuring frequency on the stress sensitivity is observed.

The relaxor nature of the material, with the rhombohedral regions that are dispersed in a cubic matrix, results in the reversibility of the dielectric properties under cycling pressure. This eliminates the pre-use poling procedure required for activation of the material as well as the depolarization and ageing processes, inherent to the materials with a macroscopic domain structure. Taking into consideration the increased permittivity and sensitivity at a lower measuring frequency, the relaxor materials from the $Na_{0.5}Bi_{0.5}TiO_3$–$KTaO_3$ system have potential applicability in pressure-sensor technologies.

6 Acknowledgements

First, I would like to thank my supervisor, Prof. Dr. Danilo Suvorov, for giving me an opportunity to conclude my education with a doctoral degree, for his guidance in my work and for his constant support and encouragement.

Special thanks to my co-supervisor, Dr. Boštjan Jančar, for his constructive suggestions and scientific discussions. I would also like to thank him for the time he spent reading and correcting my manuscripts.

Thanks to Dr. Matjaž Spreitzer for the helpful discussions that solved many problems and produced numerous ideas.

I would like to thank all the Ph.D. students and support stuff of the Advanced Materials Department for creating a pleasant working environment. Thanks to Mr. Aleksander Figelj for the software and hardware support for the electrical measurements and to colleagues from the neighbouring departments that helped me with equipment and measurements.

Thanks to Prof. Dr. Mari-Ann Einarsrud and Dr. Julian Tolchard from the Norwegian University for help with the ferroelastic measurements.

I am also indebted to my thesis committee: Prof. Dr. Boštjan Zalar, Prof. Dr. Zdravko Kutnjak and Prof. Dr. Klaus Reichmann.

Finally, I would like to thank my family for giving me an opportunity to study and for their support of my decisions. Last, but not least, very special thanks to my wife, Katja, for her encouragement, support and patience.

7 References

1 Uchino, K. *Ferroelectric Devices* (Marcel Dekker, New York, 2000).

2 Kamlah, M. Ferroelectric and ferroelastic piezoceramics – modeling of electromechanical hysteresis phenomena. *Continuum Mechanics and Thermodynamics* **13**, 219-268 (2001).

3 Ristic, L. (ed.) *Sensor technology and devices* (Artech House, London, 1994).

4 Uchino, K.; Nomura, S.; Cross, L. E.; Jang, S. J.; Newnham, R. E. Pressure gauge using relaxor ferroelectrics. *Japanese Journal of Applied Physics* **20**, L367-L370 (1981).

5 Lines, M. E.; Glass, A. M. *Principles and Applications of FE and Related Materials* (Clarendon Press, Oxford, 1979).

6 Devonshire, A. F. Theory of ferroelectrics. *Advances in Physics* **2**, 85-130 (1954).

7 Hahn, T. (ed.) *International Tables For Crystallography: A – Space-Group Symmetry* (Llewer Academic Publications, London, 1996).

8 Jaffe, B.; Cook, W. R.; Jaffe, H. *Piezoelectric Ceramics* (Academic Press, London, 1971).

9 Lynch, C. S. The effect of uniaxial stress on the electro-mechanical response of 8/65/35 PLZT. *Journal of Intelligent Materials Systems Structures* **6**, 191-198 (1996).

10 Zhang, Q.M.; Pan, W. Y.; Jang, S. J.; Cross, L.E. Domain wall excitations and their contributions to the weak-signal response of doped lead zirconate titanate ceramics. *Journal of Applied Physics* **64**, 6445 (1988).

11 Damjanovic, D.; Demartin, M. Contribution of the irreversible displacement of domain walls to the piezoelectric effect in barium titanate and lead zirconate titanate ceramics. *Journal of Physics: Condensed Matter* **9**, 4943-4953 (1997).

12 Koch, R. The intrinsic stress of polycrystalline and epitaxial thin metal-films. *Journal of Physics: Condensed Matter* **6**, 9519-9550 (1994).

13 Mitchel, R. H. *Perovskites: Modern and Ancient* (AlmazPress, Ontario, 2002).

14 Aizu, K. Possible species of 'ferroelastic' crystals and of simultaneously ferroelectric and ferroelastic crystals. *Journal of the Physical Society of Japan* **27**, 387-396 (1969).

15 E. K. H. *Phase transitions in ferroelastic and co-elastic crystals* (Cambridge University Press, Cambridge, 1993).

16 Fotinich, Y.; Carman, G. P. Stresses in piezoceramics undergoing polarization switchings. *Journal of Applied Physics* **88**, 6715-6725 (2000).

17 Mitsui, T.; Nomura, S. *Landolt-Börnstein, Group III: Crystal and Solid State Physics 16* (Spreinger-Verlag, Berlin, 1981).

18 Setter, N. (ed.) *Piezoelectric Materials in Devices* (EPFL, Lausanne, 2002).

19 Bokov, A. A.; Ye, Z. G. Recent progress in relaxor ferroelectrics with perovskite structure. *Journal of Materials Science* **41**, 31-52 (2006).

20 Kirillov, V. V.; Isupov, V.A. Relaxation polarization of $PbMg_{1/3}Nb_{2/3}O_3$(PMN) - ferroelectric with a diffused phase-transition. *Ferroelectrics* **5**, 3-9 (1973).

21 Stenger, C. G. F.; Burggraaf, A. J. Order-disorder reaction in the ferroelectric perovskites $Pb(Sc_{1/2}Nb_{1/2})O_3$ and $Pb(Sc_{1/2}Ta_{1/2})O_3$. *Physica Status Solidi A* **61**, 653-664 (1980).

22 Davies, P.K.; Akbas, M. A. Chemical order in PMN-related relaxors: structure, stability, modification, and impact on properties. *Journal of Physics and Chemistry of Solids* **61**, 159-166 (2000).

23 Mendoza, M. E.; Pelaiz-Barranco, A.; Garcia-Zaldivar, O.; Lopez-Noda, R.; Calderon-Pinar, F. Domain structure in relaxor PLZT ceramics. *Ferroelectrics* **334**, 35-42 (2006).

24 Yasuda, N.; Ohwa, H.; Asano, S. Dielectric properties and phase transitions of $Ba(Ti_{1-x}Sn_x)O_3$ solid solution. *Japanese Journal of Applied Physics* **35**, 5099-5103 (1996).

25 Guerra, J. D. S.; Venet, M.; Garcia, D.; Eiras, J. A.; Guerrero, F. Dielectric properties of $PbNb_2O_6$ ferroelectric ceramics at cryogenic temperatures. *Applied Physics Letters* **91**, 062915 (2007).

26 Yoshida, M.; Mori, S.; Yamamoto, N.; Uesu, Y.; Kiat, J. M. TEM observation of polar domains in relaxor ferroelectric $Pb(Mg_{1/3}Nb_{2/3})O_3$. *Ferroelectrics* **217**, 327-333 (1998).

27 Jin, H.Z., Zhu, J.; Miao, S.; Zhang, X. W.; Cheng, Z. Y. Ordered domains and polar clusters in lead magnesium niobate $Pb(Mg_{1/3}Nb_{2/3})O_3$. *Journal of Applied Physics* **89**, 5048-5052 (2001).

28 Bokov, A.A.; Leshchenenko, M. A.; Malitskaya, M. A.; Raevski, I. P. Dielectric spectra and Vogel-Fulcher scaling in $Pb(In_{0.5}Nb_{0.5})O_3$ relaxer ferroelectric. *Journal of Physics: Condensed Matter* **11**, 4899-4911 (1999).

29 Cohen, R.E. Origin of ferroelectricity in perovskite oxides. *Nature* **358**, 136-138 (1992).

30 Boneneau, P.; Garnier, P.; Husson, E.; Morell, A. Structural study of PMN ceramics by x-ray-diffraction between 297-K and 1023-K. *Materials Research Bulletin* **24**, 201-206 (1989).

31 Boneneau, P.; Garnier, P.; Calvarin, G.; Husson, E.; Gavarri, J. R.; Morell, A. X-ray and neutron-diffraction studies of the diffuse phase-transition in $PbMg_{1/3}Nb_{2/3}O_3$ ceramics. *Journal of Solid State Chemistry* **91**, 350-361 (1991).

32 Vakhrushev, S.; Zhukov, S.; Fetisov, G.; Chernyshov, V. The high-temperature structure of lead magnoniobate. *Journal of Physics: Condensed Matter* **6**, 4021-4026 (1994).

33 Shuvaeva, V.A.; Pirog, I.; Azuma, Y.; Yagi, K.; Sakaue, K.; Terauchi, H.; Raevskii, I. P.; Zhuchkov, K.; Antipin, Y. U. The local structure of mixed-ion perovskites. *Journal of Physics: Condensed Matter* **15**, 2413-2421 (2003).

34 Burns, G.; Dacol, F. H. Glassy polarization behavior in ferroelectric compounds $Pb(Mg_{1/3}Nb_{2/3})O_3$ and $Pb(Zn_{1/3}Nb_{2/3})O_3$. *Solid State Communications* **48**, 853-856 (1983).

35 Viehland, D.; Xu, Z.; and Payne, D. A. Origin of f spots and stress sensitivity in lanthanum lead-zirconate-titanate. *Journal of Applied Physics* **74**, 7454-7460 (1993).

36 Glinchuk, M.D.; Farhi, R. A random field theory based model for ferroelectric relaxors. *Journal of Physics: Condensed Matter* **8**, 6985-6996 (1996).

37 Bokov, A.A.; Bing, Y. H.; Chen, W.;Ye, Z. G.; Bogatina, S. A.; Raevskii, I. P.; Raevskaya, S. I.; Sahkar, E. V. Empirical scaling of the dielectric permittivity peak in relaxor ferroelectrics. *Physical Review B* **68**, 052102 (2003).

38 Viehland, D.; Jang, S. J.; Cross, L. E.; Wuttig, M. Freezing of the polarization fluctuations in lead magnesium niobate relaxors. *Journal of Applied Physics* **68**, 2916-2921 (1990).

39 Vugmeister, B. E., Rabitz, H. Dynamics of interacting clusters and dielectric response in relaxer ferroelectrics. *Physical Review B* **57**, 7581-7585 (1998).

40 Blinc, R.; Bobnar, V.; Pirc, R. Coupled spherical pseudospin-phonon model and the pressure-temperature phase diagram of relaxor ferroelectrics. *Physical Review B* **64**, 132103 (2001).

41 Glazounov, A. E.; Tagantsev, A. K. A "breathing" model for the polarization response of relaxer ferroelectrics. *Ferroelectrics* **221**, 57-66 (1999).

42 Baerwald, H.G. Thermodynamic theory of ferroelectric ceramics. *Physical Review* **105**, 480 (1957).

43 Lynch, C. S.; Chen, L.; Suo, Z.; McMeeking, R. M.; Yang, W. Crack growth in ferroelectric ceramics driven by cyclic polarization switching. *Journal of Intelligent Materials Systems Structures* **6**, 191-198 (1995).

44 Meng, Z.Y.; Cross, L. E. Determination of the electrostriction tensor components in single-crystal CaF_2 from the uniaxial stress dependence of the dielectric permittivity. *Journal of Applied Physics* **57**, 488-491 (1985).

45 M. C. *Molecular Electronics: From Principle to Practice* (Wiley-Interscience, London, 2007).

46 Haun, M. J.; Zhuang, Z. Q.; Furman, E.; Jang, S. J.; Cross, L. E. Electrostrictive properties of the lead zirconate titanate solid-solution system. *Journal of the American Ceramic Society* **72**, 1140-1144 (1989).

47 Zhang, Q.M.; Pan, W. Y.; Jang, S. J.; Cross, L.E. The pressure dependence of the dielectric response and its relation to the electrostriction. *Ferroelectrics* **88**, 147-154 (1988).

48 Cross, L.E.; Jang, S. J.; Newnham, R.E. Nomura, S.; Uchino, K. Large electrostrictive effects in relaxor ferroelectrics. *Ferroelectrics* **23**, 187-192 (1980).

49 Timco, G.W.; Schloessin, H. H. the effect of high pressure and temperature on the dielectric constant of ferroelectric perovskite ceramic PZT-4. *Ferroelectrics* **11**, 409 (1976).

50 Nishi, R.Y. Effects of one dimensional pressure on the properties of several transducer ceramics. *Journal of the Acoustic Society of America* **40**, 486 (1966).

51 Uchino, K., Nomura, S.; Cross, L. E.; Newnham, R.E.; Jang, S. J. Review: Electrostrictive effect in perovskites and its transducer applications. *Journal of Materials Science* **16**, 569-578 (1981).

52 Shishineh, M.; Sundius, C.; Shrout, T.; Cross, L. E. Direct measurement of electrostriction in perovskite type ferroelectrics. *Ferroelectrics* **50**, 219-224 (1983).

53 Haum, M. J.; Furman, E.; Jang, S. J.; Cross, L. E. Modeling of the electrostrictive, dielectric, and piezoelectric properties of ceramic PT. IEEE, *Transactions on Ultrasonics, Ferroelectrics, and Frequency Control* **36**, 393 (1989).

54 Turik, A.V.; Sidorenko, E. N. In: *Changing dielectric properties of ferroelectric ceramics by mechanical stress*. 533 (IEEE, Transactions on Ultrasonics, Ferroelectrics, and Frequency Control, Montreux, 1998).

55 Steiner, O. *Effect of uniaxial stress on dielectric permittivity of electroceramics*. (EPFL, Lausanne, 1999).

56 Zhou, D.; Kamlah, M.; Munz, D. Effects of bias electric fields on the non-linear ferroelastic behavior of soft lead zirconate titanate piezoceramics. *Journal of the American Ceramic Society* **88**, 867-874 (2005).

57 Cao, H.C.; Evans, A. G. Nonlinear deformation of ferroelectric ceramics. *Journal of the American Ceramic Society* **76**, 890-896 (1993).

58 Ha, M.S.; Jeong, S. J.; Koh, J. H.; Choi, H. B.; Sonh, J. S. Piezoelectric response of compressive loaded multilayer ceramic actuator. *Materials Chemistry and Physics* **98**, 9-13 (2006).

59 Pojprapai, S.; Jones, J. L.; Hoffman, M. domain switching under cyclic mechanical loading in lead zirconate titanate. *Journal of the American Ceramic Society* **89**, 3567-3569 (2006).

60 Yimnirun, R.; Ananta, S.; Ngamjarurojana, A.; Wongsaenmai S. Uniaxial stress dependence of ferroelectric properties of xPMN-(1–x)PZT ceramic systems. *Applied Physic*s *A* **81**, 1227-1231 (2005).

61 Zhang, Q. M.; Zhao, J. Z.; Uchino, K.; Zheng, J. H. Change of the weak-field properties of $Pb(ZrTi)O_3$ piezoceramics with compressive uniaxial stresses and its links to the effect of dopants on the stability of the polarizations in the materials. *Journal of Materials Research* **12**, 226-234 (1997).

62 Chaplya, P.M., Carman, G. P. Compression of piezoelectric ceramic at constant electric field: Energy absorption through non-180° domain-wall motion. *Journal of Applied Physics* **92**, 1504-1510 (2002).

63 Steiner, O.; Tagantsev, A. K.; Colla, E. L.; Setter, N. Uniaxial stress dependence of the permittivity of electroceramics. *Journal of the European Ceramic Society* **19**, 1243-1246 (1999).

64 Robels, U.; Arlt, G. Domain wall clamping in ferroelectrics by orientation of defects. *Journal of Applied Physics* **73**, 3454-3460 (1993).

65 Schultze, W.A.; Ogino, K. Review of literature on aging of dielectrics. *Ferroelectrics* **87**, 361-377 (1988).

66 Turik, A. V.; Sidorenko, E. N. Domain switching and dielectric properties of ferroelectric ceramics. *Ferroelectrics* **222**, 345-350 (1999).

67 Yimnirun, R.; Ananta, S.; Meechoowas, E.; Wongsaenmai S. Effects of uniaxial stress on dielectric properties lead magnesium niobate–lead zirconate titanate ceramics. *Journal of Physics D: Applied Physics* **36**, 1615-1619 (2003).

68 Yimnirun, R. ; Unruan, M.; Laosiritaworn, Y.; Ananta, S. Change of dielectric properties of ceramics in lead magnesium niobate-lead titanate system with compressive stress. *Journal of Physics D: Applied Physics* **39**, 3097-3102 (2006).

69 Yimnirun, R. Change in the dielectric properties of normal and relaxor ferroelectric ceramic composites in BT-PZT and PMN-PZT systems by an uniaxial compressive stress. *Ferroelectrics* **331**, 9-18 (2006).

70 Yimnirun, R.; triamnak, N.;Ngamjarurojana, A.; Laosiritaworn, Y.; Ananta, S. Dielectric properties of $Pb(Zr_{1/2}Ti_{1/2})O_3$–$Pb(Zn_{1/3}Nb_{2/3})O_3$ ceramics under compressive stress. *Ferroelectrics* **355**, 257-263 (2007).

71 Suchanicz, J. Axial pressure effect on a phase transition nature and ferroelectric properties of single crystal $Na_{0.5}Bi_{0.5}TiO_3$. *Journal of Physics and Chemistry of Solids* **62,** 1271–1276 (2001).

72 Suchanicz, J.; Mercurio, J. P.; Marchet, P.; Kruzina, T. V. Axial pressure influence on dielectric and ferroelectric properties of $Na_{0.5}Bi_{0.5}TiO_3$ ceramic. *Physica Status Solidi B* **225**, 459–466 (2001).

73 Suchanicz, J.; Kruzina, V. The effect of axial pressure on domain state and dielectric properties of $Na_{0.5}Bi_{0.5}TiO_3$ and related materials. *Ferroelectrics* **317**, 109–113 (2005).

74 Suchanicz, J.; Rosiek, R.; Mercurio, J. P.; Said, S. Influence of axial pressure on electric properties of $Na_{0.5}Bi_{0.5}TiO_3$–$PbTiO_3$ system. *Ferroelectrics* **300**, 107–116 (2004).

75 Suchanicz, J.; Mercurio, J. P.; Said, S.; Garbarz-Glos, B. Effect of axial pressure on electric properties of Pb-modified $Na_{0.5}Bi_{0.5}TiO_3$ ceramic. *Physica Status Solidi A* **193**, 179-186 (2002).

76 Directive 2002/95/EC of the European Parliament and of the Council. *Official Journal of the European Union* **L37**, 19-23 (2003).

77 Smolenskii, G. A.; Agranovskaya, A. I. Dielectric polarization of a number of complex compounds. *Fizika Tverdogo Tela* **1**, 1562-1572) (1959).

78 Jones, G. O.; Thomas, P. A. Investigation of the structure and phase transitions in the novel A-site substituted distorted perovskite compound $Na_{0.5}Bi_{0.5}TiO_3$. *Acta Crystallografica* **B58**, 168-178 (2002).

79 Vakhrushev, S.B.; Isupov, V. A.; Kvyatkovsky, B. E.; Okuneva, N. M.; Pronin, I. P.; Smolensky, G. A.; Syrnikov, P. P. Phase transitions and soft modes in sodium bismuth titanate. *Ferroelectrics* **63**, 153-160 (1985).

80 Suchanicz, J.; Kwapulinski, J. X-ray diffraction study of the phase transitions in $Na_{0.5}Bi_{0.5}TiO_3$. *Ferroelectrics* **165**, 249-253 (1995).

81 Zvirgzds, J. A.; Kapostinš, P. P.; Zvirgzde, J. V.; Kruzina, T. V. X-ray study of phase transitions in ferroelectric $Na_{0.5}Bi_{0.5}TiO_3$. *Ferroelectrics* **40**, 75-77 (1982).

82 Park, S. E.; Chung, S. J.; Kim, I. T. Ferroic phase transitions in $Na_{1/2}Bi_{1/2}TiO_3$ crystals. *Journal of the American Ceramic Society* **79**, 1290-1296 (1996).

83 Dorcet, V.; Trolliard, G.; Boullay, P. Reinvestigation of phase transitions in $Na_{0.5}Bi_{0.5}TiO_3$ by TEM. Part I: first order rhombohedral to orthorhombic phase transition, *Chemistry of Materials* **20**, 5061-5073 (2008).

84 Trolliard, G.; Dorcet, V. Reinvestigation of phase transitions in $Na_{0.5}Bi_{0.5}TiO_3$ by TEM. Part II: Second Order Orthorhombic to Tetragonal Phase Transition. *Chemistry of Materials* **20**, 5074-5082 (2008).

85 Pronin, I.P.; Syrnikov, P. P.; Isupov, V. A.; Egorov, V. M.; Zaitseva, N. V. Peculiarities of phase transitions in sodium-bismuth titanate. *Ferroelectrics* **25**, 395-397 (1980).

86 Sakata, K.; Masuda, Y. Ferroelectric and antiferroelectric properties of NBT–$SrTiO_3$ solid solution ceramics. *Ferroelectrics* **7**, 347-349 (1974).

87 Glazer, A.M. Classification of tilted octahedra in perovskites. *Acta Crystallographica* **B28**, 3384 (1972).

88 Jones, G.O.; Thomas, P. A. The tetragonal phase of $Na_{0.5}Bi_{0.5}TiO_3$ – a new variant of the perovskite structure. *Acta Crystallographica* **B56**, 426-430 (2000).

89 Shuvaeva, V.A.; Zekira, D.; Glazer, A. M.; Jiang, Q.; Weber, S. M.; Bhattacharya, P.; Thomas, P. A. Local structure of the lead-free relaxor ferroelectric $(K_xNa_{1-x})_{0.5}Bi_{0.5}TiO_3$. *Physical Review B* **71**, 174114 (2005).

90 Noheda, B. Structure and high-piezoelectricity in lead oxide solid solutions. *Current Opinion in Solid State and Material Science* **6**, 27-34 (2002).

91 Dkhil, B.; Kiat, J. M.; Calvarin, G.; Baldinozzi, G.; Vakhrushev, S. B.; Suard, E. Local and long range polar order in the relaxor-ferroelectric compounds $PbMg_{1/3}Nb_{2/3}O_3$ and $PbMg_{0.3}Nb_{0.6}Ti_{0.1}O_3$. *Physical Review B* **65**, 024104 (2002).

92 Kreisel, J.; Bouvier, P.; Dkhil, B.; Thomas, P. A.; Glazer, A. M.; Welberry, T. R.; Chaabane, B.; Mezouar, M. high-pressure scattering of oxides with nanoscale local structure: Application to $Na_{1/2}Bi_{1/2}TiO_3$. *Physical Review B* **68**, 014113 (2003).

93 Petzelt, J.; Kamba, S.; Fabry, J.; Noujni, D.; Porokhonsky, V.; Pashkin, A.; Franke, I.; Roleder, K.; Suchanicz, J.; Klein, R.; Kugel, G. E. Infrared, Raman and high-frequency dielectric spectroscopy and the phase transitions in $Na_{1/2}Bi_{1/2}TiO_3$. *Journal of Physics: Condensed Matter* **16**, 2719-2713 (2004).

94 Spreitzer, M.; Valant, M.; Suvorov, D. Sodium deficiency in $Na_{0.5}Bi_{0.5}TiO_3$. *Journal of Materials Chemistry* **17**, 1-9 (2007).

95 Suchanicz, J.; Mercurio, J. P.; Konieczny, K.; Kruzina, T. V. Influence of compressive stress on electric properties of $Na_{0.5-x}K_xBi_{0.5}TiO_3$ solid solutions ($x \leq 0.1$). *Ferroelectrics* **290**, 161-167 (2003).

96 Bovtun, V.; Kamba, S.; Kempa, M.; Tkač, O.; Goian, V.; Petzelt, J.; Li, J.; Wang, H.; Spreitzer, M.; Suvorov, D. Microwave and terahertz dielectric properties of $Bi_{1.5}Zn_{1-x}M_xNb_{1.5}O_{7-x}F_{yx}$ (M = Li, Ca, Zn) and $Na_{0.5}Bi_{0.5}TiO_3$-$NaTaO_3$ Ceramics. In: *The 5th International Conference on Microwave Materials and Their Applications* (Hangzhou, 2008).

97 Chen, Z. X.; Zhang, X. L.; Cross, L. E. Low-Temperature Dielectric Properties of Ceramic Potassium Tantalate ($KTa0_3$). *Journal of the American Ceramic Society* **66**, 511-515 (1983).

98 Elkechai, O.; Manier, M.; Mercurio, J. P. $Na_{0.5}Bi_{0.5}TiO_3$–$K_{0.5}Bi_{0.5}TiO_3$ (NBT–KBT) system: A structural and electrical study, *Physica Status Solidi A* **157**, 499-506 (1996).

99 Hiruma, Y.; Aojagi, R.; Nagata, H.; Takenaka, T. Ferroelectric and piezoelectric properties of $(Bi_{1/2}K_{1/2})TiO_3$ ceramics. *Japanese Journal of Applied Physics* **44**, 5040-5044 (2005).

100 Žnidaršič, M.; Spreitzer, M.; Škapin, S.; Suvorov, D. *In preparation*.

101 Merlet, C. Quantitative electron probe microanalysis: new accurate $\Phi(\rho z)$ description. *Mikrochimica Acta* **12**, 107-113 (1992).

102 Ziebold, T. O. Precision and sensitivity in electron microprobe analysis. *Analytical Chemistry* **39**, 858-861 (1967).

103 Drowart, J.; Chatillon, C.; Hastie, J.; Bonnel, D. High-temperature mass spectrometry: instrumental techniques, ionization cross-sections, pressure measurements, and thermodynamic data. *Pure and Applied Chemistry* **77**, 683-737 (2005).

104 Kennedy, B. J.; Prodjosantoso, A. K.; Howard, C. J. Powder neutron diffraction study of the high temperature phase transitions in $NaTaO_3$. *Journal of Physics: Condensed Matter* **11**, 6319–6327 (1999).

105 Shannon, R. D. Revised effective ionic radii and studies of interatomic distances in halides and halcogenides. *Acta Crystallographica* **A32**, 751–767 (1976).

106 Eitel, R. E.; Randall, C. A.; Shrout, T. R.; Rehrig, P. W.; Hackenberger, W.; Park, S. E. New high temperature morphotropic phase boundary piezoelectrics based on $Bi(Me)O_3$–$PbTiO_3$ ceramics. *Japanese Journal of Applied Physics* **40**, 5999–6002 (2001).

107 Jones, G. O.; Kreisel, J.; Thomas, P. A. A structural study of the $(Na_{1-x}K_x)_{0.5}Bi_{0.5}TiO_3$ perovskite series as a function of substitution (x) and temperature. *Powder Diffraction* **17**, 301-319 (2002).

108 Chen, X. M.; Lu, Y. T.; Jin, D. Z.; Liu, X. Q. Dielectric and Ferroelectric Characterization of Na(Ta,Nb)O_3 Solid Solution Ceramics. *Journal of Electroceramics* **15**, 21–26 (2005).

109 Michel, R. H.; Liferovich, R. P. A structural study of the perovskite series $Ca_{1-x}Na_xTi_{1-x}Ta_xO_3$. *Journal of Solid State Chemistry* **177**,4420–4427 (2004).

110 Nalbandyan V. B.; Shukaev, I. L. Na_2O-ZrO_2-M_2O_5(M-Nb,Ta) systems. *Russian Journal of Inorganic Chemistry (Engl. Translation)* **33**, 1715–1716 (1988).

111 Roth, R. S.; Parker, H. S.; Brower, W. S.; Waring, J. L. Phase equilibriums, crystal chemistry, and crystal growth of alkali oxide-metal oxide systems. In: Van Gool, W. (ed.) *Fast Ion Transparent Solids, Solid State Batteries Devices, Proceedings of NATO Advised Study Instructions.* 217-232 (Amsterdam, 1973).

112 Said, S.; Mercurio, J.-P. Relaxor behaviour of low lead and lead free ferroelectric ceramics of the $Na_{0.5}Bi_{0.5}TiO_3$–$PbTiO_3$ and $Na_{0.5}Bi_{0.5}TiO_3$–$K_{0.5}Bi_{0.5}TiO_3$ systems. *Journal of the European Ceramic Society* **21**, 1333–1336 (2001).

113 Kajfez, D.; Guillon, P. Dielectric resonator (Artech House, Dedham, 1986).

114 Suchanicz, J. Time evolution of the phase transition in $Na_{0.5}Bi_{0.5}TiO_3$. *Ferroelectrics* **200**, 319-325 (1997).

115 Ulinzheyev, A. V.; Fesenko, E. G.; Smotrakov, V.G. Twinning in ferroelastic sodium tantalite crystals. *Ferroelectrics* **111**, 261–265 (1990).

116 Suchanicz, J.; Mercurio, J. P.; Sais, S. Axial pressure effect on dielectric and ferroelectric properties of $K_{0.5}Bi_{0.5}TiO_3$ ceramics. *Ferroelectrics* **290**, 169-175 (2003).

117 Pronin, I. P.; Parfenova, N. N.; Zaitseva, N. V.; Isupov, V. A.; Smolenskii, G. A. Phase-transitions in solid-solutions of Na-Bi and K-Bi titanates. *Soviet Physics of Solid State* **24**, 1860-1863 (1982).

118 Yamada, Y.; Akutsu, T.; Asada, H.; Nozawa, K.; Hachiga, S.; Kurosaki, T.; Ikagawa, O.; Fujiki, H.; Hozumi, K.; Kawamura, T.; Amakawa, T.; Hirota, K.; Ikeda, T. Effect of B-ions substitution in $[(K_{1/2}Bi_{1/2})$-$(Na_{1/2}Bi_{1/2})](Ti$-$B)O_3$ system with B=Zr,$Fe_{1/2}Nb_{1/2}$, $Zn_{1/3}Nb_{2/3}$ or $Mg_{1/3}Nb_{2/3}$. *Japanese Journal of Applied Physics* **34**, 5462-5466 (1995).

119 Zhao, S.; Li, G.; Ding, A.; Wang, T.; Yin, Q. Ferroelectric and piezoelectric properties of $(Na, K)_{0.5}Bi_{0.5}TiO_3$ lead free ceramics. *Journal of Physics*: *Applied Physics* **39**, 2277-2281 (2006).

120 Hou, Y. D.; Hou, L.; Huang, S. Y.; Zhu, M. K.; Wang, H.; Yan, H. Comparative study of $K_{0.5}Bi_{0.5}TiO_3$ nanoparticles derived from sol–gel hydrothermal and sol–gel routes. *Solid State Communications* **137**, 658-661 (2006).

121 Li, Z. F.; Wang, C. L.; Zhong, W. L.; Li, J. C.; Zhao, M. L. Dielectric relaxor properties of $K_{0.5}Bi_{0.5}TiO_3$ ferroelectrics prepared by sol–gel method. *Journal of Applied Physics* **94**, 2548-2552 (2003).

122 Wada, T.; Toyoike, K.; Imanaka, J.; Matsuo, Y. Dielectric and piezoelectric properties of $(A_{0.5}Bi_{0.5})TiO_3$–$ANbO_3$ (A = Na, K) systems. *Japanese Journal of Applied Physics* **40**, 5703-5705 (2001).

123 Gao, F.; Zhang, C.S.; Zhao, M.; Wang, W. M.; Tian, C. S. Microstructure and piezoelectric properties of $(Na_{0.85}K_{0.15})_{(0.5)}Bi_{0.5}TiO_3$ lead-free ceramics prepared by tape casting processing. *Journal of Inorganic Materials* **21**, 1134-1140 (2006).

124 Himura, Y.; Aojagi, R.; Nagata, H.; Takenaka, T. Ferroelectric and piezoelectric properties of $(Bi_{1/2}K_{1/2})TiO_3$ ceramics. *Japanese Journal of Applied Physisics* **44,** 5040-5044 (2005).

125 Hou, L.; Hou, Y. D.; Song, X. M.; Zhu, M. K.; Wang, H.; Yan, H. Sol–gel-hydrothermal synthesis and sintering of $K_{0.5}Bi_{0.5}TiO_3$ nanowires. *Materials Research Bulletin* **41**, 1330-1336 (2006).

126 Bao, N. Z.; Feng, X.; Lu, X. H.; Yang, Z. H. Study of the formation and growth of potassium titanate whiskers. *Journal of Material Science* **37**, 3035-3043 (2002).

127 LI, G. L.; Wang, G. H.; Hong, J. M. Synthesis and characterization of $K_2Ti_6O_{13}$ whiskers with diameter on nanometer scale. *Journal of Materials Science Letters* **18**, 1865– 1867 (1999).

128 Hou, L.; Hou, Y. D.; Song, X. M.; Zhu, M. K.; Wang, H.; Yan, H. Sol–gel-hydrothermal synthesis and sintering of $K_{0.5}Bi_{0.5}TiO_3$ nanowires. *Materials Research Bulletin* **41**, 1330-1336 (2006).

129 Wada, T.; Fukui, A.; Matsuo, Y. Preparation of $(K_{0.5}Bi_{0.5})TiO_3$ ceramics by polymerized complex method and their properties. *Japanese Journal of Applied Physics* **41**, 7025-7028 (2002).

130 Chiang, Y.-M.; Birnie, D. P.; Kingery, W. D. *Physical Ceramics: Principles for Ceramic Science and Engineering* (John Wiley & Sons, Inc., New York, 1997).

131 Isupov, V. A. Ferroelectric $Na_{0.5}Bi_{0.5}TiO_3$ and $K_{0.5}Bi_{0.5}TiO_3$ perovskites and their solid solutions. *Ferroelectrics* **315**, 123-147 (2005).

132 Arlt, G. Twinning in ferroelectric and ferroelastic ceramics - stress relief. *Journal of Materials Science* **25**, 2655-2666 (1990).

133 Zhang, X. L.; Chen, Z. X.; Cross, L. E.; Schulze, W. A. Dielectric and piezoelectric properties of modified lead titanate zirconate ceramics from 4.2K to 300K. *Journal of Materials Science* **18**, 968-972 (1983).

134 Zhang, Q. M.; Wang, H.; Kim, N.; Cross, L. E. Direct evaluation of domain-wall and intrinsic contributions to the dielectric and piezoelectric response and their temperature-dependence on lead-zirconate-titanate ceramics. *Journal of Applied Physics* **75**, 454-459 (1994).

135 Zhurova, E. A.; Ivanov, Y.; Zavodnik, V.; Tsirelson, V. Electron density and atomic displacements in $KTaO_3$. *Acta Crystallographica* **B56**, 594-600 (2000).

136 Iwauchi, K.; Ikeda, Y. Magnetic and dielectric properties of $Ba_2Ti_4FeO_{13}$–$K_2Ti_6O_{13}$. *Physica Status Solidi A* **92**, 623-629 (1985).

137 Sommer, R.; Yushin, N. K.; VanderKlink, J. J. Dielectric susceptibility of PMN under DC bias. *Ferroelectrics* **107**, 307-312 (1992).

Index of figures

Index of tables

Appendix

Publications

Original scientific article

1. SPREITZER, Matjaž, KOENIG, Jakob, JANČAR, Boštjan, SUVOROV, Danilo. Enhanced tunable characteristics of the $Na_{0.5}Bi_{0.5}TiO_3$–$NaTaO_3$ relaxor-type system. *IEEE trans. ultrason. ferroelectr. freq. control*, 2007, vol. 54, no. 12, pp 2617-2622.

2. KOENIG, Jakob, JANČAR, Boštjan, SUVOROV, Danilo. New $Na_{0.5}Bi_{0.5}TiO_3$–$NaTaO_3$-based perovskite ceramics. *J. Am. Ceram. Soc.*, 2007, vol. 90, no. 11, pp 3621-3627.

3. KOENIG, Jakob, SPREITZER, Matjaž, JANČAR, Boštjan, SUVOROV, Danilo, SAMARDŽIJA, Zoran, POPOVIĆ, Arkadije. The thermal decomposition of $K_{0.5}Bi_{0.5}TiO_3$ ceramics. *J. Eur. Ceram. Soc.*, 2009, pp 1695-1701.

Published scientific conference contribution (invited lecture)

4. KOENIG, Jakob, SPREITZER, Matjaž, JANČAR, Boštjan, SUVOROV, Danilo. Structural and dielectric properties of the $Na_{0.5}Bi_{0.5}TiO_3$–$NaTaO_3$ ceramic system. NAIR, K. Madhavan (ed.). *Collection of papers presented at: MS&T'08*, Materials Science & Technology, 2008 Conference & Exhibition, October 5-9, 2008, Pittsburgh, Pennsylvania. *Ceramic Transactions vol. 204*, 2008, pp 121-127.

Published scientific conference contribution

5. SPREITZER, Matjaž, KOENIG, Jakob, JANČAR, Boštjan, SUVOROV, Danilo. $Na_{0.5}Bi_{0.5}TiO_3$-based voltage-tunable materials. TSURUMI, Takaaki (ed.). *ISAF 2007 : proceedings of the 16th IEEE International Symposium on Applications of Ferroelectrics, Nara City, Japan, May 27-31,2007*. Tokyo: The Institute of Electrical and Electronic Engineers: Ultrasonic, Ferroelectrics and Frequeny Control Society, 2007, pp 202-204.

Published scientific conference contribution abstract

6. KOENIG, Jakob, SUVOROV, Danilo. Kristalna struktura in električne lastnosti trdne raztopine $Na_{0,5}Bi_{0,5}TiO_3$ in $NaTaO_3$ = Crystal structure and electrical properties of $Na_{0.5}Bi_{0.5}TiO_3$ in $NaTaO_3$. JENKO, Monika (ed.). 14. konferenca o materialih in tehnologijah = 14th Conference on Materials and Technology, 16-18 October, 2006, Portorož, Slovenia. *Program in knjiga povzetkov*. Ljubljana: Inštitut za kovinske materiale in tehnologije, 2006, pp 50.

7. KOENIG, Jakob, JANČAR, Boštjan, SUVOROV, Danilo. Povečanje vpliva aksialne tlačne obremenitve na dielektrične lastnosti $Na_{0,5}Bi_{0,5}TiO_3$ z dodajanjem $NaTaO_3$ = Increasing the

effect of axial pressure on the permittivity of $Na_{0.5}Bi_{0.5}TiO_3$ by adding $NaTaO_3$. JENKO, Monika (ed.). 15. konferenca o materialih in tehnologijah = 15th Conference on Materials and Technology, 8-10 October, 2007 Portorož, Slovenia. *Program in knjiga povzetkov*. Ljubljana: Inštitut za kovinske materiale in tehnologije, 2007, pp 39.

8. KOENIG, Jakob, JANČAR, Boštjan, SUVOROV, Danilo. Influence of axial pressure on dielectric properties of $Na_{0.5}Bi_{0.5}TiO_3$–$NaTaO_3$ ceramics. SRDIĆ, Vladimir V. (ed.), RANOGAJEC, Jonjaua (ed.). The Seventh Students' Meeting - SM-2007 Processing and Application of Ceramics, December 6-8, 2007. *Programme and book of abstracts*. Novi Sad: Faculty of Technology, 2007.

9. KOENIG, Jakob, JANČAR, Boštjan, SUVOROV, Danilo. Phase formation and electrical properties of $Na_{0.5}Bi_{0.5}TiO_3$–$NaTaO_3$ solid solutions. 10^{th} International Conference and Exhibition of the European Ceramic Society, June 17-21, 2007, Berlin. *Programme*. ECERS, 2007.

10. SUVOROV, Danilo, SPREITZER, Matjaž, KOENIG, Jakob, ŽNIDARŠIČ, Mojca, ŠKAPIN, Srečo D., JANČAR, Boštjan. Functionalization of $Na_{0.5}Bi_{0.5}TiO_3$ for applications in electronic devices: [invited talk]. MS&T'08, Materials Science & Technology, 2008 Conference & Exhibition, October 5-9, 2008, Pittsburgh, Pennsylvania. *Abstract book*., 2008, pp 94-95.

11. KOENIG, Jakob, JANČAR, Boštjan, SUVOROV, Danilo. Decomposition of $K_{0.5}Bi_{0.5}TiO_3$. Electroceramics XI, August 31 - September 4, 2008, Manchester, UK. *Abstracts and CD proceedings*. 2008.

12. SPREITZER, Matjaž, KOENIG, Jakob, JANČAR, Boštjan, SUVOROV, Danilo. The voltage-tunability of polar phases in $Na_{0.5}Bi_{0.5}TiO_3$-based compounds. ISIF 2008, 20^{th} International Symposium on Integrated Ferroelectrics, 9-12 June 2008, Biopolis, Singapore. *Abstracts*. 2008, pp 2.